Discovering Relationship of Atomistic Structure to Generate

Stishovite Nucleation Using Convolutional Neural Networks

by

Jonathan Christen

A Dissertation Presented in Partial Fulfillment
of the Requirements for the Degree
Master of Science

Approved November 2021 by the
Graduate Supervisory Committee:

Jay Oswald, Chair
Christopher Muhich
Houlong Zhuang

ARIZONA STATE UNIVERSITY

December 2021

ABSTRACT

This research seeks to answer the question if there is a singular relationship between stishovite nucleation and the atomistic structure of the preshocked amorphous SiO_2. To do this a stishovite manufacturing method is developed in which 1,152 samples were produced. The majority of these samples did crystallize. The method was produced through two rounds of experiments and fine-tuning with the pressure damp, temperature damp, shock pressure using an NPHug fix, and sample origin. A new random atomic insertion method was used to generate a new and different SiO_2 amorphous structure not before seen within the research literature. The optimal values for shock were found to be 60 GPa for randomly atom insertion samples and 55 GPa for quartz origin samples. Temperature damp appeared to have a slight effect optimizing at 0.05 ps and the pressure damp had no visible effect, testing was done with temperature damp from 0.05 to 0.5 ps and pressure damp from 0.1 to 10.0 ps. There appeared to be significant randomness in crystallization behavior.

The preshocked and postnucleated samples were transformed into Gaussian fields of crystal, mass, and charge. These fields were divided and classified using a cut-off method taking the number of crystals produced in portions of each simulation and classifying each potion as nucleated or non-nucleated. Data in which some nucleation but not a critical amount was present was removed constituting 2.6% to 20.3% of data in all tests. A max method was also used which takes only the maximum portions of each simulation to classify as nucleating. There are three other variables tested within this work, a sample size of 18,000 or 72,728 atoms, Gaussian variance of 1 or 4 Å, and Convolutional neural network (CNN) architecture of a garden verity or all convolution along with the portioning classification method, sample origination, and Gaussian field type. In total 64 tests were performed to try every combination of variable.

No significant classifications were made by the CNNs to nucleation or non-nucleation portions. The results clearly confirmed that the data was not abstracting to atomistic structure and was random by all classifications of the CNNs. The all convolution CNN testing did show smoother outcomes in training with less fluctuations. 59% of all validation accuracy was held at 0.5 for a random state and 84% was within ± 0.02 of 0.5. It is conclusive that prenucleation structure is not the sole predictor of nucleation behavior. It is not conclusive if prenucleation structure is a partial or non-factor within nucleation of stishovite from amorphous SiO_2.

DEDICATION

To my Lord, I never thought that we would go this far together. I am very grateful.

ACKNOWLEDGEMENTS

LIST OF TABLES

LIST OF FIGURES

Chapter 1

INTRODUCTION

This research is exploring the nucleation of stishovite, a crystalline octahedral form of SiO_2 from amorphous glasses when subjected to rapid pressurization or high pressure. The goal is to discover whether a relationship exists between the prenucleation atomic structure of the glass and nucleation behavior of the glass.

1.1 Application

1.1.1 Glass Under Hypervelocity Ballistic Impacts

Figure 1 is an example of glass that has experienced hypervelocity (impacts above 3350 ft/s Roshdy G.S. Barsoum 20) impacts from projectiles in laboratory settings using spherical projectiles 500 μm in size, at velocities of 5 to 6 km/s. Pressures from impacts of these kinds range in the magnitude of one and ten of gigapascal. The cracking behavior of the glass is shown in figure 2, cone shaped cracking occurs from the pressure wave that occurs upon impact. As the projectile impacts the glass a pressure wave proceeds from the impact site conically also known as Hertzian cracking. The pressure wave compresses the glass shattering it as it moves to the end of the sample, and can produce a powered silica oxide on the nanoscale. If impact conditions are favorable non reversible densification will occur within the sample resulting from a phase change of fused silica into crystallized stishovite. The glass often seeks to
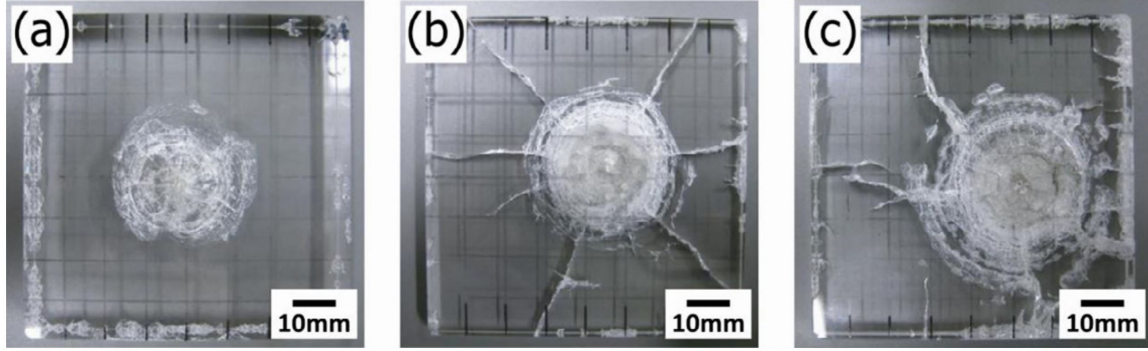
Figure 1. Broken glass samples. (a) t=15 mm, v=6.8 km/s, stainless-steel projectile, (b) t=5 mm, v=6.9 km/s, stainless-steel projectile, (c) t=10 mm, v=6.8 km/s, platinum projectile, t is glass thickness and v is velocity of projectile Kawai et al. 2013.

expand from the shattering process and cannot relieve stress due to the incoming projectile Kawai et al. 2013.

As the projectile passes through the glass it is squeezed in by the glass, this motion forces contact of the shattered glass around the projectile. Chemical reactions and friction take place across the projectile surface as it passes through the glass on the projectile surface eroding it. Some of the silica oxide may be in a plasma state from the energies of friction and impact. During the process internal fractures are propagating through the glass and lateral cracks propagate outwards from impact. The entire process often takes 10 to 40 ns and is difficult to study empirically, often this is done through xray imaging and high speed photography Roshdy G.S. Barsoum 20; Kawai et al. 2013.

The stishovite is produced within pure silica glass in the 40 to 63 GPa region of shock pressure and serves additional benefits to projectile stopping. It is has a hard crystalline structure with melting temperature that exceeds fused silica. This forms in small crystals that nucleate within the fused silica and often do so incompletely Yuan Shen and Reed 2016. Stishovite can form in common soda-lime glass, this is often tested for empirically Grujicic, Bell, Pandurangan, et al. 2011.
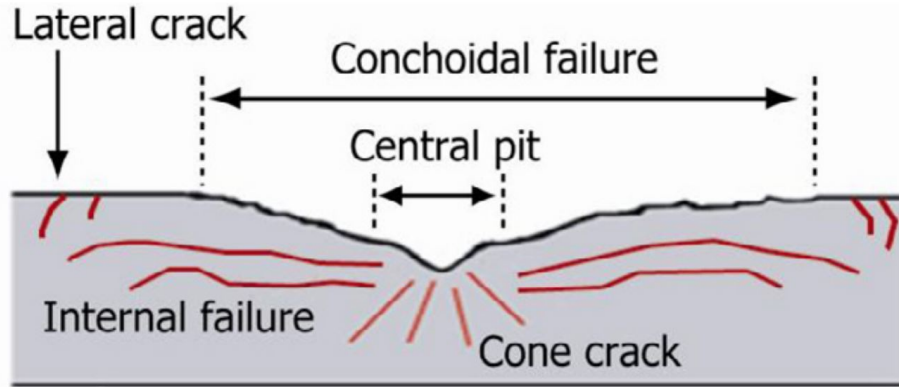
Figure 2. Crack propagation of glass from hypervelocity impact Kawai et al. 2013.

1.1.2 Defence

Modern warfighting is wrought with weapons of ever increasing levels of energy and velocity. Weapon systems have reached the point of ballistics with impact velocities in the hypervelocity region; Velocities above 3350, 3500, and 5000 $\frac{ft}{s}$ for artillery, tank launched projectiles, and small arms respectively. Shape charges operate at speeds up to 16,000 $\frac{ft}{s}$ for their copper conical payload. Silica oxide based glass is commonly used in defense application for its high strength, transparency, and energy dissipation mechanisms when subjected to extreme loading such as hypervelocity impact. It has been tested within a shield capacity since World War II. Often the glass is paired with traditional defence systems as a first layer to absorb much of a projectile's kinetic energy Roshdy G.S. Barsoum 20.

1.1.3 Space

With an estimated 500,000, 1 to 10 cm sized pieces of spaced debris and 100 million pieces of debris under 1 cm in diameter impacts are a very common occurrence in earth

orbit. In space these are often hypervelocity impacts due to the relative velocities between objects in space. Impacts have been thoroughly studied on a spaceship's metal haul but have been underrepresented in studies of glass used in thermal, optical, and electronic components of a spacecraft. The science in space impacts is similar to that of warfighting and has great cross application to that field Kawai et al. 2013.

1.1.4   High Power Laser Lenses

High powered lasers undergo stishovite crystallization due to the high temperatures glass impurities experience. Impurities within a glass lens has a higher electromagnetic radiation absorptivity, this increased absorptivity leads to higher temperatures during laser firing. This massive thermal shift within the glass at small time scales leads to a pressure wave accompanying the thermal shift. In the same way a pressure wave propagates from a hypervelocity impact a thermally generated pressure wave propagates spherically, resulting in small locally generated crystals. Pressures for stishovite nucleation from lasers in fused silica are 10 to 20 GPa.

Figure 3a displays a small lens with advanced stishovite formation from high energy laser pulses. This is can happen for commercial or military applications, including wafer manufacturing technology and laser weapon systems. Figure 3b shows the stishovite on the nanometer scale, at this resolution individual stishovite crystals are visible. The application is to improve manufacturing methods that minimises the prenucleation structures of stishovite within the glass Salleo et al. 2003.
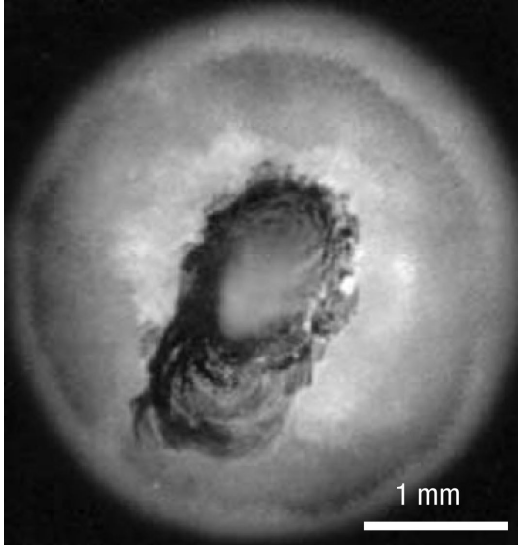
(a) Lens with stishovite formation seen as large cloud in center of lens. This is caused by high powered lasers.
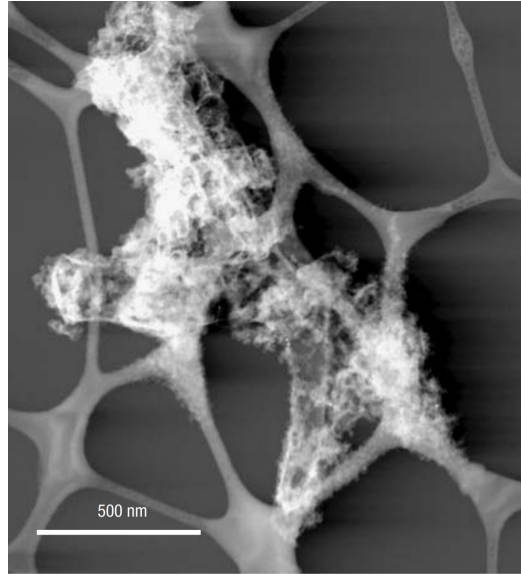
(b) Lens with stishovite formation at nanometer scale.

Figure 3. Figures showing stishovite formation Salleo et al. 2003.

1.1.5   Use Case

By understanding how nucleation occurs within glass it maybe possible to develop glasses in which stishovite formation occurs in a controlled form. This may mean more stishovite growth for impact scenarios and as minimal as possible for laser lenses. Understanding if a nucleation inducing structure exists can be a key step in the manufacture of glasses to this end.

1.2 Types of SiO$_2$ Structure

1.2.1 Fused Silica Glass

Silica oxide glass is one of the most common materials to daily life; It is uses in nearly all buildings, cookware, electronic devices, measuring devices, and automobiles. Fused silica glass is mixed with other compounds in commercial applications of soda lime glass: Na$_2$O, Al$_2$O$_3$, CaO, and trace elements Alexander et al. 2008. Other forms of glass found commonly in the modern world include lead crystal with a PbO additive to increase the reflectively of the glass. Commonly found in dishware from the last century, uranium glass known for its beautiful jade green color and is composed of an U$_3$O$_8$ additive Tepfenhart 2021. For the purposes of this thesis only pure silica glass will be studied.

Amorphous SiO$_2$ or pure fused silica glass has the lowest melting temperature of all silica oxide structures. It consist of a disordered tetrahedral structure with short range periodicity but no long range periodicity. This short range order is a function of bonding behaviors of Si and O. The O can be bridging or non-bridging, this is a unique feature of amorphous silica glass. The structure itself is a thermodynamically metastable state between a liquid and crystalline structure Biswas et al. 2018.

1.2.2 Quartz

Quartz is common to the earth's crust and is used in tools, surface finishing, glass production, and artwork. It consists of a tetrahedral or four-fold coordinated structure, with bond an average bond angle of $151 \pm 12°$. The structure in two dimensions is
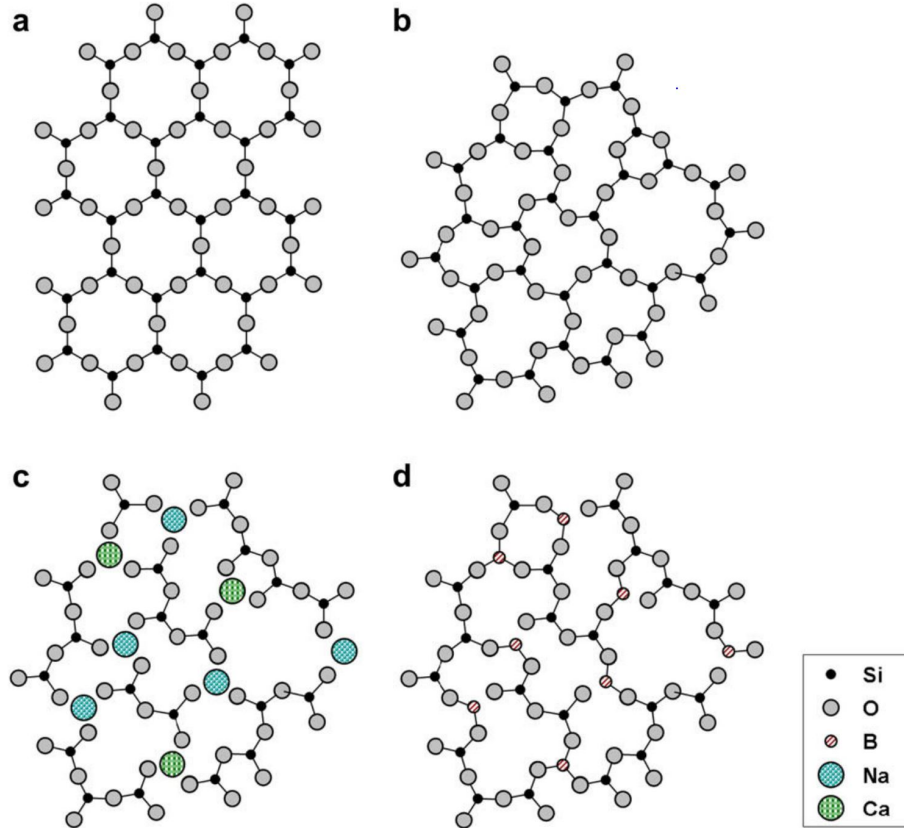
Figure 4. Various glass structures in 2D. (A) quartz (B) fused silica (C) fused silica with sodium and calcium (D) fused silica with boron Alexander et al. 2008

shown in figure 5 image (A). The average Si-O bond length of quartz is 1.8 Å with a density of $2.32\frac{\text{g}}{\text{cm}^3}$ at standard pressure standard temperature Tucker et al. 2005; Alexander et al. 2008.

1.2.3 Stishovite

Stishovite is a rare earth form of silica oxide that is found in meteorite creators, thermonuclear blasts, and earth's mantel. The structure of stishovite is six-fold coordinated silica oxide, the structure is displayed as an octahedral and is known by its eight faces and six edges show in figure 5 Wakai 201. The average bond angle
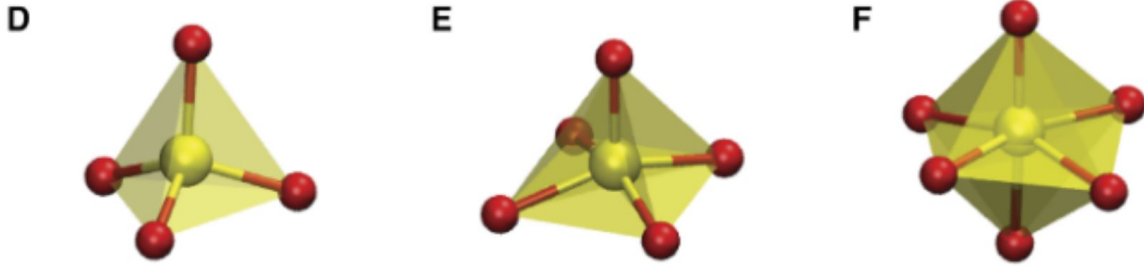
Figure 5. (E) tetrahedral crystalline quartz structure, four-fold (F) five-fold pyramidal crystalline structure (G) six-fold crystalline stishovite, Wakai 201

of stishovite is 90° and the average density at atmospheric pressure atmospheric temperature is $4.29\frac{g}{cm^3}$. The density is nearly twice that of amorphous glass at atmospheric pressures and temperatures Alexander et al. 2008.

The common creation of stishovite on earth's surface is at meteorite impacts or thermonuclear blasts. The extreme pressures and temperatures associate with these subsecond events result in the transformation of quartz or amorphous glass into stishovite El Goresy et al. 2004; Wakai 201; Lyzenga, Ahrens, and Mitchell 1983. A laboratory method that approximates this is to use a high power laser to generate the high pressures and temperatures to form stishovite. The laser generates the high pressure from the thermal shock as quartz or amorphous silica absorbs the intense electromagnetic radiation Salleo et al. 2003. Other methods of production include using a gas gun to fire small projectiles with glass tips or glass impact cites to generate the pressures needed to form stishovite Alexander et al. 2008. The earth's mantel is stishovite plentiful due to the extreme pressures and temperatures present which force SiO_2 into a stishovite form Millot et al. 2015.

1.3   Molecular Dynamics

1.3.1   Potential

Various potentials have been used to model SiO_2 using classical MD. Many of theses have been ever compounding on previous work to account for the unusual effects high pressure shocks in the tens of gigapascals Shen and Reed 2016; Cormack. and Segre 2006; Müser and Binder 2001; Beest van B. W. H. and R. A. 1990.

1.3.1.1   BKS Potential

The first known attempt for research into a potential for stishovite formation is done by Beest van B. W. H. and R. A. 1990 in consisting of coulombic term and covalent term in Buckingham form,

$$\Phi_{ij} = \frac{q_i q_j}{r_{ij}} + A_{ij} e^{-b_{ij} r_{ij}} - \frac{C_{ij}}{r_{ij}^6}$$

Where A_{ij} is a short range parameter to model electrical potential amplitude between various kinds of atoms in eV, b_{ij} is a decay term given in Å^{-1} to fit electrical potential decay, e is Coulomb's constant, C_{ij} is the coulombic repulsion term given in eV Å^6, q_i and q_j are the fitted atomic charges, and r_{ij} which represents the distance between atoms in Å. The potential itself is fitted to model empirical crystallographic behavior. It closely aligns with force field predictions for empirical bulk parameters of SiO_2 for most regions of study with some miss alignment toward the extreme valves of the parameters. Similar to most of the following potentials this potential modeled bonding behavior between tetrahedral network oxides including Al-O and P-O.

One of the notable features of SiO_2 potentials started with this publication in 1990,

the use of non physical electron bonding charges of 1.2 and -2.4 for silica and oxygen respectively. The use of non physical charges is to fit the potential to model empirical behavior Beest van B. W. H. and R. A. 1990. Other potentials include early work by Tjabane and Lowther 1999, forming stishovite from quartz at various temperatures and pressures, Ahrens 2002 with work on terrestrial mantel behavior at pressures up to 200 GPa, Pedone et al. 2006 with work into quantum simulation of silica and other oxides, and Shen and Reed 2016 with large scale work into polymorphic behavior of shocked amorphous and quartz structured silica.

1.3.2   Stishovite Formation

Shocking various kinds of silica glass samples has been done empirically and computationally. Often these tests are done physically upon pure or impure silica glass, most notably soda lime glass using lasers or ballistic impacts. The large scale ballistic impacts render the work unable to accurately identify atomic behavior during shock events. In the last century much of this behavior was inferred through x ray imaging, high speed photography, and post shock analyses. Empirical research included: crystallographic, phase transformation, impact, thermal properties, and mechanical behavior studies Roshdy G.S. Barsoum 20; Salleo et al. 2003; El Goresy et al. 2004; Osako and Kobayashi 1979; Gibbons and Ahrens 1971; Alexander et al. 2008; Tracy, Turneaure, and Duffy 2018.

MD simulations of silica glass shock behavior allows for more in depth analysis of transition behavior. Do to the extremely small timescales, empirical simulations struggle to show transition behavior on an atomic level. Much of this work includes stishovite formation studies, nucleation conditions, crystallographic behavior, and
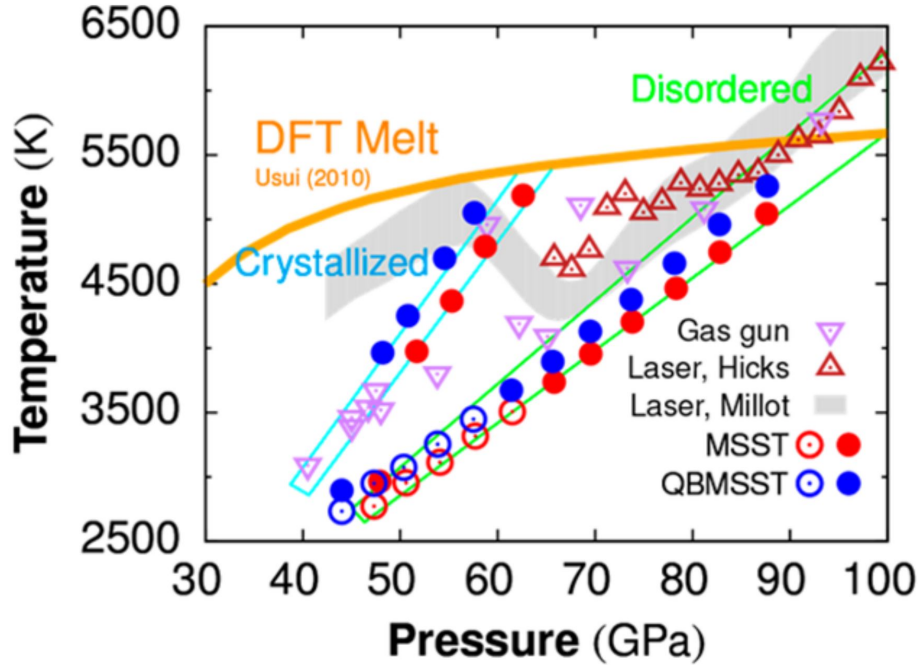
Figure 6. Graph showing the most exhaustive glass to stishovite pressure vs temperature graph in the literature. Diagonal bands of pressure and temperature that crystallization and non crystallization occurs within are shown by the blue and green lines respectively Yuan Shen and Reed 2016.

transition behavior. Properties studied include: mechanical moduli, elasticity, thermal expansion coefficient, and ultimate stresses. Some of this work includes amorphization of stishovite under extreme tension. There is a great deal of overlap between empirical and MD studies, MD work uses empirical studies as a source of parameter tuning and to validate results Beest van B. W. H. and R. A. 1990; Cormack. and Segre 2006; Osako and Kobayashi 1979; Gibbons and Ahrens 1971; El Goresy et al. 2004; Templeton. and Bishnoi 2011; Wakai 201.

A unique behavior occurs during the formation of stishovite that has been well recorded in the research, that the phase transformation is a function of pressure. Temperature change is function of the shock pressure and stishovite formation. No analytical equation has been derived to model this function but there appears to be a

strong correlation to this effect across multiple studies mentioned above. After quartz or glass are shocked it tends to fall within one of the bands whether crystallized or non crystallized.

Figure 6 shows this relationship in great detail. Crystallized simulations generally experience high temperatures and have an effective range up to 63 GPa, at which point the fused silica fails to form stishovite and falls within a disordered state. Fused silica which does not melt continues in a disordered state to higher shock pressure Yuan Shen and Reed 2016.

1.4   CNNs in MD

1.4.1   Gaussian Fields

Gaussian functions are commonly used to prepare MD samples for a CNN. The atomic position data is not transferable directly into a CNN as it is positional data, whereas a CNN uses image data. Gaussian fields transform positional data into image data by approximating the point data as an exponential function across a grid space. This is shown in figure 7 which is taken out of work by Ryczko et al. 2018, the images shows a single point defect of a missing atom with a dashed circle were the atom should be using a Gaussian field.

Most of the literature uses Gaussian functions to transform positional data into image data. Other methods did included creating binary grid fields that were set to one if an atom was in the grid space and zero with no atoms in the space. Atom class was done through the use of multiple grid fields, layering them like RGB grids. This

method was done in two and three dimensions one of which used gradient values for atoms instead of binary values Singh et al. 2018; Fukuya and Shibuta 2020.

1.4.2 CNN

Most applications of CNNs are based upon the matching the input to a known output. Often the problem in hard sciences, such as MD is to increase the speed at which a model based on physical principals can achive a value by supplementing it for an ML model and training this machine learning (ML) model to be a replacement or aid to the physical model. Often simulations that are small in size are done using density functional theory (DFT), the small simulations were directly used for training and validation sets after reviving a Gaussian field treatment. The quantity of small simulations was in the order of 10^3 to 10^4 Chmiela et al. 2017; Singh et al. 2018.
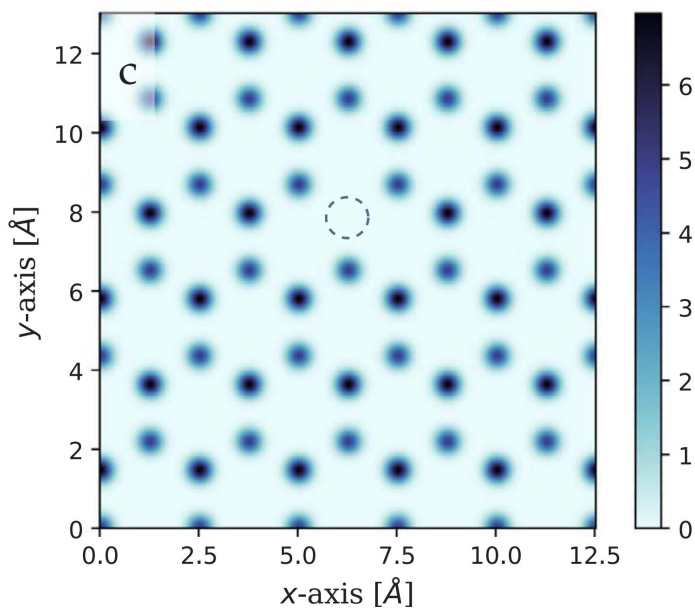
Figure 7. Example of Gaussian field of atomic structure from Ryczko et al. 2018. Single point defect of missing nitrogen atom in graphenehexal born nitrite heterostructure.

Ryczko et al. 2018 used CNNs to study atomic energies in graphene, hexagonal boron nitride (hBN), and graphene-hBN heterostructures with and without imperfections, to test a CNNs ability to predict energy values of each simulation. Imperfections were introduced into the system, single point defect with removed atom and Stone-Wales defect. The results showed 0.198 meV mean absolute error (MAE) for validation values with energy values ranging from -9 to -8 eV. A deep CNN was used with 20 layers in operation to achieve the final result, 18 layers were convolution and max pooling, one dense layer and one final classification error was present. This was a perfect application for a CNN with large data sets generated.

Different methods have developed to work within large simulations. Chew et al. 2020 studied rates of liquid-phase Brønsted acid-catalyzed reaction rates for biomass compounds. A larger simulation was produced in which the simulation was divided into portions. This study used a CNN to predict the acid-catalysed reaction rates within a solution, and was tested on different solvent systems with prediction rates an order of magnitude faster than previous methods of doing so. The final root mean squared error ranged from 0.11 to 0.81 within the best prediction model being the VoxNet CNN. 84 combinations of variables were tested within the study and the data sets appeared to be undersized. A simple convolution system was used containing ten layers total, six convolutional and pooling layers, three fully connected layers, and a single output neuron.

A more advanced way of managing large simulations is to set the input grid for the CNN around a particular point. Fukuya and Shibuta 2020 portioned a cube out of each simulation around each atom to identify the phase of each atom as solid or liquid in a biphasic system. This system used a clear dividing line at the boundary and was maintained at melting temperature. Pure Fe, W, Ni, and Si simulations were were all

classified with accuracies in the range of 93% to 96% except for Fe which achieved $\approx 90\%$ accuracy. This far exceed previous methods of atomic phase identification; The best of which, polyhedral template matching was in the range 85% to 90% accuracy for the same testing. A ten layer CNN consisting of six pooling and convolution layers, three dense layers, and two final output neurons was used.

1.4.3 Regional CNN

Defining the search size and shape for the neural network to process is done within regional CNNs (rCNN). Many vision systems use an rCNN to scan a given image and classify sections of the image. Thus, a man, woman, dog, and car can be classified from the same image with the same rCNN. An example of the architecture is given in figure 8. In which there is a CNN with a cropping program that classifies the large and important sections of the image before feeding it into a standard CNN. The cropping program is computationally intensive and uses classical vision systems in most circumstances Girshick et al. 2014.

The major drawback to this methodology applied to MD research is two fold: it requires previous knowledge of the object to be selected, and it requires heavy computation. First, the system requires a predetermined classification of what an image is which is not known in this research. Without this knowledge it is not possible to set the borders of the image cropping system, this can be highly variant based on the MD application. Secondly, classical vision systems are computationally intensive. Many classical vision systems operate serially whereas the CNN section of an rCNN can be heavily paralyzed, increasing training time and dark silica time Girshick et al. 2014.

R-CNN: *Regions with CNN features*

1. Input image
2. Extract region proposals (~2k)
3. Compute CNN features
4. Classify regions
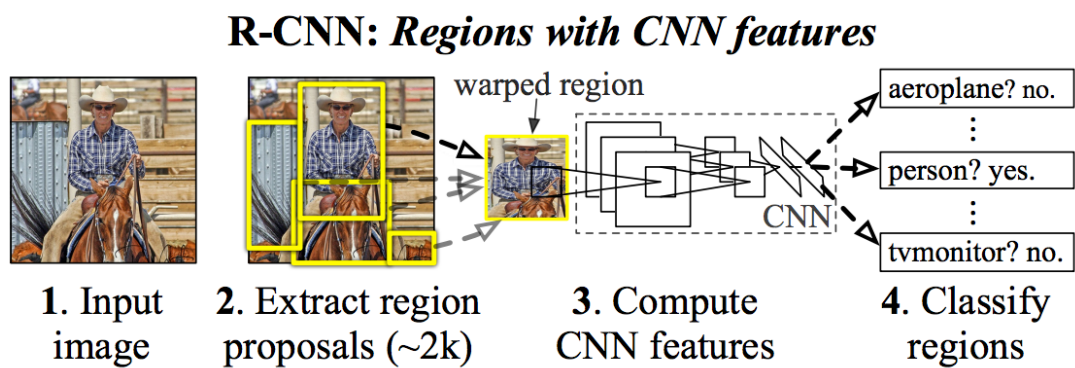
Figure 8. Example of rCNN architecture.

Chapter 2

METHODOLOGY

The methodology is broken into two main components. The first is the generation of the samples, this includes the creation, diffusion, quenching, and shock processes for all silica samples. These samples need be numerous for the CNNs to property train Chew et al. 2020; Ryczko et al. 2018. The second component is to generate Gaussian fields from the given LAMMPS dump files for mass and charge and train the simulations using the CNNs generated. Figure 9 is a process diagram of the methodology used showing all main steps. Six binary variables will be tested within the research listed in table 15.

Index	Variable	Option 1	Option 2
1	simulation seed (type)	α quartz	random
2	simulation size (atoms)	18,000	73,728
3	Gaussian σ (Å)	1	4
4	Gaussian Field (type)	mass	charge
5	CNN (type)	standard	all convolution
6	Nucleation Detector (type)	cutoff	max

Table 1. A description of what variables are being tested.

18,000 or 73,728 atoms

Quartz Seed Generation

Diffusion

Energy Minamalization

Random Seed Generation

Quench

Shock

Yes Quartz

Yes Random

Did Simuation Fail?

No

Generate Gaussian Feild

Sigma = 1 or 4 Angstron Mass or Charge

Cutoff Method

Max Method

Train on CNNs

All Convolution Or Standard

Train on CNNs

Analyze Results
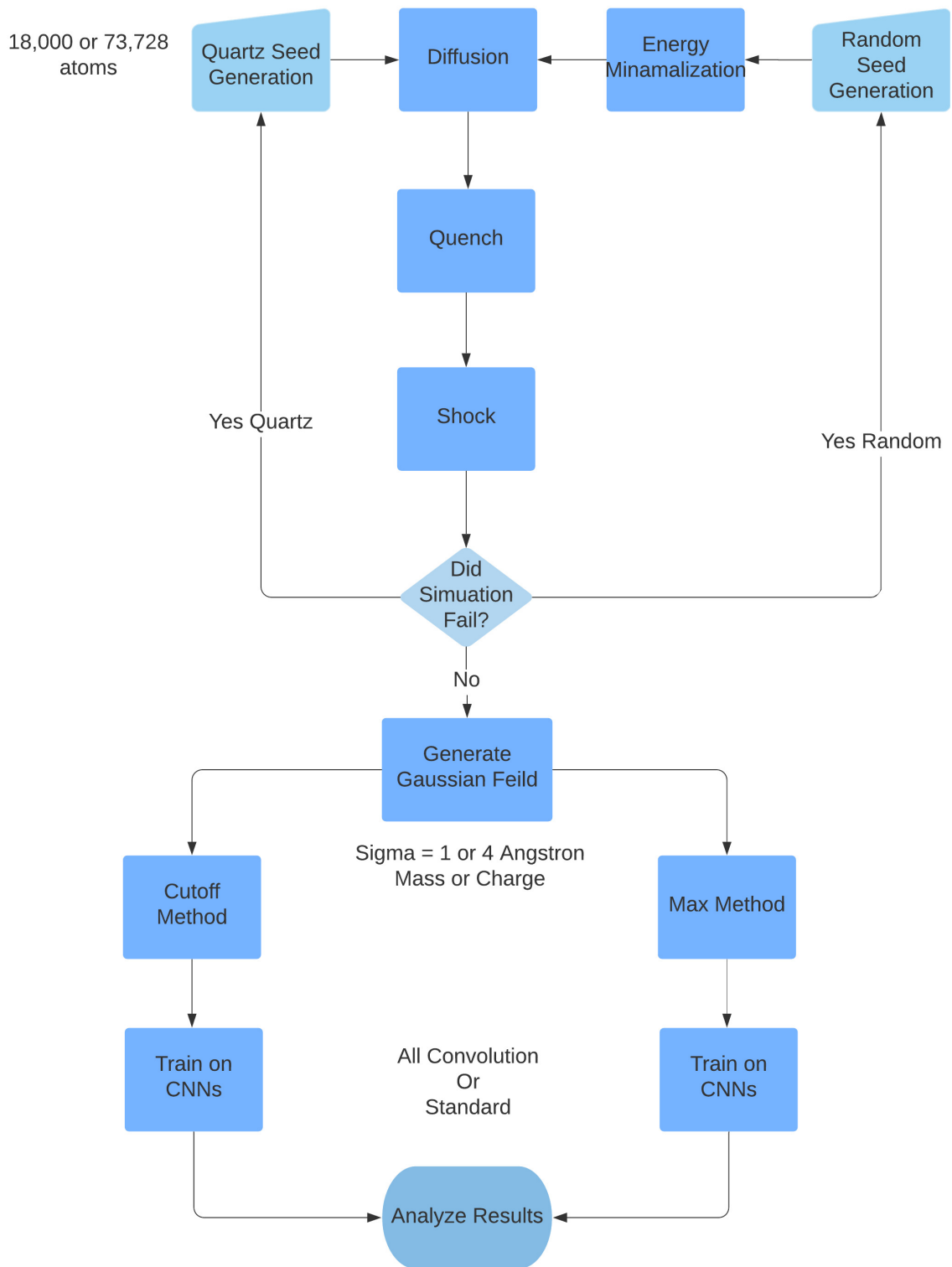
Figure 9. Process diagram for research methodology.

2.1 Potential

The potential used for this work is critical to the formation of stishovite within the samples. Related work to this thesis has been performed under the FURI and MORE grants at ASU by the same author. This work has greatly colored the understanding of stishovite formation and behavior.

2.1.0.1 Pedone et al Potential

One of the first potentials used was discovered by Pedone et al. 2006 to correctly model the behavior of ionic and semi-ionic oxides. This predominately included melting and quench simulations of silica glasses with various impurities arising from DFT studies. This is the most complete potential found to date with 29 different elemental interactions. The potential was used for the MORE grant research to model the behavior of SiO_2 with Na_2O concentrations of 0%, 5%, 10%, 20%, and 30% concentrations. This coincides with later work studying the mechanical properties of alkaline glasses with impurities Cormack. and Segre 2006. The focus of the research was to identify a point at which crystallization will not occur due to the concentration of impurities within a system.

$$U(r) = \frac{q_i q_j}{r_{ij}} e^2 + D_{ij}[\{1 - e^{-a_{ij}(r-r_o)}\}^2 - 1] + \frac{C_{ij}}{r^{12}}$$

The Podone et al work is based on empirical behavior and did include nonphysical charges for Si, Na, and O of 2.4, 0.6, and -1.2 respectively. During implementation the entire term was maintained as a continuous function and set with an atomic cut off

q_i, q_j (C)	D_{ij} (eV)	a_{ij} (Å^{-2})	r_o (Å)	C_{ij} (eV Å^{12})
Na$^{0.6}$-O$^{-1.2}$	0.023363	1.763867	3.006315	5.0
Si$^{2.4}$-O$^{-1.2}$	0.340554	2.006700	2.100000	1.0
O$^{-1.2}$-O$^{-1.2}$	0.042395	1.379316	3.618701	22.0
Si$^{2.4}$-Si$^{2.4}$				1.0
Na$^{0.6}$-Na$^{0.6}$				5.0
Na$^{0.6}$-Si$^{2.4}$				5.0

Table 2. Pedone et al Potential

at 5 Å. From 5 Å to 5.5 Å a small quadratic curve fit was made to take the residual energy and guide it to zero, making for a smooth transition.

Another common feature of alkaline glass potentials in literature is removal of all but the Coulombic forces when dealing with atoms of positive charge. The Si-Si, Na-Na, and Si-Na terms only include the Coulomb charges and Coulomb repulsion is modeled as $\frac{C_{ij}}{r^{12}}$. These charges are critical and promote long range atomistic structure which can be seen in a pair distribution function Wakai 201; Pedone et al. 2006.

None of the simulations for the potential including the pure silica oxide simulations proved to be effective in the formation of stishovite while using simulation sizes of 18,000 atoms derived from pure quartz. In order to form stishovite, larger simulation sizes and a longer potential cutoff of 10 Å was used and resulted in some stishovite formation varying by sample. It has remained in this methodology as an option for others or future work within the area if it is desired to add ionic impurities within the glass. Understanding the effect of ions within the nucleation behavior of silica or alkaline glasses would be a natural outgrowth of this research and would be expected to have applications across materials of other alkaline glasses which form six-fold coordination structure.

2.1.0.2 Modified BKS Potential

Shen and Reed 2016 picked up the BKS potential and modified it to support the formation of stishovite under high pressure shocks. High pressure shocks are a difficult problem as the potential must be accurate from atmospheric pressure to >100 GPa under rapid loading. Rapid loading is the most difficult demonstration of a potential's accuracy. The previous BKS potential exhibits a risk of failure under rapid pressure loading. Most of the early work into stishovite formation was based upon static loading conditions and modeled the behavior of the silica oxide from quartz to stishovite. If the BKS potential, or any of the other early potentials are used, atoms at the shock wave exhibit very strange interactions form the extremely close resulting atomic proximity Beest van B. W. H. and R. A. 1990; Brazhkin, Voloshin, and Popova 1991.

To model the shock behavior Shen and Reed 2016 computed only silica-silica, silica-oxygen, and oxygen-oxygen interactions are fitted to DFT simulation results. The core of the Buckingham potential is kept within the modified BKS potential: Coulombic interaction, Moorse function, and Coulombic repulsion.

$$
\phi_{ij}(r_{ij}) = \begin{cases} k(r_{ij} - r_{ij}^m)^2 + w_{ij} & r_{ij} < r_{ij}^m \\ \frac{q_i q_j}{r_{ij}} e2 + A_{ij} e^{\frac{-r_{ij}}{\rho_{ij}}} - \frac{C_{ij}}{r_{ij}^6} - \left(A_{ij} e^{\frac{-r_c}{\rho_{ij}}} - \frac{C_{ij}}{r_c^6} \right) & r_{ij}^m < r_{ij} < r_c \\ \frac{q_i q_j}{r_{ij}} e2 & r_c < r_{ij} \end{cases}
$$

The first term, with a radius less than r_{ij}^m models close atomic interactions and corrects for shock wave behavior by the choice of coefficient w_{ij}. The second term, from

q_i, q_j (C)	A_{ij} (eV)	$a_{ij}(\rho^{-2})$	C_{ij} (eV ^{6})	r_{ij}^m (Å)	w_{ij} (eV)
Si$^{2.4}$-O$^{-1.2}$	18003.7572	0.20521	133.5381	1.1936	-27.3050
O$^{-1.2}$-O$^{-1.2}$	1388.773	0.36232	175	1.439	20.782
Si$^{2.4}$-Si$^{2.4}$					

Table 3. Modified BKS Potential

r_{ij}^m to r_c which includes a longer cut off region to that of the original BKS potential makes a continuous transition across the r_c boundary. Failure to generate a smooth transition zone is responsible for peculiar interactions in MD simulations at which atoms favor one or the other side of the cutoff region. Lastly, an extended region in which the coulombic interactions dominate before the LAMMPS force field takes over. The extended Coulombic interaction was mentioned in the paper as a critical part of the potential, allowing crystallization information to propagate to non crystallized regions more effectively. In the case of modeling amorphous glass $r_c = 6$ Å is the cutoff distance for the Buckingham term. In the case of a quartz crystal $r_c = 10$ Å. The maximum cutoff distance for the potential is $r_{ij} = 10$ Å. The terms not given in table 3 are k=100 (eV*Å) an estimated constant and $e = 8.9876e9$ N*m^2/C^2 the Coulmbic constant. Computational costs prohibits cutoff region extension and the inverse squared radial energy behavior yields greatly diminished returns for doing so. Only amorphous structured silica oxide was shocked. Subsequently, the potential for amorphous silica oxide was used exclusively with an $r_c = 6$ Å cut off distance for all samples.

The potential was programmed into a Python file which outputs a table with four columns; index column starting at one. the shortest vector between atoms, energy of the atoms, and force of the atoms. This table has three sections one for each interaction: oxygen-oxygen, oxygen-silica, and silica-silica using standard LAMMPS convention. The computational cost of calculating energy and force for every atomic placement

is high and the experiments are many. It is better utilization of computational time to output a single discrete table and proceed to approximate each atom as being at a given distance within the table than to calculate the energies and forces for every atomic interaction during simulation. For this study a radial resolution of 0.001 Å was used.

2.2 Sample Genesis 1

2.2.1 α-Quartz Seeded Experiments

The simulation consisted of using a data file consisting of 144 atoms in a perfect α-quartz lattice propagated to 18,000 simulations. After melting a diffusion step was preformed to allow divergence of each simulation before a quench. The fix NPHug or Hugoniostat command was used to perform the shock testing ranging from 50-70 GPa, temperature damping of 0.05-0.5 ps, and pressure damping of 0.1-10.0 ps. It is hypothesized that stishovite formation is a function of pressure, source atomistic structure, pressure damp, and temperature damp. The results did yield stishovite in accordance with the hypothesis.

Throughout the simulations a timestep of 0.5 fm is used in accordance with previous work done under the MORE grant. This small timestep is needed during the shock phase to generate stishovite, to large a timestep will yield no stishovite nucleation. Symmetric boundary conditions were used throughout the simulation process.

2.2.1.1   Simulation Creation

The α-quartz seeded experiments were created using the generic file consisting of a perfect quartz lattice of 144 atoms. The structure is copied 5 times in all 3 Cartesian directions to make a larger crystal consisting of 125 the original file. The resulting simulation consists of 18,000 atoms with a size of 49.160 Å x 85.147 Å x 54.054 Å. The subsequent atomic velocities were randomized using the randint attribute of the random library in the Python language. This is the first and most critical divergent property of each simulation that results in particular solutions of differing atomistic structure. The velocities where subsequently scaled to 300 K with the LAMMPS velocity create command.

The file for the α-quartz is a generic file containing a quartz structure for use in simulation, it can be easily copied to create larger simulations. The size of this data file is 9.832 Å x 1.703 Å x 1.081 Å and contains 144 atoms or 48 silica atoms and 96 oxygen atoms.

2.2.1.2   Melt

The melt is performed using LAMMPS' fix NVT from 300 Kto 6000 Kfor 500 ps or 113 K/ps. Due to the high temperature of 6000 Kthe system was maintained at constant volume. The melting temperature of quartz is known to be about 1873 K at atmospheric pressure Brown and Bursten 2000, far below the chosen temperature to melt in the MD simulation. During phase transformation quartz would generally have magnitudes of time longer to melt. Melting glass at 6000 K causes it to behave much like heterogeneous butter when heated some segments break bonds and melt quickly

while others linger in an elevated temperature environment. The melting temperature of quartz in the picosecond to nanosecond range is not known, 6000 K was chosen and is known to be within a Goldilock's zone, if the simulation is ran at 10,000 K LAMMPS will lose atoms in the simulation from the extreme energies created from the constant volume fix and much lower will not yield melting quickly enough. This was derived though experimentation.

2.2.1.3   Diffusion

The next step was to hold the temperature at 6000 K for 200 ps using an NVT fix, before concluding with an NPT fix of 6000 K at constant pressure of 100 bar for 1 ns. The temperature damp is 100 fs and pressure damp is 2 ps. This step offered additional time for melting as well as diffusion. It is important to allow for diffusion of the molten silica oxide to create differing atomistic structures. The choice for diffusion time is based upon previous work under the FURI grant. Later in the thesis a test was done showing that 1 ns of quench at 2700 Kyielded ample diffusion of ≈ 11.2 Å for Si atoms. The high pressure during diffusion is to prevent the simulation from vaporizing. The exact value of pressure was decided for under earlier work to prevent vaporization.

2.2.1.4   Quench

The quench process is broken into two steps: quenching and depressurization. The first step of quenching takes the temperature from 6000 K to 300 K in 0.95 ns or at a rate of 0.6 K/ps. This was done using an NPT command with temperature damp of 1 ps and pressure damp of 1 ps, the pressure was held at 1000 bar. The quench

rate of 0.6 K/ps matches the work of Yuan Shen and Reed 2016. The pressure set to 1,000 bar, to prevent vaporization of the molten glass which occurs at lower pressure values.

Step two is depressurization, in which the glass is taken from 1,000 bar to 1 atm in 100 ps using an NPT fix. The pressure damp is 0.1 ps and temperature damp is 50 fs. The depressurization step allows the glass to homogenize to the new environment and stress relive before shock.

2.2.1.5   Shock

The shock is the most critical part of the MD simulations and the most temperamental and the goal of shock is to yield consistent crystallization with results matching literature values. The hypothesis is that stishovite formation is a function of shock pressure, atomistic structure, pressure damp, and temperature damp.

Ravelo et al. 2004 did significant work into Hugoniostat curves with three methods of shocking cartographic structures: NVHug, NPHug, and, NEMD. The chosen and most common method for classical MD is the NPHug command which has been used in the prior work of this author. Yuan Shen and Reed 2016 used the MSST shock command which uses shock velocity and converts it into a pressure wave, in general the MSST command is more temperamental than the NPHug command. The NPHug command shocks entire domain in a given plane using an energy conservation equation to maintain physical behavior,

$$T_t - T = \frac{\frac{1}{2}(P + P_0)(V_0 - V) + (E_0 - E)}{N_{dof}k_B}$$

T is the temperature in Kelvin, P is axial pressure in Pa, E is the energy in

26

electronvolt, V is the volume in $\mathring{A}^3$, N_{dof} is the number of degrees of freedom and, k_B is the Boltzmann constant. The 0's represent the initial state and the current state is given without a subscript. In the case of this research only the ZZ axis was shocked resulting in a piston like behavior of the simulation.

Pressure and temperature damp control the response of the system. Classical MD simulations undergo standard controls behavior in which the pressure damp or temperature damp can be unstable, under damped, critically damped, or over damped. The effect of these terms are shown in figure 10 below as a refresher to systems theory; In which the β_p=0 term shows a system with no artificial dampening, this system is under damped resulting in oscillatory behavior. β_p=5 system receives a dampening factor of 5 ps, this system has mild overshoot before going to its final stress value and is known as critically damped, or ideally damped. Critically damped refers to a system at optimal dampening, in which the minimal time is needed to reach a final valve with a range, usually the range is ±2% of the final valve.

A poor value for the temperature damp or pressure damp will result in a system with ever increasing temperature or pressure before simulation failure, or a system that will not crystallize. Both of these extremes were experienced in previous work. To test the given hypothesis that the pressure damp and temperature damp effect the formation of stishovite these values will be tested within a range of their recommended value from LAMMPS documentation Sandia 2021:

$$\text{pressure damp} = 1000 * \text{timestep}$$

$$\text{temperature damp} = 100 * \text{timestep}$$

Lastly, the shock pressure controls crystallization; this is the most obvious empirical factor in crystallization. It is clear from the literature that crystallization for amorphous silica systems is most likely to form in the range of 50 to 70 GPa. If the shock pressure
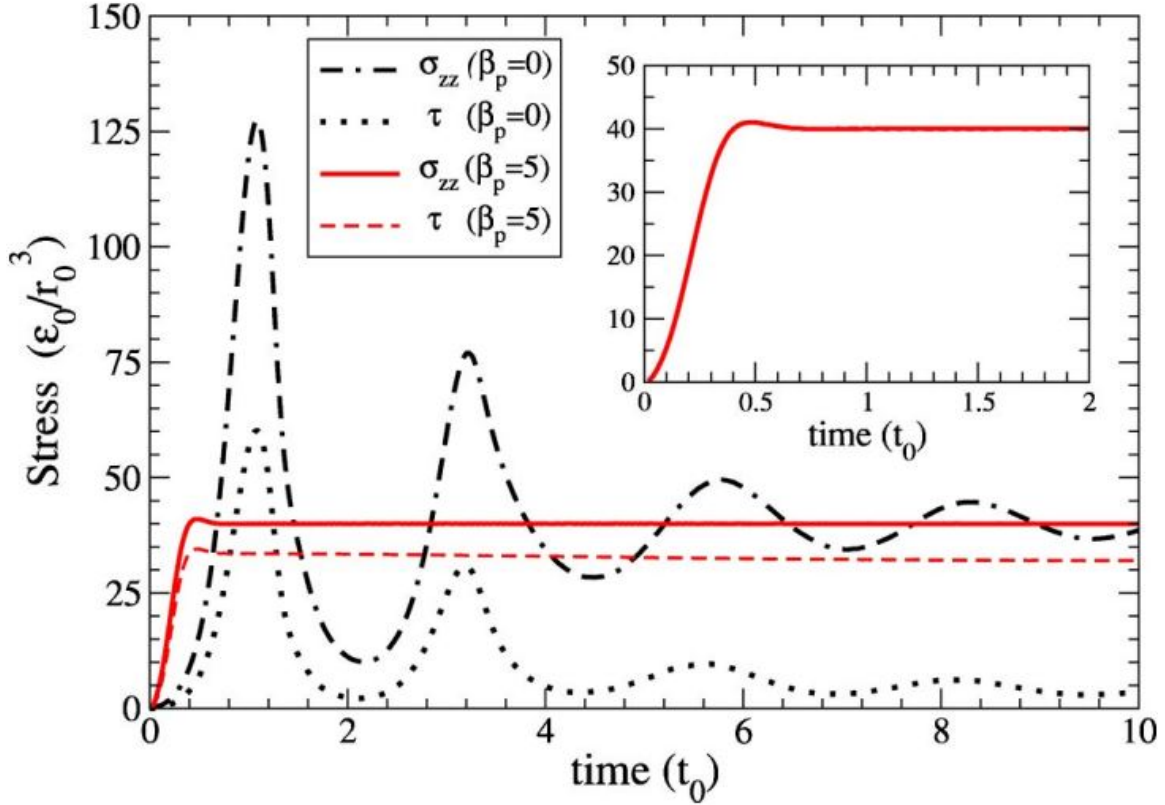
Figure 10. Example of Hugoniot curve from Revelo et al work in which β_p is the pressure dampening in ps Ravelo et al. 2004.

is too high the glass will be disordered and fail to nucleated. If the energy is to low no crystallization will occur from to little energy in the system. The energy level can change the folding structure of amorphous or α-quartz structure silica oxide into stishovite at different values of shock pressure Ahrens 2002; Dong, Zhu, and Chen 2015; Yuan Shen and Reed 2016; Tracy, Turneaure, and Duffy 2018.

2.2.1.6 Experiment

Tests were done ranging pressure damp, temperature damp and shock pressure on a single quench data file to test for quartz crystallization. No special selection was

made for the input file and the file was the same for all shock tests. For the sake of time only one file was used and no averages were acquired. The pressure ranged from 50 to 70 GPa as 50 GPa, 55 GPa, 60 GPa, 65 GPa, and 70 GPa. The temperature damp ranged from 50 to 500 fm as 50 fs, 100 fs, and 500 fs. These values were chosen around 100 times the timestep of 0.5 fs according to LAMMPS documentation. The pressure damp was ranged from 100 fs to 10 ps as approximate 1000 times the 0.5 fs timestep according to LAMMPS documentation. Pressure damp values were tested as 100 fs, 1 ps, and 10 ps. Dump file was added to record all atom positions every 10,000 timesteps or 5 ps. All test results are seen in table 4 with categorical averaging Sandia 2021.

Density values showed no significant change from literature. Visual Molecular Dynamics (VMD) is a software tool to visualize molecular files, it did display clear crystallization of some samples. Density has no to a very minor change from pre and post glass crystallization based upon this data. Density was assumed to be the key factor in crystallization of glass, often the literature refers to the process as permanent densification Grujicic, Bell, Pandurangan, et al. 2011.

Shock pressure in the range of 55 to 60 GPa yielded the most reliable formation of stishovite for nearly all tested systems. It is important to note that for three of four systems outside this pressure range, crystallization occurred at temperature damp 50 fs. There appears to be some favoring of lower temperature damp values during crystallization, the reason for this is unknown and no indication of this is given within the literature. Some very minor densification appears to have happened. In the 55 GPa shock region the lowest density is the only simulation that did not crystallize. One of two crystallized simulations in each, the 50 GPa and 65 GPa ranges had the highest density. All of these findings are very minor with less than 1% difference to

other within the same shock pressure. No significant density information appears from the averaging of any particular category of temperature damp or pressure damp within the systems.

P_{shock} (GPa)	P_{shock} (ps)	T_{damp} (ps)	Stishovite (Positive)	ρ $\left(\frac{g}{cm^3}\right)$	P_{shock} (GPa)	P_{shock} (ps)	T_{shock} (ps)	Stishovite (Positive)	ρ $\left(\frac{g}{cm^3}\right)$
50	0.1	0.05		4.394	60	10.0	0.50	Positive	4.528
50	0.1	0.10		4.395	60	all	all		4.531
50	0.1	0.50		4.396	60	0.1	all		4.535
50	1.0	0.05		4.398	60	1.0	all		4.525
50	1.0	0.10		4.395	60	10.0	all		4.534
50	1.0	0.50		4.398	60	all	0.05		4.516
50	10.0	0.05	Positive	4.399	60	all	0.10		4.545
50	10.0	0.10	Positive	4.428	60	all	0.50		4.532
50	10.0	0.50		4.396	65	0.1	0.05	Positive	4.541
50	all	all		4.400	65	0.1	0.10		4.539
50	0.1	all		4.395	65	0.1	0.50		4.541
50	1.0	all		4.397	65	1.0	0.05	Positive	4.554
50	10.0	all		4.408	65	1.0	0.10		4.542
50	all	0.05		4.397	65	1.0	0.50		4.540
50	all	0.10		4.406	65	10.0	0.05		4.541
50	all	0.50		4.397	65	10.0	0.10		4.543
55	0.1	0.05	Positive	4.506	65	10.0	0.50		4.540
55	0.1	0.10	Positive	4.483	65	all	all		4.542
55	0.1	0.50	Positive	4.502	65	0.1	all		4.540
55	1.0	0.05	Positive	4.469	65	1.0	all		4.545
55	1.0	0.10	Positive	4.505	65	10.0	all		4.541
55	1.0	0.50	Positive	4.489	65	all	0.05		4.545
55	10.0	0.05	Positive	4.532	65	all	0.10		4.541
55	10.0	0.10	Positive	4.494	65	all	0.50		4.540
									Continued on next page

Table 4 – continued from previous page

P_{shock}	P_{shock}	T_{damp}	Stishovite	ρ	P_{shock}	P_{shock}	T_{shock}	Stishovite	ρ
(GPa)	(ps)	(ps)	(Positive)	$\left(\frac{g}{cm^3}\right)$	(GPa)	(ps)	(ps)	(Positive)	$\left(\frac{g}{cm^3}\right)$
55	10.0	0.50	Positive	4.515	70	0.1	0.05		4.589
55	all	all		4.499	70	0.1	0.10		4.591
55	0.1	all		4.497	70	0.1	0.50		4.590
55	1.0	all		4.488	70	1.0	0.05		4.588
55	10.0	all		4.514	70	1.0	0.10		4.588
55	all	0.05		4.502	70	1.0	0.50		4.591
55	all	0.10		4.494	70	10.0	0.05		4.589
55	all	0.50		4.502	70	10.0	0.10		4.387
60	0.1	0.05	Positive	4.520	70	10.0	0.50		4.588
60	0.1	0.10	Positive	4.536	70	all	all		4.567
60	0.1	0.50	Positive	4.548	70	0.1	all		4.590
60	1.0	0.05		4.492	70	1.0	all		4.589
60	1.0	0.10	Positive	4.563	70	10.0	all		4.521
60	1.0	0.50	Positive	4.521	70	all	0.05		4.589
60	10.0	0.05	Positive	4.536	70	all	0.10		4.522
60	10.0	0.10	Positive	4.537	70	all	0.50		4.590

Table 4. α-quartz seeded SiO_2 crystallization tests Sample Genesis 1. All variables not listed in the table were homogeneous throughout testing and all tests were performed upon the same quench data file. Only the shock pressure, pressure damp, and temperature damp are changed within the simulations. The shock lasted 1.5 ns. The density listed for each shock value is the average of the final 20 log file outputs, or an average of the final 10 ps of the simulation. Stishovite was tested positive with the occurrence of six-fold crystallographic structure.

2.2.2 Randomly Seeded Silica Experiments

The following steps of simulation generation, atomic insertion, diffusion, and quench all occurred under the same file to simplify, whereas the initialization/melting/diffusion and quench occurred separately within the quartz simulations. All quench file pressure is kept to standard sea level atmospheric pressure of 101.325 kPa with a 1.0 fs timestep, the timestep for shock is kept at 0.5 fs. Symmetric boundary conditions were maintained throughout.

2.2.2.1 Simulation Creation

The sample is produced using two simulation boxes of the same size for different elements. The simulation size is dictated by the number of the Si atoms,

$$L = 3.5 \; Si^{1/3} \; \text{Å}$$

Which gives a volumetrics increase of 3.5 Å^3 for each additional SiO_2 pair, this is equivocal to standard temperature standard pressure amorphous silica glass with density of 2.33 g/cm^3. Two boxes were then created using the dimensions of (L,L,L)

The first box is to insert the Si atoms and the second box is to insert the O atoms. The Si and O atoms are inserted using the random function from LAMMPS to create atoms with all pair combinations. This method of generating two simulation boxes with Si and O simulation respectively has been done in a previous MORE grant with success. This is a novel form of SiO_2 network generation not heretofore seen within the research literature. The purpose is to generate additional atomistic configuration variance to test its nucleation behavior.

2.2.2.2 Energy Minimization

Subsequent computation dangers occur from the random atomic insertion that can lead to simulation failure. Overlapping atoms defined as atoms well within proximity that will not be seen in any physical system did occur. The highly nonphysical atomistic arrangements are common from the create atoms random function. In early versions of the simulation no steps were taken to minimize energy which resulted in failed simulations, energy interactions between atoms became so high they exited the simulation box effectively crashing LAMMPS. To rectify this an NVE fix was set with a maximum energy of 1 eV . This was done for 1 ps with the temperature held at 2700 K. Following this fix no further simulation failures occurred.

2.2.2.3 Diffusion

The second concern with the create atoms random insertion command is the non physical atomistic arrangement that occurs. To compensate a diffusion step was performed to allow for atomic mixing to occur, the thermo style included an Si mobility measure which measures the average distance of all Si atoms from the initial starting coordinates. The O atoms did not require this measure as it is redundant, the lighter O atom are subject to higher atomic mobility and will subsequently diffuse faster than the significantly heavier Si atoms. Some preliminary simulations did include O diffusion which was over two times that of Si.

The diffusion step was held during a molten state at 2700 K for 1 ns. The final solution was optimized for Si diffusion of $\approx$11.5 Å, going beyond this value is difficult as diffusion distance obeys a power law. The 25 simulations showed diffusion of

11.189 ± 0.2475 Å with a minimum and maximum of 10.974 Å and 12.347 Å, showing very low variation amongst simulations. A temperature damp of 0.1 ps and pressure damp of 2.0 ps was used.

2.2.2.4 Quench

Quenching was very similar to that done in the quartz seeded experiments, the process used a quench rate of 0.6 k/ps resulting in a quench from 2,700 K to 300 K in 4 ns. Temperature damp and pressure damp of 0.1 ps and 1.0 ps were used for the process. No simulations underwent vaporization as in the quartz seeded experiments, it appears that the usage of 2700 K is below the vaporization threshold at atmospheric pressure. This value was tuned as a 3000 K and 2900 K value for diffusion and quench did lead to vaporization of simulation in the quench section.

2.2.2.5 Shock

Two shock experiments ensued within this section, the first one was the first experiment in the thesis work chronologically. This was before a system of stishovite measurement was implemented resulting in only data file output, therefore no dump files existed for testing purposes. All shocks were maintained fro 1.5 ns.

2.2.2.5.1 Shock Test 1

The first shock experiment was performed using an NPHug fix for 51, 55, and 59 GPa. In keeping with the general hypothesis of classical MD stishovite formation

a three dimensional sweep consisting of the temperature damp for points 0.1, 1.0, and 10.0 ps and pressure damp seep of points 4, 6, 8, 10, 12, 15, 20, 25, and 30 ps was done. The results are given as the final density, the input simulation density is 2.34 $\frac{g}{cm^3}$. All simulations used the same input file to remove variation. No significant correlation occurred within the density across simulations, the changes in density for nearly all simulations are <0.5% and the remainders are less than <1%. Changes in densification where expected to be significant and obvious. It was concluded at the time that no crystallization occurred. There was likely significant crystallization based upon later results. Discovered post testing is that the densification is often measured after pressure unloading, a very obvious fact in imperial study that is not so in MD. If the shock pressure was subsequently unloaded the large and irreversible densification should have been present Grujicic, Bell, Glomski, et al. 2011.

2.2.2.5.2   Shock Test 2

The second shock test was done to match the work done within the quartz seeded shock experiment, with shock pressures of 50, 55, 60, 65, 70 GPa, temperature damp ranges of 0.05, 0.1, and 0.5 ps, and pressure damp ranges of 0.1, 1.0, and 10.0 ps. As this experiment was carried out the simulations were stopped after a small number of iterations. Table 6 shows the results, all simulations except system 128 at 50 GPa failed. The temperature became wildly unstable and the simulation ended in an error prematurely. From log file reviews it appears the maximal limit of double point precision was exceeded forcing AGAVE to crash. It is believed that the system became unstable and failed in osculation similar to a unstable system as referenced in the work of Ravelo et al. 2004. In the Sample Generation Stage 2 it may be more clear as

System Number	P_{damp} (ps)	T_{damp} (ps)	51 GPa (kg/m^3)	55 GPa (kg/m^3)	59 GPa (kg/m^3)
122	4.0	0.1	4.468	4.499	4.510
123	4.0	1.0	4.419	4.504	4.502
124	4.0	10.0	4.459	4.496	4.507
125	6.0	0.1	4.460	4.496	4.536
126	6.0	1.0	4.465	4.498	4.528
127	6.0	10.0	4.465	4.498	4.522
101	8.0	0.1	4.462	4.504	4.546
102	8.0	1.0	4.463	4.491	4.523
103	8.0	10.0	4.463	4.501	4.518
104	10.0	0.1	4.458	4.502	4.516
105	10.0	1.0	4.458	4.499	4.533
106	10.0	10.0	4.465	4.496	4.535
107	12.0	0.1	4.460	4.500	4.528
108	12.0	1.0	4.463	4.501	4.523
109	12.0	10.0	4.461	4.496	4.514
110	15.0	0.1	4.460	4.512	4.518
111	15.0	1.0	4.447	4.503	4.530
112	15.0	10.0	4.466	4.512	4.516
113	20.0	0.1	4.458	4.495	4.525
114	20.0	1.0	4.459	4.506	4.520
115	20.0	10.0	4.459	4.493	4.510
116	25.0	0.1	4.458	4.500	4.518
117	25.0	1.0	4.470	4.498	4.542
118	25.0	10.0	4.463	4.508	4.509
119	30.0	0.1	4.460	4.500	4.532
120	30.0	1.0	4.464	4.502	4.512
121	30.0	10.0	4.445	4.511	4.480

Table 5. Randomly seeded silica amorphization trials without dump files, test zero. The numbers below each shock pressure indicate the final density taken as the last ten log file output values or 5 ps; these outputs were given every 0.5 ps. No dump files were created to verify crystallization.

System Number	P_{damp} (ps)	T_{damp} (ps)	50 GPa (kg/m^3)	55 GPa (kg/m^3)	60 GPa (kg/m^3)	65 GPa (kg/m^3)	70 GPa (kg/m^3)
128	10.0	0.05	4.375	4.333	4.454	4.531	4.563
129	10.0	0.10	4.337	4.330	4.452	4.395	4.501
130	10.0	0.50	3.462	3.746	3.966	3.269	4.442
131	1.0	0.05	2.963	3.618	3.531	3.683	4.088
132	1.0	0.10	4.134	4.044	4.276	3.122	3.573

Table 6. Second randomly seeded crystallization test. All tests were done with the same input file and all variables not listed in the table were homogeneous throughout trials. The numbers listed for each shock value is the final density of the shock simulation taken as the average of the last ten log file outputs or 5 ps; Log file outputs are created every 0.5 ps. All but experiment 128 at 50 GPa failed.

some systems do appear to fail based on the quench file. A small number of future simulations later underwent the same experience, crashing repeatedly after rerunning the shock simulations only to discover the problem was solved by rerunning the quench simulation.

2.2.3 Summary

Crystallization is only confirmed in the seeded quartz experiments. It is likely that crystallization occurred within the zero test of randomly seeded trials and this cannot be substantiated as not dump files were generated. The pressure was the strongest predictor of shock formation with shocks almost exclusively occurring in the 55 to 60 GPa range. Temperature damp had a mild effect on shock formation with a maximization of 0.05 ps and pressure damp did not appear to have any effect.

Some other important issues within the systems were the vaporization of quartz seeded simulations and failed randomly seeded simulations. All but one of the second randomly seeded experiments underwent a crash from uncontrolled temperature values within the system, with unknown origin.

2.3 Sample Genesis Stage 2

The previous stage of sample generation contained a list of unsolved problems that are fixed within this sample generation. The final result is the ability to manufacture large quantities of stishovite crystal. Chiefly amongst the changes was standardization of code and implementation of previous research. The code comes from the randomly seeded simulations and was subsequently modified to have identical flow amongst the new quartz seeded and randomly seeded simulations.

The new sample manufacturing flow is as follows:

$$\text{Simulation Generation} \rightarrow \text{Diffusion} \rightarrow \text{Quench} \rightarrow \text{Shock}$$

This was done with two sets of files. One in which contains the shock while the other contains the simulation generation, diffusion, and quench. The first section of up to the shock utilized a timestep of 1 fs, a slightly less conservative value that conserved computational time. This 1 fs timestep was used in the work of Cormack. and Segre 2006; Yuan Shen and Reed 2016. The shock simulation maintained a 0.5 fs time step to ensure crystallization behavior. Boundary conditions across all steps were symmetric.

2.3.1 Simulation Generation

The process for seeding the quartz simulation was similar to that of Sample Genesis 1. The α-quartz file is propagated five or eight times in each direction resulting in 125 or 512 copies, 18,000 and 72,728 atoms respectively. Quartz simulation sizes were 49.160 Å x 85.147 Å x 54.054 Å for 18,000 atoms or 78.656 Å x 136.236 Å x 86.486 Å for 72,728 Å atoms.

The process for seeding the randomly inserted simulations did not change. Two simulation boxes were generated based upon the number of Si atoms used to size the simulation as a cube with a global density of 2.33 g/cm^3. Si atoms were inserted using the random function in LAMMPS into simulation box one and the O atoms were inserted as twice the number of Si atoms into simulation box two. A change was made to remove the melt, this was considered an unneeded step. The velocity is be set to the desired diffusion temperature.

2.3.2 Diffusion

Each file received the same random vector by using the randnt in python and setting the velocity to match 2700 K. It was found though experimentation that 3000 K vaporized the simulation like in the original α-quartz files, and 2900 K has some vaporized simulations. 2700 K was decided upon as it seemed to produce the highest diffusion before vaporization within 200 K. Both simulations underwent 1 ns of diffusion which showed in previous research to yield 11.189 ± 0.2475 Å of travel distance for each Si atom, while the O experienced ≈ 2.5 as much. The pressure damp used is 2.0 ps and temperature damp is 0.1 ps. The pressure is maintained at 1 atm throughout.

The randomly inserted simulations underwent an initial energy minimization step using an NVE with a limit of 1 eV to prevent overlapping atoms causing LAMMPS to fail. This NVE limit was carried out for 1 ps to stabilize the system.

2.3.3 Quench

The quench was performed at a rate of 0.6 K/s using an NPT fix. The total time to quench from 2700 K to 300 K was 4 ns, with a pressure of 1 atm. The pressure damp used was 1 ps and temperature damp used was 0.1 ps. With the much lower temperature the simulation only took 6 hours to run for a 18,000 atom simulation and 12 hours for a 72,728 atom simulation using a Nvidia V100.

2.3.4 Shock

The shock testing was done using the NPHug command with varying parameters of shock pressure, temperature damp, and pressure damp. This resulted in another three dimensional parameter study similar to that in Sample Genesis 1. The shock process in Sample Genesis 1 had shown some progress even though it had failed overall to produce stishovite for the randomly seeded simulations. It was believed that the process itself is ideal despite the poor results, and that the simplification and consistency of the new codes to handle both the quartz seeded and randomly seeded simulations will result in an outcome of stishovite. The simulation will be executed for 1 ns as opposed to the 1.5 ns used previously. Research focus is on nucleation of stishovite not full maturation, this choice saves 33% memory space for unneeded data and increases the rate at which samples are produced. The dump files containing all needed atomic positions are updated every 0.5 ps for the entirety of the simulation, resulting in 201 separate dump steps for each sample.

A set of tests is performed with the same hypothesis of Sample Genesis 1 that the shock pressure, initial structure, pressure damp, and temperature damp are

Figure 11. Quartz seeded, 50 GPa shock pressure, temperature damp 50 fs, and pressure damp 0.1 ps. Example of simulation that did not crystallize. The larger red atoms represent the Si atoms and smaller green atoms represent the O atoms. Notice the atoms are fairly randomly distributed and have no long range coordination.
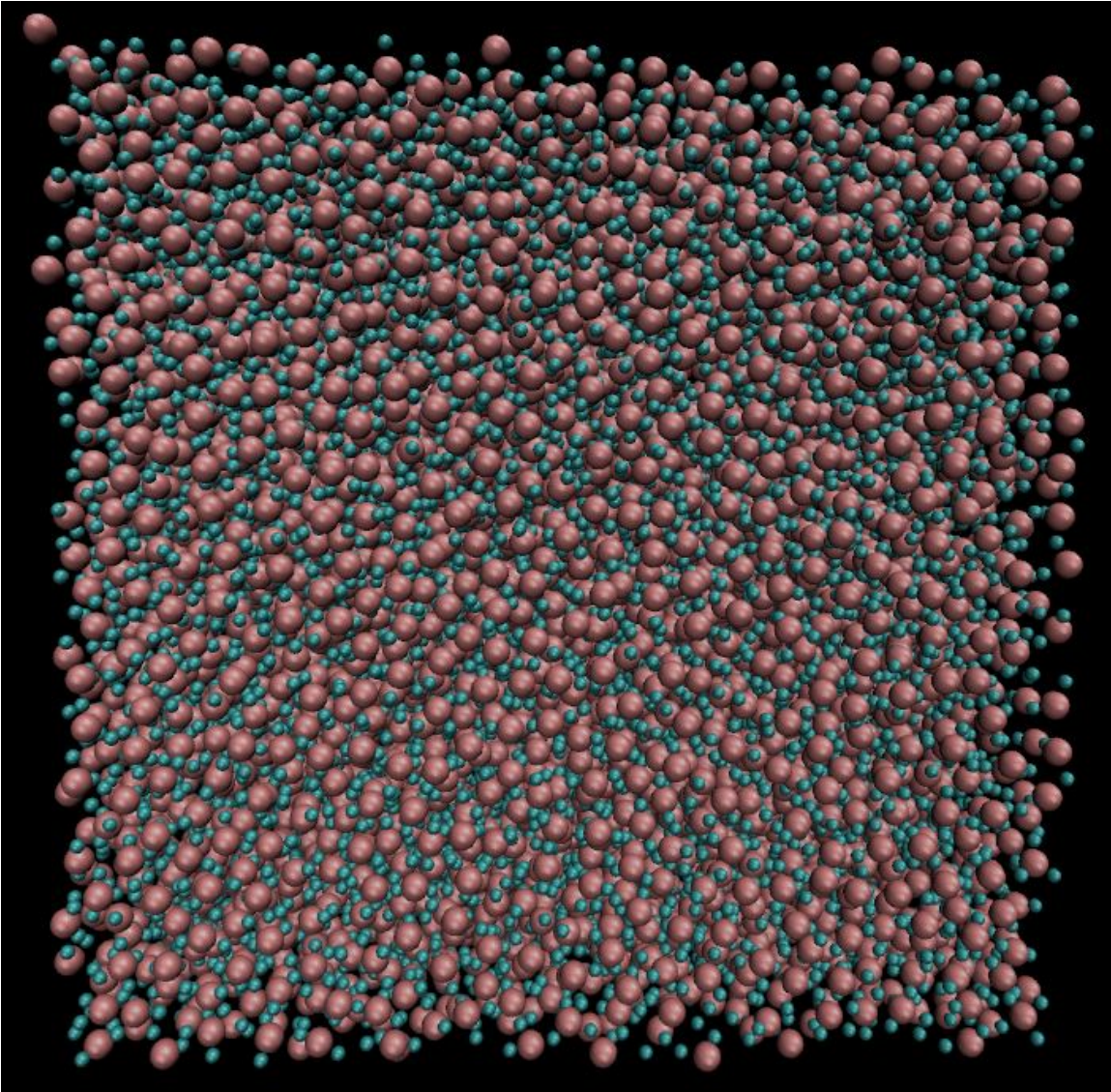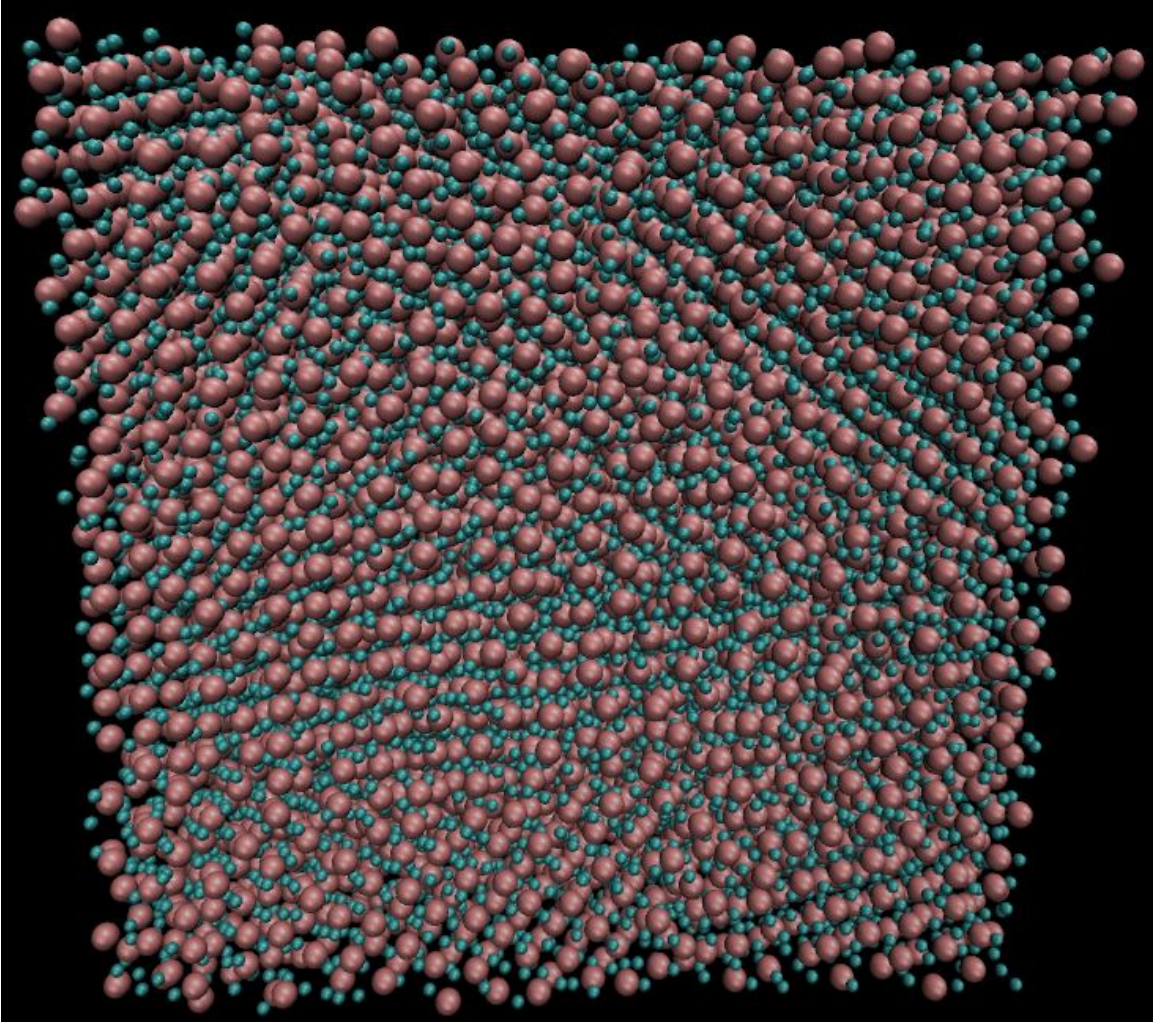
Figure 12. Quartz seeded, 55 GPa shock pressure, temperature damp 0.5 ps, and pressure damp 0.1 ps. Example of simulation that did crystallize. The larger red atoms represent the Si atoms and smaller green atoms represent the O atoms. Notice the atoms are strictly organized in certain regions, these regions are the grains of the crystal.

primary variables controlling crystallization. The studies performed are done so in a similar fashion to Sample Genesis 1: shock pressures of 50, 55, 60, 65, and 70 GPa, temperature damp of 0.05, 0.1, and 0.5 ps, and pressure damp of 0.1, 1, and 10 ps. The study was done on the quartz seeded and randomly seeded simulations by using the same input file from each for all shocks.

Tables for this round of tests include the densities and temperatures at the start, end, and difference of the two for each simulation. This was done by taking averages of data across the simulation; for the simulation start the average is taken from 50 ps to 100 ps. The start is taken at 50 ps to allow the system to stabilize from its initial state at standard temperature standard pressure. The final results are taken as the last 50 ps average of each simulation or the 950 ps to 1000 ps region.

P_{shock} (GPa)	Stishovite (Positive)	P-damp (ps)	T-damp (ps)	ρ_{start} $(\frac{g}{cm^3})$	ρ_{end} $(\frac{g}{cm^3})$	$\Delta\rho$ $(\frac{g}{cm^3})$	T_{start} (K)	T_{end} (K)	ΔT (K)
STD				0.004	0.0037	0.0054	49.6	142.7	76
50		0.1	0.05	4.397	4.407	0.0098	2620	2694	74
50		0.1	0.10	4.395	4.402	0.0068	2634	2701	67
50		0.1	0.50	4.395	4.406	0.0117	2631	2706	74
50		1.0	0.05	4.393	4.403	0.0101	2634	2708	75
50		1.0	0.10	4.397	4.407	0.0108	2621	2699	78
50		1.0	0.50	4.396	4.406	0.0101	2635	2705	70
50		10.0	0.05	4.395	4.405	0.0103	2631	2701	70
50		10.0	0.10	4.393	4.400	0.0070	2629	2704	75
50		10.0	0.50	4.397	4.403	0.0060	2621	2695	73
55	Positive	0.1	0.05	4.453	4.466	0.0125	2938	3064	125
55		0.1	0.10	4.454	4.456	0.0026	2928	2989	61
55		0.1	0.50	4.455	4.457	0.0025	2923	2989	65
55		1.0	0.05	4.449	4.458	0.0094	2929	2980	52
								Continued on next page	

Table 7 – continued from previous page

P_{shock} (GPa)	Stishovite (Positive)	P-damp (ps)	T-damp (ps)	ρ_{start} $(\frac{g}{cm^3})$	ρ_{end} $(\frac{g}{cm^3})$	$\Delta\rho$ $(\frac{g}{cm^3})$	T_{start} (K)	T_{end} (K)	ΔT (K)
55		1.0	0.10	4.449	4.455	0.0064	2939	3004	65
55		1.0	0.50	4.450	4.458	0.0087	2940	2984	44
55		10.0	0.05	4.455	4.459	0.0042	2938	3006	68
55	Positive	10.0	0.10	4.454	4.465	0.0114	2932	3092	160
55		10.0	0.50	4.452	4.459	0.0064	2934	3009	75
60	Positive	0.1	0.05	4.501	4.539	0.0377	3213	4185	972
60		0.1	0.10	4.504	4.505	0.0012	3204	3208	5
60	Positive	0.1	0.50	4.503	4.558	0.0552	3200	4178	978
60		1.0	0.05	4.503	4.503	-0.0004	3194	3220	26
60	Positive	1.0	0.10	4.501	4.524	0.0230	3199	4543	1345
60	Positive	1.0	0.50	4.503	4.526	0.0232	3199	4567	1368
60	Positive	10.0	0.05	4.503	4.562	0.0597	3199	4397	1198
60	Positive	10.0	0.10	4.503	4.547	0.0437	3208	4626	1418
60	Positive	10.0	0.50	4.501	4.529	0.0281	3201	4284	1083
65	Positive	0.1	0.05	4.551	4.571	0.0202	3452	4752	1300
65		0.1	0.10	4.550	4.550	0.0001	3450	3451	1
65	Positive	0.1	0.50	4.550	4.591	0.0410	3451	4821	1369
65		1.0	0.05	4.549	4.550	0.0008	3448	3450	2
65	Positive	1.0	0.10	4.548	4.574	0.0266	3449	4855	1405
65	Positive	1.0	0.50	4.550	4.595	0.0445	3454	4685	1231
65	Positive	10.0	0.05	4.550	4.570	0.0203	3444	4944	1500
65	Positive	10.0	0.10	4.551	4.565	0.0145	3449	4636	1187
65	Positive	10.0	0.50	4.549	4.588	0.0386	3443	4330	888
70		0.1	0.05	4.597	4.596	-0.0009	3702	3703	2
70		0.1	0.10	4.597	4.596	-0.0008	3702	3707	5
70		0.1	0.50	4.597	4.596	-0.0008	3697	3707	10
Continued on next page									

Table 7 – continued from previous page

P_{shock}	Stishovite	P-damp	T-damp	ρ_{start}	ρ_{end}	$\Delta\rho$	T_{start}	T_{end}	ΔT
(GPa)	(Positive)	(ps)	(ps)	$\left(\frac{g}{cm^3}\right)$	$\left(\frac{g}{cm^3}\right)$	$\left(\frac{g}{cm^3}\right)$	(K)	(K)	(K)
70		1.0	0.05	4.597	4.596	-0.0009	3698	3705	6
70		1.0	0.10	4.597	4.597	0.0006	3703	3708	6
70		1.0	0.50	4.597	4.596	-0.0004	3705	3703	-2
70		10.0	0.05	4.597	4.597	0.0009	3700	3703	3
70		10.0	0.10	4.596	4.597	0.0008	3695	3699	4
70		10.0	0.50	4.597	4.596	-0.0007	3700	3703	3

Table 7. Quartz seeded silica amorphization trials generation 2. This was a test use the same quench file as an input to all tests. The simulation was executed for 1 ns. The start values are given as an average of 50-100 ps and the end valves are taken as an average of the last 50 ps.

P_{shock}	Stishovite	P-damp	T-damp	ρ_{start}	ρ_{end}	$\Delta\rho$	T_{start}	T_{end}	ΔT
(GPa)	(Positive)	(ps)	(ps)	$\left(\frac{g}{cm^3}\right)$	$\left(\frac{g}{cm^3}\right)$	$\left(\frac{g}{cm^3}\right)$	(K)	(K)	(K)
STD				0.004	0.0037	0.0054	49.6	142.7	76
50		0.1	0.05	4.380	4.386	0.0060	2896	2948	52
50	Positive	0.1	0.10	4.382	4.391	0.0088	2898	2956	58
50		0.1	0.50	4.383	4.392	0.0089	2901	2966	65
50		1.0	0.05	4.386	4.387	0.0010	2894	2933	39
50		1.0	0.10	4.382	4.391	0.0083	2891	2945	54
50	Positive	1.0	0.50	4.381	4.400	0.0188	2890	3092	202
50		10.0	0.05	4.384	4.391	0.0080	2890	2982	92
50		10.0	0.10	4.383	4.386	0.0034	2897	2944	47
50		10.0	0.50	4.386	4.391	0.0051	2898	2941	43
55	Positive	0.1	0.05	4.433	4.521	0.0881	3183	4330	1147
55	Positive	0.1	0.10	4.433	4.454	0.0206	3181	4497	1316
								Continued on next page	

Table 8 – continued from previous page

P_{shock}	Stishovite	P-damp	T-damp	ρ_{start}	ρ_{end}	$\Delta\rho$	T_{start}	$_{end}T$	TΔ
(GPa)	(Positive)	(ps)	(ps)	$(\frac{g}{cm^3})$	$(\frac{g}{cm^3})$	$(\frac{g}{cm^3})$	(K)	(K)	(K)
55	Positive	0.1	0.50	4.433	4.489	0.0560	3183	4195	1012
55	Positive	1.0	0.05	4.433	4.487	0.0542	3181	4256	1075
55	Positive	1.0	0.10	4.434	4.517	0.0831	3177	4212	1035
55	Positive	1.0	0.50	4.432	4.472	0.0399	3183	4132	948
55	Positive	10.0	0.05	4.434	4.498	0.0639	3185	4334	1150
55	Positive	10.0	0.10	4.435	4.505	0.0710	3184	4177	993
55	Positive	10.0	0.50	4.433	4.487	0.0540	3180	4295	1115
60		0.1	0.05	4.481	4.480	-0.0007	3454	3452	-2
60		0.1	0.10	4.480	4.481	0.0008	3445	3451	5
60		0.1	0.50	4.483	4.480	-0.0022	3446	3448	2
60		1.0	0.05	4.480	4.482	0.0013	3446	3452	7
60	Positive	1.0	0.10	4.481	4.485	0.0039	3439	3530	91
60		1.0	0.50	4.482	4.481	-0.0011	3448	3451	3
60	Positive	10.0	0.05	4.482	4.497	0.0142	3444	4783	1339
60		10.0	0.10	4.481	4.481	0.0006	3438	3450	13
60	Positive	10.0	0.50	4.483	4.518	0.0354	3441	4907	1467
65		0.1	0.05	4.528	4.528	0.0000	3721	3719	-1
65		0.1	0.10	4.527	4.528	0.0008	3720	3723	3
65		0.1	0.50	4.529	4.528	-0.0006	3723	3719	-4
65		1.0	0.05	4.529	4.529	-0.0002	3719	3723	5
65		1.0	0.10	4.528	4.529	0.0010	3729	3723	-6
65		1.0	0.50	4.528	4.529	0.0006	3728	3718	-11
65		10.0	0.05	4.529	4.528	-0.0003	3726	3720	-7
65		10.0	0.10	4.529	4.529	0.0001	3719	3724	5
65		10.0	0.50	4.529	4.528	-0.0011	3725	3721	-4
70		0.1	0.05	4.575	4.575	0.0000	3995	3993	-2

Table 8 – continued from previous page

P_{shock}	Stishovite	P-damp	T-damp	ρ_{start}	ρ_{end}	$\Delta\rho$	T_{start}	$_{end}T$	$T\Delta$
(GPa)	(Positive)	(ps)	(ps)	$(\frac{g}{cm^3})$	$(\frac{g}{cm^3})$	$(\frac{g}{cm^3})$	(K)	(K)	(K)
70		0.1	0.10	4.575	4.575	-0.0001	3995	4005	11
70		0.1	0.50	4.575	4.575	-0.0006	4007	4006	-2
70		1.0	0.05	4.575	4.574	-0.0008	4004	3996	-8
70		1.0	0.10	4.575	4.575	-0.0004	4010	4012	2
70		1.0	0.50	4.575	4.576	0.0011	4011	4012	2
70		10.0	0.05	4.575	4.576	0.0008	4000	4001	0
70		10.0	0.10	4.575	4.575	-0.0004	4011	4004	-7
70		10.0	0.50	4.575	4.575	0.0000	4002	4006	4

Table 8. Randomly seeded silica amorphization trials generation 2. This was a test use the same quench file as an input to all tests. The simulation was executed for 1 ns. The start values are given as an average of 50-100 ps and the end valves are taken as an average of the last 50 ps.

2.3.5   Shock Test Results

The quartz seeded simulations experienced very predictable behavior for crystallization, the 60 to 65 GPa range is the region in which shocks occurred. There were two crystals formed at 55 GPa. There appears to be no effect of temperature damp or pressure damp on crystallization. The randomly seeded simulations have crystallization at the 50 GPa to 60 GPa region and all systems crystallized at 55 GPa, showing that shock pressure is the primary factor within crystallization. In this case there was an apparent effect of temperature damp, of the five cases crystallized outside of the 55 GPa four of them had a temperature damp of 0.05 ps which is significant

and aligned with results from Sample Genesis 1. The pressure damp does not appear to affect crystallization within the systems.

The systems underwent a temperature transformation during shock similar to that seen in figure 6. Looking at the 55 GPa randomly seeded simulations the starting temperature is 3182±2 K and ending temperature is 4270±104 K recorded in the literature 2600 K and 4300 K respectively. The 60 GPa quartz seeded simulations starting temperature is 3234±83 K and ending temperature is 4442±200 K; reported in figure 6 is $\approx$ 3300 K and $\approx$ 4900 K respectively. The final solution closely aligns with literature values for ending temperatures and may duffer at start temperatures due to the time taken as 10 ps in Shen and Reed 2016 t0 50 to 100 ps in this work. Further differences likely occurred due to the different shock methods used, MSST and NPHug.

Simulations at higher shock pressures such as 65 GPa and 70 GPa went into a disordered state, shown by the very low δT valve coupled with high T value at the beginning and end. The 70 GPa simulations are $\approx$ 4000 K and have skipped the nucleation phase within the shock and went directly to 4000 K within the first 100 ps of the simulation. There was no stop and hold in the disordered samples as in the stishovite forming samples.

There is distinct densification that has occurred within the simulations, howbeit it is much lower than previously expected. Each system that crystallized increased in density on the order of 10^{-2} g/cm^3 and the none crystallized systems increased in density on the order of 10^{-3} to 10^{-4} g/cm^3. These are based on average values with minor exceptions present. the only major exception is that of the randomly seeded simulations at 55 GPa in which the average densification is 5.90e-3 g/cm^3, results shown in figure 9.

Quartz Seeded (GPa)	Crystallized $\left(\frac{\text{g}}{\text{cm}^3}\right)$	Non-Crystallized $\left(\frac{\text{g}}{\text{cm}^3}\right)$	Randomly Seeded (GPa)	Crystallized $\left(\frac{\text{g}}{\text{cm}^3}\right)$	Non-Crystallized $\left(\frac{\text{g}}{\text{cm}^3}\right)$
55	1.20e-2	5.73e-3	50	1.38e-2	5.79e-3
60	3.86e-2	3.85e-4	55	5.90e-3	No Data
65	2.94e-2	4.40e-4	60	1.78e-2	5.90e-3

Table 9. Densification of systems taken as an average of each category. There is no data for the randomly seeded simulations at 55 GPa are all crystallized systems.

There appears to be a crystallization distribution working in the random and quartz seeded simulations. Some pressures can experience strong instances of crystallization and others low instances of crystallization. Based upon the results in Sample Genesis 1 and 2 there is a density function for crystallization strongly correlated to pressure and loosely correlated to temperature damp within the values of temperature damp 0.05 to 0.50 ps and pressure damp 0.1 to 10.0 ps.

2.3.6   summary of Tests

From the previous tests it is possible to conclude that crystallization is a strong function of shock pressure and initial state, a possible and weak function of temperature damp, and does not appear to be a function of pressure damp. The occurrence of shock appeared to be a density function. The structure of the glass pre shock changed the shock pressure ranges for crystallization. In the case of the quartz seeded simulations the optimal value for shock was 60 GPa, while it was 55 GPa in the randomly seeded tests. This was a very strong correlation. The temperature damp is a minor effect of the system with enhanced crystallization at 0.05 ps. More research should be done in this area, this is enough data to manufacture large numbers of simulations for this research.

2.3.7   Mass Simulations

With the previous data from each experiments all processes up to the shock are held constant. The chosen pressure damp and temperature damp for the shocks are 10 ps and 50 fs respectively. Pressure damp of 10 ps was chosen as it is a more theoretically stable choice even though it does not appear to effect the simulation. Temperature damp of 50 fs was chosen as it appears to promote crystallization. The shock pressure is constant: 55 GPa for the randomly seeded experiments and 60 GPa for the quartz seeded experiments. The shock pressure was chosen to achieve the highest possible number of crystals.

In an effort to add some variability within the simulations different simulation sizes were chosen. These different sizes are known to produce different grain size and different crystallographic formation Yuan Shen and Reed 2016. The sizing is done for the quartz seeded simulation with 5x5x5 and 8x8x8 copies of the α-quartz file. The randomly seeded quartz received the appropriate atom insertion to match the quartz seeded work of 18,000 and 73,728 atoms respectively. The goal was to produce as many simulations as possible, ideally this was 500 5x5x5 simulations and 100 8x8x8 simulations of both seed kinds based on temporal studies and available computational resources. AGAVE hard drives became overloaded during the course of this research, university wide. In turn two weeks of operational time were lost and the 8x8x8 simulations were not able to reach 100, table 10 shows the final counts.

$\approx \frac{1}{10}$ to $\frac{1}{15}$ of all samples crashed during shock. These simulations were performed again without success by redoing the shock file, after redoing the quench and shock the simulations were successful. There appears to be some atomic configuration in quench output which leads to large oscillatory behavior and failure of shock simulations.

Atoms ($\frac{\text{atom}}{\text{simulation}}$)	Quartz Seeded (simulation number)	Randomly Seeded (simulation number)
18,000	500	500
73,728	80	72

Table 10. Densification of systems taken as an average of each category. There is no data for the randomly seeded simulations at 55 GPa as all systems crystallized.

Non-crystallized simulations were not removed or performed again to increase data integrity and allow future research to be done on the data set.

2.4   Gaussian Field

2.4.1   Function

The use of Gaussian field is common in the case of MD applications within CNNs and is the most widely used way of achieving a grid formation for CNNs Ryczko et al. 2018; Springenberg et al. 2014. It approximates any data point as a smooth particle acting upon the entire feature plain. Whereas, the exact data point previously contained all relevant information the entire plane contains this information within it after applying the Gaussian. This takes the previous data points acting as a delta functions and forms it into a continuously smooth function which contains the characteristic information of all points.

The Gaussian in this application is a one dimensional function applied across the entire simulation. To compress the three dimensional data into one dimensional form the geometric summation is taken,

$$d = \sqrt{i^2 + j^2 + k^2}$$

Gaussian function is given as,

$$f(\mathrm{d}) = \frac{\mathrm{v}}{\sigma^3 \sqrt{8\pi^3}} \exp\left(-\frac{1}{2}\frac{d-\mu}{\sigma^2}\right)$$

Were σ is the standard deviation of the distribution in this case $\sigma(1) = 1$ Å giving it a direct physical meaning. This parameter was later tuned to achieve optimal performance. μ is the mean of all input data within the simulation.

It is important to note that the the simulation has symmetric boundary conditions. To address the symmetric boundary conditions some basic logic is used,

$$\mathrm{d(i, j, k)} = \begin{cases} \mathrm{i, j, k,} & \text{if i, j, k} \leq \frac{\delta\mathrm{i, }\, \delta\mathrm{j, }\, \delta\mathrm{k}}{2} \\[2ex] \delta\mathrm{i, }\, \delta\mathrm{j, }\, \delta\mathrm{k} - \mathrm{i, j, k,} & \text{if i, j, k} > \frac{\delta\mathrm{i, }\, \delta\mathrm{j, }\, \delta\mathrm{k}}{2} \end{cases}$$

Where only one i, k, or k index is used at one time and all are used. This takes the shortest distance to the atom in any dimension regardless of boundary.

2.4.2 Field

To calculate the Gaussian field the Gaussian function is applied to all atoms within the simulation with the distance taken from a single grid point. In essence moving the origin to each grid point and calculating the function for all data,

$$\mathrm{Grid\ Point(d)} = \sum_{\mathrm{Atom}=1}^{\mathrm{All\ Atom}} f(\mathrm{i, j, k})$$

2.4.3 Normalization

The system is normalized to maintain equality across the system. Neural Networks work best with normalized inputs. This is because different data input and different

variable values can distort the outcome of the neural network. Inserting an extreme value of data or variable can become over represented or under represented within the network, thus bias the system to become dominated by or ignoring an extreme valve of data or variable. To counteract this the variable is normalized in which it is limited in scope to a certain size. In most cases this is to force all values of all data and variables to be limited to $0 \leq \text{Value} \leq 1$.

In this case the value is normalized to the variable but is not contained between 0 and 1. This is not of a concern as only one input and one output variable will be used at a time. The normalization function used is,

$$d = \frac{d}{\sigma^3 \sqrt{8\pi^3}}$$

Where d is some data point value. This function is based upon the one dimension normalizing value cubed to account for system three dimensional.

2.4.4   Computational Optimization

Applying the Gaussian function across all atoms within each sample is computationally intensive and is a $O(N^3)$ problem with respect to single dimention simulation size. To manage this explosive computation only atoms within a region surrounding the grid point are applied to the that grid points Gaussian functions significantly lowering computational time. For this application the region given is,

$$i, j, k_{\text{cutoff}} = \frac{5\sigma}{\delta i, \delta j, \delta k}$$

Where i, j, k are the Cartesian distances and δi, δj, δk are the lengths of the simulation box respectively. This simple method is highly scalable and very effective for this application.

2.4.5 Size

In this use case all simulations are calculated with the same sized grid of 64 by 128 by 128. The relative sizing was chosen because of the effect of the NPHug compression causing the simulation to flatten like a pancake during shock. This caused the resulting simulations to be within $\approx 15\%$ of the relative grid sizing used. Making the sizing exact may cause the generation of unusual numbers with poor numerical factorization. It was deemed more critical to maintain maximal CNN usability than to maintain exact sizing to the simulations.

The exact sizing was chosen for its complete factorization into 2 and that it was large enough to capture accuracy of atomic position with a safety factor. Later plots will show high quality atomic visibility. Ideally the system would have been as refined as possible. This is limited to the computational intensiveness of the system. Every doubling of dimensional resolution yields a n^3 increase in data or 8 times the previous system size.

2.4.6 Gaussian Mass Field

The mass is one of the simplest and most likely causes of crystal formation. The atomic structure caries an inherent mass density field that is unique to each simulation. It is also one of the easiest fields to calculate and can be done readily with the lamps dump files. All mass fields are calculated at the 0 time step of the shock file in which the temperature is 300 K and pressure is 1 atm. A minor modification is made to each Gaussian function in which the leading coefficient is multiplied by the atomic mass of the Si and O atoms respectively. In this case Si=28.855 amu and O=15.999 amu.
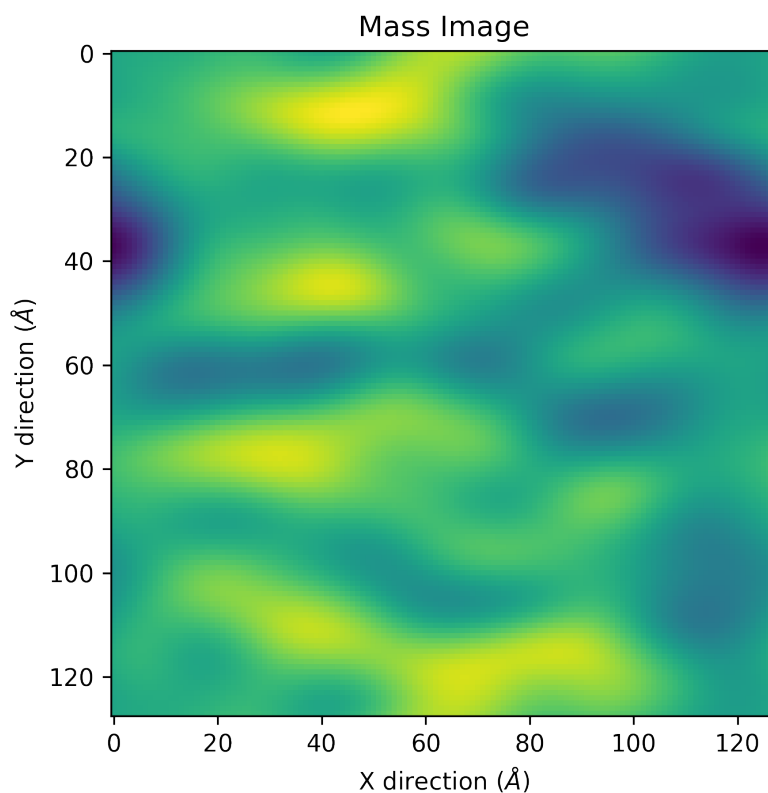
Figure 13. Mass Gaussian field from array 8 simulation 1. Displayed is Z direction at 0 Å.

To make the result physically meaningful a minor modification is done,

$$\text{mass Gaussian grid } \frac{\text{g}}{\text{cm}^3} = \text{mass Gaussian grid} \frac{\text{g}}{\text{mol\AA}^3} * \frac{1 \text{ mol}}{6.023e23} * \frac{1e24\text{\AA}^3}{\text{cm}^3}$$

This will likely have no effect upon the training on the CNN as it applies a linear operator upon the entire system thus, maintaining characteristic behavior and normalization. It is a wise thing to do if the data is used for any other purpose.
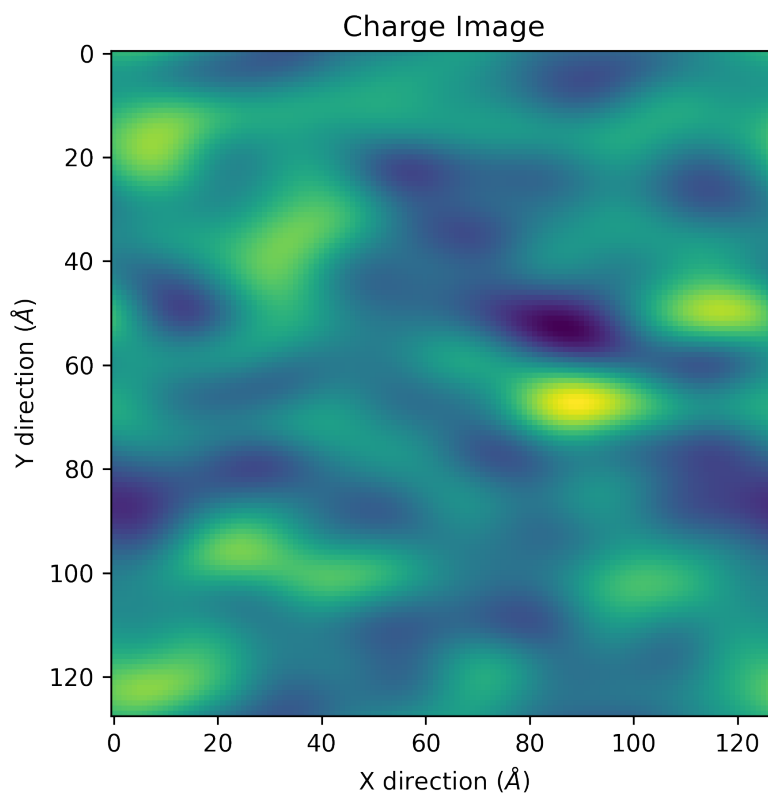
Figure 14. Charge Gaussian field from array 8 simulation 1. Displayed is Z direction at 0 Å.

2.4.7 Gaussian Charge Field

The charge grid is also directly translatable to a Gaussian field without any additional step and is done within the same fashion as is the mass Gaussian field. This may or may not have an effect upon the resulting nucleation of the system. All charge fields are calculated at the 0 time step of the shock file in which the temperature is 300 K and pressure is 1 atm. The Si and O atoms are given a leading coefficient of 2.4 eV and -1.2 eV respectively, as is done in the MD potential. The resulting units of the system are $eV/Å^3$.

2.4.8 Gaussian Crystal Density Field

The Crystal density field follows the same behavior as is seen within the mass and charge Gaussian fields. An extra step is taken to calculate which atoms are crystal-like using the spherical harmonic function of the next section. Only Si atoms are calculated as to there crystallinity and non crystal-like atoms receive a zero leading coefficient in the Gaussian function. The crystal-like atoms have their original leading coefficient leaving it to be an effective coefficient of 1 when acting upon the Gaussian field. This leaves most of the simulation to receive a null valve and gives a starry sky appearance to the simulation at low values of σ as seen in Appendix B.

2.5 Spherical Harmonics

Spherical harmonics are often used to describe varies oscillating states and positions of atoms and molecules. There are four criteria to determine in an SiO_2 atom is crystal-like.

First, structural changes to compute diffraction patterns are given by Debye's equation. This equation gives diffraction patterns for amorphous silica,

$$I = I_0 \sum_{i,j} f_i f_j \frac{\sin q d_{ij}}{q d_{ij}}$$

I is the diffraction intensity at angle 2θ, I θ is the incident intensity, f_i are structural factors Doyle and Turner 1968 for Si and O atoms, q is the diffracted wave vector $4\pi \sin \theta / \lambda$, and d_{ij} are distances between all atomic pairs. In the application of Debye's equation it is necessary to omit periodic boundary conditions. This equation supplies the needed diffraction intensity to determine crystal-like bonds in the following criteria.
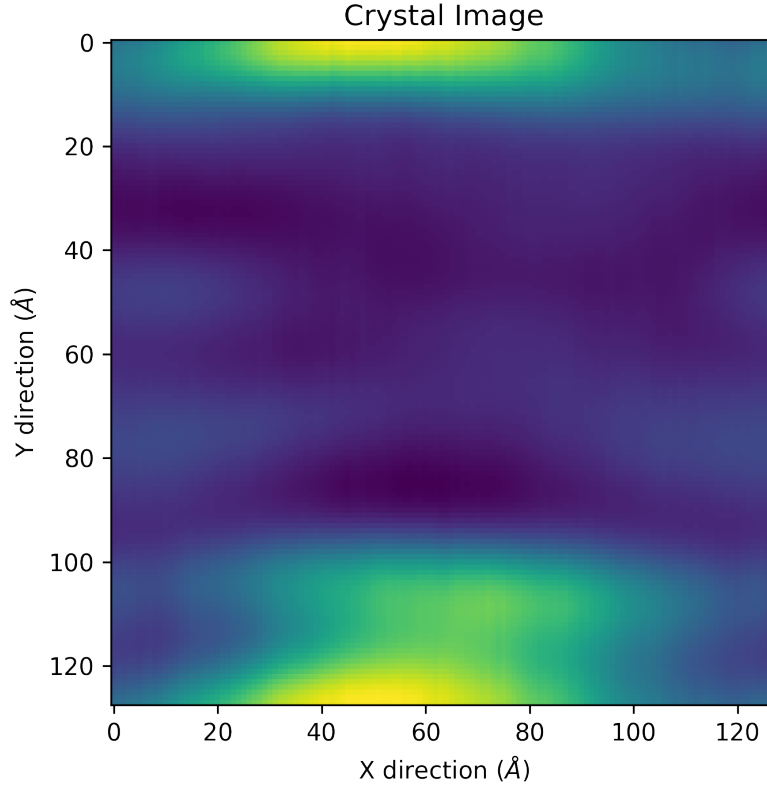
Figure 15. Crystal Gaussian field from array 8 simulation 1. Displayed is Z direction at 0 Å.

The Steinhardt parameter is used to visualize shock results and for crystal identification Steinhardt, Nelson, and Ronchetti 1983.

$$q_{lm}^{s_1 s_2} = \frac{1}{\mid N_{s_1}^{s_2} \mid} \sum_{k \in N_{s_1}^{s_2}} Y_{lm}^*(\theta_k, \sigma_k)$$

Y_{lm}^* is the spherical harmonic functions, s_1 represents the central atom type and s_2 represents the surrounding atom type $N_{s_1}^{s_2}$ surrounding atoms. θ_k, σ_k are the polar angles of atom k in set $N_{s_1}^{s_2}$. To identify crystallised atoms it is necessary that local atoms must be entirely s_2 type and must not be s_1 type, neighboring s_1 type atoms must be of similar configuration as type s_1 Rein ten Wolde, Ruiz-Montero, and Frenkel 1996. For this application the diffraction intensity needs to be l=6 on a silicon

network where type s_1 and s_2 are Si. Because l=6 and s_1 is the same as s_2 all further notation will be in q_{6m}, dropping the redundant s terms and substituting l for 6. When calculating the crystal-like bonds, only bonds within 3.64 Å are applicable Qi. and Reed 2015. Distances above this are not nearest like neighbor atoms. The cutoff function is given as the geometric sum of the data dimensionality in this case $r = \sqrt{x^2 + y^2 + z^2}$ for a real space Cartesian system.

The Steinhardt parameter is used for calculating the dot product of the charge between neighbors as given below,

$$q_6(i) * q_6(j) = \frac{\sum_{m=-6}^{6} q_{6m}(i) * q_{6m}(j)}{|| q_{6m}(i) || * || q_{6m}(j) ||}$$

A dot product of $q_{lm}^{s_1 s_2} \geq 0.812$ indicates crystal-like bonds. This is of course using the silicon network with l=6 criteria from the Steinhardt parameter. If using an O, l=4 will display all instances of crystal-like O atoms for the oxygen network.

Lastly, it is assumed that,

$$\frac{1}{2} \geq \frac{\text{count } q_l(i) * q_6(j) \geq 0.812}{\text{count of all } s_1 = s_2 \in r \leq 0.812}$$

Or that the number of crystal-like atoms given by the dot product of like atoms is greater than half of the total number of like atoms within the cutoff region of 3.64 Å Qi. and Reed 2015. This filters out disordered pairs and boundary atoms.

A short summary of spherical harmonic methods to discover crystal-like boundary conditions follows. First the Debye's equation is used to calculate diffraction patterns within the silica oxide that can be used to identify stishovite. Secondly, the atomic charge can be calculated using the Stienhardt principal, which can in tern be used to calculate the dot product of the charge of two like atoms. If the dot product of two like atoms is greater than 0.814 Å the atomic pair is crystal-like. This can be done for a silicon network and oxygen network, in this case the crystal-like atom indicator

is only done for Si atoms. Thirdly, all atoms must be within 3.64 Å. Fourthly, all crystal-like atoms must have more than 50% crystal like bonds.

2.6 Selecting Gaussian σ

By varying density field resolution Gaussian behavior changes and density resolution becomes a new variable. A large σ value and the Gaussian fields will appear as early pictures of electromagnetic background radiation gathered by the Hubble telescope, a homogeneous mush with no distinguishing features. A small σ value will compress the Gaussian function into a delta-like function. The Gaussian peaks will be to small to be captured by the grid of 64x128x128 and some values will be over and under represented.

Various σ values where tested and plotted, the appendix contains experimental results to each plot, each tested value is shown in table 11. The simulations are divided in 3x3 plots varying equally in the third dimension, moving from ZZ= 0 Å or grid layer= 0 in the z direction four grid values or pixels at a time. Each experiment ended in slightly different sizes due to the MD processes and pixels are counted instead of Å units. The second set of plots, ΔV plots show the first ΔV in the system or divide the system into $\frac{1}{64}$ of the entire system as this will be the data that the CNNs receive for classification. Blue values within the plots represent minima and warm colors maxima, for crystal plots the blue= 0. This test was only done with the mass and crystal field, the charge was not included.

The 1 Å and 4 Å cases were selected as the final values to be used. 4 Å yields a diffusive system with strong atomistic meta structure visible, it is designed to study the meta structure for possible linkage to nucleation; The 1 Å case is designed to

Tested Value	In Å
1	4
4	2
8	$\sqrt{2}$
16	1
32	$\frac{1}{\sqrt{2}}$
64	$\frac{1}{2}$

Table 11. Values tested for σ. The tested value is the raw number into the code while the second value is the value converted to angstrom.

identify nucleation linkage to individual atoms. The 1 Å case clearly displays atoms with low resolution to avoid misrepresentation from small Gaussian curves.

2.7 Classification Design

Neural networks are generally robust in terms of their architectural design but are highly susceptible to poor training data. Since neural networks are trained within an isolated system in which no other inputs than what are provided by the programmer, they fail to recognize concepts not within their immediate scope. In this application the output is known and the input is not clearly defined. The goal of this section is to design an optimal system to classify the output or the nucleation site to the prenucleation structure. This is complicated by not knowing if a relationship exists and what the shape of a nucleation structure is if it exists is.

2.7.1 Cutoff Method

2.7.1.1 Concept

Ryczko et al. 2018 used the simplest method to manage large simulations, splicing them and predicting upon the spliced section. In the case of that literature the spliced section is centered around the object of interest for each spice. The technique is optimal for this research and cannot be executed in the same way. It is prohibited by not having an effective way to center each splice directly around a nucleation zone, doing so would take an extensive system to define a nucleation cluster and then draw a boundary around it. Most samples contain multiple nucleation sites that maybe overlapping which will need to be accounted for in the design of any system. A similar method is used in which the simulation is evenly divided into subsections called ΔV. The concept is shown in figure 16 were a large cube is divided into many small cubes. Once the samples are divided they can be classed as nucleation and non-nucleation ΔVs. Each respective ΔV with class of nucleating or non-nucleating can be fed into the CNN and and trained against this class. The charge and mass field is trained as nucleating or non-calculating, after this section the crystal field in no longer used and is not used in the CNN section.

2.7.1.2 Crystal-like Atom Count

The shock samples contain dump file readouts of atomic position every 0.5 fs. This output can be used to track crystal-like atoms across time using the spherical harmonic equations seen in the previous section. This is the method to generate the

Figure 16. Display of dividing simulations into smaller equal topographical and characteristic shape parts **Swiss Harmony**.

crystal Gaussian field. The crystal growth follows a nucleation, explosive growth, and coalescence phase found within Shen and Reed 2016. The nucleation phase is dominated by no crystal-like atoms present until an initial nucleation occurs which grows slowly until reaching a critical mass of crystal like atoms. After reaching this value a change in crystal growth is seen and the sample grown into a crystal quickly.

Not indicated in the literature and discovered within this research is the fluctuation within crystal-like atom count across the temporal dimension. During the nucleation phase the crystal-like atom count varies increasing and decreasing with each dump file step. Every shocked experiment contains 0 to 5 initial crystal-like atoms which is noise within the system. Therefore, no uniform timestep is appropriate for each

simulation. A "critical crystal" range was used to identify the optimal number of crystal-like atoms in a sample to to use that dump file timestep to generate the crystal Gaussian field. When a sample reaches 9 to 17 crystal-like atoms for any given dump file timestep, that dump file timestep is translated into a crystal Gaussian field. Again, the mass and charge Gaussian fields are created at the zeroth timestep before shock is applied, and the crystal Gaussian field is created at the occurrence of nucleation. Some simulations did not nucleate and were not used in the final analysis; Some simulations skipped 9 to 17 crystal-like atoms jumping from a low to high number of crystal-like atoms between timesteps, these samples were not included within the final analysis.

2.7.1.3 ΔV Implementation

Creation of each ΔV is done is by splicing the sample into small regions which can be given binary classification as nucleation or non-nucleation zones. Figure 16 show the basic concept behind this methodology in which the rectangular prism sample is broken into multiple sub rectangular prisms of the same dimensional relationships. Samples are divided into four sections per dimension. Resulting in 4x4x4 or 64 new sub simulation systems referred to as ΔV for Δ volume. The four parts per dimension is chosen because the simulation sizes are factors of two. The reduction in image size goes from 64x128x128 pixels per sample to 16x32x32 pixels per ΔV.

The size of a prenucleation zone is unknown, the ΔVs may not be larger enough to properly isolate the prenucleation structure. The same algorithm is applied to the 18,000 and 73,728 sized samples, resulting in relative sizes of ΔV shown in table 12.

Dimensions	18,000 atom	73,728 atom
1	1	1.6
2	1	2.56
3	1	4.096

Table 12. Relative size chart of ΔV 18,000 to 73,720 atom simulations.

In this way the nucleation size is accounted for as a variable by sample size. The large samples have ΔVs four fold the volume of the small samples.

2.7.1.4 Classification

Classification of each ΔV is done in a binary format with nucleation and non-nucleation class. Taking the summation of crystallization of each ΔV,

$$C = \sum_{i=1}^{16} \sum_{j=1}^{32} \sum_{k=1}^{32} c$$

Where C is the crystal value of a ΔV and c is the crystal value at one grid point, given that 16, 32 and, 32 are the final positions in the x, y, and z grid values of each ΔV.

The next step is to define the cutoff region in which a ΔV simulation is nucleated or non-nucleated.

$$\text{Class} = \begin{cases} \text{Nucleation, if CCC} \leq \text{ C} \\ \text{Non-Nucleation, if CCC} \geq \text{ 0.85C} \\ \text{Removed, if 0.85CCC} < \text{C} < \text{CCC} \end{cases}$$

CCC represents the critical crystal cutoff, a tuned value for classification of ΔV. If the summation of a ΔV crystal value is greater than or equal to the CCC that ΔV is classified as nucleating for all Gaussian fields: mass, charge, and crystal. For simulations less than 85% of the CCC value the ΔV is classified as non-nucleating, applying to its mass, charge, and crystal fields.

65

If the data is less than the CCC and greater than or equal to 85% of the CCC the data is removed, the crystal, mass, and charge fields of that ΔV will not be used. Data close to the CCC is likely to contain some crystal-like atoms or be on the boundary of a nucleation site, this data is removed from usage. Removing this data simplifies the modeling process and removes opportunity for misclassification. The boundaries for each ΔV are drawn arbitrarily to the nucleation of stishovite and some nucleation sites are split or the nucleation site is very close to the boundary of ΔV; For the purposes of identifying a relationship between nucleation and atomistic structure this data is removed from the data sets used by the CCNs to avoid misclassification.

The crystal fields are no longer used in the proceeding sections, their sole purpose was for classification. The charge and mass fields for each ΔV will be used in the appropriate category of nucleating and non-nucleating to feed into the CNNs.

2.8 Convolutional Neural Network

2.8.1 Model

The goal of this research is to establish if a relationship exists between prenucleation structure and nucleation behavior, high model accuracy is not need to establish if this relationship exists. Therefore, only simple CNNs were tested under the presupposition later models can be refined to increase system accuracy. This research two similar architectures were tested. Many of the model components were kept equal, the convolution and pooling layers altered for each model. This change was to exploit opportunity for failure via poor pooling and convolution design. It is unlikely that

this will occur significantly enough to prompt failure to distinguish a relationship between prenucleation structure and nucleation if it exists.

Both of these models originated from a model designed to classify computed tomography (CT) scans of chests to detect tuberculosis. This model was done with a binary classification, ether the patient had tuberculosis or did not and used a 3D CNN. The research was successful to achieve a 67.5% classification accuracy at predicting tuberculosis. This was higher than all 2D CNNs listed and ranks fifth of all models at time of publishing Hasib Zunair Aimon Rahman 2020. The high success rate and utilization of a binary classification is why this model was chosen to be the starting point for the CNN of this research.

The number of dense output layers was increased to two layers instead of one from the original CT scan CNN. Adding additional layers allows for the discovery of more advanced structures and features within the data. This is known as feature recognition and is performed serially within a neural network, meaning that more complex features follow those of simpler complexity. Adding a layer allows for two levels of feature to be recognized instead of one. This maybe useful or it maybe redundant within the system and will result in an increase training time. There is a small risk of increased over fitting within the system due to this design. The additional hidden layer should permit abstracting to unfavorable imaging were part of the nucleation structure is missing or cut off.

The CNNs used in this research are very small compared to many systems of today and many systems used within MD. Many systems start with much larger input images and use many more steps within the network. CNN's used by tech giants such as google have formed systems a dozen times the size of the CNN used in this research, with advanced feedback loops. GoogleLeNet is one of the smaller systems in
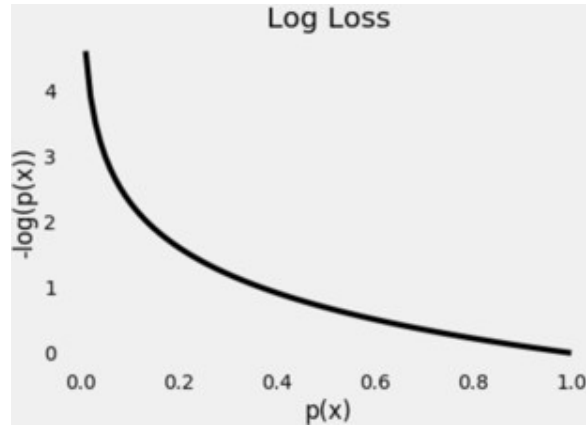
Figure 17. Log loss/binary entropy function for correct prediction of object Godoy 2018.

the tech industry and is 52 Layers thick compared to the seven and eight used within this research and is 80% to 50% the size of a standard CNN used with MD Alake 2020; Singh et al. 2018; Ryczko et al. 2018; Springenberg et al. 2014.

Understanding the scales used is important to understanding the application. The small CNNs used here should provide excellent indication to weather or not the method itself is applicable. The larger systems in industry and in the other research referenced are often not used to test a new hypothesis but increase the accuracy of a system to a known fact Hasib Zunair Aimon Rahman 2020. The simpler system has few failure modes to that of a large system. It has also been shown that CNN structure is often not a principal component of accuracy Springenberg et al. 2014. Both networks use a single output neuron with a sigmoid function. Classification number is n+1 output neurons, forcing the operation into a nucleation or non-nucleation state.

The optimizer used within the training is Adam and the loss is calculated using binary entropy or log loss. The log loss fiction is shown in 17,

$$loss = -\log(p(x))$$

were p(x) is the probability of prediction for the true case. The random prediction

receives a value of one. Incorrect predictions are more heavily penalized than correct predictions are incentivized Godoy 2018. The dropout rate was held at 0.1 for each hidden dense layer within both CNNs, as was done in the work of Hasib Zunair Aimon Rahman 2020. The dropout rate serves to increased the abstraction and robustness of the two systems. With 10% deactivation for each epoch redundant neurons and networks within the dense layers should develop. This in turn will translate to better validation accuracy.

80% of data in each array is randomly selected for the training set and 20% is kept for the test set and is constant across all experiments. In each system an early stopping criteria was implemented at which the system stops training if the validation accuracy has not changed within the past 15 epochs. This is on the lengthy side and gives the model ample room to adjust before stopping at which point the model is very likely to be over fitted. The over fitting will be stopped by an exit within the code if the validation loss increases significantly. The validation loss is the best numerical approximation of over fitting within the system.

The learning rate of each CNN also shares the same learning behavior as in the Hasib Zunair Aimon Rahman 2020 work. An initial learning rate of $\mathrm{Lr}_0 = 0.0001$ is used and follows a decaying exponential function. The exponential appears as,

$$\mathrm{Lr}_i = \mathrm{Lr}_0 * \mathrm{D}^{\frac{\mathrm{epoch}_i}{\mathrm{decay}}}$$

the decay is given as 100,000 for the models used and i represents the current epoch count. The current epoch number will decrease the learning rate until it goes to 1e-6 exponentially. The exponential decay of learning rate slows the rate at which gradient decent occurs and promotes convergence. Oscillations can occur at local minima that will cause the weight to bounce around the minima. Slowing the rate of decent over
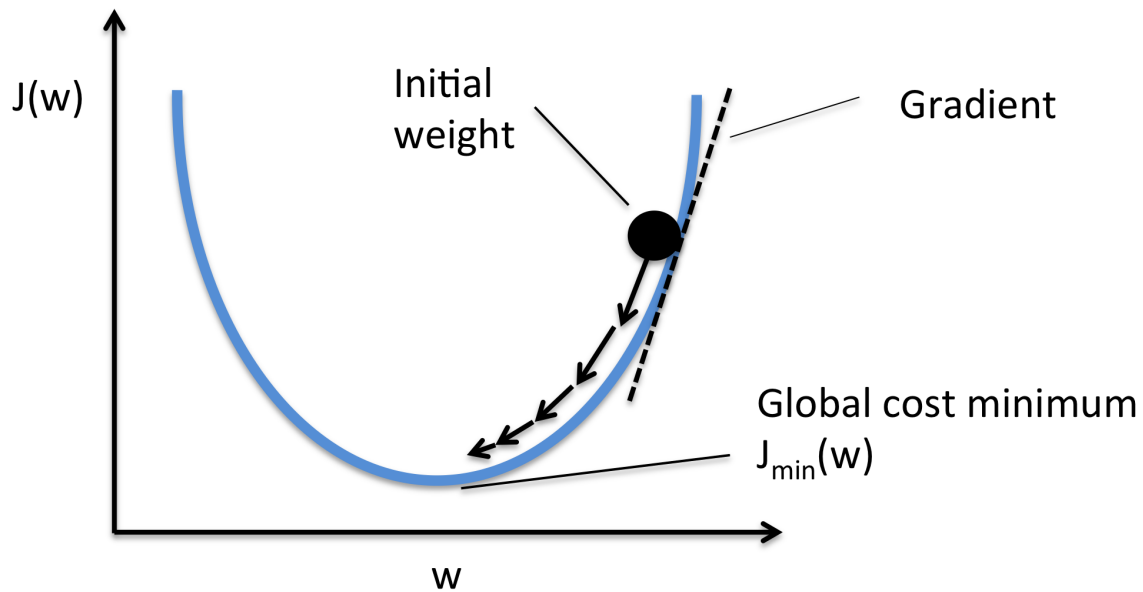
Figure 18. Example of single dimension gradient decent Raschka 2020.

epochs will allow the system to reach the local minima at an ever slowing rate, similar to figure 18.

To construct the systems Tensorflow was the ML distribution used and the most popular of all ML libraries Boone 2021. The new Tensorflow 2 library features direct integration of Karas library and full linear algebra ability similar to that of Numpy within it. It is the most user friendly library available and runs on nearly all hardware manufactures and models. Using this system greatly streamlined the research and eliminated much of the low level work behind the building the CNN's. This allowed the library to run on any high performance computing node within the ASU AGAVE cluster, it automatically selects the GPU or CPU and manages the necessary integration. The major drawback is that the library is large and takes ≈3 to 4 minutes to load onto any given node and perform initial hardware integration on that node.

2.8.2 Standard Convolutional Neural Network
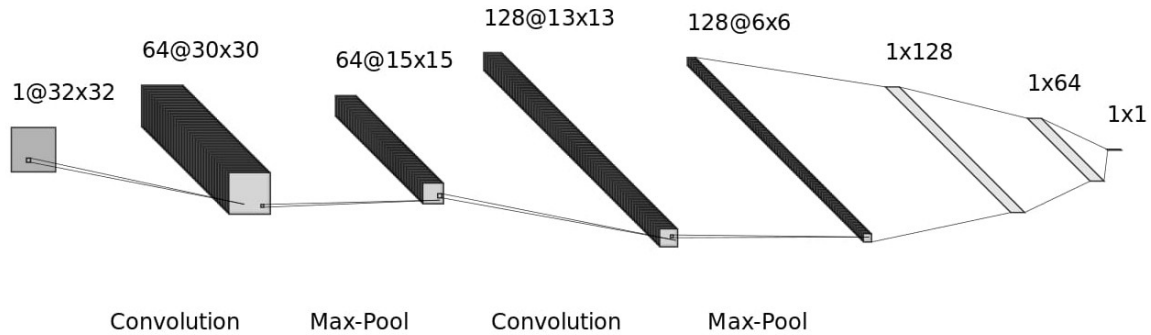
Figure 19. Standard CNN model, the third dimension of the system is not shown.

The standard model is nearly identical to that used in the Hasib Zunair Aimon Rahman 2020 literature code for these CNNs. The original three dimensional CNN was designed for images 128x128x128 in size, the size of a ΔV is 16x32x32; Due to the size reduction one convolution and one max-pool layer were removed from the network. Each convolution and max-pool cycle were doubled the number of filter used, the initial system started at 64 filters. Each activation layer uses stock relu activation layer for the convolution with 3x3x3 kernel size at stride of one. The pooling layers used 2x2x2 filters with stride of two. The system contained a total of 248,321 trainable parameters with 384 non trainable parameters, the parameters are listed in table 13, the graphical model is shown in figure 19.

2.8.3 All Convolution Convolutional Neural Network

The all convolution CNN was inspired by computer science literature of using simpler way of structuring a CNN, Springenberg et al. 2014. The research showed that simpler convolutional systems can outperform more complex systems of standard

Layer	Kernel	Activation	DxLxW	Filters	Parameters
Input			16, 32, 32		0
Convolution	3x3x3x1	relu	14, 30, 30	64	1792
Max Pooling	2x2x2x2		7, 15, 15	64	0
Batch Normalization			7, 15, 15	64	256
Convolution	3x3x3x1	relu	5, 13, 13	128	221312
Max Pooling	2x2x2x2		2, 6, 6	128	0
Batch Normalization			2, 6, 6	128	512
Global Pooling Average			128		0
Dense		relu	128		16512
Dropout		0.1	128		0
Dense		relu	64		8256
Dropout		0.1	64		0
Dense			1		65
Total Parameters	248,705				
Trainable Parameters	248,321				
Non-Trainable Parameters	384				
Initial Learning Rate	0.0001				
Decay Steps	100,000				
Decay Rate	0.96				
Epochs	100				
Early Stopping	15 Epochs				

Table 13. Parameters and design of the stock CNN. The kernel dimensions are given as length, width, depth, and stride.

architecture. Using the CIFAR-10 data set the classification error was reduced to 7.25%, the lowest seen of all networks to date with the second placing CNN at 7.97%; Data augmentation was implemented for this set. On the CIFAR-100 classification the system scored third place with 33.71% accuracy compared to 26.39% at top place. It does show a tendency toward higher accuracy at a smaller classification sizes making it an excellent choice to test within the bounds of this research.

An all convolution neural network was made out of the stock CNN architecture. The previous features of starting with 64 filters and doubling the number was maintained, to a final third layer consisting of 256 filters. The max pooling layers were removed and an additional convolution layer was added. The convolution layers used the same
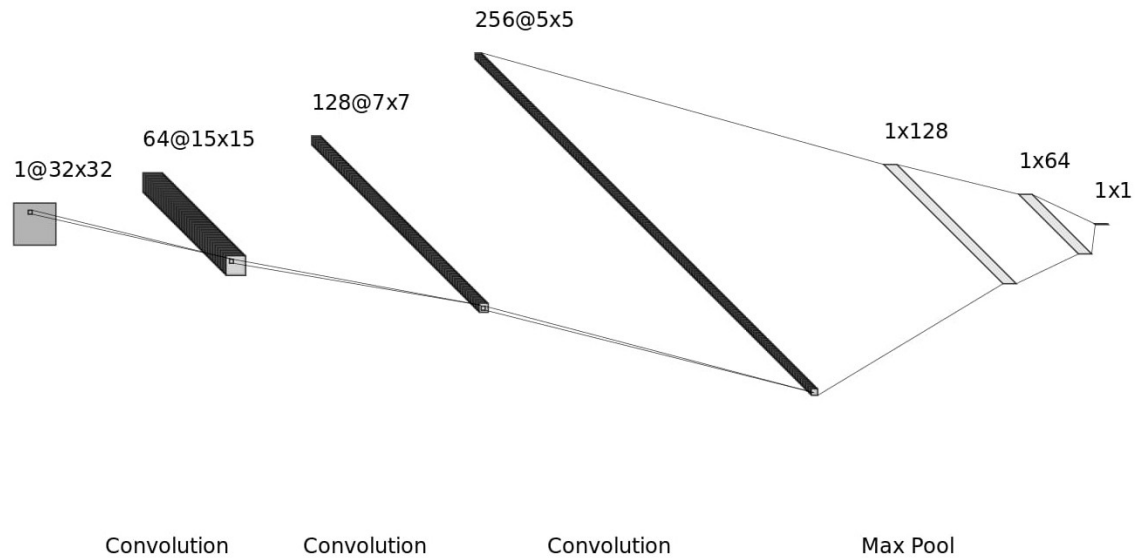
Figure 20. All convolution CNN model, the third dimension of the system is not shown.

kernel size of 3x3x3 with an increased stride of two instead of one to reduce image size. The total number of trainable parameters is five fold that of the standard CNN architecture with 1,150,209 trainable parameters and 896 non-trainable parameters. The new network is displayed in figure 20 and the parameters are listed in table 14.

Layer	Kernel	Activation	DxLxW	Filters	Parameters
Input			16, 32, 32		0
Convolution	3x3x3x2	relu	7, 15, 15	64	1792
Batch Normalization			7, 15, 15	64	256
Convolution	3x3x3x2	relu	3, 7, 7	128	221312
Batch Normalization			3, 7, 7	128	512
Convolution	3x3x3x1	relu	1, 5, 5	256	884992
Batch Normalization			1, 5, 5	256	1024
Global Pooling Average			128		0
Dense		relu	128		32896
Dropout		0.1	128		0
Dense		relu	64		8256
Dropout		0.1	64		0
Dense			1		65
Total Parameters	1,151,105				
Trainable Parameters	1,150,209				
Non-Trainable Parameters	896				
Initial Learning Rate	0.0001				
Decay Steps	100,000				
Decay Rate	0.96				
Epochs	100				
Early Stopping	15 Epochs				

Table 14. Parameters and architecture of the all convolution CNN. The kernel dimensions are given as length, width, depth, and stride.

Chapter 3

RESULTS

3.1   Hypothesis

Up to this point there has been an underlying assumption that the prenucleation structure of amorphous SiO_2 relates to the nucleation of that SiO_2. There is a belief in a "eureka" structure underlying the sample in which nucleation occurs. The hypothesis is that this prenucleation structure has a sole relationship with the nucleation of amorphous SiO_2 into stishovite as a function of high pressure shock, notably those from hypervelocity impacts.

To support nucleation behavior being apart structure a different argument is to be had. One in which variation within the lattice of quartz or atomistic structure of SiO_2 indicates nucleation inducing behavior. This is not clear from literature, current work into stishovite formation inclines the believer to this end. A reoccurring event when shocking SiO_2 is that if a sample nucleates it often nucleates quickly, within 100-200 ps based upon this research. If nucleation has not occurred by this point holding the pressure longer will not generate nucleation Yuan Shen and Reed 2016.

The use of a CNN to indicate the if this structure exists was done specifically for back propagation. If the hypothesis is proven correct on a CNN then it can be propagated to show the underlying Gaussian field that generated the structure and thus the atomistic structure. Therefore, permitting that structure to be modeled. This means doing the work of solving two problems in one thesis; Proving the relationship and solving for the underlying structure at the same time if the hypothesis is true.

3.2   Variables Tested

This work tests six variables with binary options totaling 64 experiments or 2^6. The last variable will be explained within the second CNN structural relationship indication method (CNNSRIM) which serves as a validation of the first result. The first five variables will be tested within each CNNSRIM, totaling 32 or 2^5.

Index	Variable	Option 1	Option 2
1	sample seed (type)	quartz	random
2	sample size (atoms)	18,000	73,728
3	Gaussian σ (Å)	1	4
4	Gaussian Field (type)	mass	charge
5	CNN (type)	standard	all convolution
6	Nucleation Detector (type)	cutoff	max

Table 15. A description of what variables are being tested within this research.

The first variable is the seed type of each experiment for the manufacture of the SiO_2. The random atom insertion is done by randomly inserting atoms into the LAMMPS sample at a size that yields amorphous SiO_2 standard pressure standard temperature. The quartz was generated by copying a generic α quartz file and repeating this structure in three dimensions.

The second variable was done by controlling for sample size, to which the atom number is related to the number of α quartz files used in a linear direction. In this case a 5x5x5 and 8x8x8 sized was used, propagating 18,000 and 73,728 atoms per sample respectfully.

The third variable is the variance or σ of the Gaussian function which translates to Å in real length. The 1 Å Gaussian fields gave detail showing the atomic position of all atom. The 4 Å Gaussian fields showed a great deal of meta structural behavior in which individual atoms were not identifiable.

The forth variable is the Gaussian field type. From the LAMMPS dump file the charge and mass fields were produced to be compared with crystallized experiments. The fields were produced by applying the mass or charge as the leading coefficient of the Gaussian function to each atom.

The fifth variable to be accounted for is the CNN architecture. The standard architecture is almost identical to the work done by Hasib Zunair Aimon Rahman 2020 for identification og tuberculosis using CT scans. The second architecture is based an all convolutional image reduction system inspired by Springenberg et al. 2014.

3.3 Input

3.3.1 Making Arrays

To control for the first four variables data arrays were produced to be used as inputs into the CNNs. The arrays contain three Gaussian fields each the crystal, mass, and charge. The first three variables seed, size, and σ are listed in table 16. The fourth variable is given by the data within the array: crystal, mass, and charge.

It is important to note that all samples are not included in the arrays. The spherical harmonic method used to identify crystal like atoms has wide variation in output. Many of the samples were not included as the dump file timesteps jumped atoms too quickly to allow for proper nucleation between 9 to 17 atoms, or the sample did not nucleate. The crystal-like atom range was necessary for the cutoff method. The cutoff method is designed to handle atoms of approximately the same crystal number. The next object of interest in this regard is the difference between output variable size of the same input. Arrays 1 and 2, 3 and 4, 5 and 6, and 7 and 8 are

77

all receiving the same input dump file and are not all sending out the same number of samples. This is likely due to the nature of the program produced, running on largely paralleled C++ scripts which interacts with the OS without delay. During the time of the data was processed the AGAVE cluster was being worked on and was in a sudo-functional state. With a large data set that spans multiple cores it could vary well be the script is not being performed correctly due to hard drive access problems and some files are being skipped by mistake. No error prompts did occur.

Array	Made (sim)	Used (sim)	Critical (ΔV)	Nuc (ΔV)	Non Nuc (ΔV)	Non (ΔV)	Zero (sim)	Seed (type)	Size (atom)	σ (Å)
1	500	275	60	1008	16094	498	55	Random	18000	1
2	500	332	60	1330	19328	590	60	Random	18000	4
3	72	44	37.5	214	2409	193	9	Random	73728	1
4	72	71	37.5	462	3670	412	10	Random	73728	4
5	500	367	55	1752	20990	746	62	Quartz	18000	1
6	500	221	55	1400	12215	529	24	Quartz	18000	4
7	80	48	35	114	3670	412	4	Quartz	18000	1
8	80	29	45	224	1090	334	7	Quartz	73728	4

Table 16. Results of the cutoff method to produce arrays in which to feed the CNN. Arrays 1 to 4 are randomly seeded, arrays 5 to 8 are quartz seeded, arrays 1, 2, 5, 6 are 18,000 atom, arrays 3, 4, 7, 8 are 73,728 atom, arrays 1, 3, 5, 7 use a $\sigma = 1$ Å, and arrays 2, 4, 6, 8 use a $\sigma = 4$ Å. Categories made and used show how many of the MD generated dump files were made and used respectfully. Critical criteria, nucleation, non-nucleation, non-used, and zero are the short results of the cutoff method. Critical criteria is the critical crystal count for the ΔV samples, a non-physical number to decided if a ΔV is crystallized. Nucleation (Nuc), non-nucleation (Non Nuc), and unused (Non) show the results of cutoff method with regards to ΔV. The zero category is how many samples received no nucleated ΔVs.

3.3.2 Cutoff Method

Table 16 shows the summarized results of the cutoff method in which the vast majority of all data across each array is non-nucleated, 88.61%. 7.25% of data is nucleated and 4.14% of data is unused, all the values are taken as array averages. In most arrays the unused data is smaller than the nucleated or non-nucleated categories, an exception is made for arrays 7 and 8. Arrays are 1, 2, 5, and 6 have nucleation counts that are ≈ 2 times the size of the unused data. The categories are abbreviated as nucleation (Nuc), non-nucleation (Non Nuc), and unused (Non).

A surprising feature is the extremes of the method. After meticulously checking the code these results appear to be valid from the methodology presented. The zero category shows how many samples were not awarded a ΔV within the nucleation category. At first appearance this maybe alarming to the reader. ΔV boundaries

are constant and the samples are believed to nucleate randomly. Under the correct circumstances a nucleation site can intersect the boundaries of four or eight ΔV sites, these sited will be categorized as unused in the final analysis and placed into the unused (Non) category removing them from the data set. Removing the ΔVs are set to optimize the discovery of a prenucleation structure responsible for nucleation.

Multiple nucleation sites per sample was seen within the crystal Gaussian fields. A few outliers received large numbers of nucleation ΔV within a sample, sometimes greater than ten. The vast majority of all data was 0-5 nucleation sites per sample. Full histograms of the number of nucleation classifications per sample can be found within appendix B. Each array contains an associated cutoff method histogram showing nucleations per sample.

The critical crystal number was tuned for each sample separately based upon the resulting histogram. Each histogram was tuned to minimize the number of large nucleation counts per sample. The average size of nucleation to non-nucleation is 9.76% or $\approx \frac{1}{10}$ any miss labeled data which is not removed by the unused classification has <9.76% chance of seeing into the non-nucleation category if miss labeled as nucleation. This is due to training the CNNs on an equal number of nucleation and non-nucleation data.

3.4   CNN Structural Relationship Indication Method 1

3.4.1   First Test

The first test of the CNNSRIM1 system yielded amazing 96-98% for every experiment. No mater what the array, architecture, or field used. This accuracy was high

from the initial epoch around 76% to 92% and rose to $> 95\%$ within 5 epochs. This accuracy persisted into the validation set and the loss functions were also low.

After plotting a histogram of classification confidence for each validation sample it became clear exactly what was happening. The CNNs are extremely confident that all ΔVs were non-nucleating. The CNNs did not receive an even number of data from each category during this training. Thus, 96% to 98% of each array was non-nucleating. A perfect example of poor training data selection, it did serve as a validation of CNN functionality for both architectures. The networks did correctly find the minimal loss function value and optimal selecting criteria to achieve the highest possible accuracy in validation. All proceeding tests received an even number of nucleation and non-nucleation structures. The non-nucleating ΔVs used were randomly selected to prevent taking all data from a few samples.

3.4.2   Results

The results from each category, meta data, summarized experiments, and individual experiments will be analyzed in this order. Each section's initial analysis will be performed within isolation to allow for a clear and robust conclusion to be drawn.

3.4.2.1   Meta Results

The average validation accuracy is 0.495 ± 0.0271 across all 32 tests within CNNSRIM1. The value includes the 0.5 accuracy or the random case in which the CNNs are equivocal to a coin toss. The variance among samples for validation accuracy is very low indicating that most of the tests are close to a random result.

This in no wise indicates if one class either nucleation or non-nucleation is classified well and the other is not, if both are equally poor, or if the tests contain experiments mixed between the two. The validation loss is high with a value of 1.304 ± 1.0228 and is varying widely across the sample space. In the log loss function a value at one indicates the sample is unsure what the category is. The models are poorly abstracting to the validation set and are divergent from the results seen with the training loss and training accuracy. The training accuracy and loss have values of 0.575 and 0.642 respectively. This does indicate the models are training to the training sets correctly. The models are very over fitted and have not appeared to abstract to atomistic structure.

3.4.2.2 Summarized Experiments

In table 18 the key feature is again the validation accuracy and validation loss values. The validation accuracy appears to be hovering at 0.5 for all samples. The value 0.5 appears 59% of the time or 19 of the 32 samples. This is shows no correlation in the experiments to any relationship between prenucleation structure or nucleation sites. The other 13 experiments are in a similar case and are hovering at ≈ 0.5 in both directions the only validation accuracy seen outside of 0.5 ± 0.05 is sample 25 which is 8% worse at classifying the data than random chance. Array 7 is the array used in sample 25 contains 228 ΔVs giving it 46 ΔVs in which to validate the tests, a small number explaining how the accuracy can be so low statistically. The perfect 0.5 validation accuracies indicate random chance and no corollary value, this is expected as the validation tests sets are in the hundreds of units for arrays 1, 2, 5, and 6 where most of these values occur.

The training sets show training across almost all sets. The training sets in most cases did correctly train to the training data. In experiments 4, 21, and 32 the training sets have very slight correlations within the negative direction. Experiment 15 is given to random chance with a training accuracy of 0.5. Some samples, 10 and 26 trained to a high degree of accuracy in the 0.8 range. This shows no failure within the models in terms of their process and the three negative corollary values maybe due to a poor local location minima within the cost function on the data set.

Comparing the loss values of the training and validation sets show highly divergent behavior. The loss values between almost all experiments are much higher for the validation set which routinely exceeds one 11 times while training validation never does so. Nor in a single case is the validation loss below the training loss. The combinations of reasonable training set values, high validation loss, and near random validation accuracy point to a non-correlation event within the data. Even over fitting should not yield such a random an outcome within the validation accuracy.

3.4.2.3   Experimental Level

Next is to analyse the results based upon individual experiments comparing the loss per epoch graph, accuracy per epoch graph, and class predication value histograms. All of these are available to the reader in appendix C. It should be known that every histogram plot contains 10 divisions, some plots do look a bit more like lines due to nearness of data. It should also be noted that no sample reached 100 epochs. Its set numerical limit, all CNNSRIM1 graphs were stopped by early stopping criteria, either the limits of no fluctuation in validation accuracy for 15 epochs was reached or the validation loss is poor.

Training behavior is dominated by slowly decreasing loss graphs and increasing training accuracy, at times the decrease in training loss is very mild to nonexistent. Experiments fall into two major classes; First, the validation accuracy remains at or very near to 0.5, second, validation accuracy bounces across the graph rapidly centering at ≈ 0.5. The validation loss often fluctuates about the domain space with epochs working its way in an upward direction. The best looking graph is experiment 9 which clearly shows some positive training of the validation set at the expense of the loss function which moves in the increasing direction. A notable experiment is 32 in which the training loss remains constant while the training accuracy decreases.

Histograms are key to understanding the experiments. Nearly all histograms have a very narrow width centering around 0.5. The worst cases are experiments 4, 10, 12, 16, 20, 24, 25, 28, 29, and 32 which all have near zero width in their respective histograms and have trained to random chance at 0.5. These samples often received reasonable training values in table 18. The remaining histograms contained narrow widths and hovered around 0.5. An exception to this rule are experiments 7, 11, 26, 27, and 31 did have some divergence from the 0.5 line and appeared to behave in a more traditional way. It should also be clearly stated that no significant difference was seen between either the nucleation or non-nucleation categories within the histograms. The CNNs were not bad at classifying the data in one category but were universally equivalent to random chance. This rules out a relationship in one data category.

3.4.2.4 Results Indexing

Testing was done with an even number of nucleating and non-nucleating ΔV. This yielded the summarized results seen within table 18 and the full results seen

Category	Average	Standard Deviation
Loss Train	0.642	±0.0820
Loss Validation	1.304	±1.0228
Accuracy Train	0.575	±0.0948
Accuracy Validation	0.495	±0.0271

Table 17. Averages and standard deviation for all indexes in CNNSRIM1.

in appendix C. 32 experiments were performed each one contains an epoch to loss and epoch to accuracy graph within appendix C. The final epoch value was given for each line: training loss, valuation loss, training accuracy, and validation accuracy. The second chart provided with each sample is a histogram of the confidence intervals for the categorization of all validation data. In the case of this chart crystal refers to the nucleation or non-nucleating behavior of the ΔV. Positive refers to a correct classification and negative refers to an incorrect classification. Table 18 shows the short version of all the testing done for CNNSRIM1. The first five variables are listed for each test or index on the left side. On the right side the loss function values and accuracy values for the last epoch is shown. The data array used to feed the CNN is also shown. Table 17 contains the average and standard deviation of the loss and accuracy values.

Index	Array	Seed (type)	Size (atom)	σ (Å)	CNN (type)	Gauss (type)	Loss (train)	Loss (val)	Acc (train)	Acc (val)
1	1	Random	18000	1	Conv	Mass	0.605	3.045	0.610	0.506
2	1	Random	18000	1	Conv	Charge	0.609	1.365	0.590	0.498
3	1	Random	18000	1	Stand	Mass	0.692	0.749	0.520	0.500
4	1	Random	18000	1	Stand	Charge	0.694	0.695	0.490	0.500
5	2	Random	18000	4	Conv	Mass	0.650	2.542	0.538	0.491
6	2	Random	18000	4	Conv	Charge	0.647	1.103	0.547	0.493
7	2	Random	18000	4	Stand	Mass	0.695	0.782	0.507	0.507
										Continued on next page

Table 18 – continued from previous page

Index	Array	Seed (type)	Size (atom)	σ (Å)	CNN (type)	Gauss (type)	Loss (train)	Loss (val)	Acc (train)	Acc (val)
8	2	Random	18000	4	Stand	Charge	0.693	0.693	0.505	0.500
9	3	Random	73728	1	Conv	Mass	0.510	1.058	0.748	0.542
10	3	Random	73728	1	Conv	Charge	0.395	1.920	0.808	0.542
11	3	Random	73728	1	Stand	Mass	0.686	0.727	0.587	0.514
12	3	Random	73728	1	Stand	Charge	0.689	1.252	0.552	0.500
13	4	Random	73728	4	Conv	Mass	0.628	3.685	0.649	0.500
14	4	Random	73728	4	Conv	Charge	0.658	0.876	0.625	0.464
15	4	Random	73728	4	Stand	Mass	0.694	0.729	0.500	0.507
16	4	Random	73728	4	Stand	Charge	0.693	0.694	0.482	0.500
17	5	Quartz	18000	1	Conv	Mass	0.593	0.694	0.578	0.500
18	5	Quartz	18000	1	Conv	Charge	0.587	0.700	0.592	0.500
19	5	Quartz	18000	1	Stand	Mass	0.691	0.718	0.533	0.454
20	5	Quartz	18000	1	Stand	Charge	0.688	0.695	0.519	0.500
21	6	Quartz	18000	4	Conv	Mass	0.695	0.843	0.488	0.500
22	6	Quartz	18000	4	Conv	Charge	0.694	0.704	0.509	0.500
23	6	Quartz	18000	4	Stand	Mass	0.694	0.708	0.512	0.489
24	6	Quartz	18000	4	Stand	Charge	0.693	0.694	0.495	0.500
25	7	Quartz	18000	1	Conv	Mass	0.612	0.959	0.668	0.421
26	7	Quartz	18000	1	Conv	Charge	0.371	2.783	0.860	0.500
27	7	Quartz	73728	1	Stand	Mass	0.690	0.759	0.508	0.400
28	7	Quartz	73728	1	Stand	Charge	0.695	0.721	0.532	0.500
29	8	Quartz	73728	4	Conv	Mass	0.625	2.893	0.661	0.500
30	8	Quartz	73728	4	Conv	Charge	0.606	4.508	0.664	0.500
31	8	Quartz	73728	4	Stand	Mass	0.694	0.745	0.543	0.500
32	8	Quartz	73728	4	Stand	Charge	0.693	0.698	0.484	0.500

Table 18 – continued from previous page

Index	Array	Seed	Size	σ	CNN	Gauss	Loss	Loss	Acc	Acc
		(type)	(atom)	(Å)	(type)	(type)	(train)	(val)	(train)	(val)

Table 18. summary results of CNNSRIM1 experiments. The five variables being tested are listed on the middle columns along with the array used to feed the CNNs for each experiment on the left. The right side contains the final epoch's loss and accuracy for training and validation data for each experiment.

3.4.3 Summary

It appears that there is no relationship within the experiments regarding the prenucleation structure and nucleation behavior. Three levels of analysis were performed: meta analysis, experiment summary, and individual experiment. In each case the solution was marked with near or at random validation accuracy, and high validation loss. Variation did occur with regards to training values, some experiments trained to the training set very well. The results of the training data show that no apparent error occurred within the training process of the models. The data was thoroughly randomized across multiple steps and the input ΔV experiments were vetted to allow no biasing of the data.

The key to understanding the experiments is the extreme narrow width of the validation histograms in which the predicted value of each class is at 0.5 or close to it. This indicates that the experiments are trained for at random as no significant distinctions exist between training and validation sets. Only extremely minor adjustments in weights were seen in the histogram, showing heavy over fitting to the training

set. No difference was seen cross-category in regards to the histograms, showing no relationship to nucleation and prenucleation structure.

3.5 CNN Structural Relationship Indication Method 2

3.5.1 Introduction

Previously, only five variables were tested. There maybe question in regards to the validity of the cutoff method to classify the ΔV data. The cutoff method is not the optimal solution but is expected to yield results with few miss classifications. It was deemed the weakest point in the research, and another method of classification was developed to validate the results. This new method of ΔV classification utilizes the previous five variables and the variable max classification method. This new system of study is referred to as CNNSRIM2. The concept behind the max classification method is to take the ΔV with the maximum crystal summation of all ΔVs within the sample. This of means that any nucleation site on a boundary will be only partially included or miss classified, samples with multiple nucleation sites will have only the best ΔV classified for nucleation.

Within the non-nucleation class of ΔV some nucleated and partially nucleated miss classification will occur. There are 64 ΔVs per sample and 63 non-nucleation ΔVs using this method. If every sample contained one misclassified ΔV it would make up 1.6% of the data, after removing all redundant data within the data sets only $\approx 1.6\%$ of the non-nucleated data would be misclassified. This is due to the intensive randomization steps taken to ensure no bias in within the data sets and final selection of equal numbers of nucleating and non-nucleating ΔVs to be used as

examples. At this stage the CNNs do not need a high degree of accuracy; Only a level of accuracy that is significantly more than random chance and some indication that abstract training on the ΔV samples is occurring. It would take an average of 6.25 misclassified ΔVs within each sample to reach 10% non-nucleation misclassification, the cutoff method found of 0 to 5 nucleation sites per sample for the majority of data far below 6.25.

It should be clearly noted that this reduces the size of the data sets by over a factor of 4 in most cases when compared to the cutoff method. The data sets are now the size of the sample inputs times two, to see this size refer to table 16 and look at the used column. Only one ΔV is nucleating and the set is always to remain balanced, therefore it is twice the sample number. Experiments using arrays 3, 4, 7, and 8 should be looked at with more scrutiny due to there small data sizes.

3.5.2 Result

After rerunning all the experiments with the new max classification method an identical table set to CNNSRIM1 was produced for CNNSRIM2. Note that the indexing method across tables is the same for that of CNNSRIM1. The proceeding analysis of the results will follow the same format as was done in previous CNNSRIM1 review: meta analysis, summarized experiments, and individual experiments.

3.5.2.1 Meta Analysis

Table 19 shows the averages of all experiments within CNNSRIM2, there are two numbers almost identical to those within table 17; The training loss with 3% difference

and the validation accuracy with 0.2% difference. The standard deviations are slightly larger in CNNSRIM2 than CNNSRIM1 and are still narrow with differences lower than 18.8% for all categories ignoring validation loss. Valadation accuracy is near random with 0.5 being within the 95% confidence interval indicating that no training is occurring on features within the atomistic structure; Rather training is correlated to something within the training set that is not present within the validation set; Training accuracy is 0.61 with 0.494 validation accuracy. The validation loss is high at a value of 1.043, 68% greater training losses showing sever over fitting within experiments and near random prediction chance. The CNNs did train to the given training data, shown as low training loss and training accuracy of 0.619 and 0.610 respectively. Collectively this is the same as the case seen CNNSRIM1 and shows over fitting of the model and no ability to abstract to the atomistic structure present.

3.5.2.2 Summarized Experiments

19 of the 32 or 59.4% of the experiments have random validation accuracy values of exactly 0.5, four more have values within ± 0.02 of 0.5. 71.9% of experiments have validation accuracies within ± 0.02 of random. Many of these values often received good training accuracies and were training on the given training sets, with 12 of the 32 experiments receiving >0.6 training accuracy. The validation losses are high across the different experiments with 9 of the 32 or 28.1% of the values receiving a loss higher than one. The highest validation loss is 3.630 in experiment 5 with a training loss of 0.618 or $\frac{1}{6}$ that of the validation loss. In every case except experiments 28 and 32 the validation loss was higher than within the training set, these exceptions were within 1% difference. In some experiments, notably 3, 8, 20, and 32 achieved lower training

accuracy than validation accuracy. Experiment 32 was an exceptional experiment with accuracies of 0.413 and 0.417 for train and validation respectively.

There are a few notable experiments in CNNSRIM2; Experiment 32 which showed an ability in training and validation to correlate negatively to the data. This is likely not of consequence, 58 ΔVs used in the experiment leaving a validation set size of 12, leaving the final solution subject to more variation. Experiments 9, 13, and 14 showed validation accuracies above 0.53 at 0.611, 0.536, and 0.607 respectively. Experiment 9 is likely a chance outcome, the validation loss is 5.4 times that of the training loss; Experiments 13 and 14 also have validation losses that are higher than all experiment training losses. All of these experiments came from smaller sized arrays and may show some relationship in isolation between atomistic structure and nucleation of stishovite. Experiments 13 and 14 share the same experiment seeding, experiment size, Gaussian distribution σ, and CNN architecture.

3.5.2.3 Experimental Level

Epoch graphs found within appendix D, show superior training in the all convulsion CNN architecture than the stock CNN architecture, best seen in experiments 1 to 4. The training losses go down relatively smooth while the validation losses increases with time for all convolutional CNN architecture. The training accuracy quickly increases in a sudo linear fashion and the validation accuracy remains around 0.5. The stock CNN architecture shows a retardation to the training set in which it trains but does so in an erratic manner. Experiment 7 is a perfect example of this the epoch graph resembles a seismograph undergoing an earthquake. At times there appears to be

Category	Average	Standard Deviation
Loss Train	0.619	±0.1010
Loss Validation	1.043	±0.6004
Accuracy Train	0.610	±0.1141
Accuracy Validation	0.494	±0.0480

Table 19. Averages and standard deviation for all indexes in CNNSRIM2.

little to no training taking place. This is the same case for validation accuracy which fluctuates heavily across the epoch graph.

23 of 32 or 71.9% of prediction histograms have 0.1 or less prediction value width centered at 0.5. They appear more like lines drawn at the 0.5 place. This displays an inability to train and to predict, only very minute changes within the ΔV data sets are being trained for and the model is very unsure of the classifications. All but two experiments 9 and 14 do not have prediction validations centred directly at 0.5. Some experiments do have a better overall spread reaching prediction widths of 0.4 in other experiments.

Experiment 13's histogram is a line at 0.5 indicating that it is training to minute changes within the data and is unsure of experimental outcome. The favorable validation accuracy displayed by experiment 13 was seen within it's epoch. The overall trend of this experiment is over fitting and increasing validation loss, it reached a 0.851 over training value.

Experiment 9 had a well disperse series of predictions across the histograms. It seemed to have a strong prediction of non-nucleation sites with a poor and week prediction of nucleation sites. Some nucleation sites were heavily misclassified as non-nucleation sites. It did seem to predict validation reasonably well and even reduced validation loss during some epochs. It does not seem to strongly indicate a clear relationship between training and validation epochs, rather the validation

accuracy fluctuates heavily across epochs. The validation loss is very high during most epochs, if it is correctly abstracting to the validation set it is doing so in an unorthodox way.

Experiment 14 showed varying results when its prediction values were plotted to a histogram. It more correctly predicted non-nucleation sites and randomly predicted nucleation sites. If a nucleation site was predicted correctly the model was often reasonably sure of the value, if it wrongly misclassifed a nucleation site it was often very sure. The epoch graph did not appear promising to a relationship. The model trained on the training set very well. It showed increasing validation losses over epochs and ended on a value close to the starting point with wide fluctuations across epochs. The validation accuracy was fluctuating around 0.5 for most of the training, the last 12 epochs were spent within the greater than 0.5 region. Due to the small size of the validation set, 28 ΔVs, the high validation loss, and the extreme fluctuations in validation accuracy the result is likely a statistical artifact and the model is not abstracting onto the atomistic structure.

Index	Array	Seed (type)	Size (atom)	σ (Å)	CNN (type)	Gauss (type)	Loss (train)	Loss (val)	Acc (train)	Acc (val)
1	1	Random	18000	1	Conv	Mass	0.611	1.575	0.591	0.473
2	1	Random	18000	1	Conv	Charge	0.607	1.040	0.602	0.482
3	1	Random	18000	1	Stand	Mass	0.700	0.707	0.468	0.500
4	1	Random	18000	1	Stand	Charge	0.691	0.702	0.520	0.509
5	2	Random	18000	4	Conv	Mass	0.618	3.630	0.605	0.492
6	2	Random	18000	4	Conv	Charge	0.637	1.001	0.539	0.500
7	2	Random	18000	4	Stand	Mass	0.689	0.791	0.549	0.485
8	2	Random	18000	4	Stand	Charge	0.697	0.707	0.461	0.500
9	3	Random	73728	1	Conv	Mass	0.309	1.670	0.843	0.611
									Continued on next page	

Table 20 – continued from previous page

Index	Array	Seed (type)	Size (atom)	σ (Å)	CNN (type)	Gauss (type)	Loss (train)	Loss (val)	Acc (train)	Acc (val)
10	3	Random	73728	1	Conv	Charge	0.544	0.826	0.700	0.500
11	3	Random	73728	1	Stand	Mass	0.652	1.787	0.643	0.500
12	3	Random	73728	1	Stand	Charge	0.691	0.747	0.529	0.500
13	4	Random	73728	4	Conv	Mass	0.441	0.944	0.851	0.536
14	4	Random	73728	4	Conv	Charge	0.409	0.743	0.825	0.607
15	4	Random	73728	4	Stand	Mass	0.688	0.897	0.579	0.500
16	4	Random	73728	4	Stand	Charge	0.693	0.900	0.553	0.500
17	5	Quartz	18000	1	Conv	Mass	0.603	0.891	0.599	0.500
18	5	Quartz	18000	1	Conv	Charge	0.608	0.693	0.592	0.500
19	5	Quartz	18000	1	Stand	Mass	0.686	0.698	0.539	0.500
20	5	Quartz	18000	1	Stand	Charge	0.698	0.694	0.502	0.500
21	6	Quartz	18000	4	Conv	Mass	0.673	0.791	0.599	0.466
22	6	Quartz	18000	4	Conv	Charge	0.667	0.770	0.599	0.511
23	6	Quartz	18000	4	Stand	Mass	0.688	1.318	0.514	0.500
24	6	Quartz	18000	4	Stand	Charge	0.691	1.445	0.534	0.500
25	7	Quartz	18000	1	Conv	Mass	0.548	0.748	0.737	0.500
26	7	Quartz	18000	1	Conv	Charge	0.410	2.112	0.789	0.500
27	7	Quartz	73728	1	Stand	Mass	0.675	1.044	0.553	0.500
28	7	Quartz	73728	1	Stand	Charge	0.697	0.695	0.526	0.500
29	8	Quartz	73728	4	Conv	Mass	0.546	0.693	0.696	0.500
30	8	Quartz	73728	4	Conv	Charge	0.556	0.691	0.717	0.500
31	8	Quartz	73728	4	Stand	Mass	0.610	0.745	0.739	0.333
32	8	Quartz	73728	4	Stand	Charge	0.693	0.693	0.413	0.417

Table 20 – continued from previous page

Index	Array	Seed	Size	σ	CNN	Gauss	Loss	Loss	Acc	Acc
		(type)	(atom)	(Å)	(type)	(type)	(train)	(val)	(train)	(val)

Table 20. summary results of CNNSRIM2 experiments. The five testing variables are listed on the left side along with the data array used to feed the CNNs. The right side contains the final epoch's loss and accuracy for training and validation data.

3.5.3   Summary

Overall most models were of little more effectiveness than a coin toss, the CNNs showed no signs of abstracting to the atomistic structures fed into the systems. The systems correctly trained upon the given models which is shown on all three levels of analysis by decreasing training losses and increasing training accuracies to above 0.8. The validation loss often reached incredibly high values with nine of the experiments reaching above one and some multiple folds higher than their respective training losses.

Experiments 9, 13, and 14 did show a potential indication of training to atomistic structure based upon validation accuracy. All of which was addressed in detail within the previous sections. Experiment 13 was invalidated by its validation prediction accuracy histogram which was set to 0.5 for all cases with very minor deviations from this value. Experiments 9 and 14 may show abstraction to atomistic structure but do so in a very lose way with indications of being a statistical occurrence by their small validation set sizes, validation loss behavior, and overall validation set fluctuations across epochs.

3.6   Summary

3.6.1   Stishovite Formation

3.6.1.1   Review

The research into stishovite formation within quartz and randomly seeded amorphous SiO_2 samples was not a part of the research hypothesis. This work has taken many months to perform and the methodology was perfected in a way that led to the production of 1,152 samples, most of which produced stishovite. This aspect of the research should be mentioned as part of the results even though it is within the methodology chapter. Experimental results for this work is highly similar to the work done by Shen and Reed 2016 and was performed using different methods of shocking the experiment. Due to time and requirement constraints another hypothesis and research project was not made out of sample crystallization behavior, perhaps it can be so in the future. A full statistical analysis was not performed due to the lack of repeated preshock structures in testing.

3.6.1.2   Results

Two rounds of testing was done on quartz and randomly seeded SiO_2 in an amorphous state after melting and quenching of the sample. The first round of testing was to find the repeatedly spoken of irreversible deification seen within MD and empirical studies. This notable densification was mot found within the work.

The second round of the experiments aligned with work done by Yuan Shen and

Reed 2016. It is clear from the increase in initial shock temperature to final shock temperature whether or not the sample had formed stishovite or remained in an unaltered state. Disordered samples raise initial temperature within the first 50 ps and remain at that temperature until end of sample. Any densification experienced is done within the first 50 ps of process or falls within 10^{-3} to 10^{-4} g/cm^3. Stishovite forming samples experience a rise in temperature between the 100 ps and 1 ns position. As the stishovite crystal(s) grow in size the temperature of the sample increases to a value in or close to that predicted by Yuan Shen and Reed 2016. Temperature of a sample is a direct function of shock pressure Ahrens 2002. It was discovered that the crystallized samples do experience a densification on the order of 1 to 2 magnitudes greater than non crystallized samples from 50 ps to the 1 ns after shock application. Densification is on the order of 10^{-2} to 10^{-3} g/cm^3 under pressure loading.

As discovered during testing the shock pressure is the biggest driver of stishovite formation within a sample. There is a band of 10 GPa or greater in which a sample will nucleate. Nucleation is not constant and appears to be a function of probability within they system. Certain values towards the middle of the distribution almost always nucleate while values farther away tend to not nucleated as often. Pressure damp timescales do not appear to effect the formation of stishovite within a range of 0.1 ps to 10 ps. Within the temperature damp range of 0.05 ps to 0.1 ps the samples will form stishovite, 0.05 ps seems to form crystal slightly more often within the quartz seeded samples. The quartz seeded samples generated optimal stishovite at a shock pressure of 55 GPa with an average densification of $5.90e - 3 \frac{\text{g}}{\text{cm}^3}$, the random seeded samples did so at 60 GPa with an average deification of $1.78e - 2 \frac{\text{g}}{\text{cm}^3}$.

3.6.1.3   Random Atom Insertion

Another feature of the work is the use a new method to form an SiO_2 matrix using random atom insertion. This successfully formed stishovite and did so better than the quartz seeded samples. There has been no previously mentioned work into a method of this kind to generate SiO_2 and expose the shock to high pressure. It is clear from the experiments that the atomistic structure differs between the quartz seeded and randomly seeded samples. This is shown by the different stishovite formation behavior under various shock pressures.

3.6.2   Atomistic Structure and Nucleation

The results of both the CNNSRIM1 and CNNSRIM2 show the same general behavior within experiments. Experiments are often dominated by near random validation accuracy and high validation loss values. The CNNs were tested before being implemented and showed correct abstraction behavior. They did train effectively on the training set and showed valid and expected behavior across various epochs. The histograms of validation prediction values within both the CNNSRIM1 and CNNSRIM2 were often centered at 0.5 with a very small width. More than half of the data had a prediction width less than 0.1 in these histograms. This extreme narrowness was more in CNNSRIM2 than in CNNSRIM1.

In CNNSRIM2 there were three instances that the CNN might be abstracting to the atomic structure of the samples, experiment 9, 13, and 14. After careful analysis experiment 13 was shown to be invalid. Experiments 9 and 14 maybe undergoing some abstraction, this is unlikely. The validation accuracies were highly variant across

epochs and validation loses high. No other samples showed reasonable training to the data presented. This is likely a statistical artifact as some samples with no relationship will show some semblance of validity if enough experiments are performed. In context of the experimental factors and other experiments this is likely a statistical artifact.

3.7   Discussion

It may seem strange to support results which show atomistic structure is not responsible for stishovite nucleation within amorphous SiO_2. Most of the research focus was placed heavily upon ensuring valid methodology after the samples were produced and clean data management. Some underlying effects of molecular behavior maybe responsible for the outcome. The following section will seek to address what may have happened and why no relationship was discovered.

3.7.1   How else can nucleation occur

3.7.1.1   Atomistic Rearrangement

No work is done and no literature found into the atomistic behavior of amorphous SiO_2 during shock. The process is a violent event with massive interatomic energies, so much so that various atomic potentials were developed to model this behavior do to the close atom proximity Pedone et al. 2006; Yuan Shen and Reed 2016. The figures 22 and 23 show an example of a sample generated in this research before the shock and after 2 ps. The sample has flattened like a pancake and has been reduced by a factor of 2 in the direction of the piston and effectively doubles in density. The work
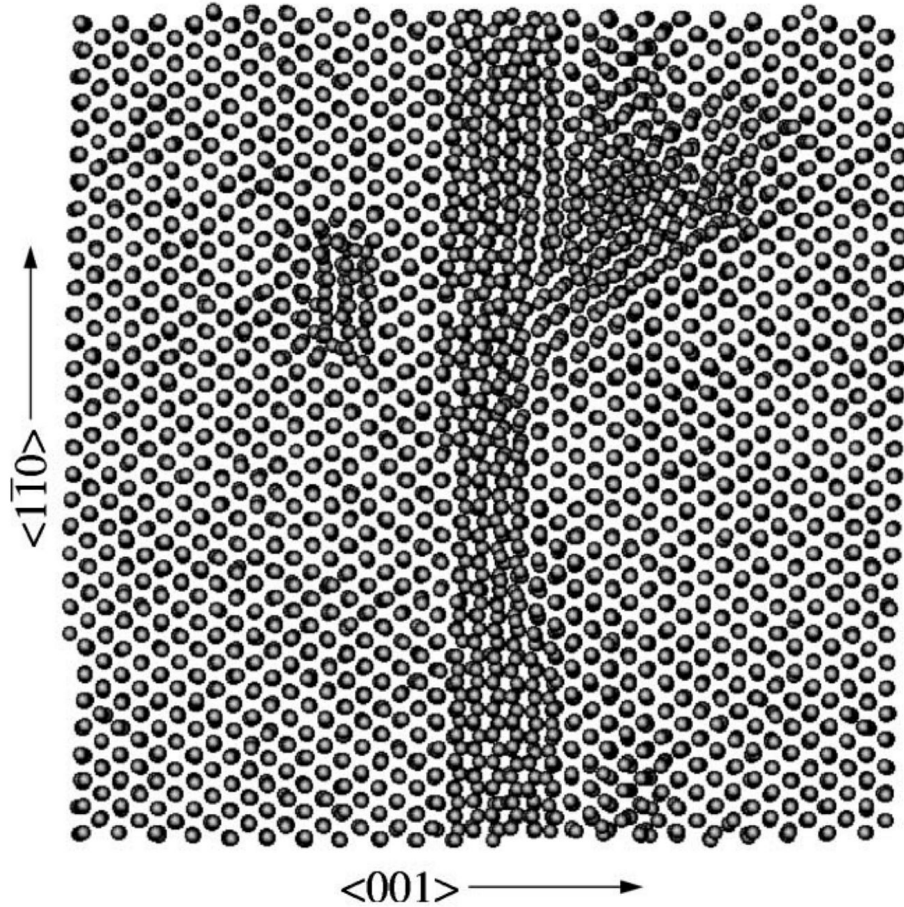
Figure 21. HPHug shock wave in progress taken from Ravelo et al. 2004.

done by Ravelo et al. 2004 shows a crystal under shock in figure 11 of that paper shows a top view of atoms under going an NPHug shock. During a NUHug shock the atoms are shown moving intensely as the wave hits them causing them to greatly condense, shown in figure 21.

It maybe that the intense shock not only moves the atoms during shock but causes a rearrangement of these atoms. The pre and post shocked sample may not only have changed relative shape but changed atomistic structure. Therefore the structure that the CNNs received may not be the structure in which nucleation occurred. If this happened it still leaves the hypothesis to be valid, the structure tested for did not have
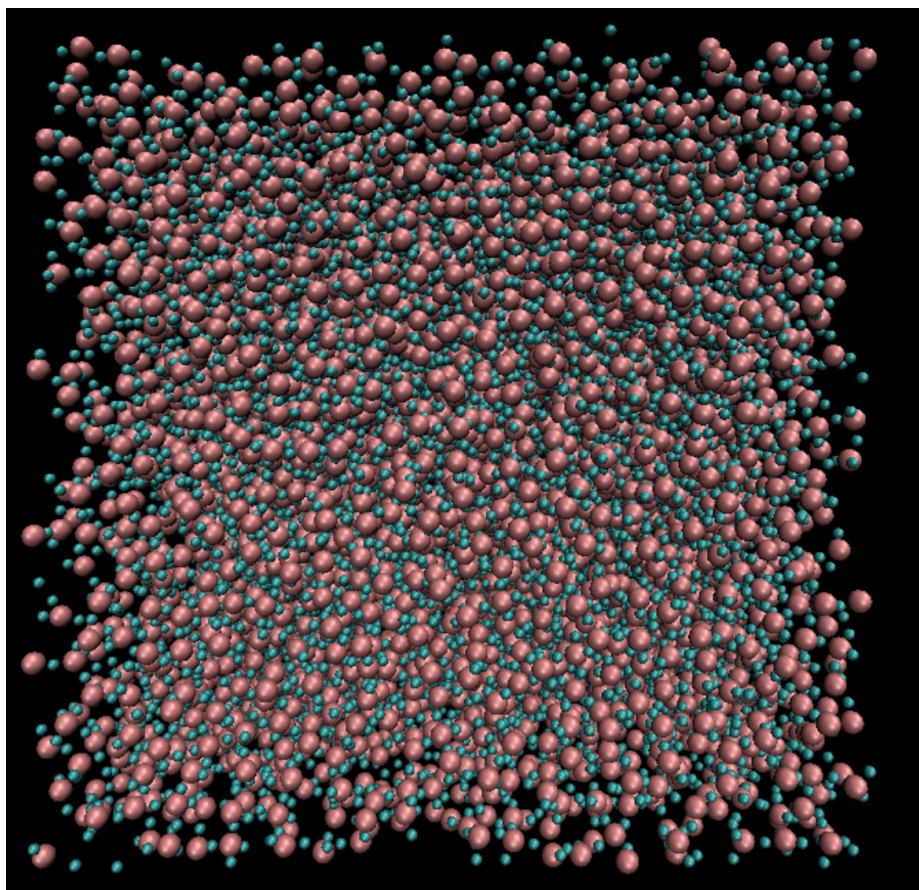
Figure 22. Example of random atom insertion 18,000 atom sample before 60 GPa shock.

a direct relationship with the final structure. This is amplified by the amorphous state of the samples used within this research. Amorphous SiO_2 is in a liquid arrangement and is the lowest density structure of the SiO_2 available within solidifed form. It would be the most likely material to support atomic rearrangement as no long range structure is present.
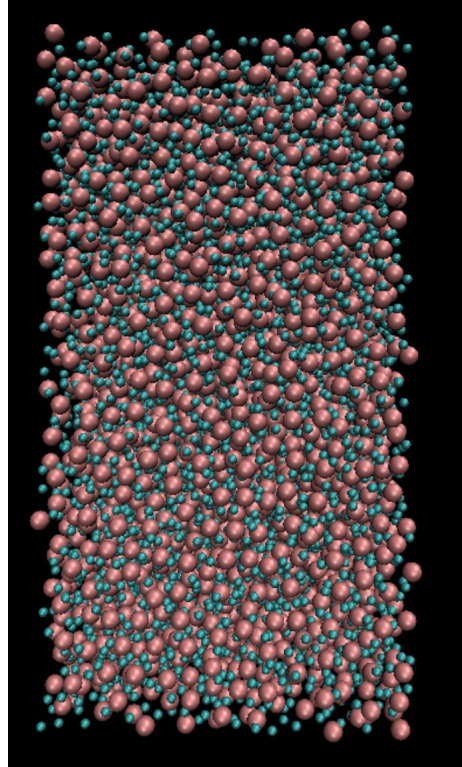
Figure 23. Example of random atom insertion 18,000 atom sample after 2 ps at 60 GPa shock.

3.7.1.2 No Atomistic Relationship

Based upon this research atomistic configuration is not the primary driver of nucleation. It maybe that the high resolution atomic interactions of various kinds move atoms into a position which triggers a nucleation event. This would be a valid hypothesis based upon this research results. This means that the underlying structure is of no consequence to the nucleation event.

3.7.1.3   Nucleation Sites Everywhere

Another likely event is that atomistic structure is a precursor to nucleation but atomic interactions are the driving force. The nucleation inducing structures would be triggered after a molecular event took place. This would mean that prenucleation structure maybe present throughout the sample leaving the CNNs unable to classify a differing structures. There could be large numbers of nucleation precursors within each sample making the CNNs unable to indicate a difference between nucleation and non-nucleation structure.

3.7.2   Improvements

An improvement that could have been made is with the prenucleation structure. The structure was acquired from one dump file in which the atoms are not in their average state. If multiple dump files were used an average atomic position could be generated. Making Gaussian charge and mass fields of each dump file into an averaged charge or averaged mass Gaussian field. This would be a more rigorous way to perform the research. Due to the small fluctuations in atomic position it is unlikely this would be a driver for the null hypothesis receiving validation in this research.

The methodology of nucleation classification was not optimal. Ideally, the nucleation site would always have been centered in each ΔV sample, similar to how each atom was isolated for phase in the work of Fukuya and Shibuta 2020. This can account for multiple nucleation sites within each sample. This would have been implemented by taking the sum of crystallization across the sample and then isolating nucleation sites. Isolation would have been done by taking the centroid inertia of

each crystallization region by giving each atom a crystal inertia mass value. Using this method more samples could have been used by removing the upper bound of crystal counts for the Gaussian field creation; The upper bound of crystal counts needed to be similar across samples and would not be needed in a system that can handle relative crystal counts. This would allow for better CNN classification as neural networks prefer images with the object to be classified at center. This can be somewhat "cheated for" by the use of two classes in which multiple structures can be classified as nucleating or non-nucleating.

The reason that this method was not used is due to the engineering behind it. It would be its own vision systems project that would require far more time than the research allotted to complete and increases the number of failure modes in the system by increasing complexity. Creating ΔVs across boundary conditions would have been needed as well as the ability to account for overlapping ΔV conditions. The thesis time frame did not allow for another major engineering project to be undertaken.

Chapter 4

CONCLUSION

4.1   Preamble

The resulting work contains a multifaceted effort to generate simulations and effectively test whether prenucleation structure is the sole driver of stishovite nucleation. Within the the composite of this work a detailed research and development project was done across two rounds of experiments to generate stishovite in a reliable method from random atom insertion and quartz starting structure. This resulted in the manufacture of 1,154 separate samples.

A sophisticated Gaussian field generation program was designed to translate the simulations from LAMMPS dump files in atomic position to pixelated data which can be used by two CNNs. This included a small study into the variance of the Gaussian function to optimize the input data into the CNNs.

Two methodologies for regionalizing and classifying the data as a nucleation or non nucleation zone. These methods varied drastically in there design. The second methodology served to verify the results of the first.

A total of six variables were tested for within the system, 64 experiments in total were performed. The process was thoroughly reviewed and error was checked for within each step of the pipeline.

4.2 Statement

After the intensive and exhaustive study done upon this topic it is time to draw to a close. The hypothesis is: The prenucleation structure of stishovite is the sole determinate of stishovite nucleation, therefore a direct and clear relationship exists between the prenuclation structure that is different from other structures within an SiO_2 network.

The designed experiments clearly tested this beyond a reasonable degree of rigour. Using a CNN should have discovered any relationships with the system and has been done so in previous MD applications Chmiela et al. 2017; Ryczko et al. 2018; Singh et al. 2018; Fukuya and Shibuta 2020. The experiments were designed to establish that the hypothesis is true which gave ample favor to its outcome. This was an unfavorable bias toward the hypothesis that further verifies the null hypothesis outcome. For the experiment to be successful a few experiments would need to be trainable upon the any data set and abstract to the validation set, leaving room for false positive results.

In a surprising outcome 62 of the 64 experiments strongly showed no correlation within the samples and were effectively very sophisticated coin tossing machines when applied to the validation set. They were not able to abstract in consistent atomistic structure. Two of the experiments may have shown some relationship; These experiments were very lose in their ability to classify the validation set and showed numerous signs of being a statistical artifact. In conclusion none of the 64 experiments provided abstraction to atomistic structure. This is after correctly classifying a test set to justify their validity. The CNN networks were based upon previously published work into a binary classification system that scored fifth within its given category Hasib Zunair Aimon Rahman 2020. Gaussian functions are not a new technique to

be used with CNNs on MD data and have achieved high rates of previous success Ryczko et al. 2018. The methodology of dividing the sample is reasonable and may incur minor difficulties in classification. A binary class system should allow for the abstraction of partially present features to be identified within the system and classify correctly, even if this would not occur in a large number of classes.

For the before mentioned reasons it does not appear that atomistic structure is the sole driver of nucleation within amorphous SiO_2. Due to the multitude of variables tested there appears to be no reasonable option for complete failure of all systems to detect an underlying repeating structure. The weakest point of the research is the methodology for classifying the simulations, for this reason CNNSRIM2 was developed which used a different classification system to classify each ΔV. Even with somewhat noisy classification data a weak classification should have appeared which showed a relationship is present. If doing the work again it would be ideal to have a greater depth of knowledge into imaging technologies.

4.3 Future Research

4.3.1 Atomic Interactions

Structure may still be an important factor within the nucleation of stishovite within an amorphous SiO_2 sample. It seems likely that the prenuclation structure from this research is not the sole factor in nucleation. To test if atomistic structure is partial factor to nucleation of an SiO_2 network repeated shock testing can be performed; In which each SiO_2 sample is repeatedly shocked from the same starting structure and a nucleation heat map is created. This can be done by summing all crystal-like atoms

across each simulation with a given weight, such that if the same atom is crystal-like repeatedly it shows up more intensely with a higher value. If there is strong regional favoritism atomistic structure is likely a factor of nucleation. This research was not designed to test for a partial factor as all non-nucleated SiO_2 was assumed to be of a different non-nucleating structure.

4.3.2   Post Shock Structure

The research does not rule out if the post shock structure is a sole factor within the nucleation process. It is needful to see if the shock process transforms the atomistic structure of the preshock sample. Relative atomic positions will change as the sample undergoes compression. The question is if the absolute atomistic structure changes. This could be tested by creating a relationship matrix of atomic bonding before and after shock. If the atomic bonding is equivocal before and after shock no characteristic atomistic structural changes have occurred. The percentage of atomistic structural change can be given by percent if it occurs. If significant changes have occurred it would be recommended to run the data through the same experiments seen within this research on post shocked pre nucleated structure. CNNSRIM 1 and 2 are fully plumbed only the input files would change.

REFERENCES

Ahrens, Sheng-Nian Luo. Tahir Cagin. Alejandro Strachan. William A. Goddard III. Thomas J. 2002. "Molecular dynamics modeling of stishovite." *Earth and Planetary Science Letters* 202 (April): 147–157.

Alake, Richmond. 2020. *Deep Learning: GoogLeNet Explained.* https://towardsdatasience.com/deep-learning-googlenet-explained-de8861c82765, December.

Alexander, C Scott, LC Chhabildas, WD Reinhart, and DW Templeton. 2008. "Changes to the shock response of fused quartz due to glass modification." *International Journal of Impact Engineering* 35 (12): 1376–1385.

Beest van B. W. H., Kramer G. J., and Santen van R. A. 1990. "Force fields for silicas and aluminophosphates based on ab initio calculations." *Physical Review Letters* 64 (January): 1955–1958.

Biswas, Ripan K, Prosenjit Khan, Smita Mukherjee, Anoop K Mukhopadhyay, Jiten Ghosh, and K Muraleedharan. 2018. "Study of short range structure of amorphous Silica from PDF using Ag radiation in laboratory XRD system, RAMAN and NEXAFS." *Journal of Non-Crystalline Solids* 488:1–9.

Boone, James. 2021. *Why TensorFlow is so Popular Today.* https://galeon.com/why-tensorflow-is-so-popular-today/, July.

Brazhkin, VV, RN Voloshin, and SV Popova. 1991. "The kinetics of the transition of the metastable phases of SiO2, stishovite and coesite to the amorphous state." *Journal of non-crystalline solids* 136 (3): 241–248.

Brown, Eugene Lemay Jr., Theodore, and Bruce Bursten. 2000. *Chemistry: The Central Science.* 884. Upper Saddle River, NJ: Prentice Hall.

Chew, Alex K, Shengli Jiang, Weiqi Zhang, Victor M Zavala, and Reid C Van Lehn. 2020. "Fast predictions of liquid-phase acid-catalyzed reaction rates using molecular dynamics simulations and convolutional neural networks." *Chemical science* 11 (46): 12464–12476.

Chmiela, Stefan, Alexandre Tkatchenko, Huziel E Sauceda, Igor Poltavsky, Kristof T Schütt, and Klaus-Robert Müller. 2017. "Machine learning of accurate energy-conserving molecular force fields." *Science advances* 3 (5): e1603015.

Cormack., Alfonso Pedone. Gianluca Malavasi. M. Cristina Menziani. Alastair N., and Ulderico Segre. 2006. "A New Self-Consistent Empirical Interatomic Potential Model for Oxides Silicates and Silica-Based Glasses." *Journal Physics Chemistry B* 110:11780–11795.

Dong, Juncai, Hailiang Zhu, and Dongliang Chen. 2015. "Universal elastic-hardening-driven mechanical instability in α-quartz and quartz homeotypes under pressure." *Scientific reports* 5 (1): 1–9.

Doyle, PA t, and PS Turner. 1968. "Relativistic Hartree–Fock X-ray and electron scattering factors." *Acta Crystallographica Section A: Crystal Physics, Diffraction, Theoretical and General Crystallography* 24 (3): 390–397.

El Goresy, Ahmed, Leonid Dubrovinsky, Thomas G Sharp, and Ming Chen. 2004. "Stishovite and post-stishovite polymorphs of silica in the shergotty meteorite: their nature, petrographic settings versus theoretical predictions and relevance to Earth's mantle." *Journal of Physics and Chemistry of Solids* 65 (8-9): 1597–1608.

Fukuya, Teppei, and Yasushi Shibuta. 2020. "Machine learning approach to automated analysis of atomic configuration of molecular dynamics simulation." *Computational Materials Science* 184:109880.

Gibbons, Rex V, and Thomas J Ahrens. 1971. "Shock metamorphism of silicate glasses." *Journal of Geophysical Research* 76 (23): 5489–5498.

Girshick, Ross, Jeff Donahue, Trevor Darrell, and Jitendra Malik. 2014. "Rich feature hierarchies for accurate object detection and semantic segmentation." In *Proceedings of the IEEE conference on computer vision and pattern recognition,* 580–587.

Godoy, Daniel. 2018. *Understanding binary cross-entropy / log loss: a visual explanation.* https://towardsdatascience.com/understanding-binary-cross-entropy-log-loss-a-visual-explanation-a3ac6025181a.

Grujicic, M, WC Bell, PS Glomski, B Pandurangan, BA Cheeseman, C Fountzoulas, and P Patel. 2011. "Multi-length scale modeling of high-pressure-induced phase transformations in soda-lime glass." *Journal of Materials Engineering and Performance* 20 (7): 1144–1156.

Grujicic, M, WC Bell, B Pandurangan, BA Cheeseman, C Fountzoulas, P Patel, DW Templeton, and KD Bishnoi. 2011. "The effect of high-pressure densification on ballistic-penetration resistance of a soda-lime glass." *Proceedings of the Institution of Mechanical Engineers, Part L: Journal of Materials: Design and Applications* 225 (4): 298–315.

Hasib Zunair Aimon Rahman, Joseph Paul Cohen, Nabeel Mohammed. 2020. "3D Image Classification From CT Scans." *Cornell University,* 1–12.

Kawai, Nobuaki, Kenji Tsurui, Kairi Moriguchi, Sunao Hasegawa, and Eiichi Sato. 2013. "Damage evolution in SiO2 glass subjected to hypervelocity impact." *Procedia Engineering* 58:702–708.

Lyzenga, Gregory A, Thomas J Ahrens, and Arthur C Mitchell. 1983. "Shock temperatures of SiO2 and their geophysical implications." *Journal of Geophysical Research: Solid Earth* 88 (B3): 2431–2444.

Millot, Marius, Natalia Dubrovinskaia, Ana Černok, Stephan Blaha, Leonid Dubrovinsky, David G Braun, Peter M Celliers, Gilbert W Collins, Jon H Eggert, and Raymond Jeanloz. 2015. "Shock compression of stishovite and melting of silica at planetary interior conditions." *Science* 347 (6220): 418–420.

Müser, MH, and K Binder. 2001. "Molecular dynamics study of the α–β transition in quartz: elastic properties, finite size effects, and hysteresis in the local structure." *Physics and Chemistry of Minerals* 28 (10): 746–755.

Osako, Masahiro, and Yoji Kobayashi. 1979. "Thermal diffusivity of stishovite." *Physics of the Earth and Planetary Interiors* 18 (2): P1–P4.

Pedone, Alfonso, Gianluca Malavasi, M Cristina Menziani, Alastair N Cormack, and Ulderico Segre. 2006. "A new self-consistent empirical interatomic potential model for oxides, silicates, and silica-based glasses." *The Journal of Physical Chemistry B* 110 (24): 11780–11795.

Qi., Yuan Shen. Shai B. Jester. Tingting. and Evan J. Reed. 2015. "Nanosecond homogeneous nucleation and crystal growth in shock-compressed SiO2 Supplementary Material." *Nature Materials,* 1–21.

Raschka, Sebastian. 2020. *Gradient Descent and Stochastic Gradient Descent.* http://rasbt.github.io/mlxtend/user_guide/general_concepts/gradient-optimization/.

Ravelo, R, BL Holian, TC Germann, and PS Lomdahl. 2004. "Constant-stress Hugoniostat method for following the dynamical evolution of shocked matter." *Physical Review B* 70 (1): 014103.

Rein ten Wolde, Pieter, Maria J Ruiz-Montero, and Daan Frenkel. 1996. "Numerical calculation of the rate of crystal nucleation in a Lennard-Jones system at moderate undercooling." *The Journal of chemical physics* 104 (24): 9932–9947.

Roshdy G.S. Barsoum, Philip J. Dudt. 20. "Emerging Class of Materials for Armor and Blast Protection." *AMMTIAC Quarterly* 4:11–14.

Ryczko, Kevin, Kyle Mills, Iryna Luchak, Christa Homenick, and Isaac Tamblyn. 2018. "Convolutional neural networks for atomistic systems." *Computational Materials Science* 149:134–142.

Salleo, Alberto, Seth T Taylor, Michael C Martin, Wendy R Panero, Raymond Jeanloz, Timothy Sands, and François Y Génin. 2003. "Laser-driven formation of a high-pressure phase in amorphous silica." *Nature materials* 2 (12): 796–800.

Shen, Yuan, and Evan J Reed. 2016. "Quantum nuclear effects in stishovite crystallization in shock-compressed fused silica." *The Journal of Physical Chemistry C* 120 (31): 17759–17766.

Singh, Rahul, Aayush Sharma, Onur Rauf Bingol, Aditya Balu, Ganesh Balasubramanian, Duane D Johnson, and Soumik Sarkar. 2018. "3D Deep Learning with voxelized atomic configurations for modeling atomistic potentials in complex solid-solution alloys." *arXiv preprint arXiv:1811.09724,* 1–10.

Springenberg, Jost Tobias, Alexey Dosovitskiy, Thomas Brox, and Martin Riedmiller. 2014. "Striving for simplicity: The all convolutional net." *ICLR,* 1–14.

Steinhardt, Paul J, David R Nelson, and Marco Ronchetti. 1983. "Bond-orientational order in liquids and glasses." *Physical Review B* 28 (2): 784.

Templeton., M Grujicic. W C Bell. B Pandurangan. B A Cheeseman. C Fountzoulas. P Patel. D W, and K D Bishnoi. 2011. "The effect of high-pressure densifiction on ballistic-penetration resistance of a soda-lime glass." *Proceedings of the Institution of Mechanical Engineers, Part L: Journal of Materials: Design and Applications* 225:298–315.

Tepfenhart, Ossiana. 2021. *46 Different Types of Glass.*

Tjabane, M, and JE Lowther. 1999. "Molecular dynamics study of quartz into stishovite." *Physica B: Condensed Matter* 270 (1-2): 164–171.

Tracy, Sally June, Stefan J Turneaure, and Thomas S Duffy. 2018. "In situ X-ray diffraction of shock-compressed fused silica." *Physical review letters* 120 (13): 135702.

Tucker, MG, DA Keen, MT Dove, and K Trachenko. 2005. "Refinement of the Si–O–Si bond angle distribution in vitreous silica." *Journal of Physics: Condensed Matter* 17 (5): S67.

Wakai, Masaaki Misawa. Emina Ryuo. Kimiko Yoshida. Rajiv K. Kalia. Aiichiro Nakano. Norimasa Nishiyama. Fuyuki Shimojo. Priya Vashishtam .Fumihiro. 201. "Picosecond amorphization of SiO_2 stishovite under tension." *Nature Materials* 3:1–7.

Yuan Shen, Tingting Qi, Shai B. Jester, and Evan J. Reed. 2016. "Nanosecond homogeneous nucleation and crystal growth in shock-compressed SiO_2." *Nature Materials* 15:60–66.

APPENDIX A

RESOLUTION TESTS

(a) Mass

(b) Crystal
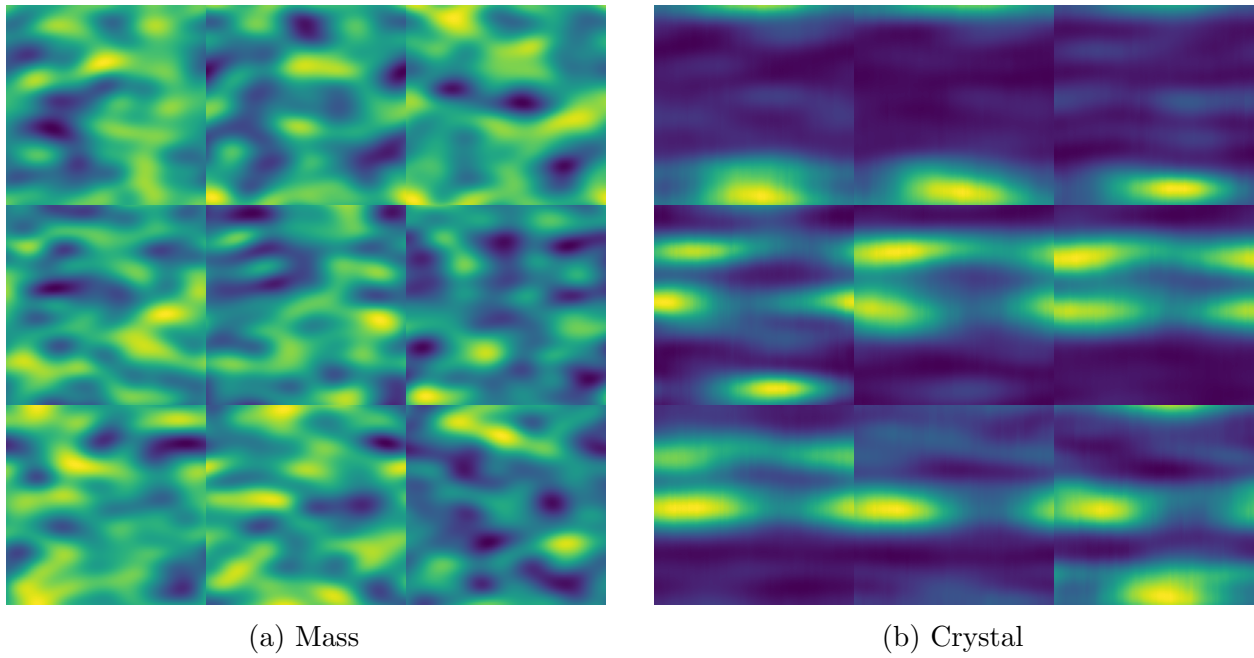
Figure 24. Gaussian field, simulation 300, quartz seeded, 18,000 atoms, 4 Å = σ.

(a) Mass

(b) Crystal
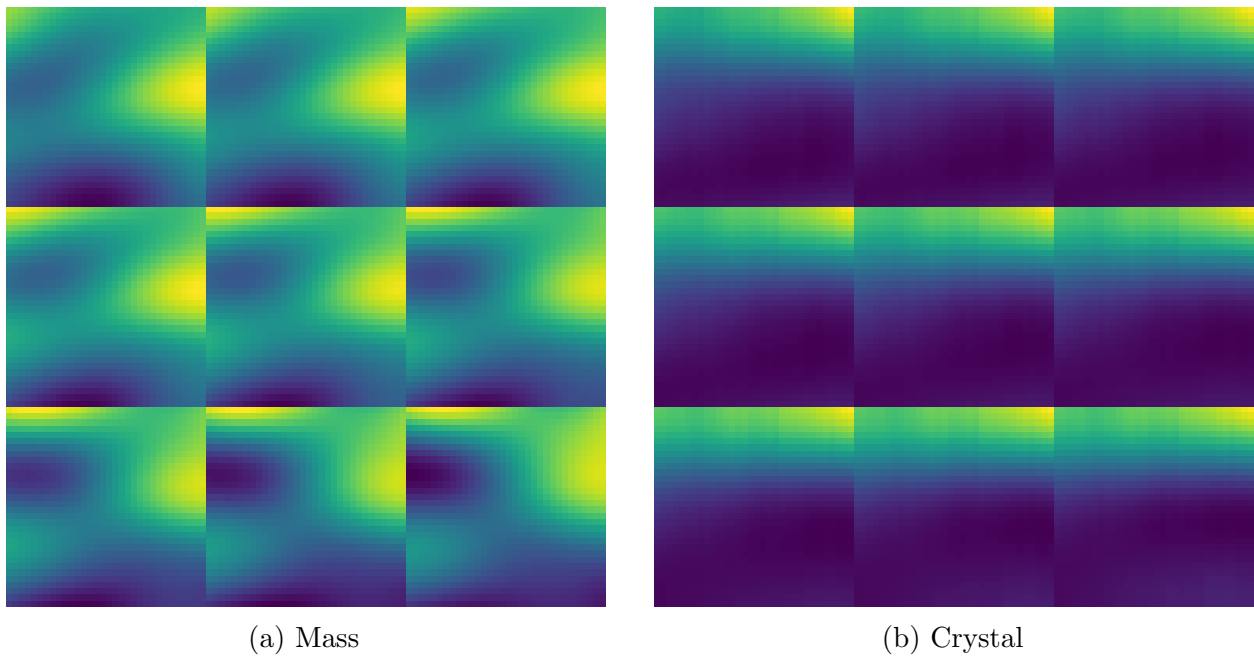
Figure 25. Gaussian field, simulation 300, quartz seeded, 18,000 atoms, 4 Å = σ. These are the ΔV subsections, section 1 of 64

(a) Mass   (b) Crystal
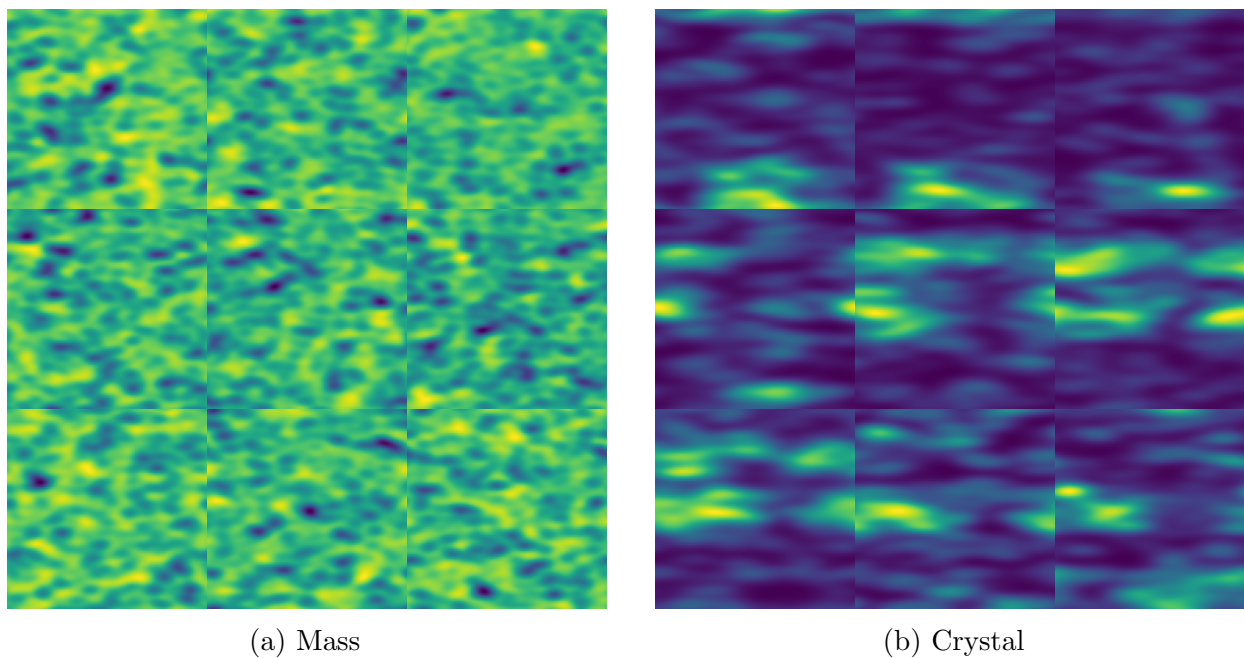
Figure 26. Gaussian field, simulation 300, quartz seeded, 18,000 atoms, 2 Å $= \sigma$.

(a) Mass   (b) Crystal
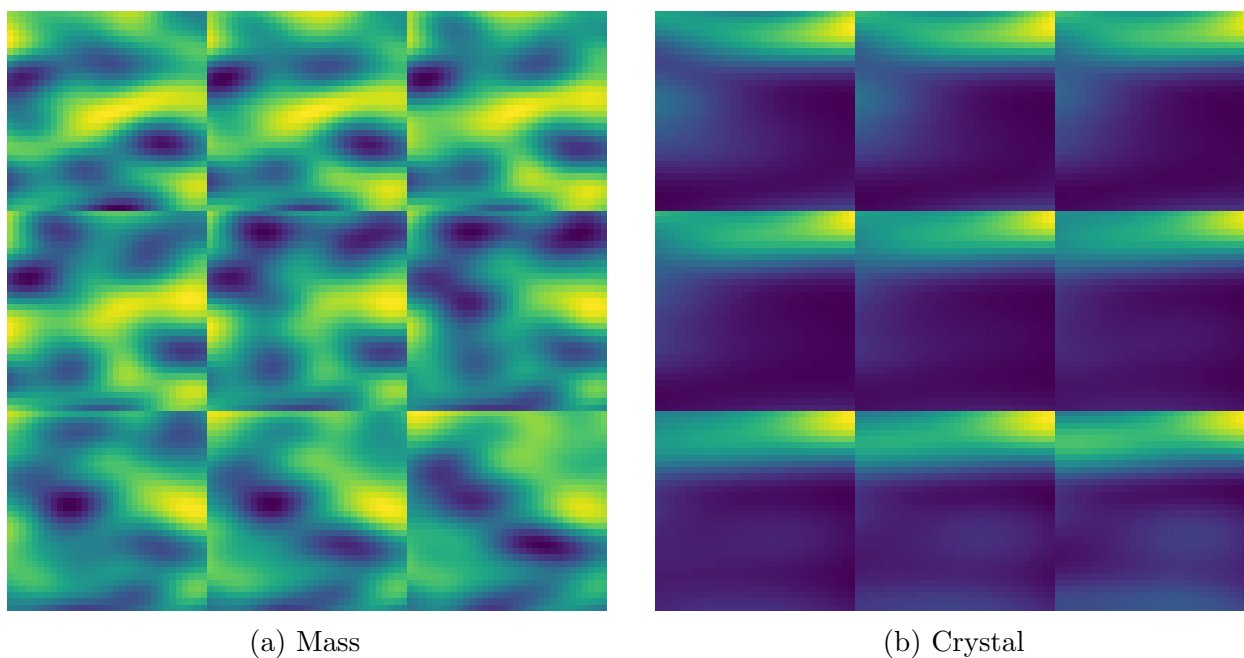
Figure 27. Gaussian field, simulation 300, quartz seeded, 18,000 atoms, 2 Å $= \sigma$. These are the ΔV subsections, section 1 of 64

116

(a) Mass   (b) Crystal
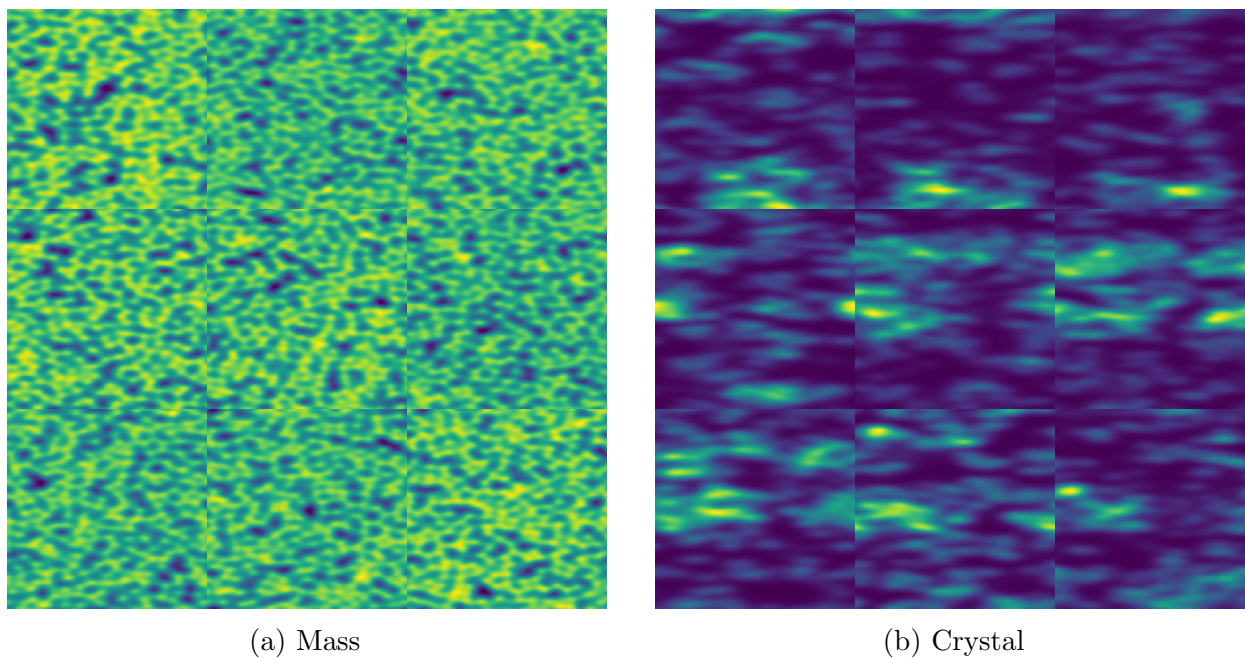
Figure 28. Gaussian field, simulation 300, quartz seeded, 18,000 atoms, $\sqrt{2}$ Å $= \sigma$.

(a) Mass   (b) Crystal
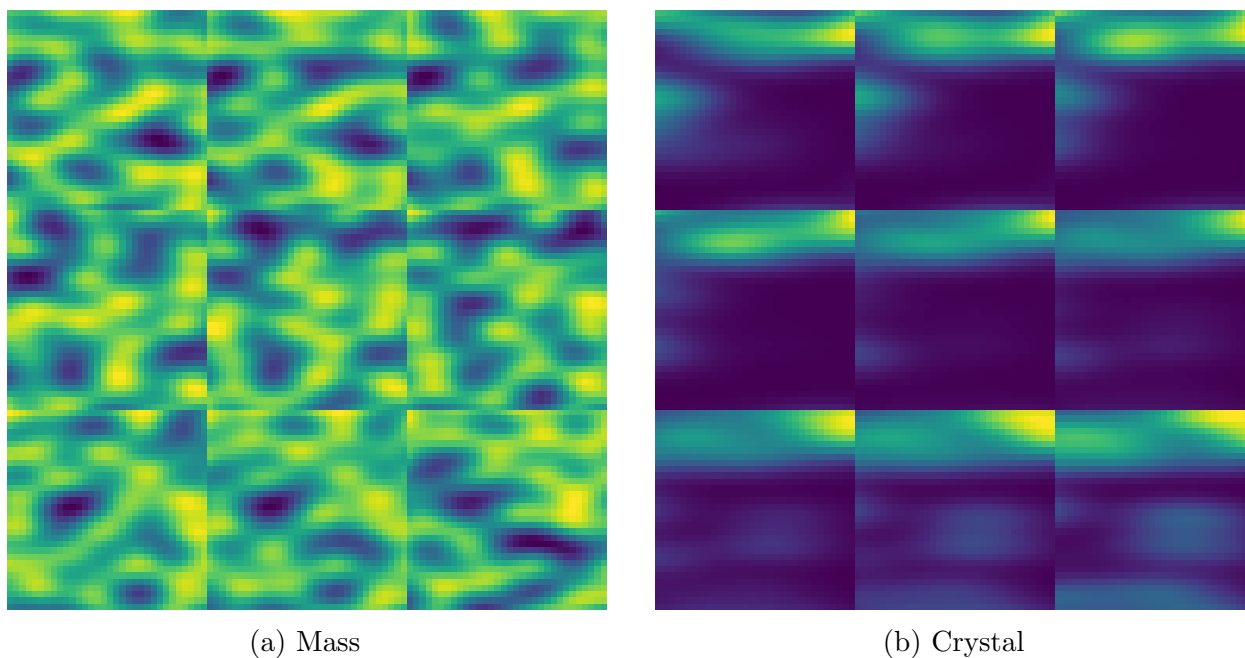
Figure 29. Gaussian field, simulation 300, quartz seeded, 18,000 atoms, $\sqrt{2}$ Å $= \sigma$. These are the ΔV subsections, section 1 of 64
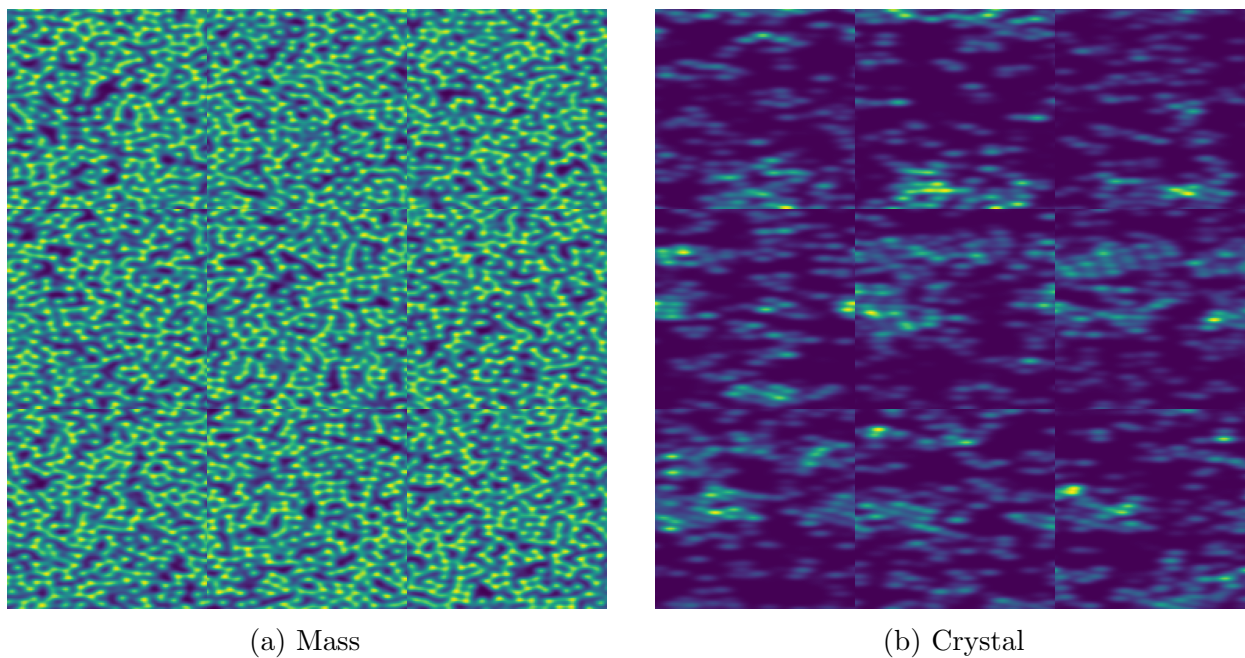
(a) Mass

(b) Crystal

Figure 30. Gaussian field, simulation 300, quartz seeded, 18,000 atoms, 1 Å $= \sigma$.
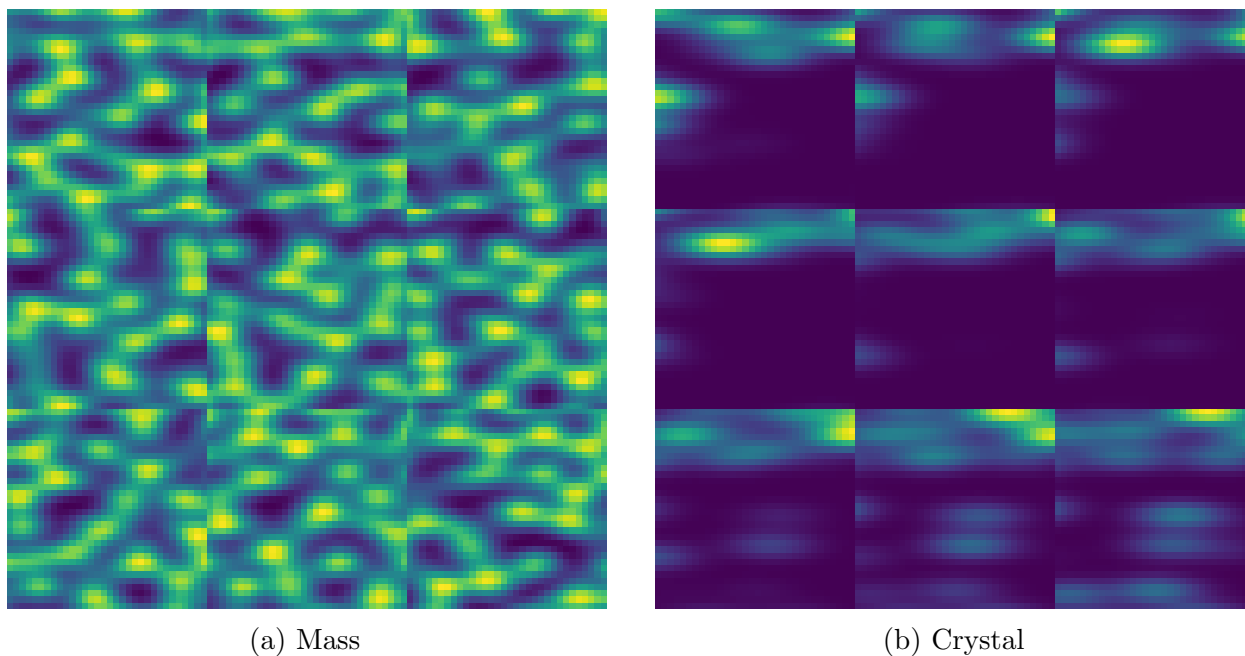
(a) Mass

(b) Crystal

Figure 31. Gaussian field, simulation 300, quartz seeded, 18,000 atoms, 1 Å $= \sigma$. These are the ΔV subsections, section 1 of 64
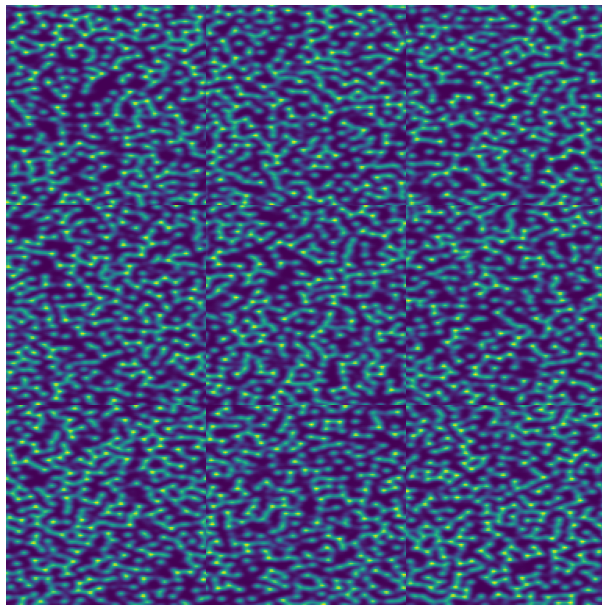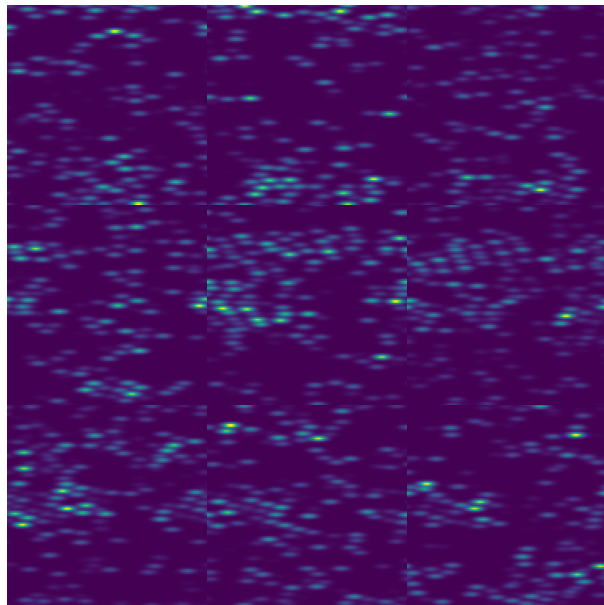
(a) Mass

(b) Crystal

Figure 32. Gaussian field, simulation 300, quartz seeded, 18,000 atoms, $1/\sqrt{2}$ Å $= \sigma$.
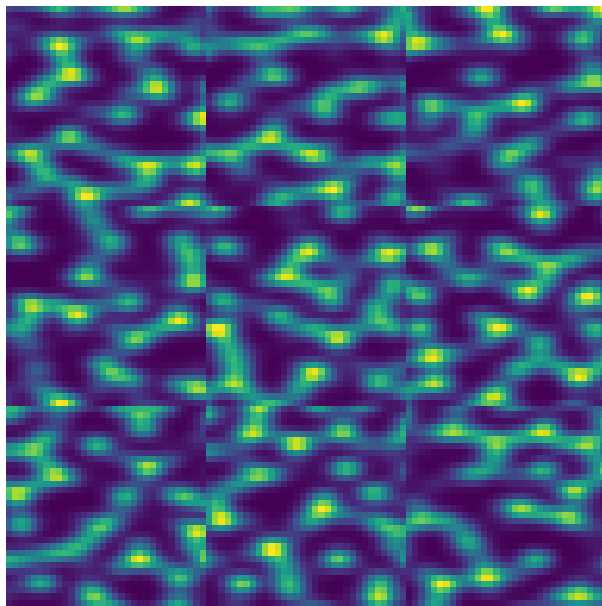
(a) Mass
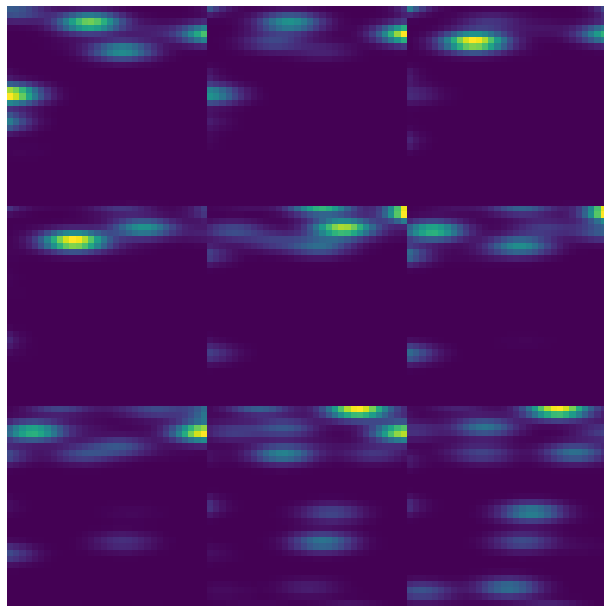
(b) Crystal

Figure 33. Gaussian field, simulation 300, quartz seeded, 18,000 atoms, $1/\sqrt{2}$ Å $= \sigma$. These are the ΔV subsections, section 1 of 64

(a) Mass

(b) Crystal
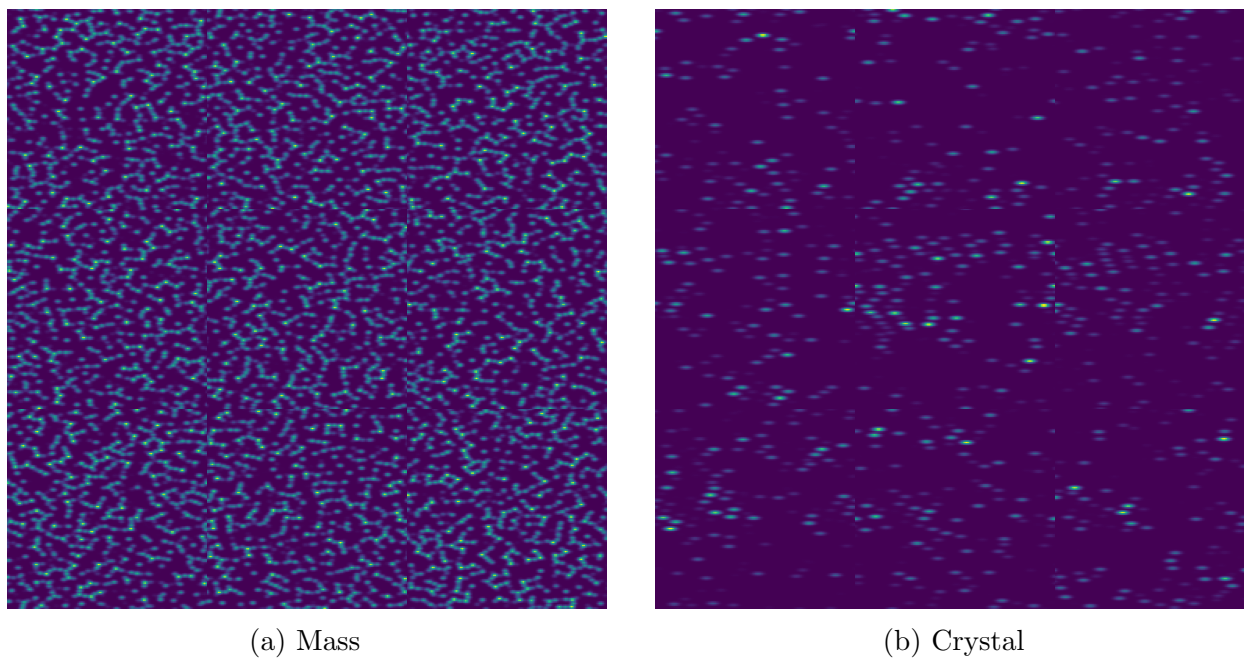
Figure 34. Gaussian field, simulation 300, quartz seeded, 18,000 atoms, $1/2$ Å $= \sigma$.

(a) Mass
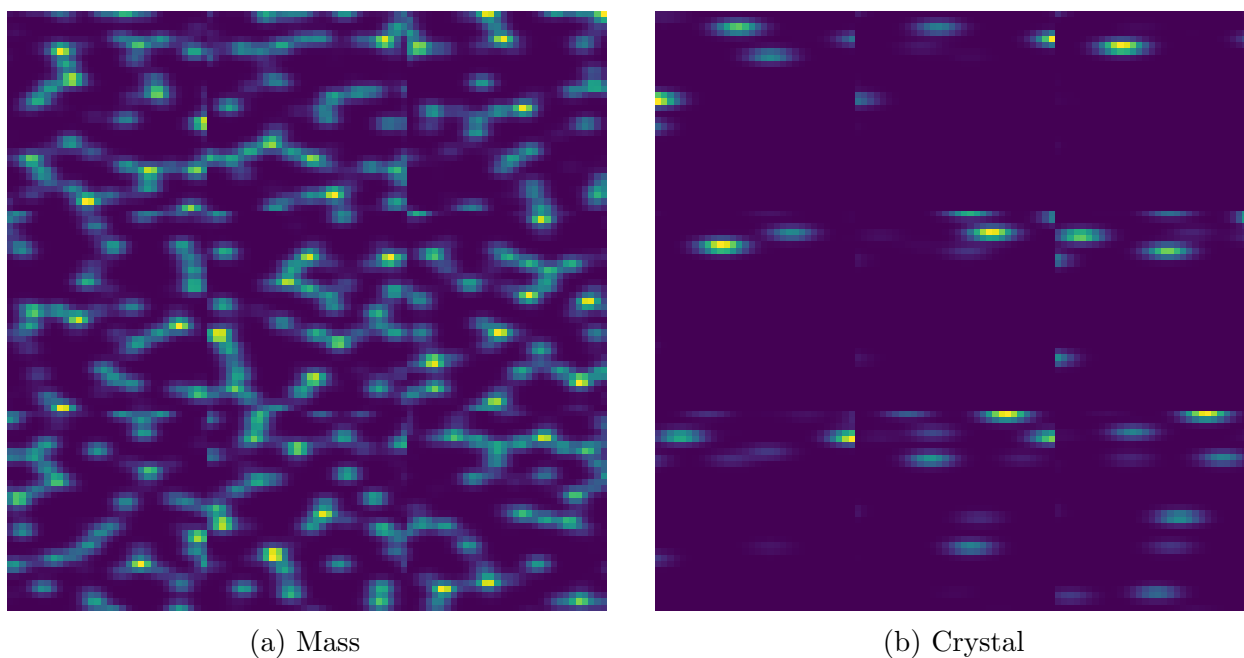
(b) Crystal

Figure 35. Gaussian field, simulation 300, quartz seeded, 18,000 atoms, $1/2$ Å $= \sigma$. These are the ΔV subsections, section 1 of 64

APPENDIX B

ARRAY HISTOGRAMS
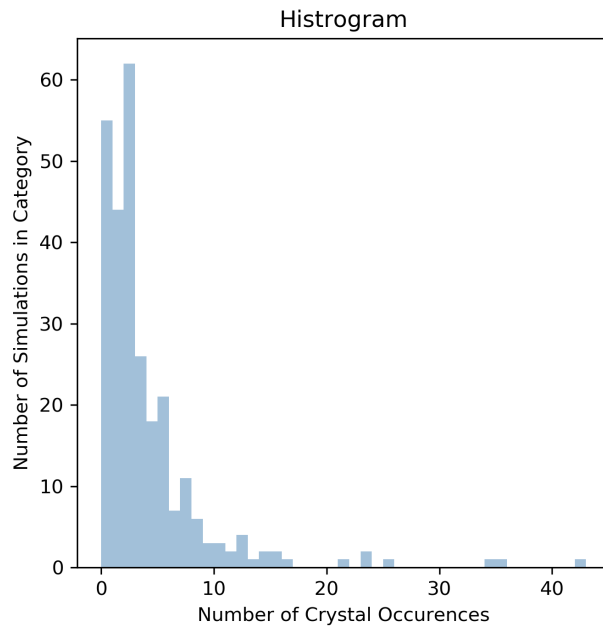
Figure 36. Array 1, histogram of calculated nucleation sites using a critical crystal value = 60.
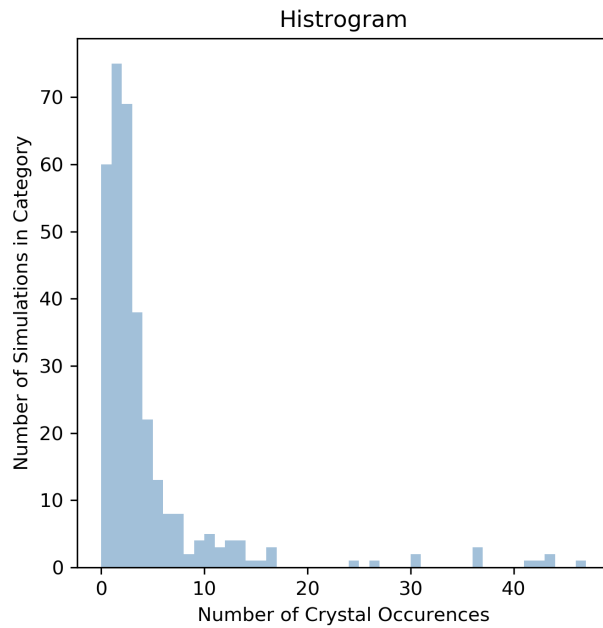
Figure 37. Array 2, histogram of calculated nucleation sites using a critical crystal value = 60.
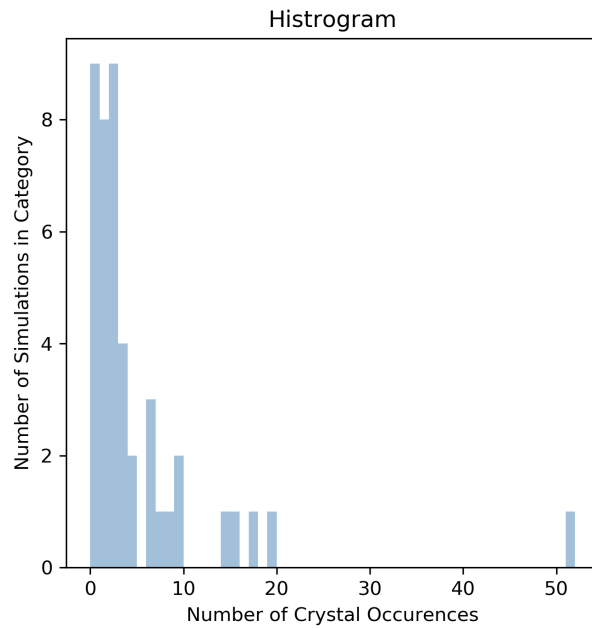
Figure 38. Array 3, histogram of calculated nucleation sites using a critical crystal value =
37.5.
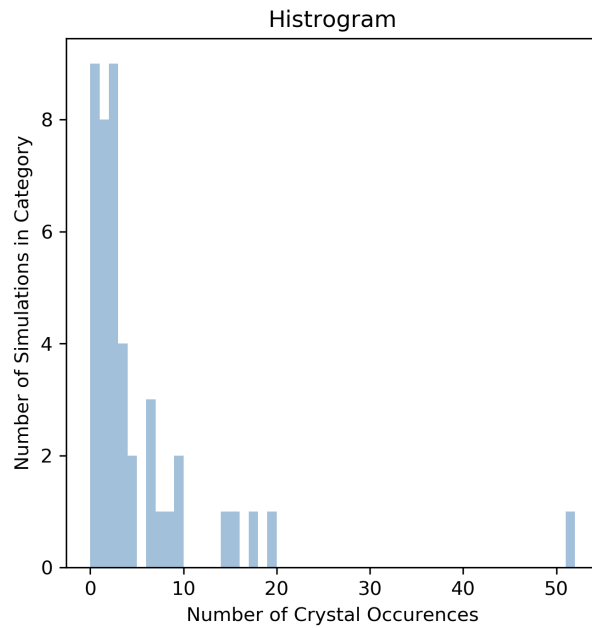
Figure 39. Array 4, histogram of calculated nucleation sites using a critical crystal value =
37.5.
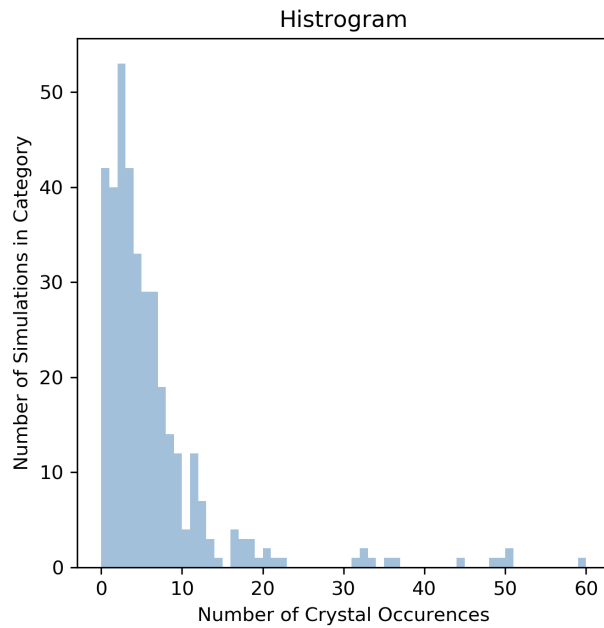
Figure 40. Array 5, histogram of calculated nucleation sites using a critical crystal value = 50.
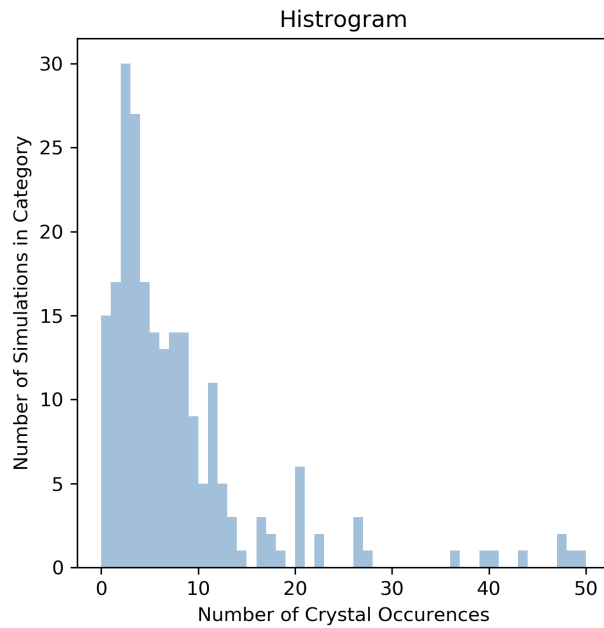
Figure 41. Array 6, histogram of calculated nucleation sites using a critical crystal value = 50.
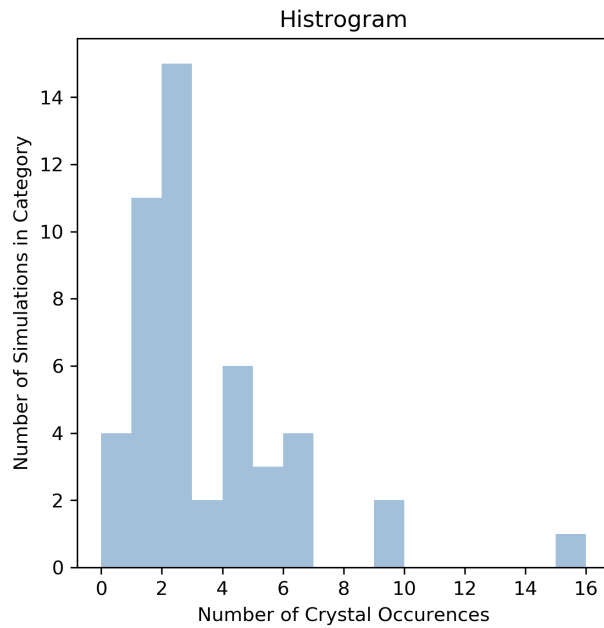
Figure 42. Array 7, histogram of calculated nucleation sites using a critical crystal value = 34.
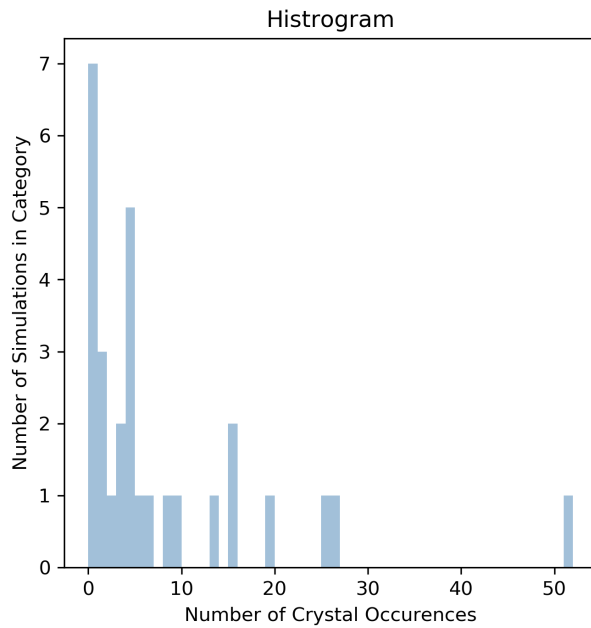
Figure 43. Array 8, histogram of calculated nucleation sites using a critical crystal value = 45.
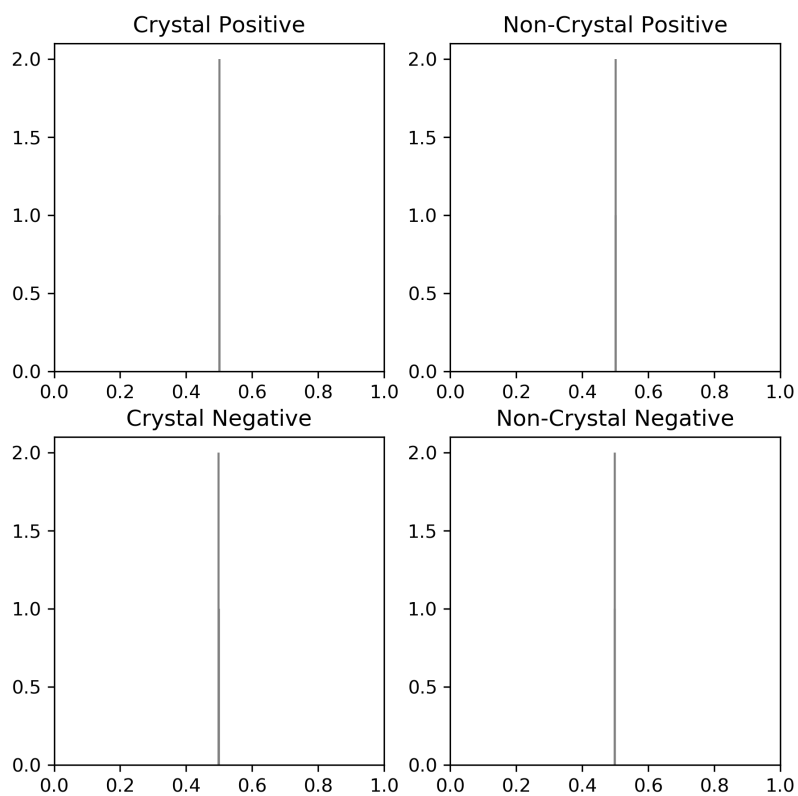
APPENDIX C

CNNSRIM1 RESULTS
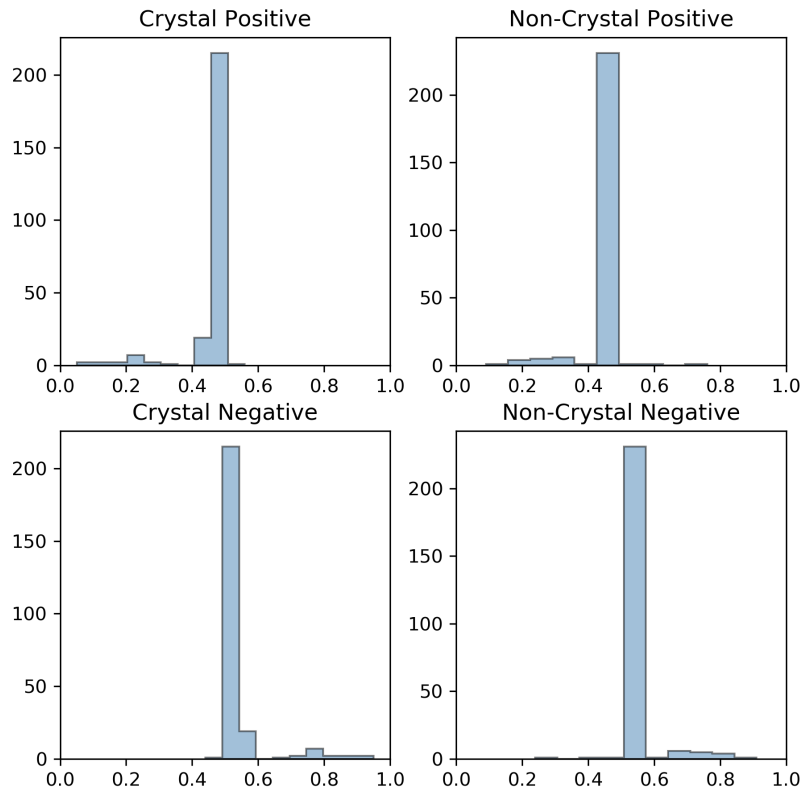
Figure 44. Histograms of validation set results for index 1 using CNNSRIM1.

Figure 45. Chart of CNN training for index 1 using CNNSRIM1.
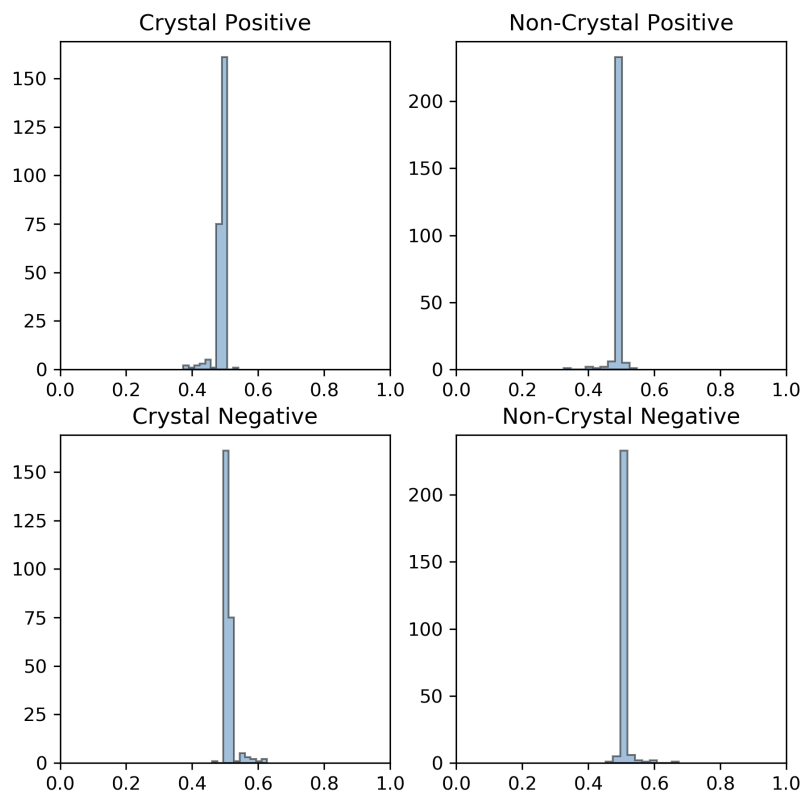
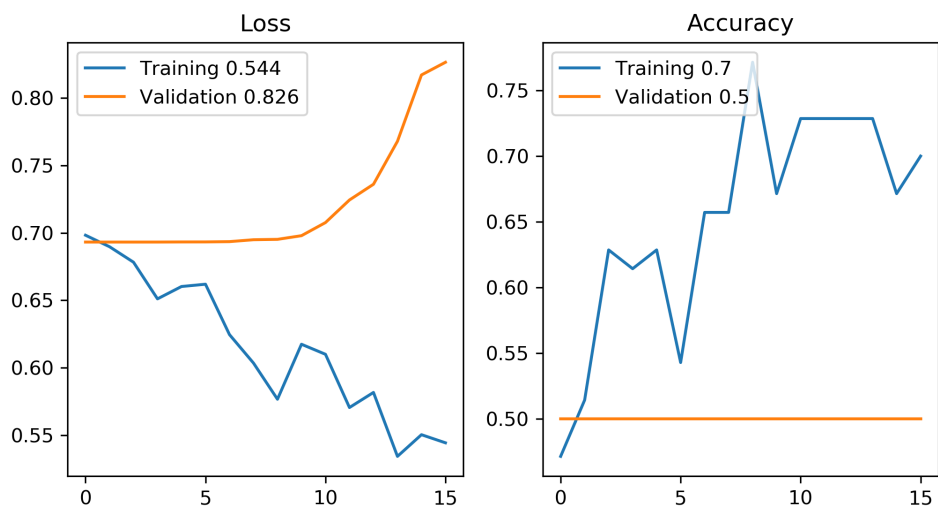Figure 46. Histograms of validation set results for index 2 using CNNSRIM1.
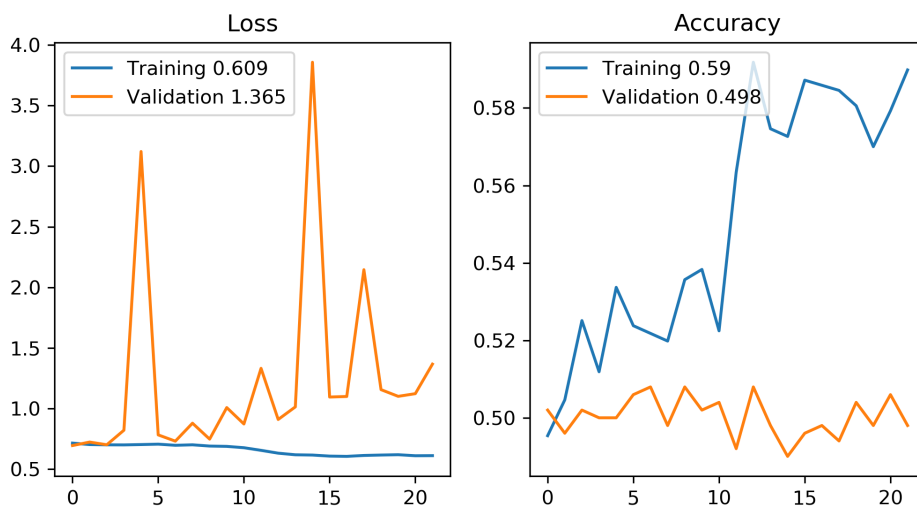
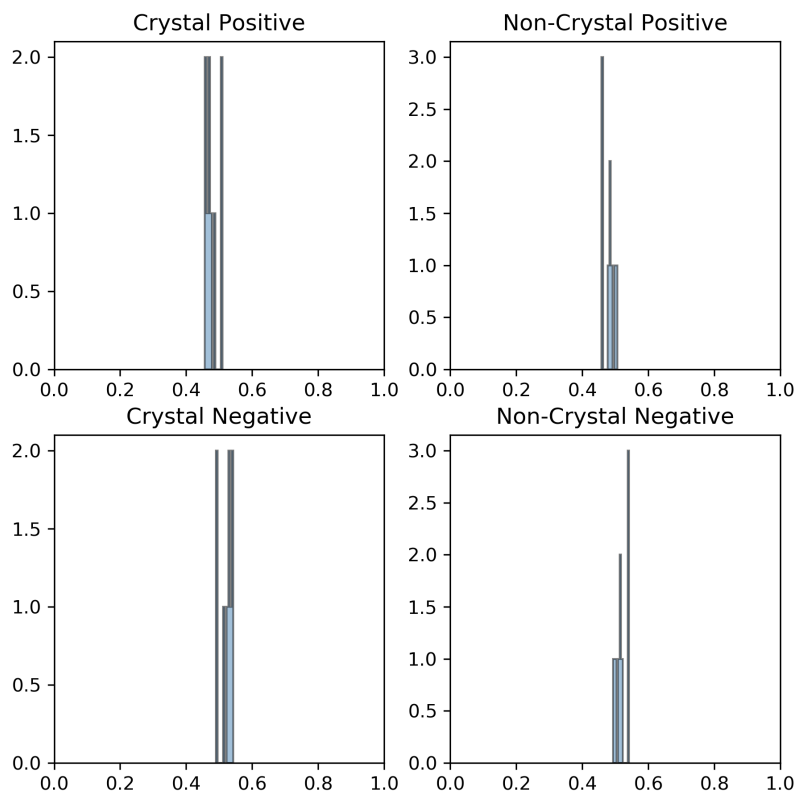Figure 47. Chart of CNN training for index 2 using CNNSRIM1.
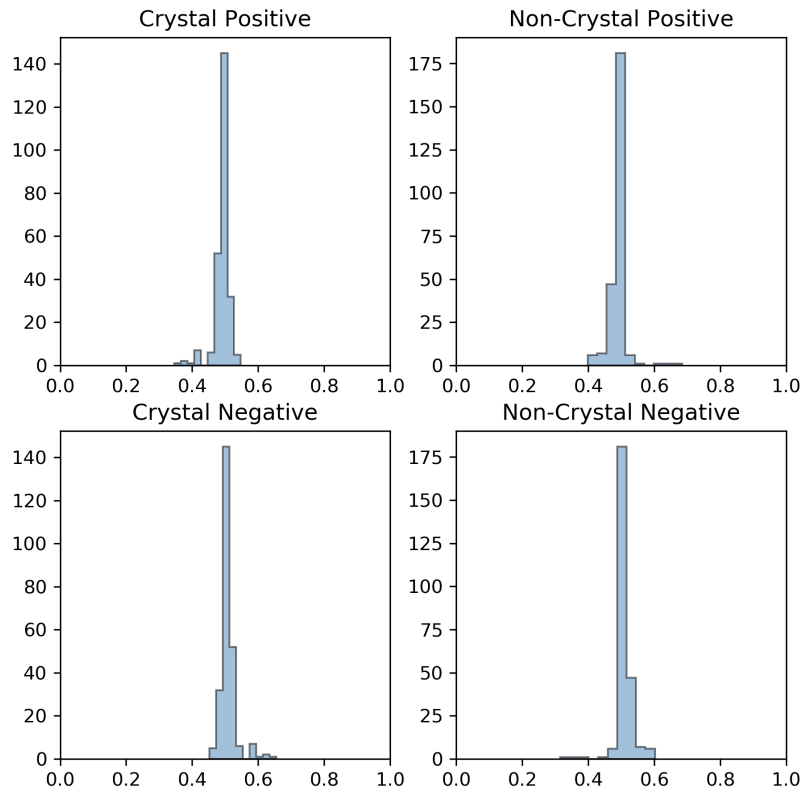
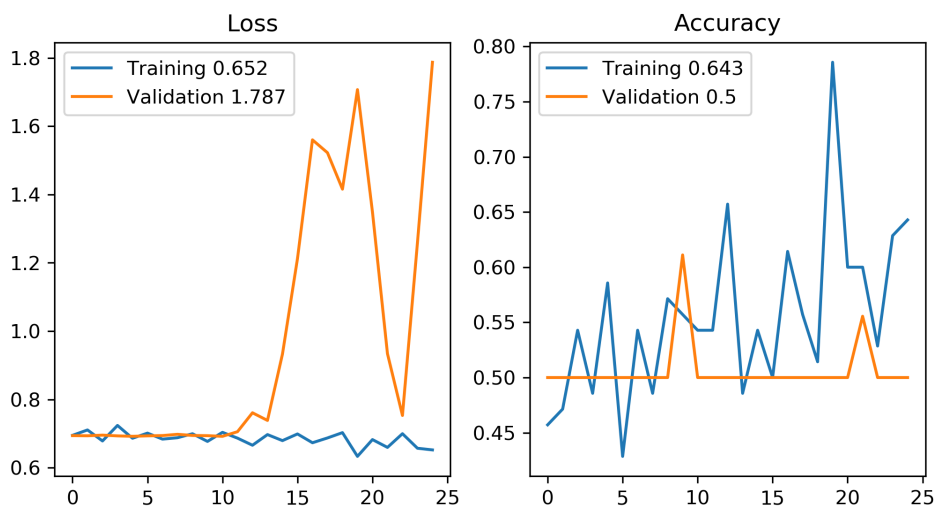Figure 48. Histograms of validation set results for index 3 using CNNSRIM1.
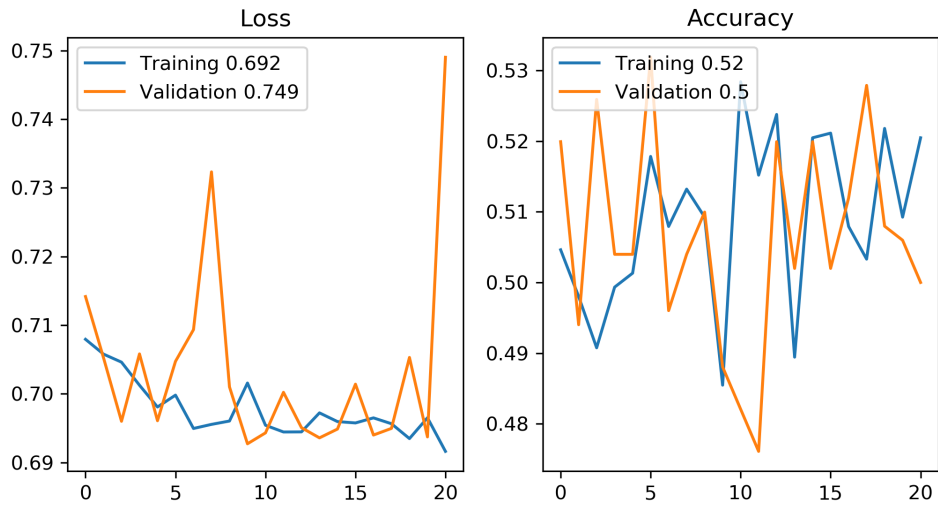
Figure 49. Chart of CNN training for index 3 using CNNSRIM1.
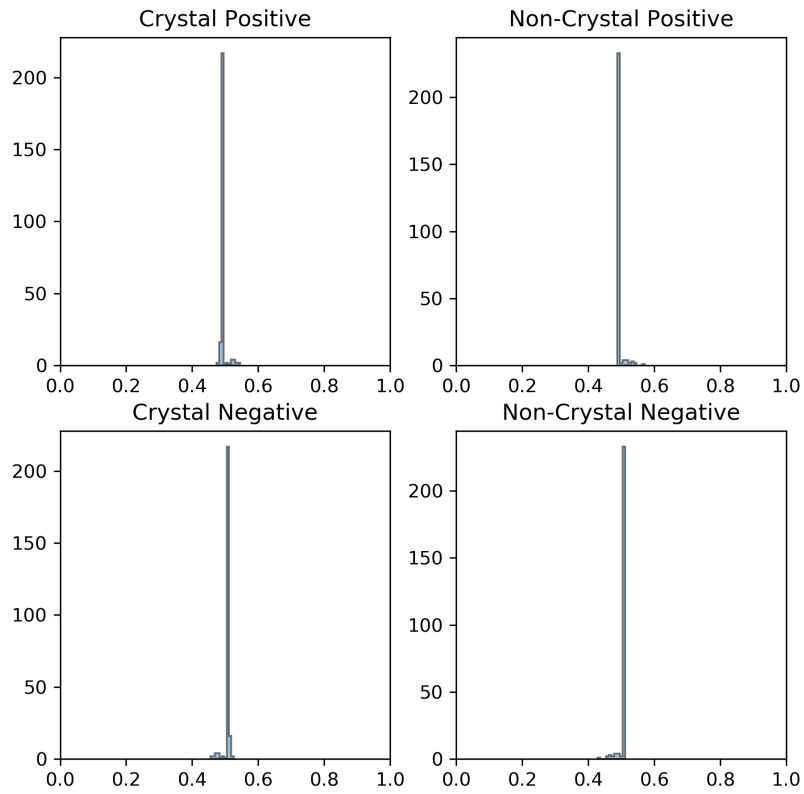
Figure 50. Histograms of validation set results for index 4 using CNNSRIM1.
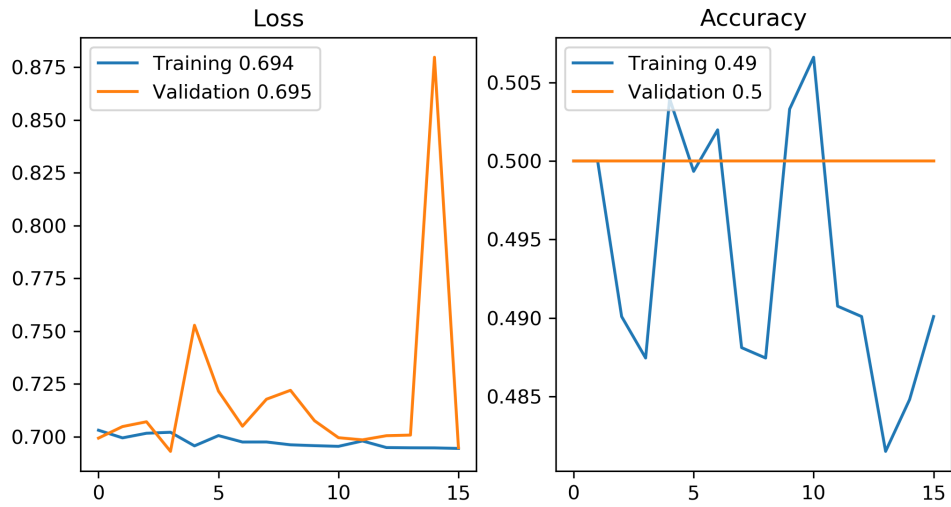
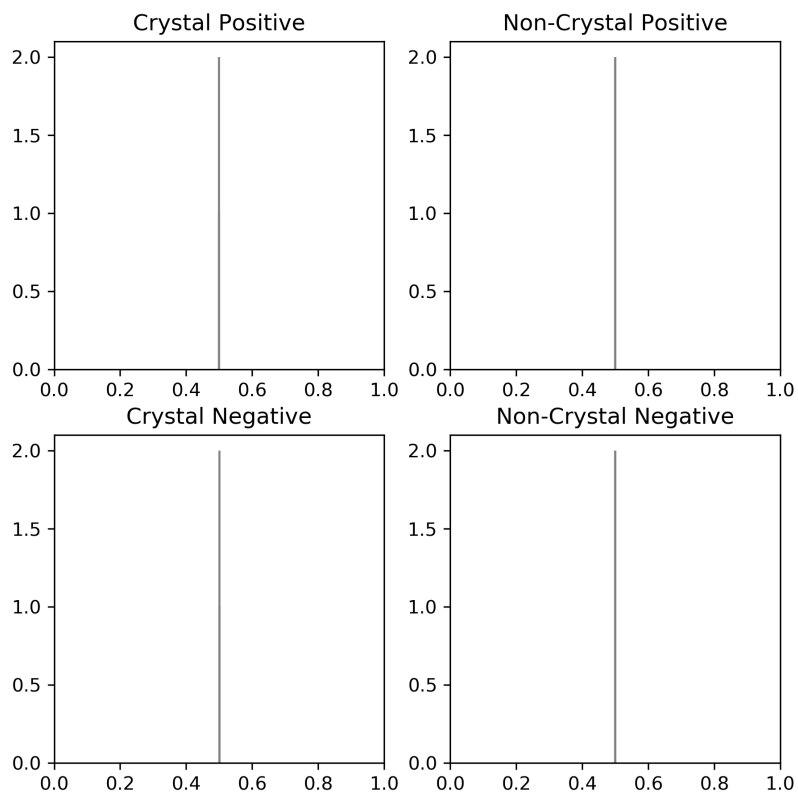Figure 51. Chart of CNN training for index 4 using CNNSRIM1.
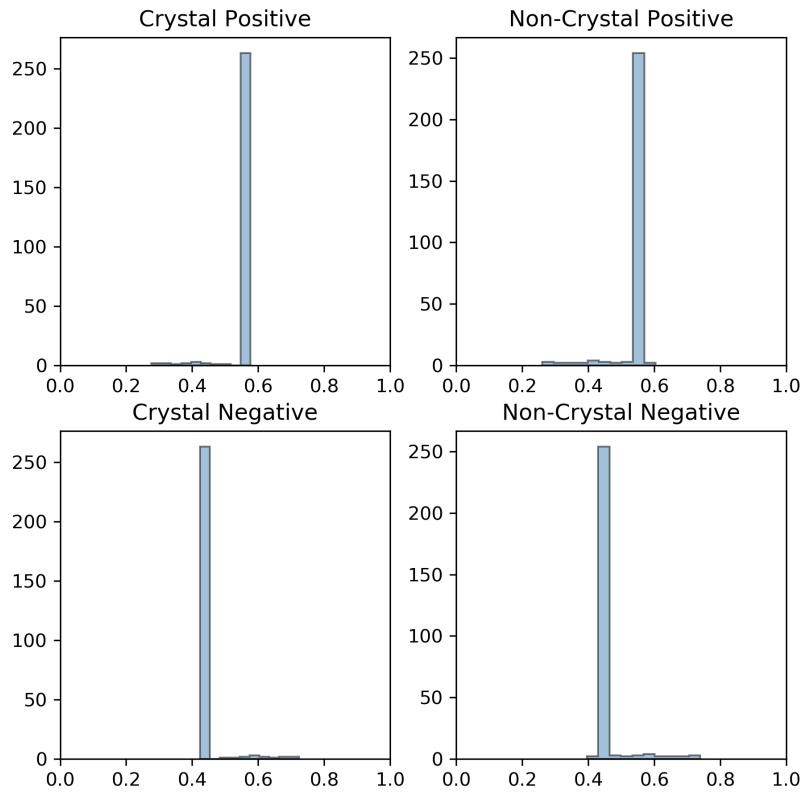
Figure 52. Histograms of validation set results for index 5 using CNNSRIM1.
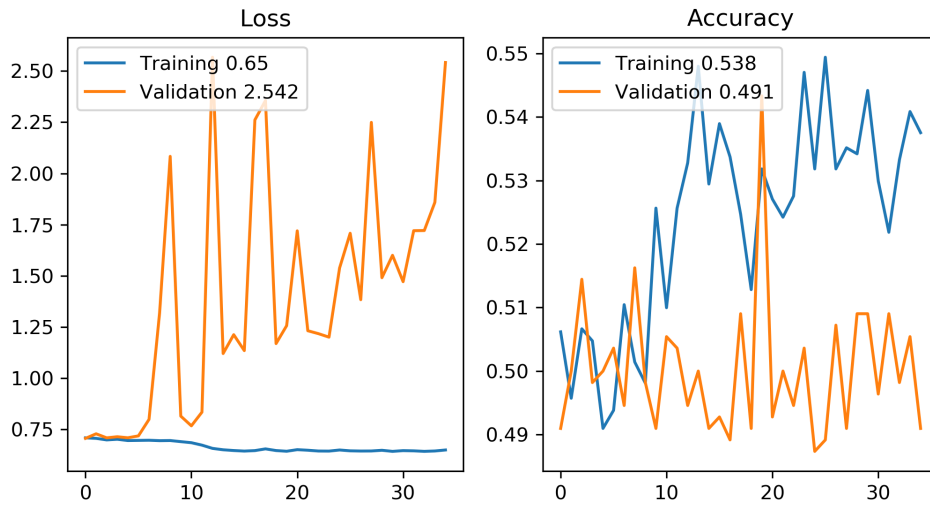
Figure 53. Chart of CNN training for index 5 using CNNSRIM1.
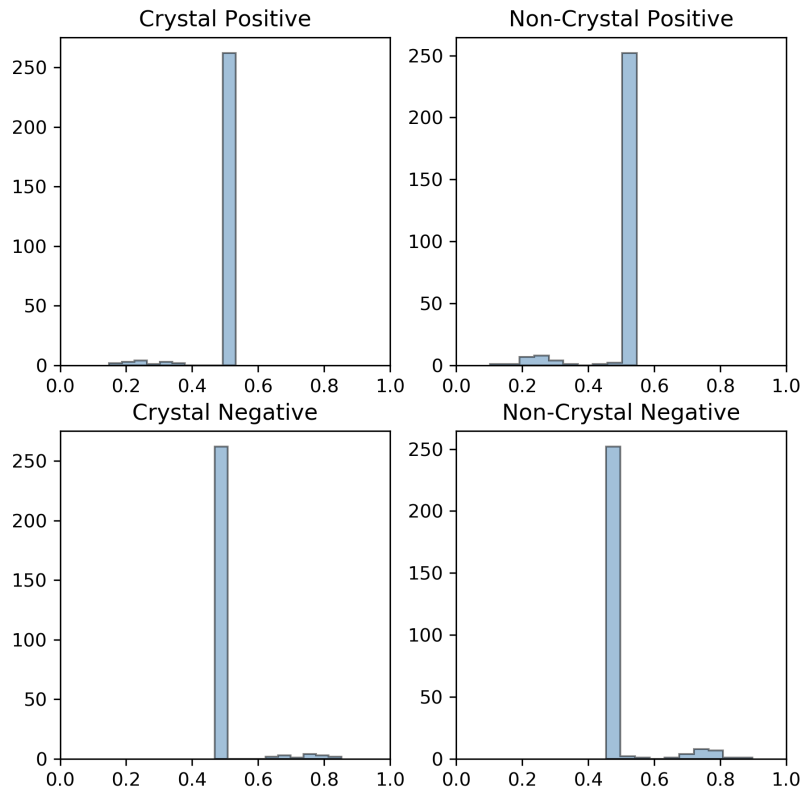
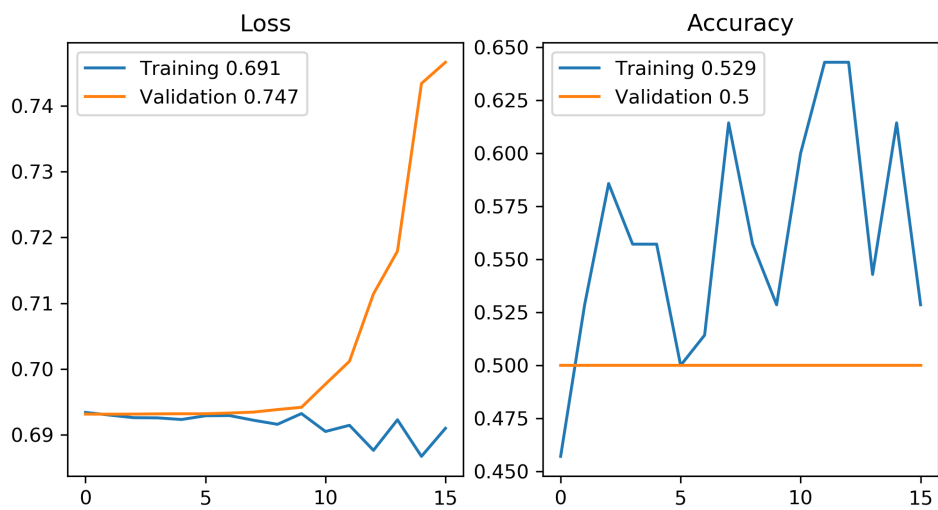Figure 54. Histograms of validation set results for index 6 using CNNSRIM1.
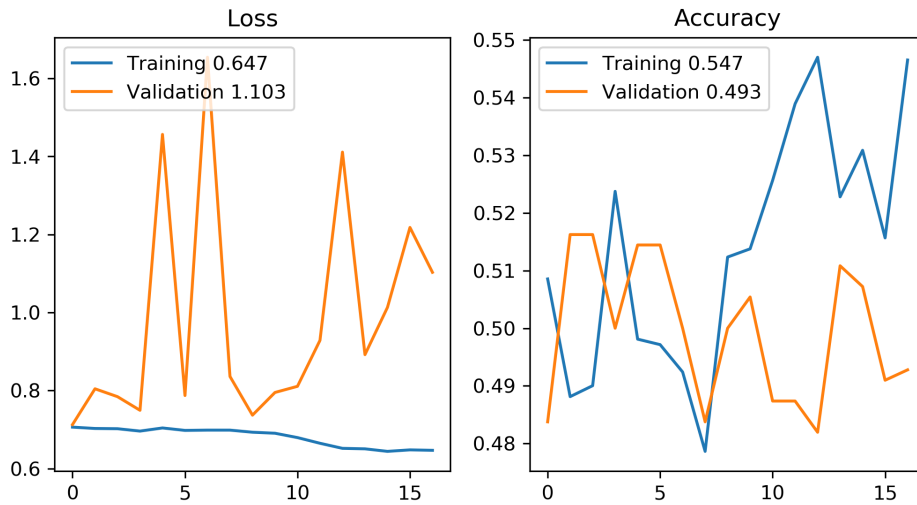
Figure 55. Chart of CNN training for index 6 using CNNSRIM1.
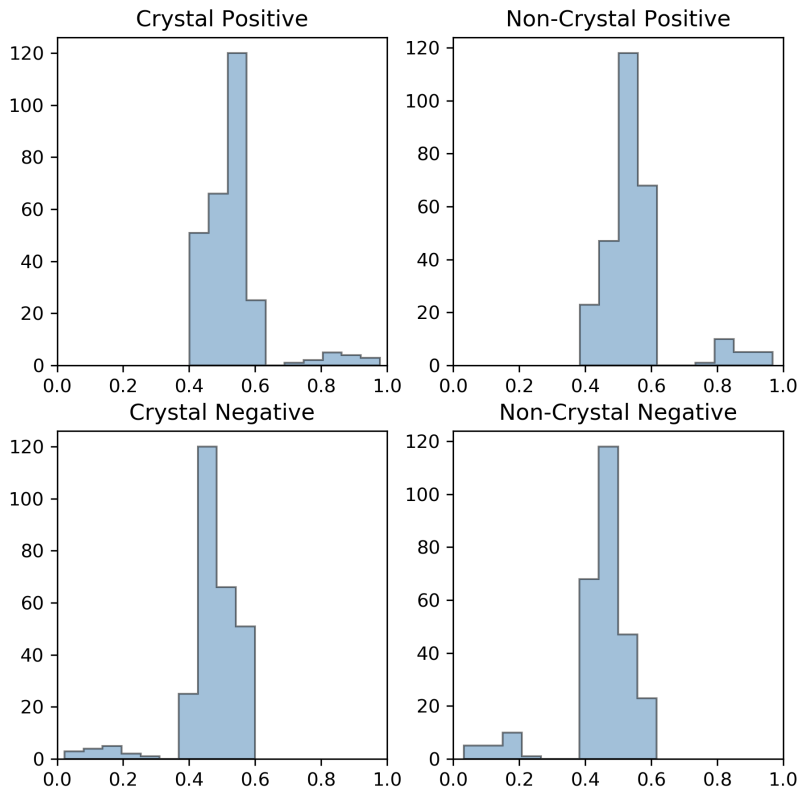
Figure 56. Histograms of validation set results for index 7 using CNNSRIM1.
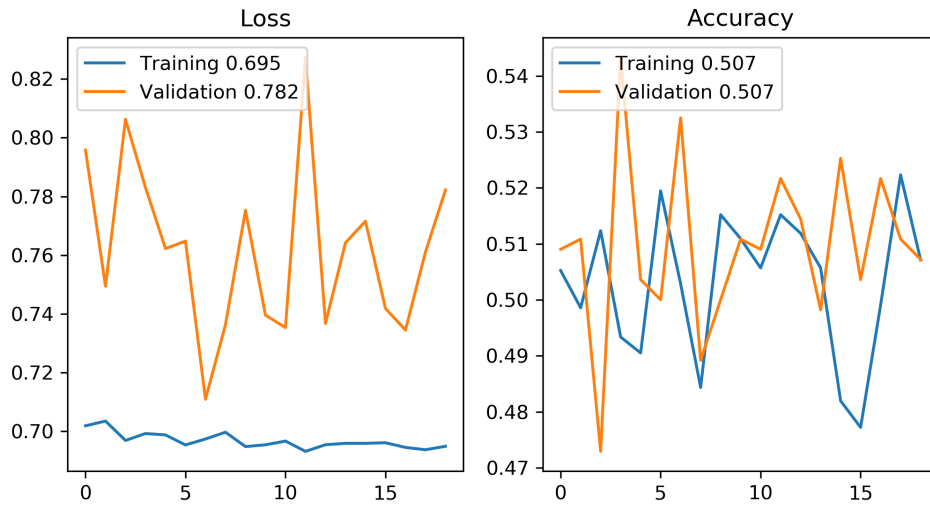
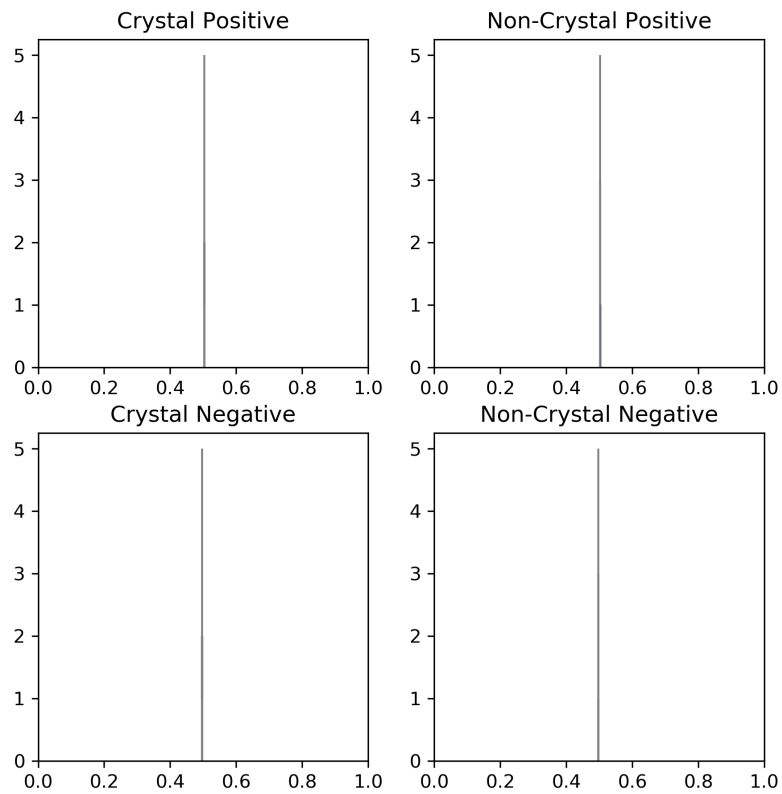Figure 57. Chart of CNN training for index 7 using CNNSRIM1.
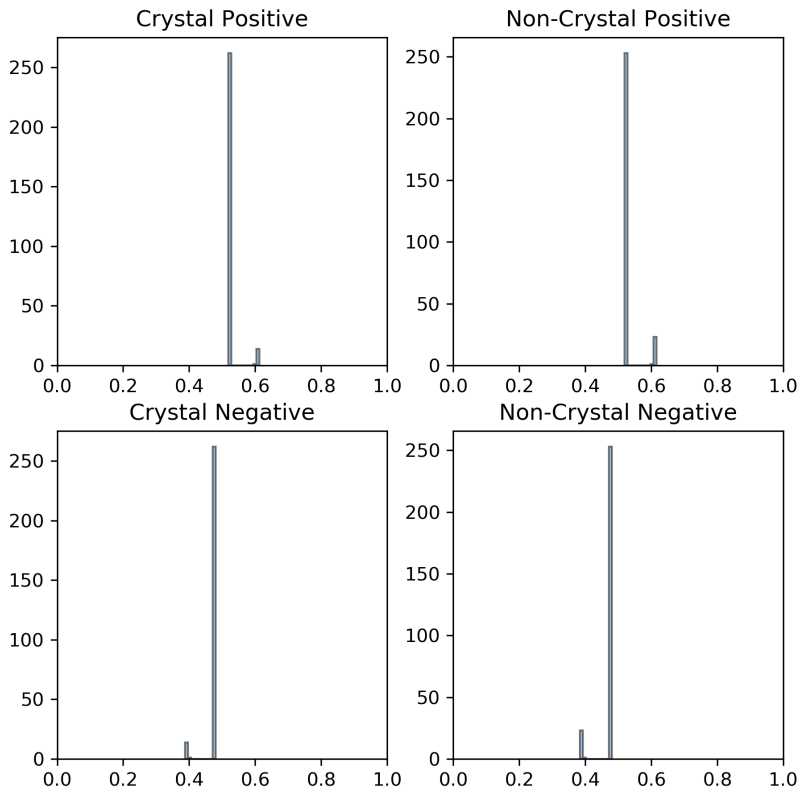
Figure 58. Histograms of validation set results for index 8 using CNNSRIM1.
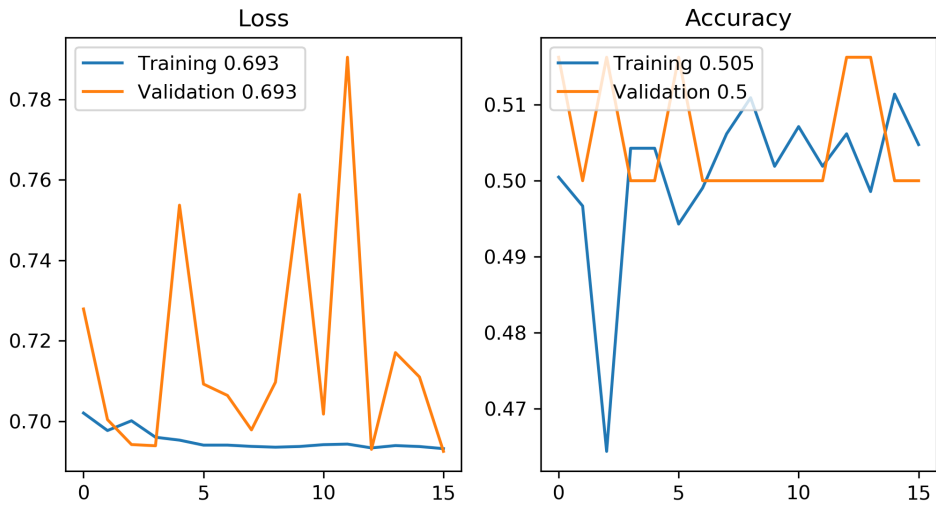
Figure 59. Chart of CNN training for index 8 using CNNSRIM1.
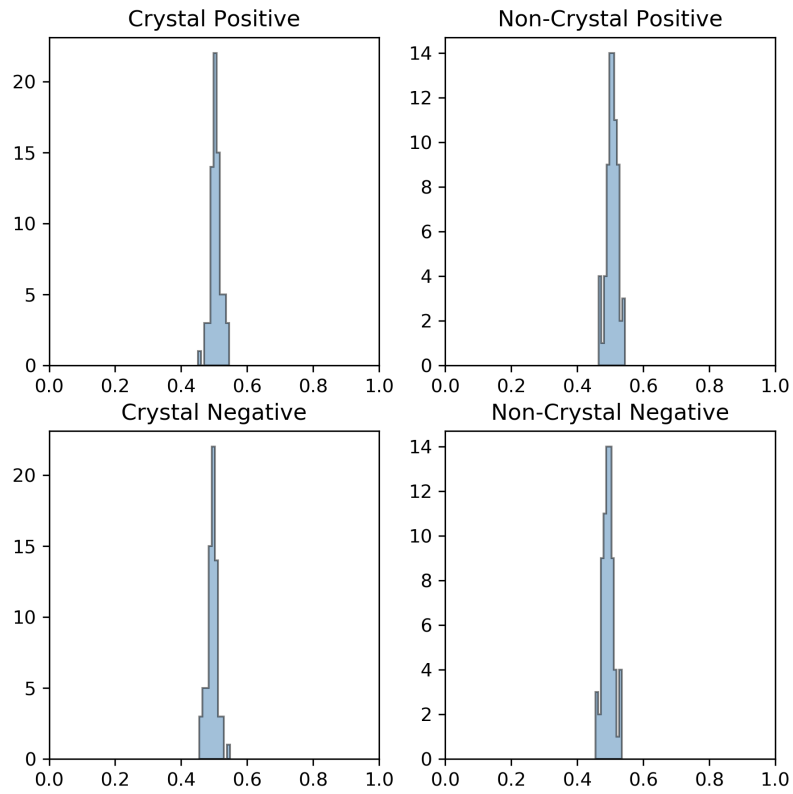
Figure 60. Histograms of validation set results for index 9 using CNNSRIM1.
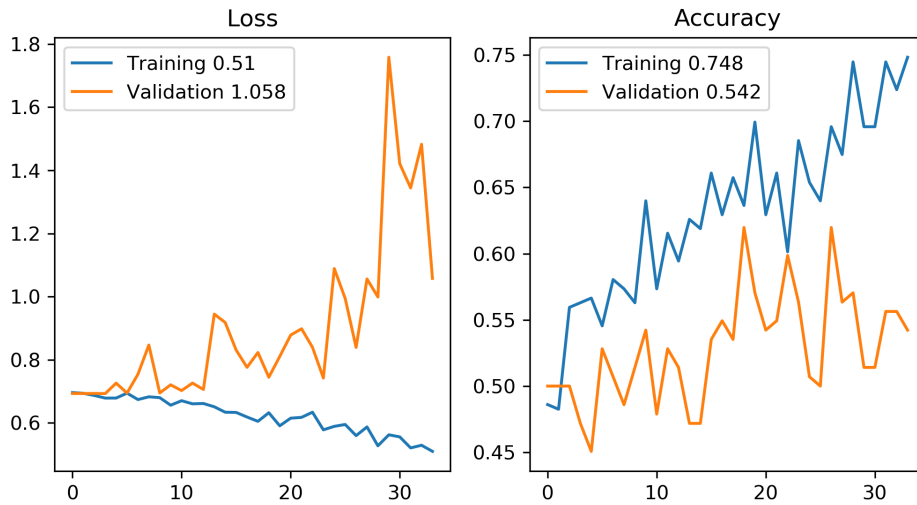
Figure 61. Chart of CNN training for index 9 using CNNSRIM1.
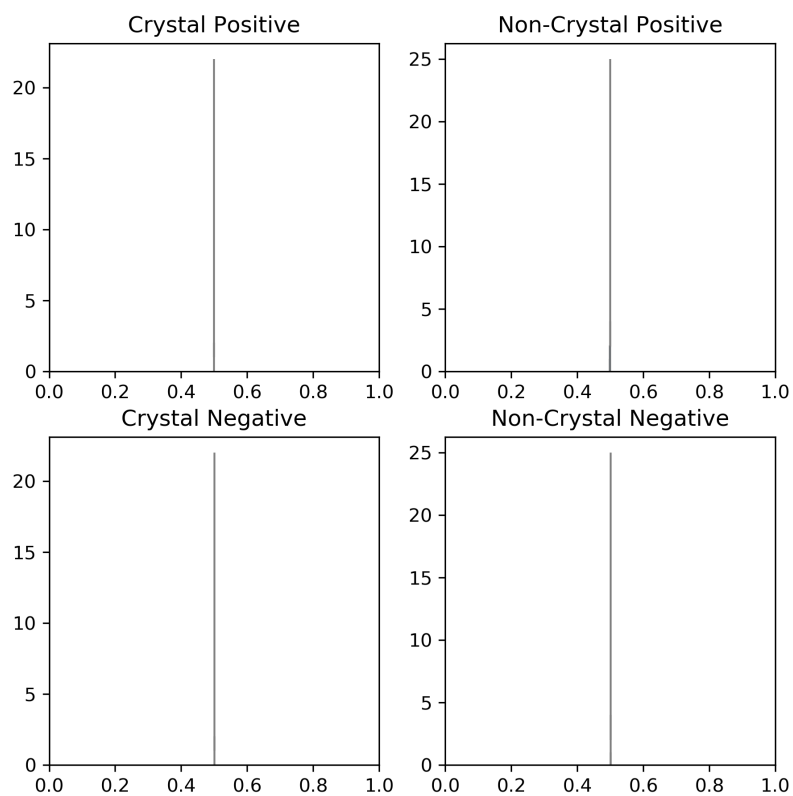
Figure 62. Histograms of validation set results for index 10 using CNNSRIM1.
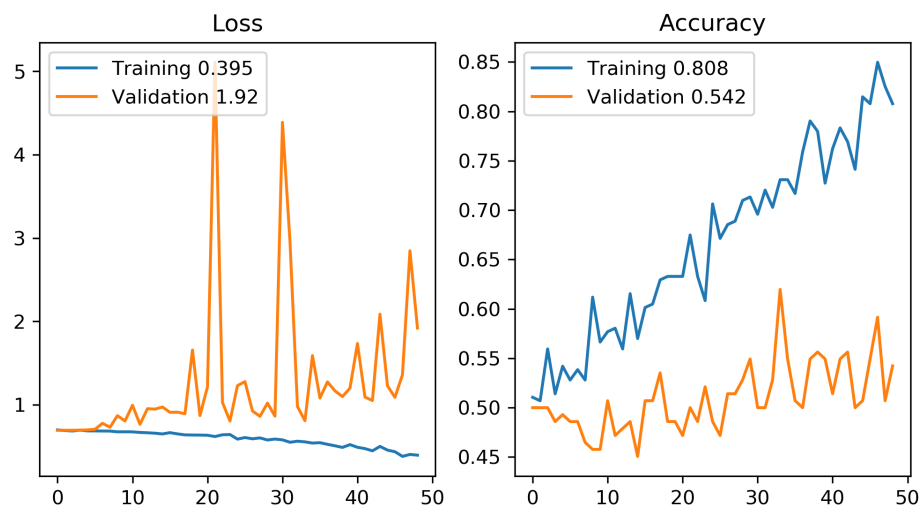
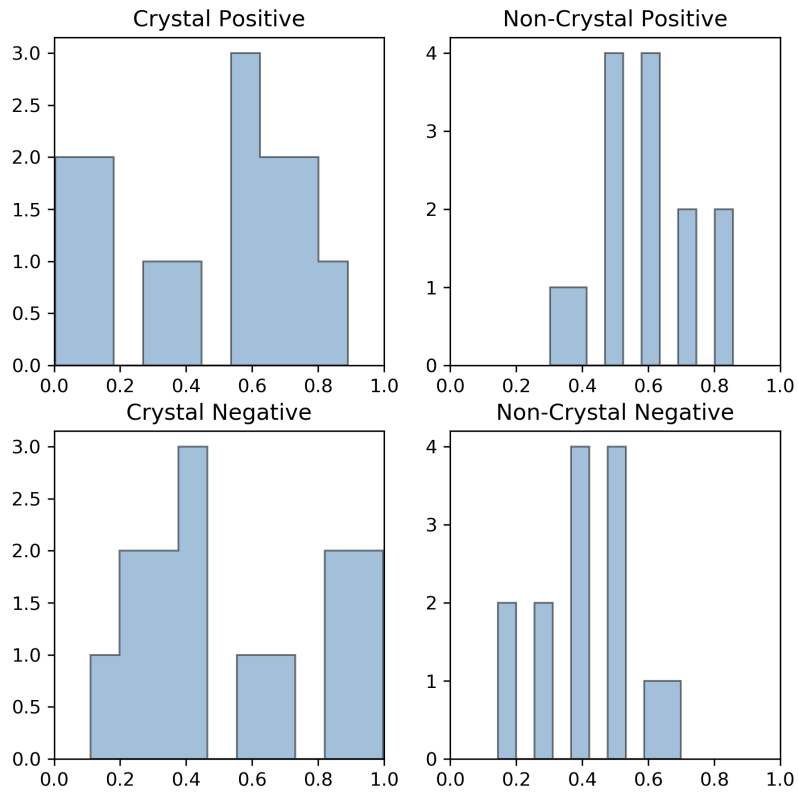Figure 63. Chart of CNN training for index 10 using CNNSRIM1.
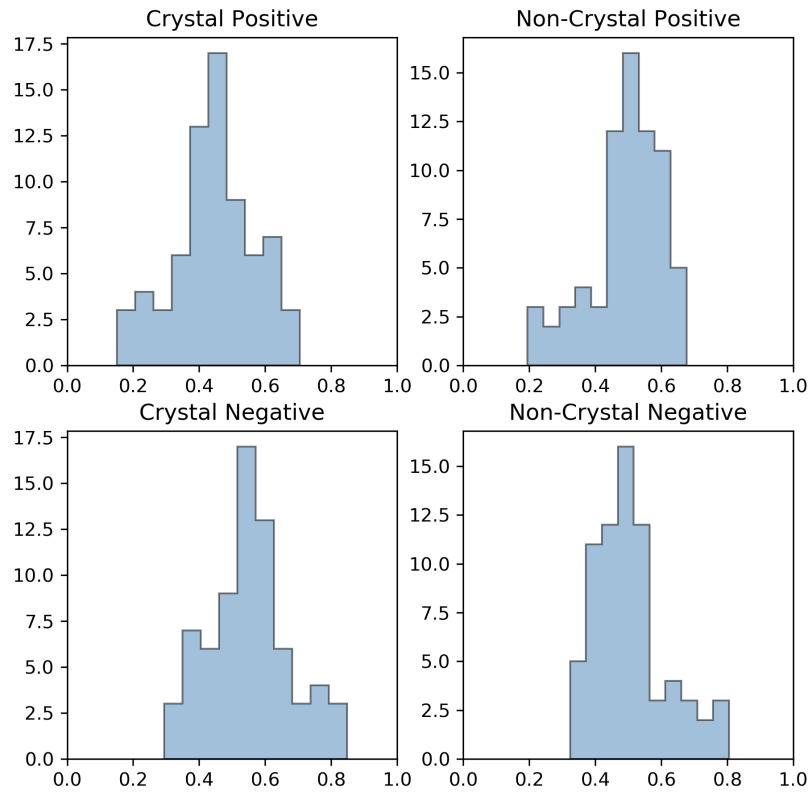
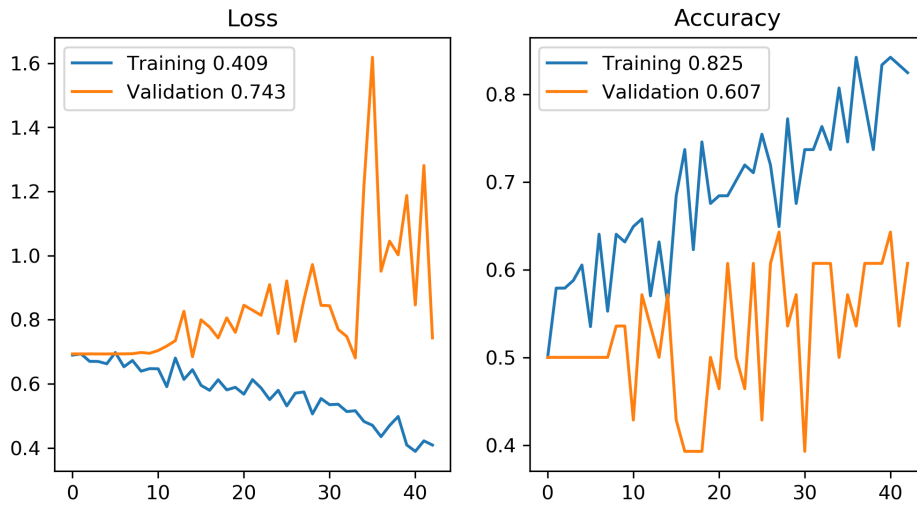Figure 64. Histograms of validation set results for index 11 using CNNSRIM1.
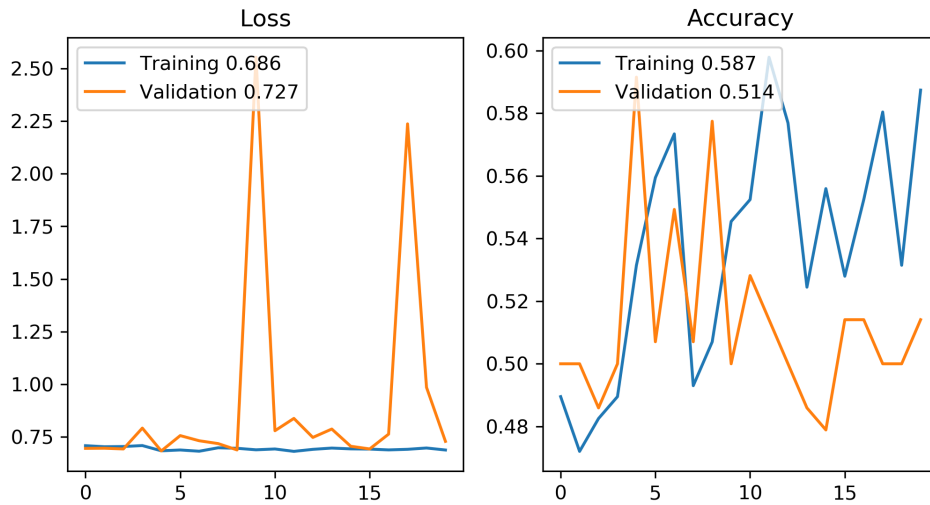
Figure 65. Chart of CNN training for index 11 using CNNSRIM1.
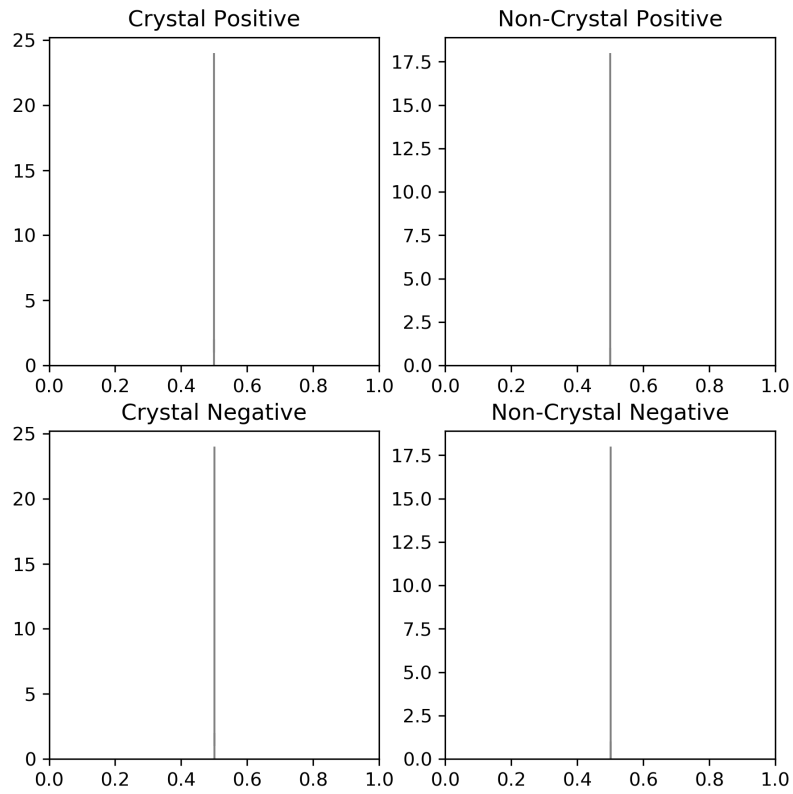
Figure 66. Histograms of validation set results for index 12 using CNNSRIM1.
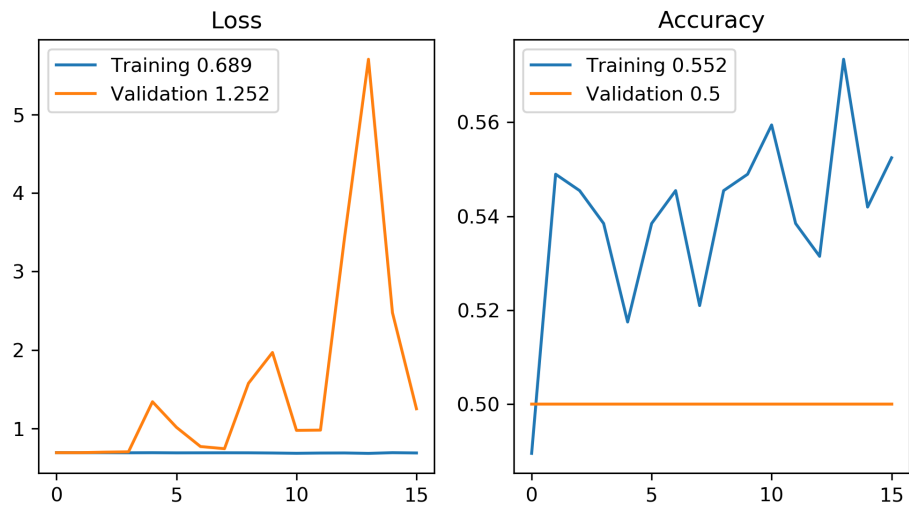
Figure 67. Chart of CNN training for index 12 using CNNSRIM1.
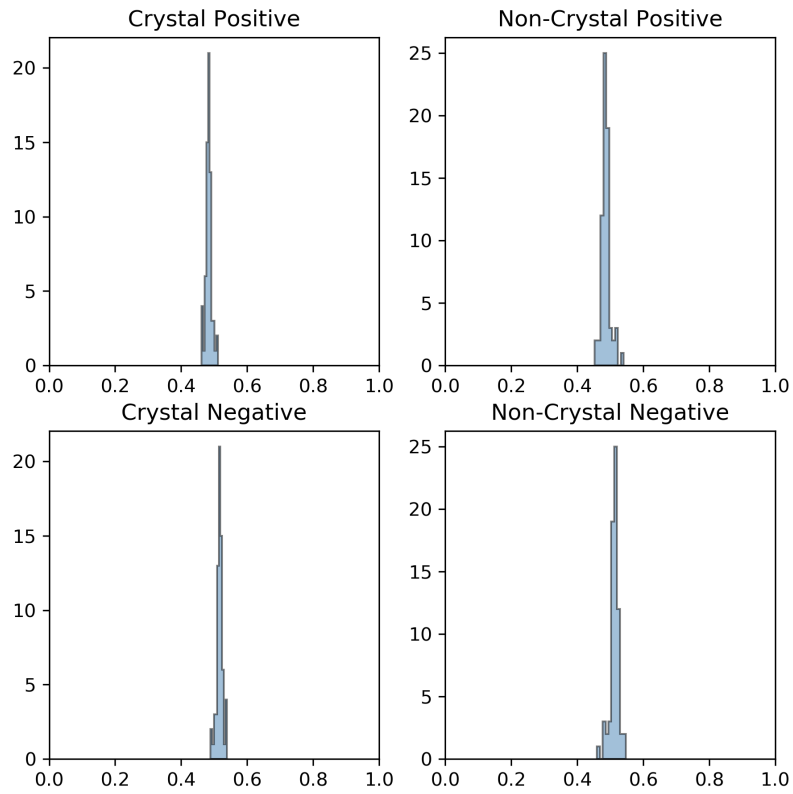
Figure 68. Histograms of validation set results for index 13 using CNNSRIM1.
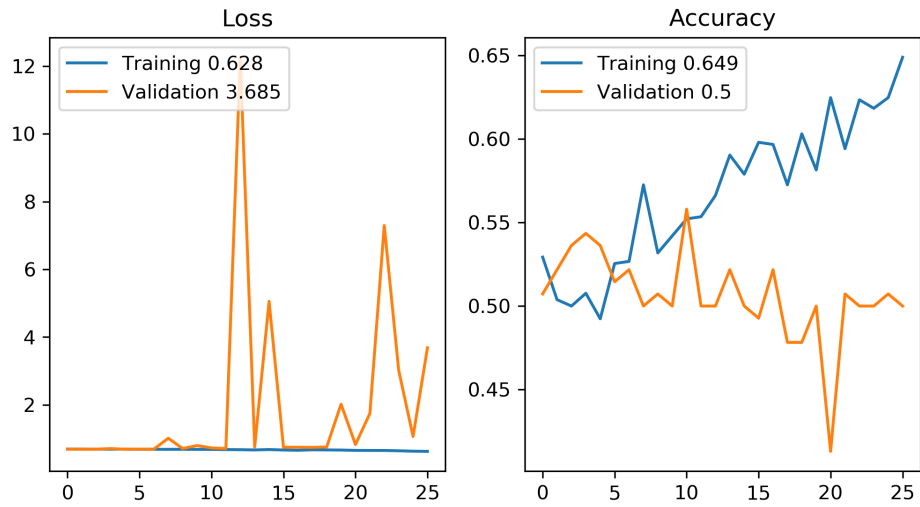
Figure 69. Chart of CNN training for index 13 using CNNSRIM1.
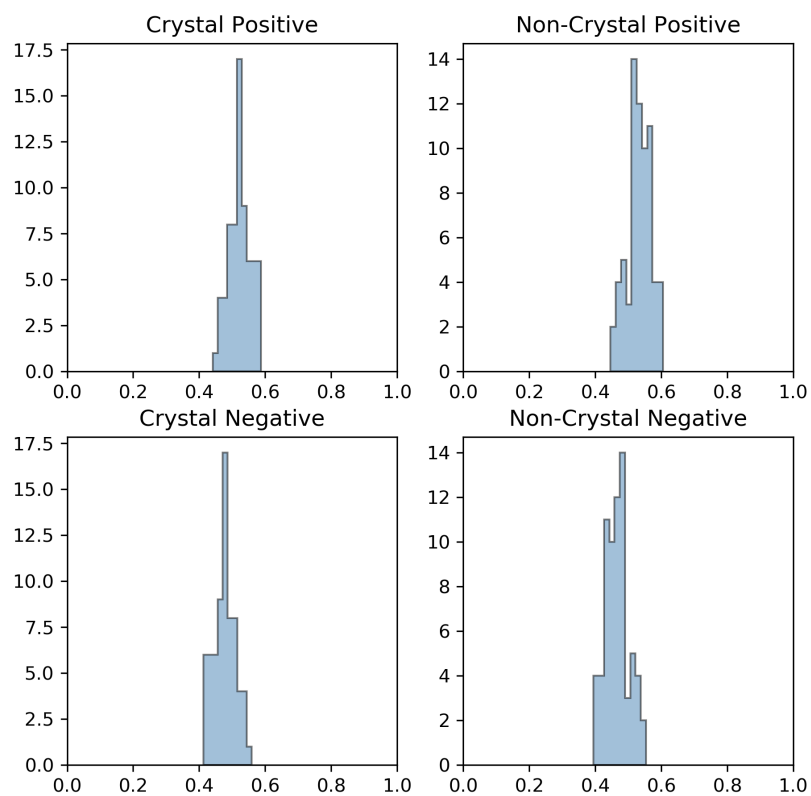
Figure 70. Histograms of validation set results for index 14 using CNNSRIM1.
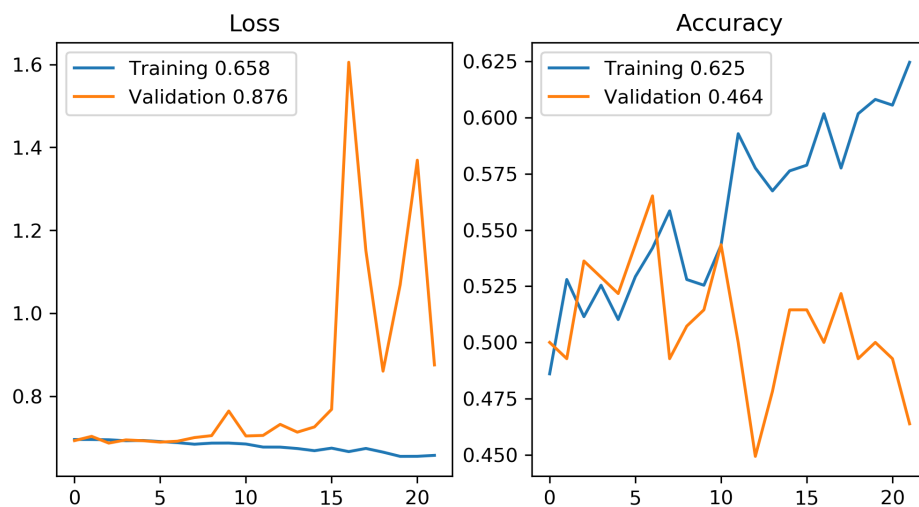
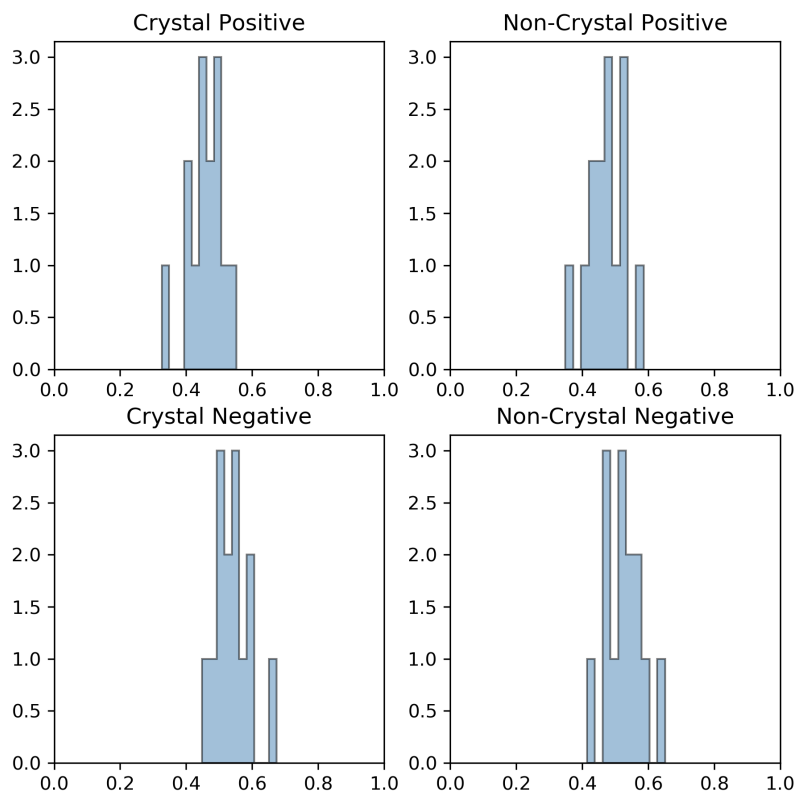Figure 71. Chart of CNN training for index 14 using CNNSRIM1.
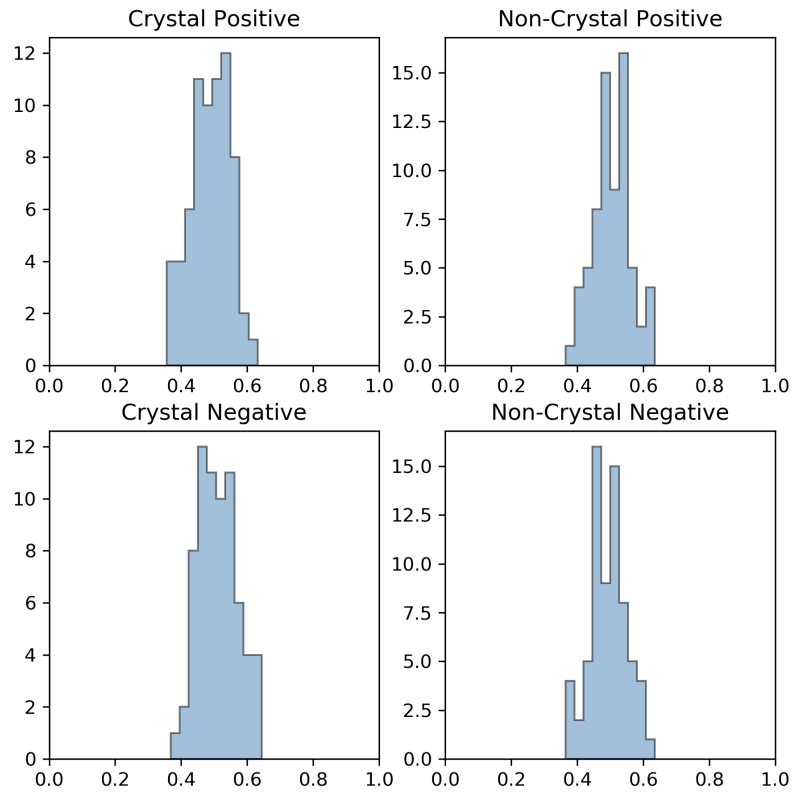
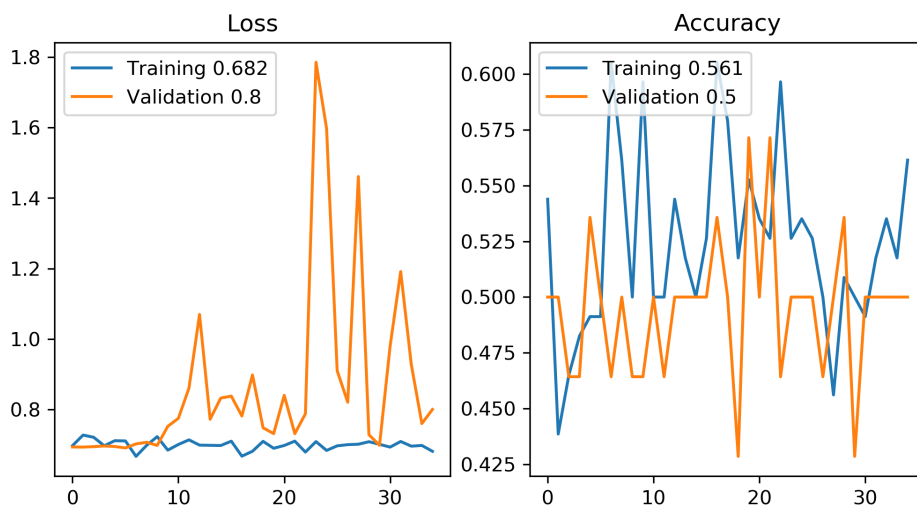Figure 72. Histograms of validation set results for index 15 using CNNSRIM1.
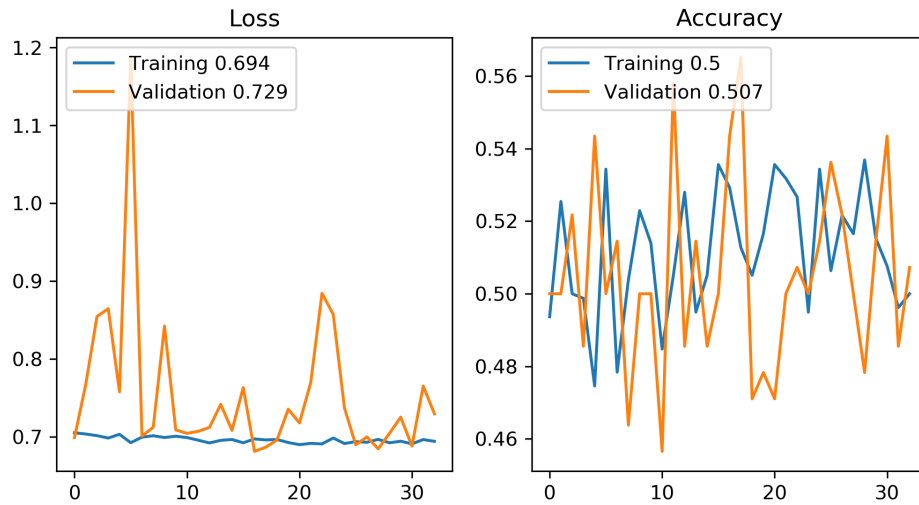
Figure 73. Chart of CNN training for index 15 using CNNSRIM1.
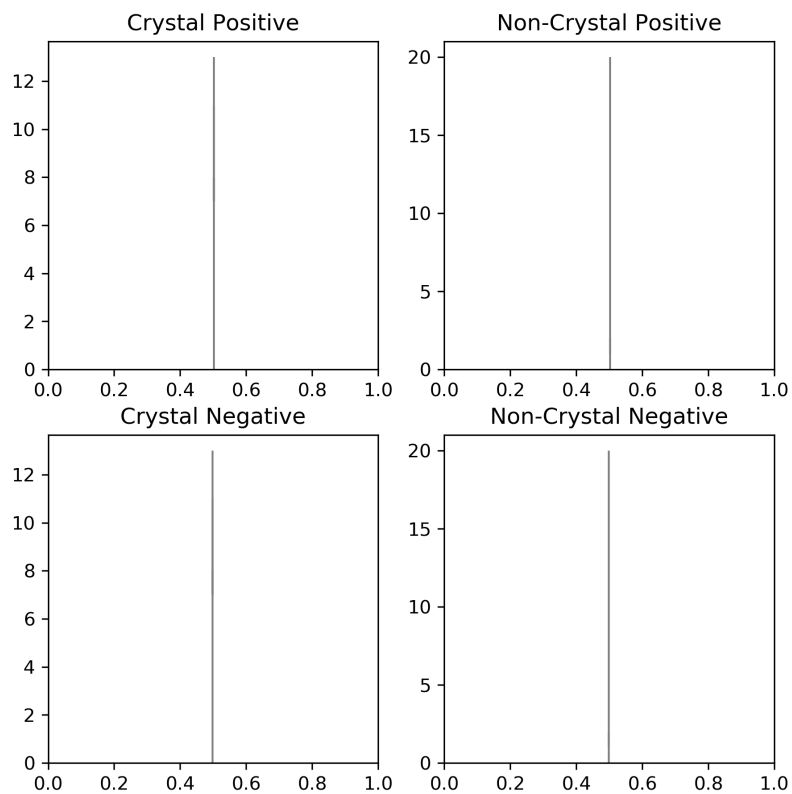
Figure 74. Histograms of validation set results for index 16 using CNNSRIM1.
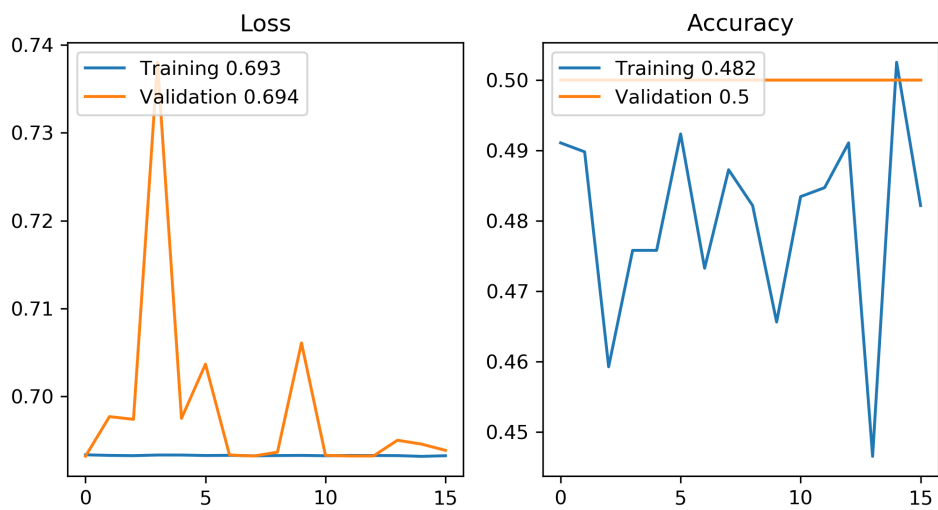
Figure 75. Chart of CNN training for index 16 using CNNSRIM1.
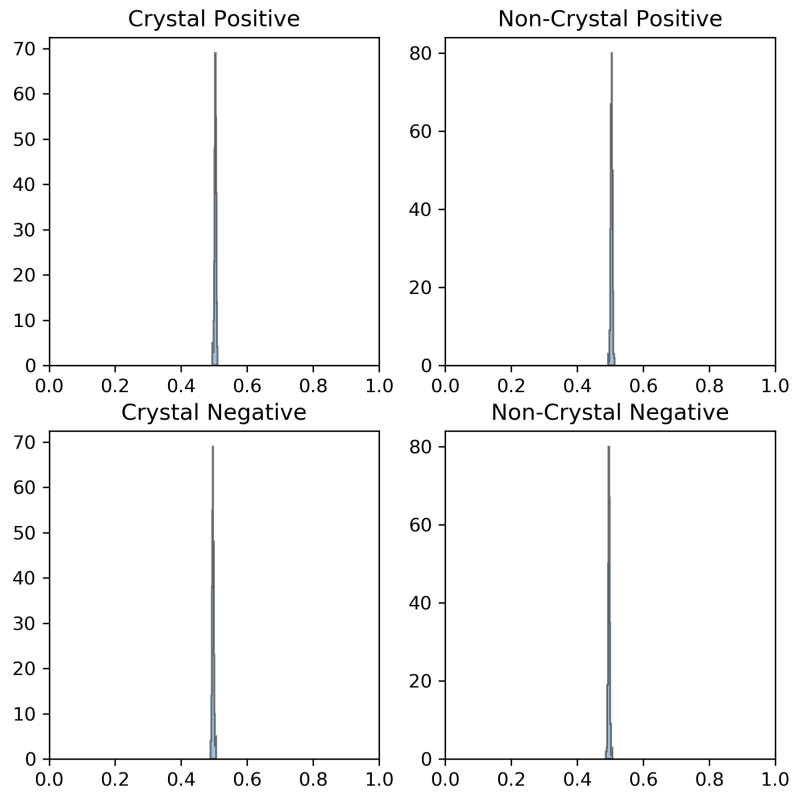
Figure 76. Histograms of validation set results for index 17 using CNNSRIM1.
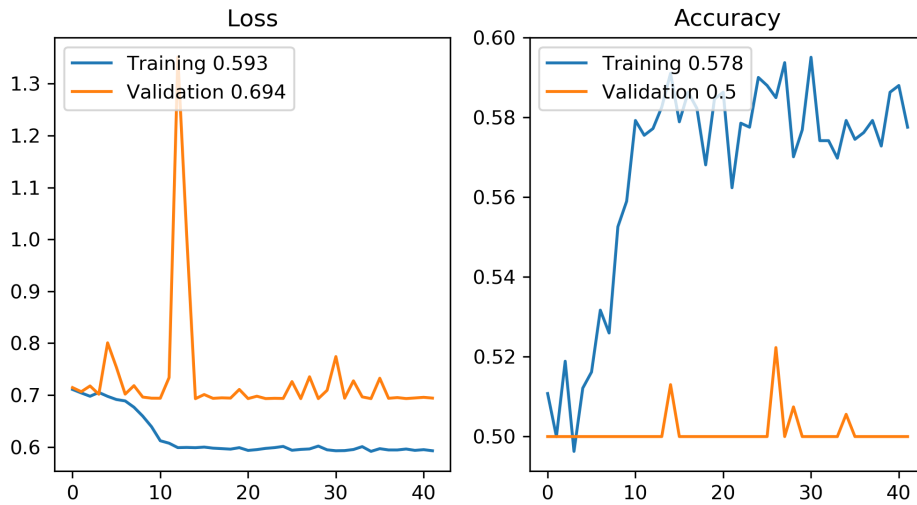
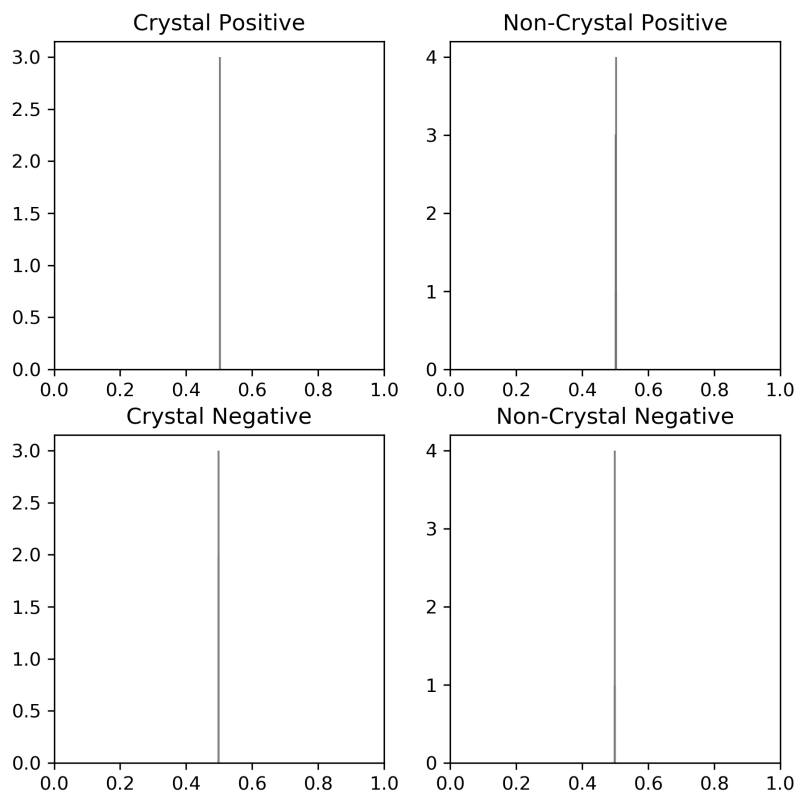Figure 77. Chart of CNN training for index 17 using CNNSRIM1.
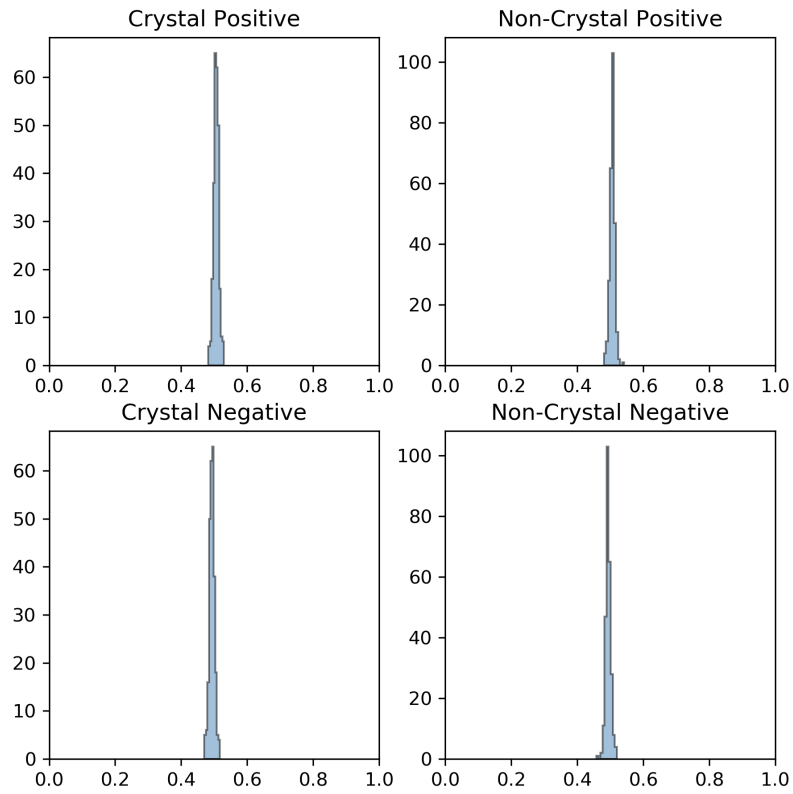
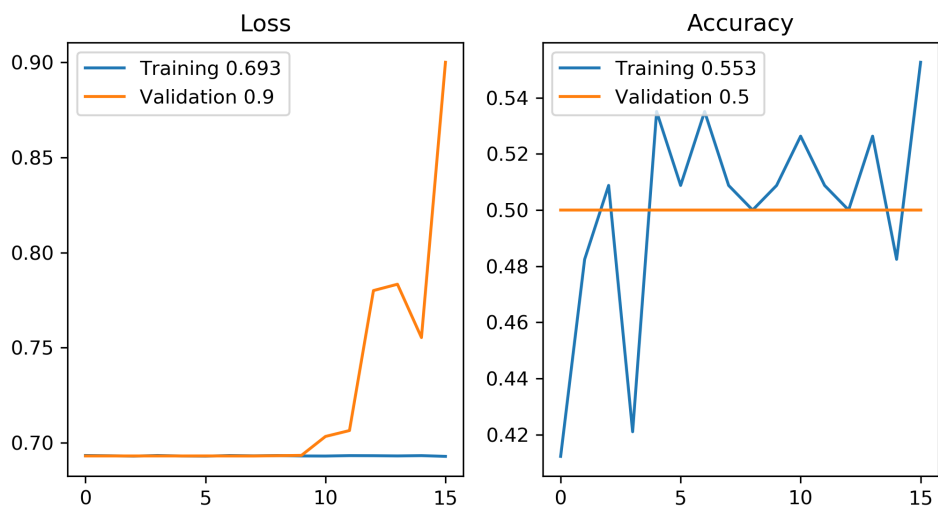Figure 78. Histograms of validation set results for index 18 using CNNSRIM1.
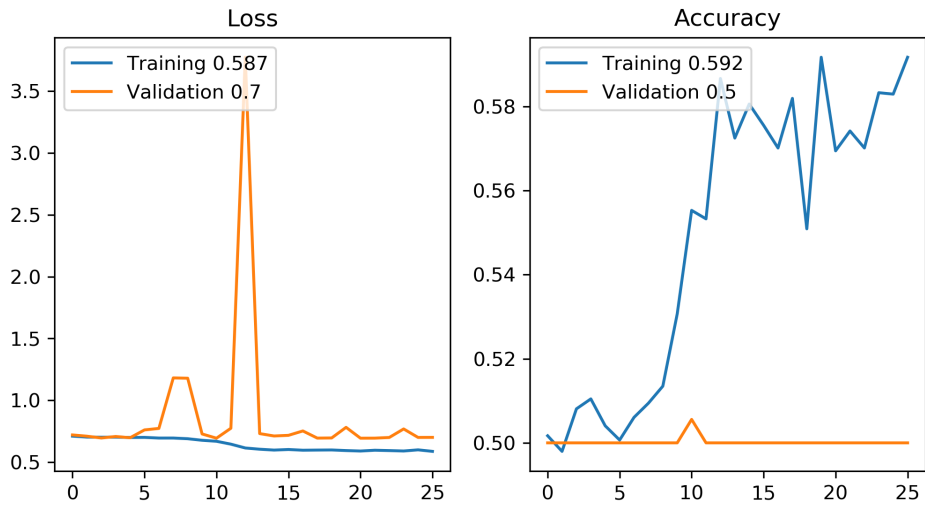
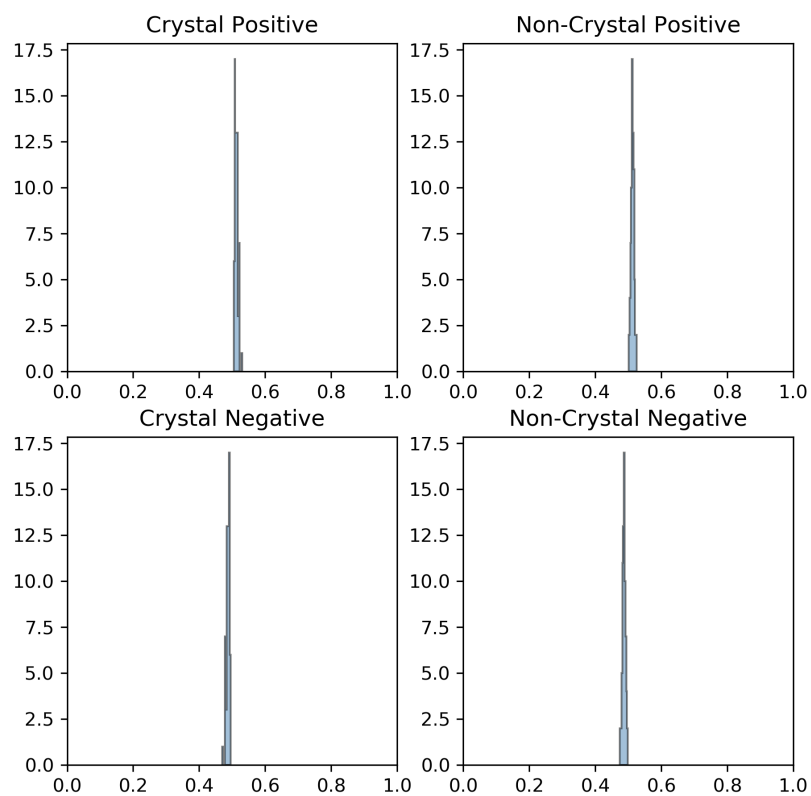Figure 79. Chart of CNN training for index 18 using CNNSRIM1.
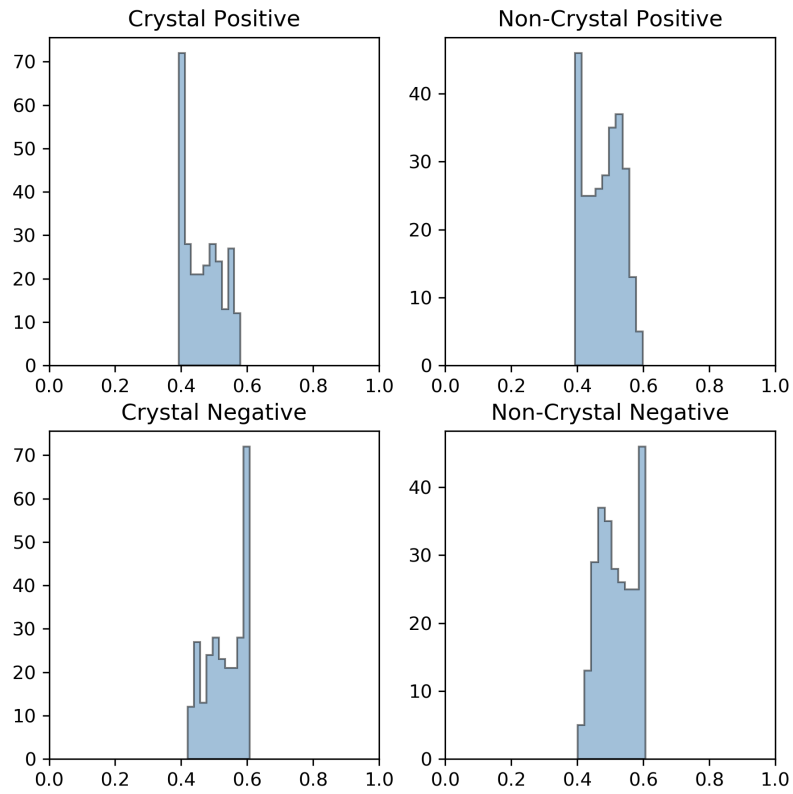
Figure 80. Histograms of validation set results for index 19 using CNNSRIM1.
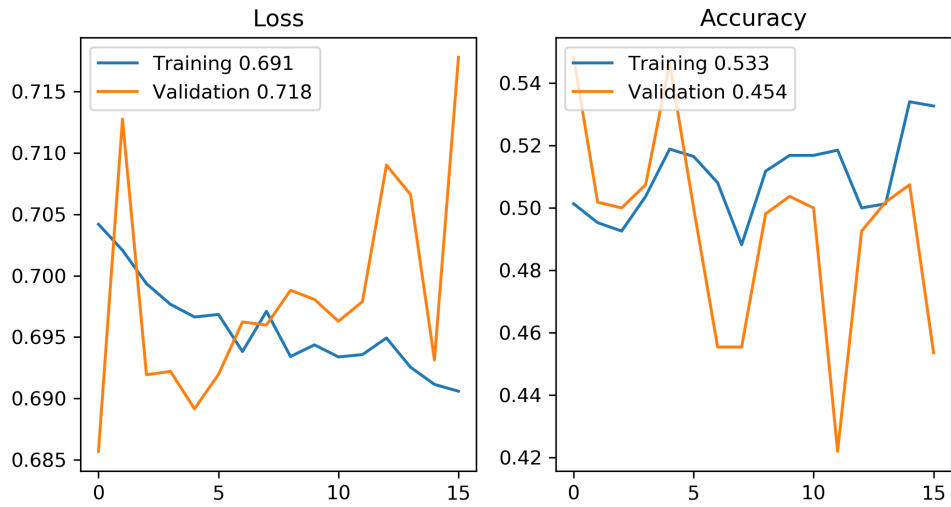
Figure 81. Chart of CNN training for index 19 using CNNSRIM1.
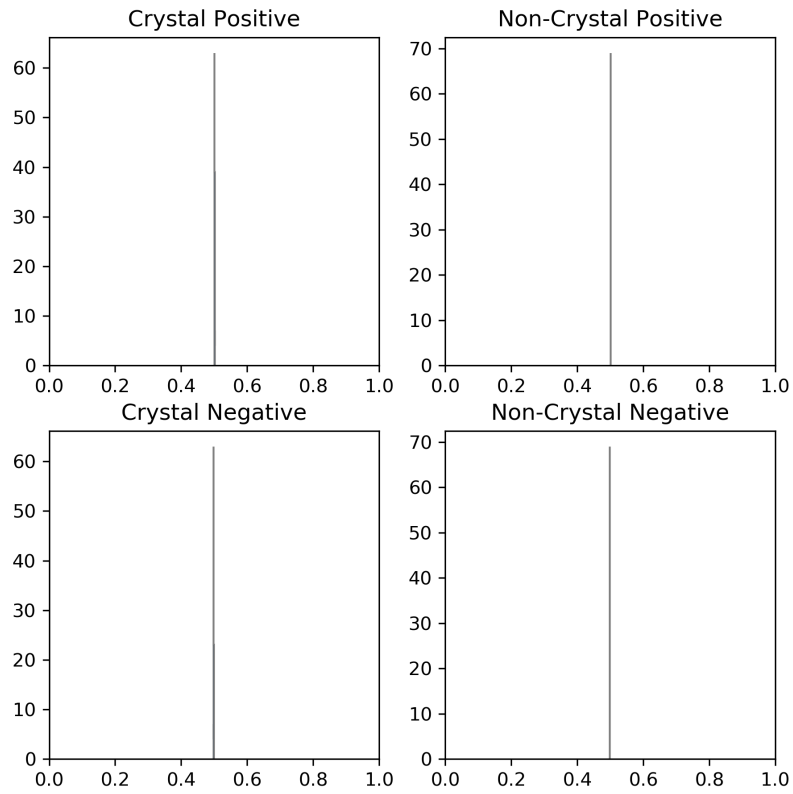
Figure 82. Histograms of validation set results for index 20 using CNNSRIM1.
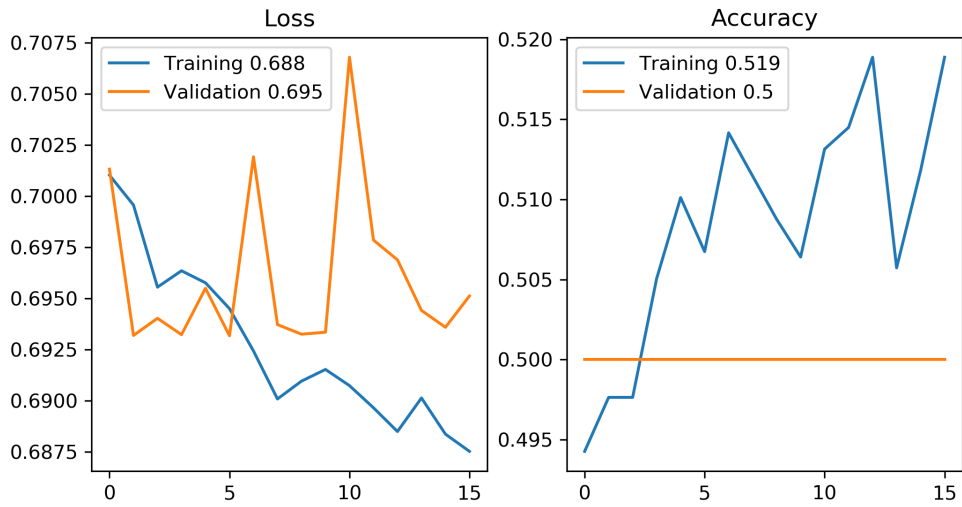
Figure 83. Chart of CNN training for index 20 using CNNSRIM1.
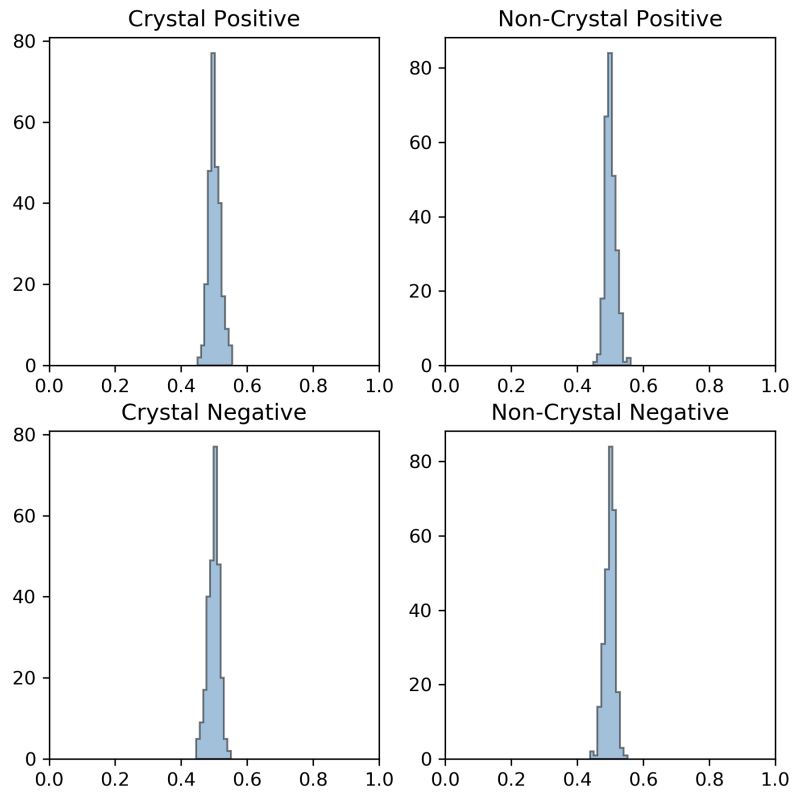
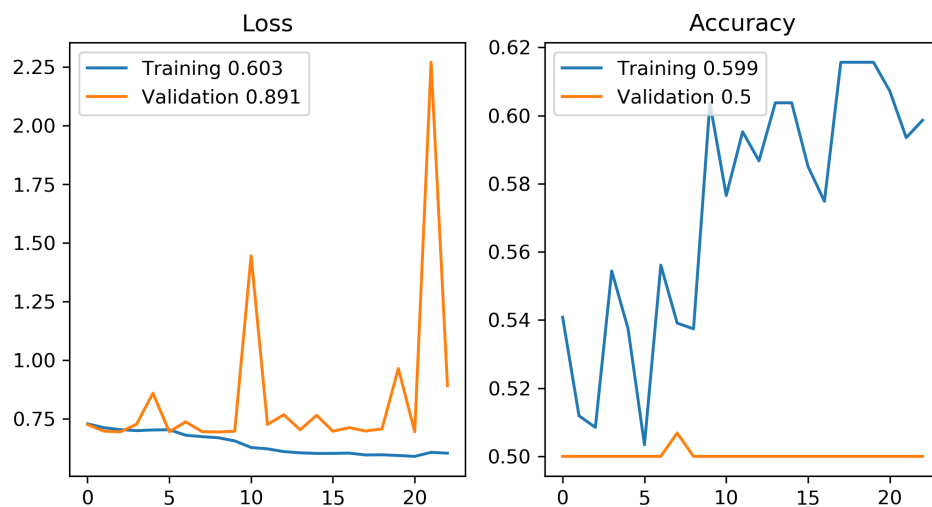Figure 84. Histograms of validation set results for index 21 using CNNSRIM1.
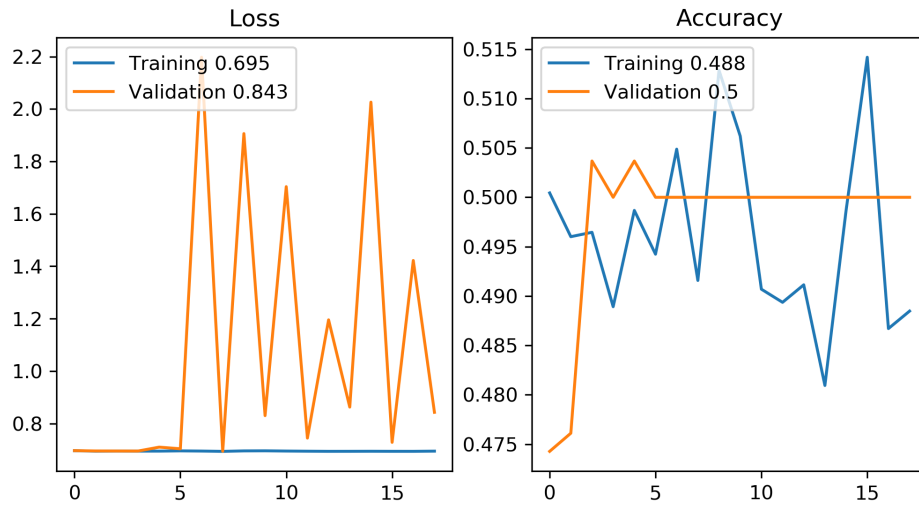
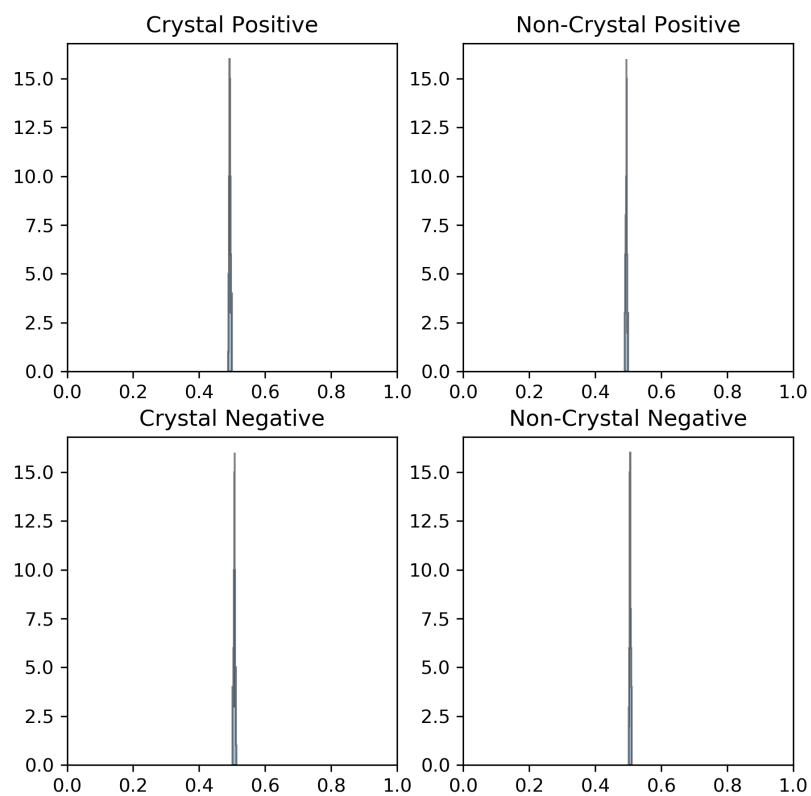Figure 85. Chart of CNN training for index 21 using CNNSRIM1.
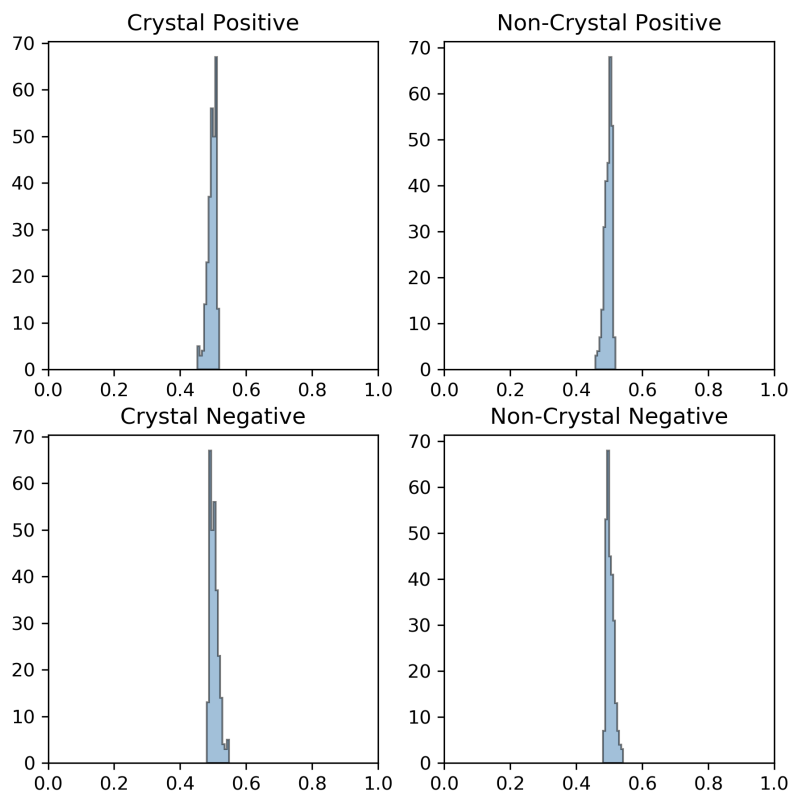
Figure 86. Histograms of validation set results for index 22 using CNNSRIM1.
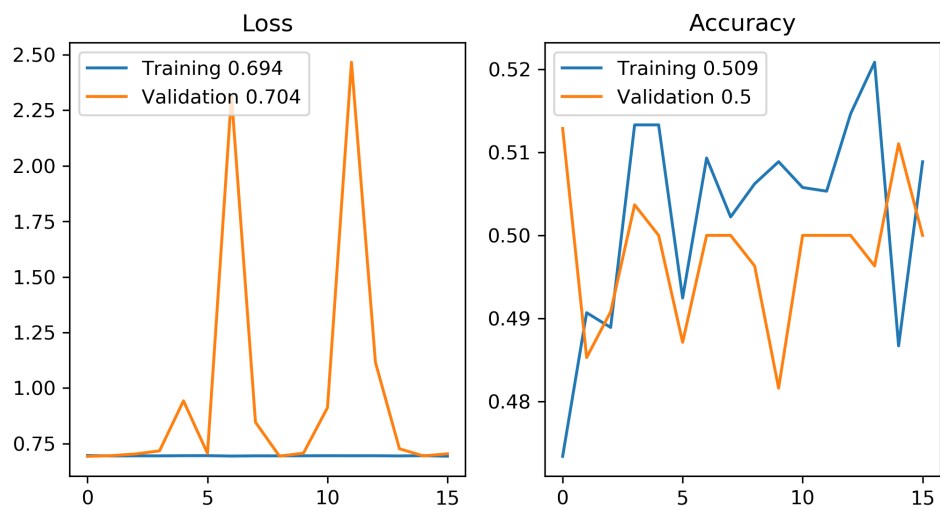
Figure 87. Chart of CNN training for index 22 using CNNSRIM1.
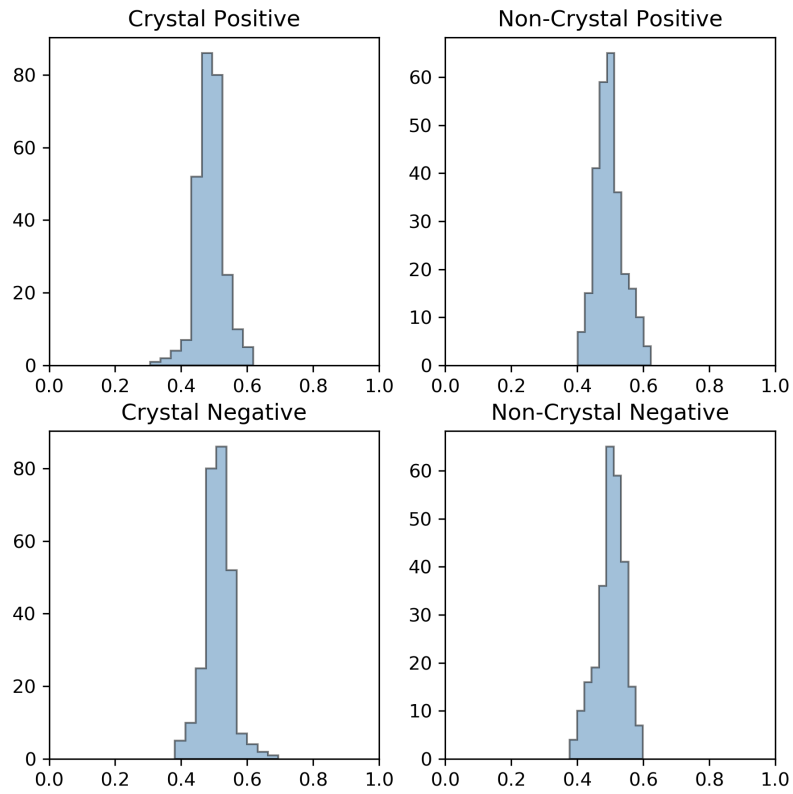
Figure 88. Histograms of validation set results for index 23 using CNNSRIM1.
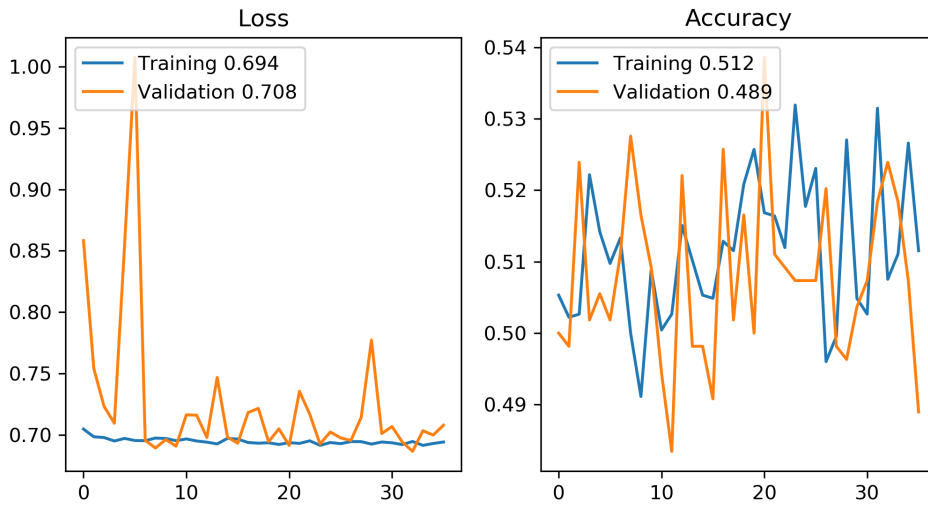
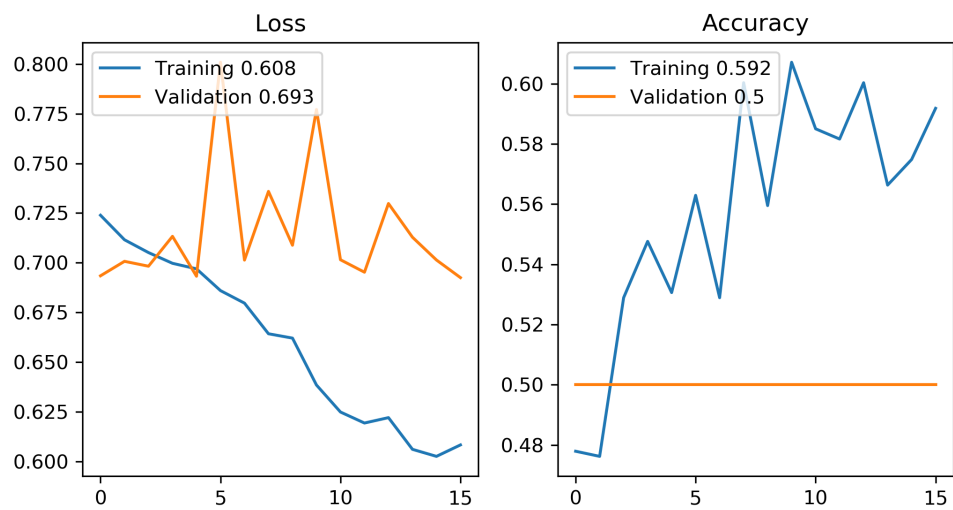Figure 89. Chart of CNN training for index 23 using CNNSRIM1.
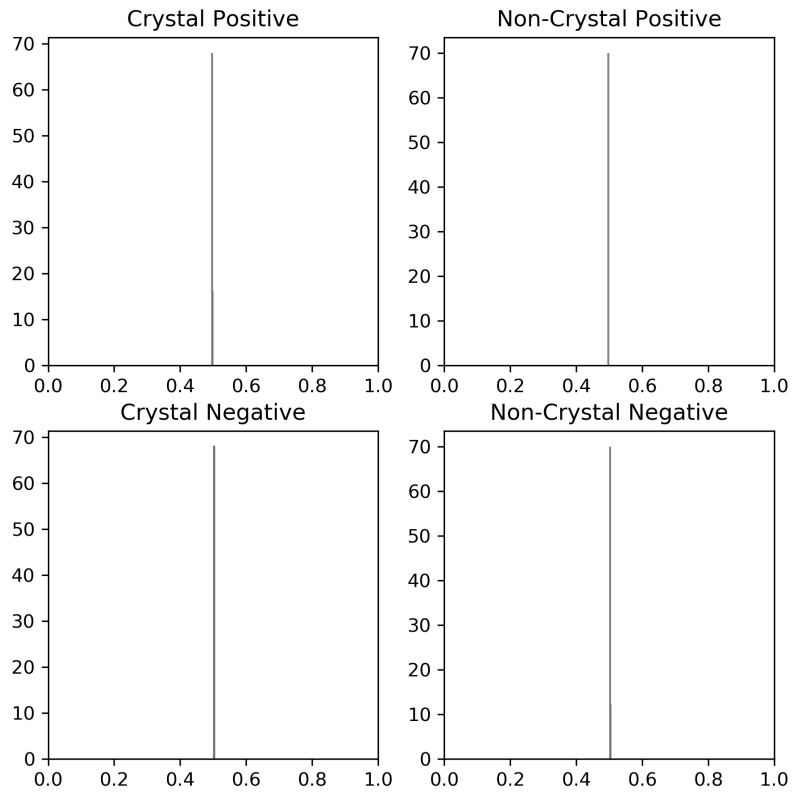
Figure 90. Histograms of validation set results for index 24 using CNNSRIM1.
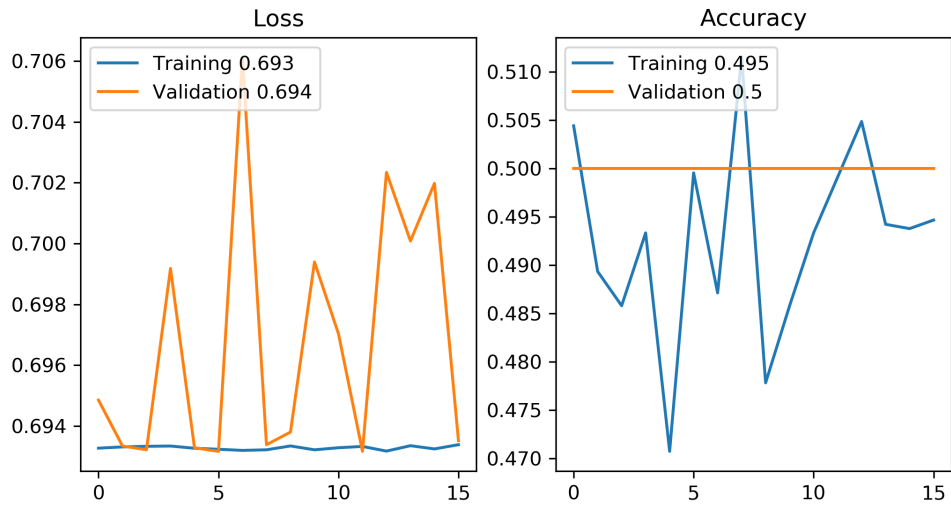
Figure 91. Chart of CNN training for index 24 using CNNSRIM1.
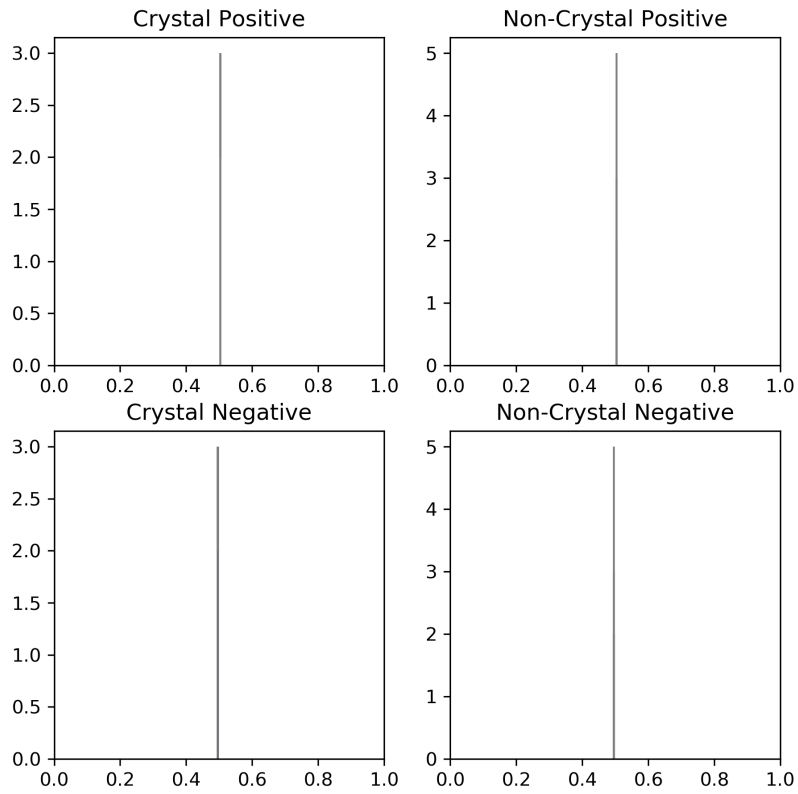
Figure 92. Histograms of validation set results for index 25 using CNNSRIM1.
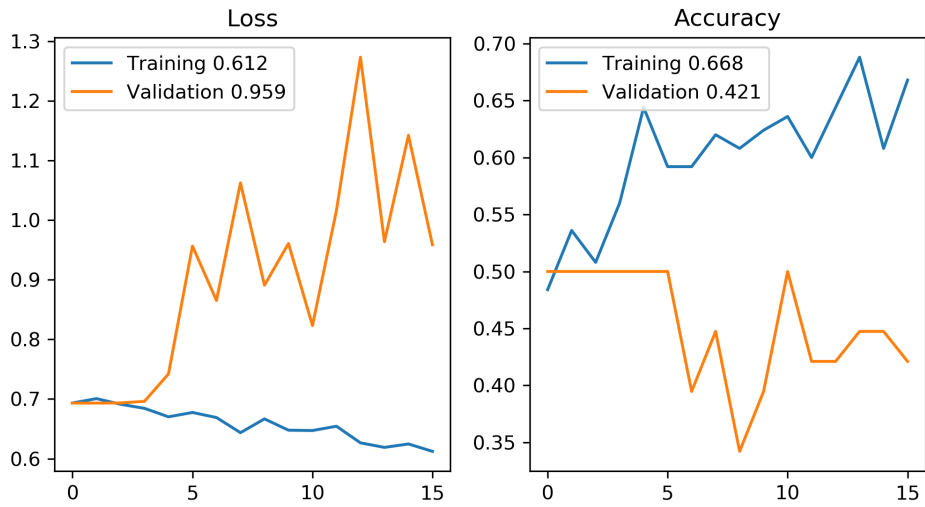
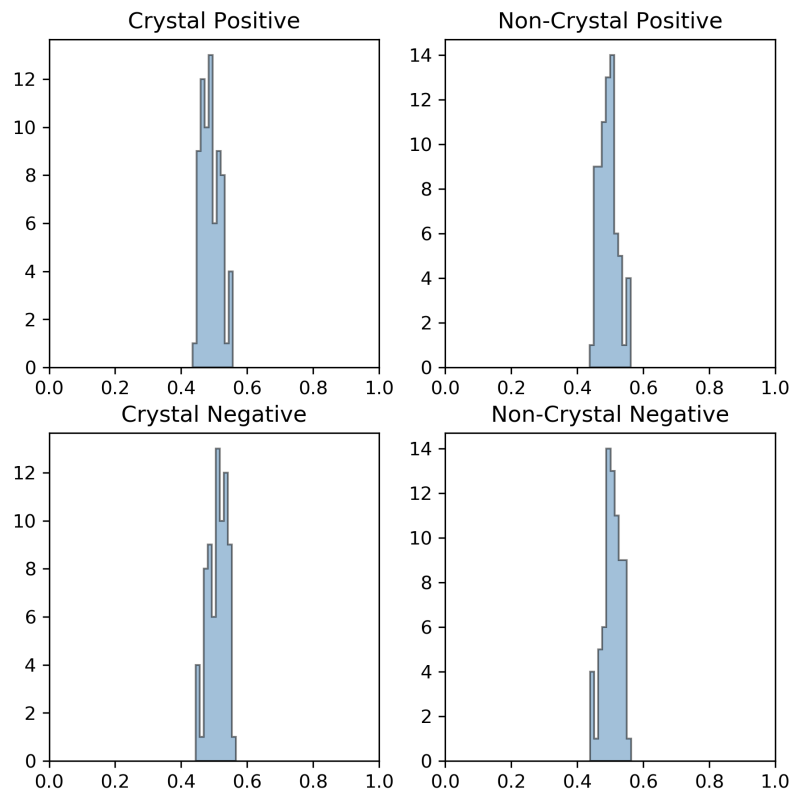Figure 93. Chart of CNN training for index 25 using CNNSRIM1.
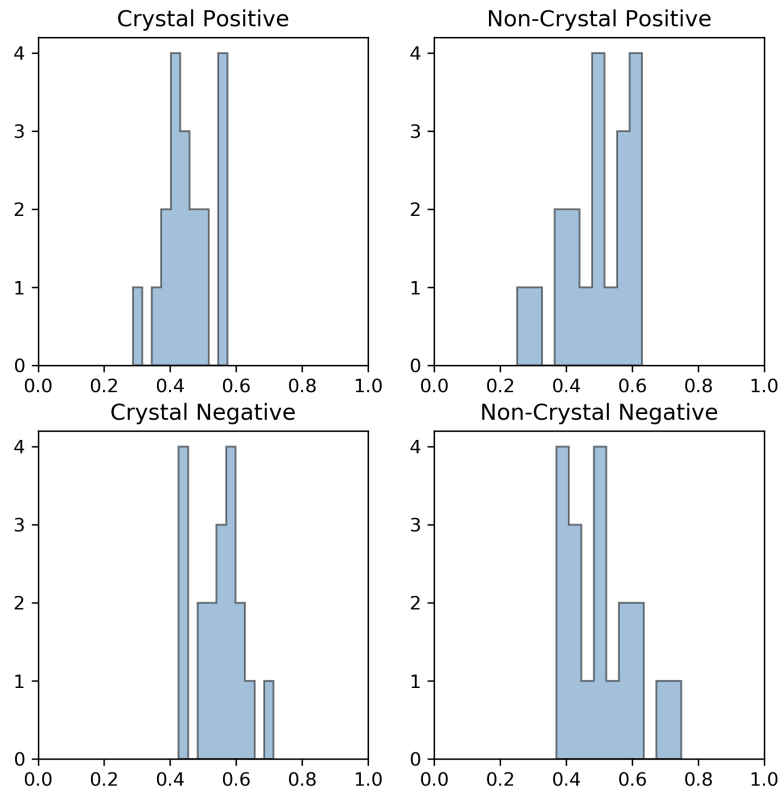
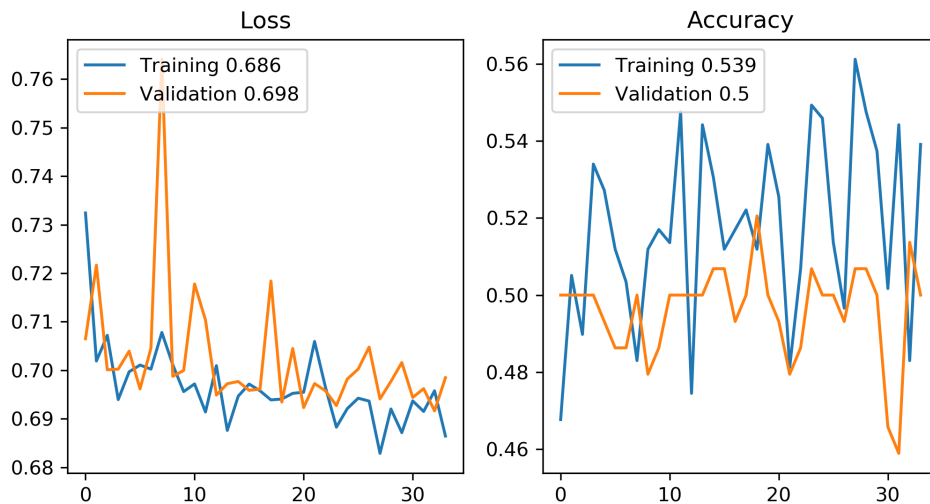Figure 94. Histograms of validation set results for index 26 using CNNSRIM1.
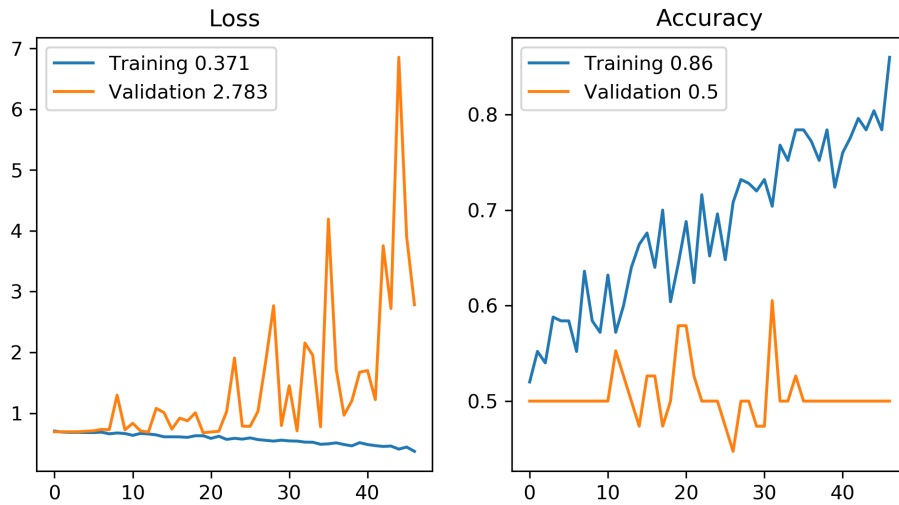
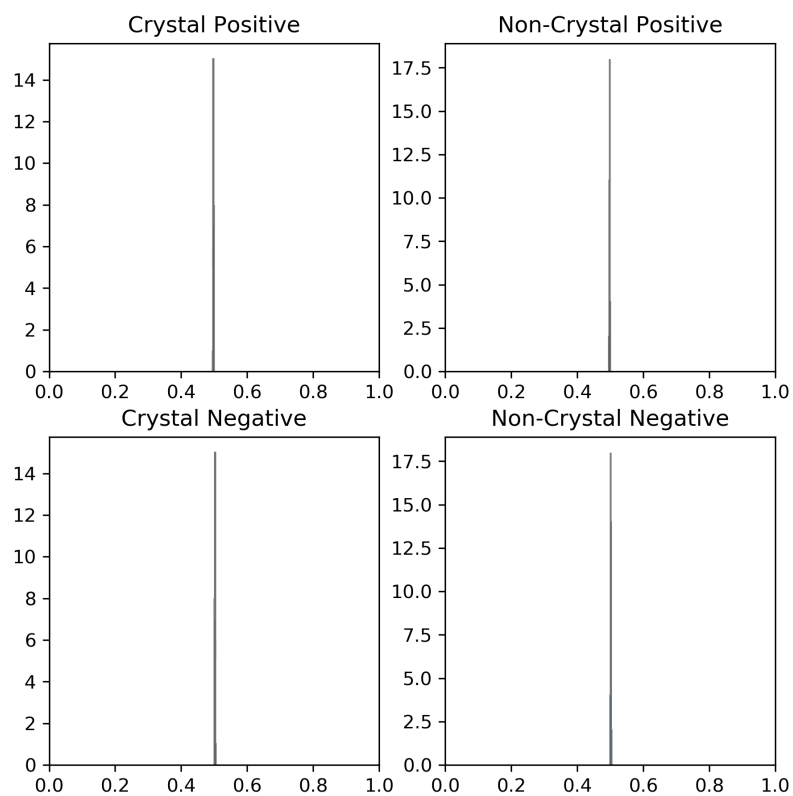Figure 95. Chart of CNN training for index 26 using CNNSRIM1.
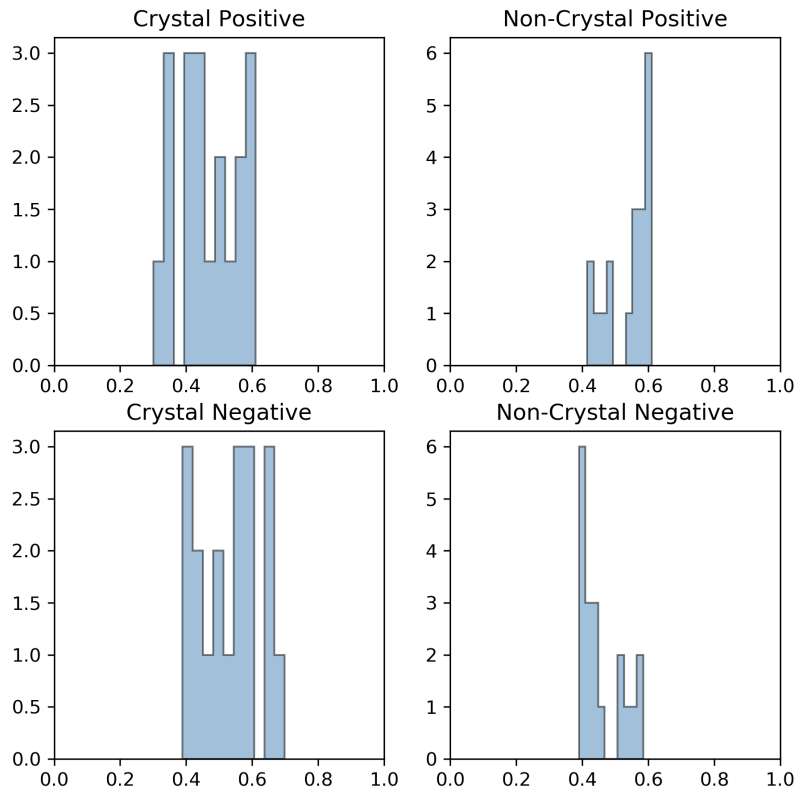
Figure 96. Histograms of validation set results for index 27 using CNNSRIM1.
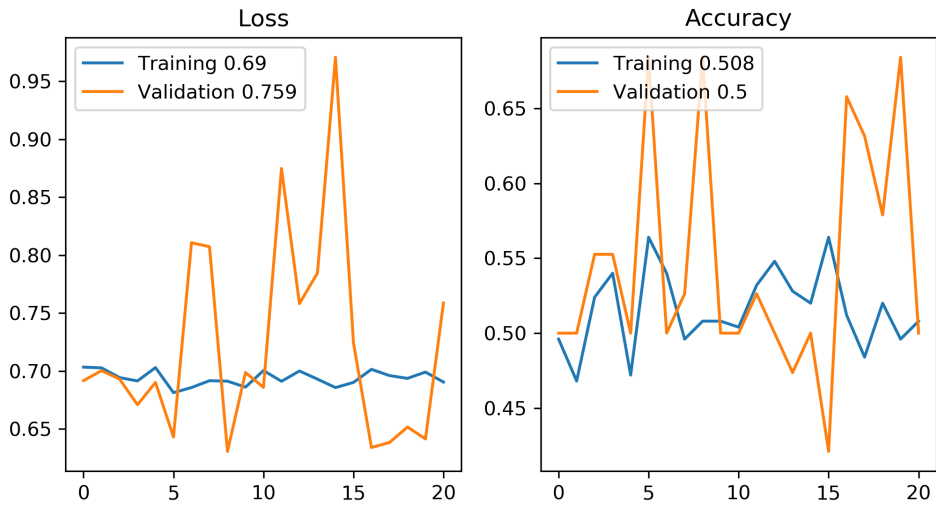
Figure 97. Chart of CNN training for index 27 using CNNSRIM1.
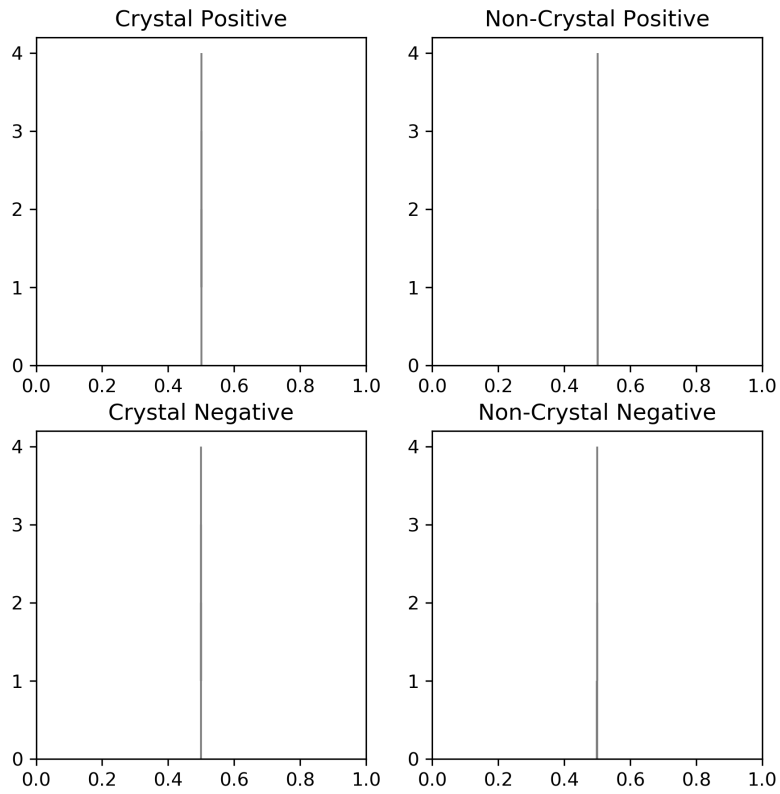
Figure 98. Histograms of validation set results for index 28 using CNNSRIM1.
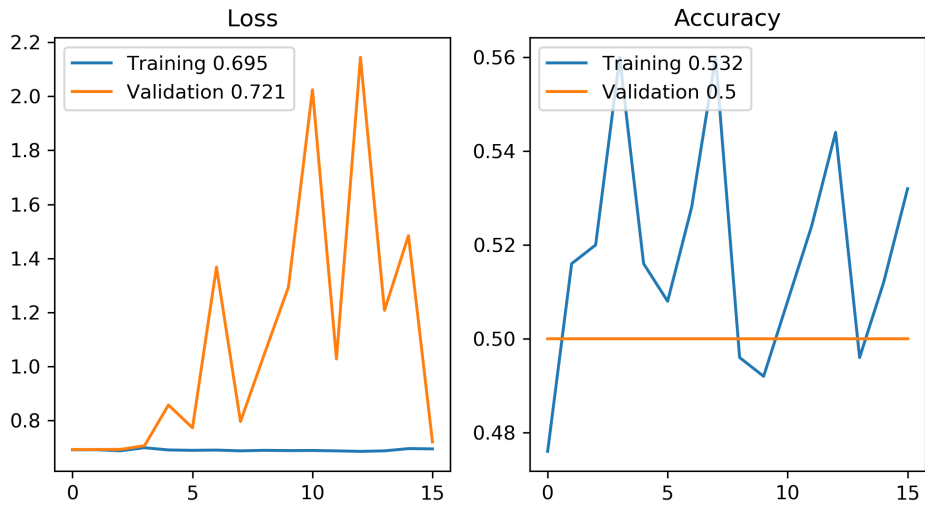
Figure 99. Chart of CNN training for index 28 using CNNSRIM1.
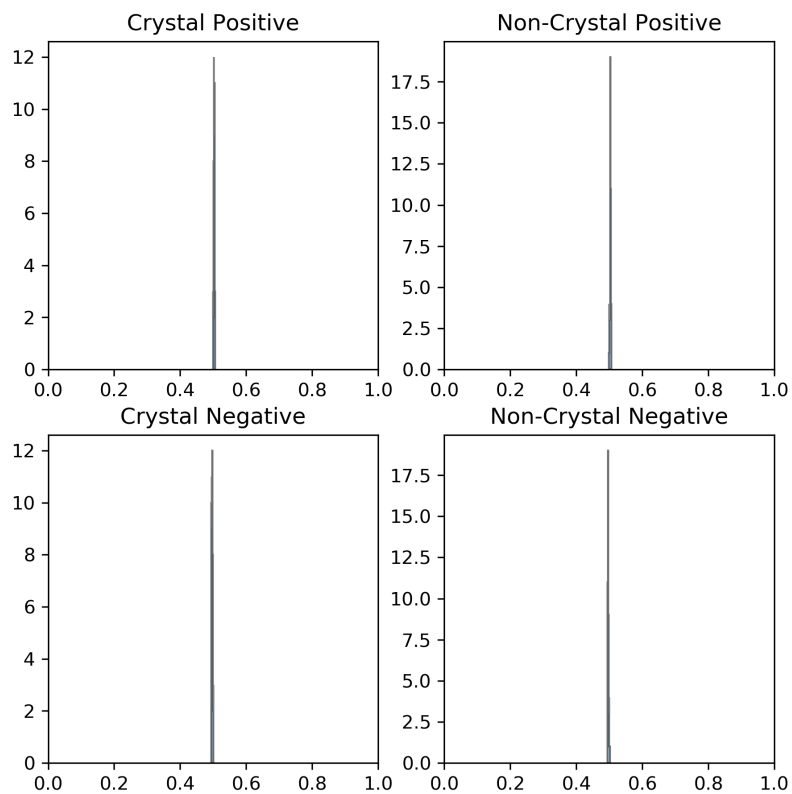
Figure 100. Histograms of validation set results for index 29 using CNNSRIM1.
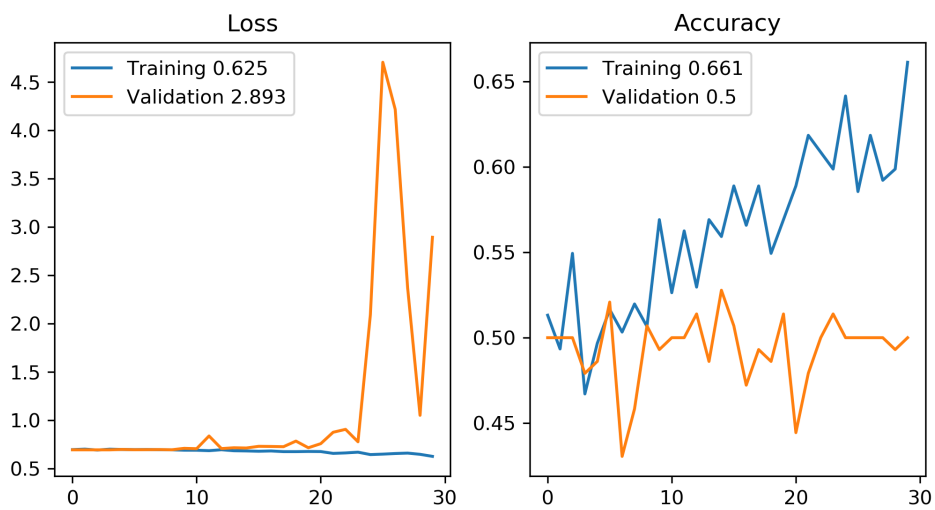
Figure 101. Chart of CNN training for index 29 using CNNSRIM1.
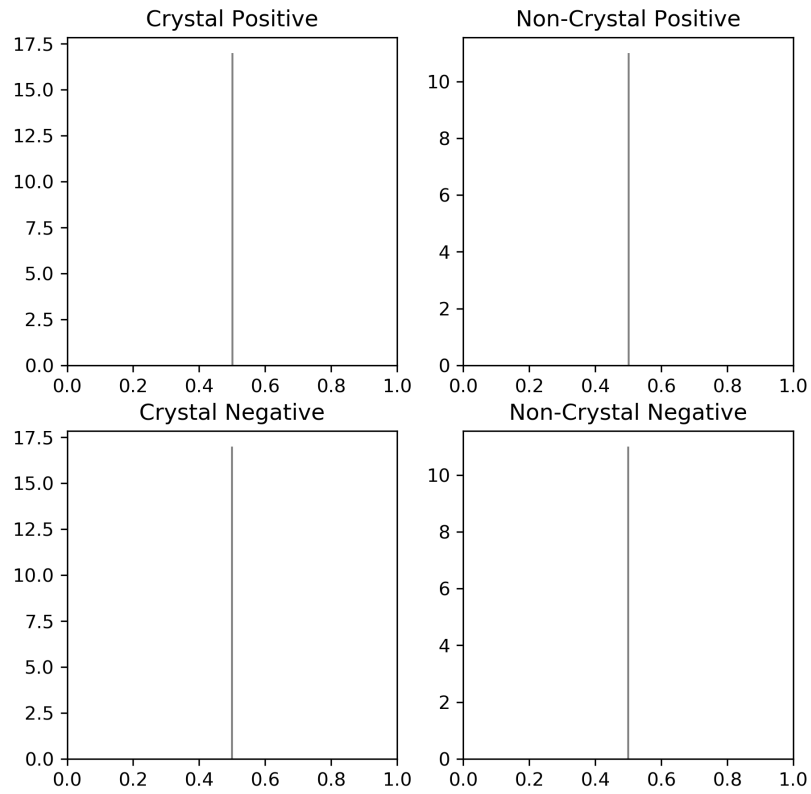
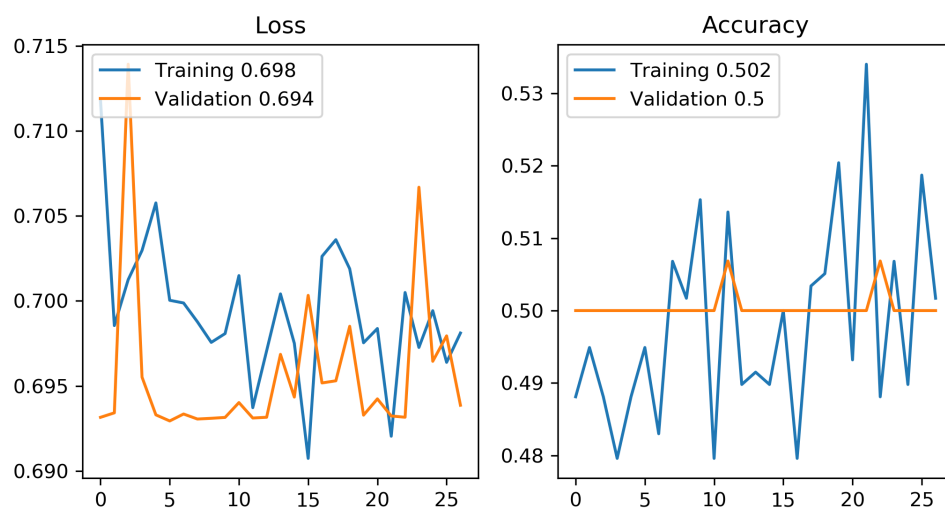Figure 102. Histograms of validation set results for index 30 using CNNSRIM1.
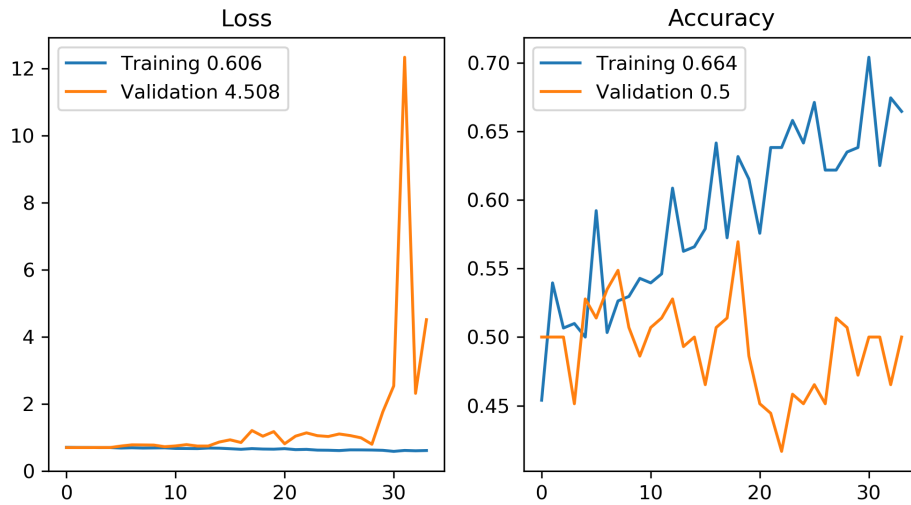
Figure 103. Chart of CNN training for index 30 using CNNSRIM1.
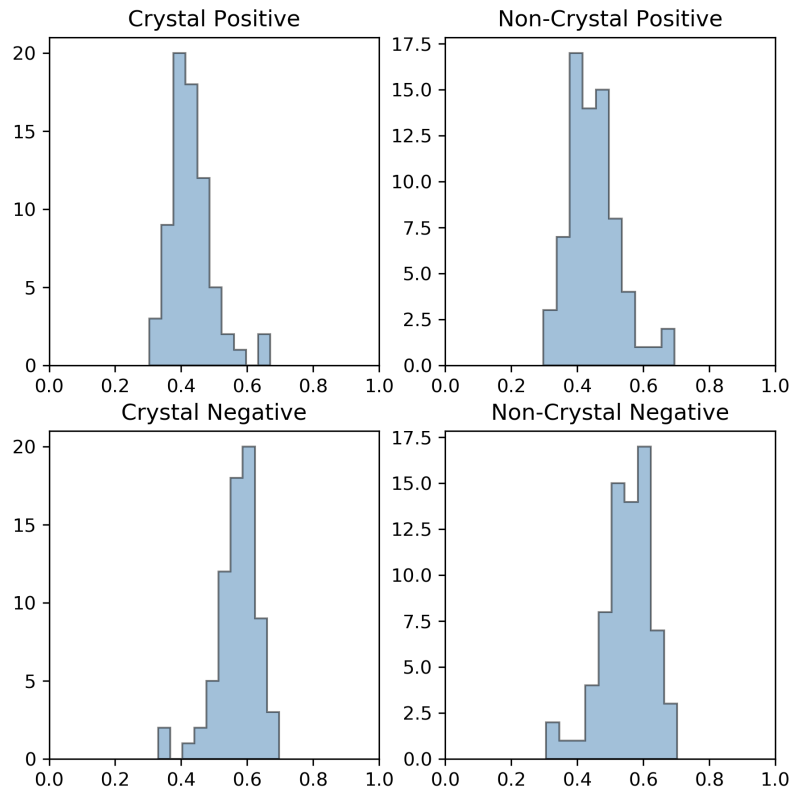
Figure 104. Histograms of validation set results for index 31 using CNNSRIM1.
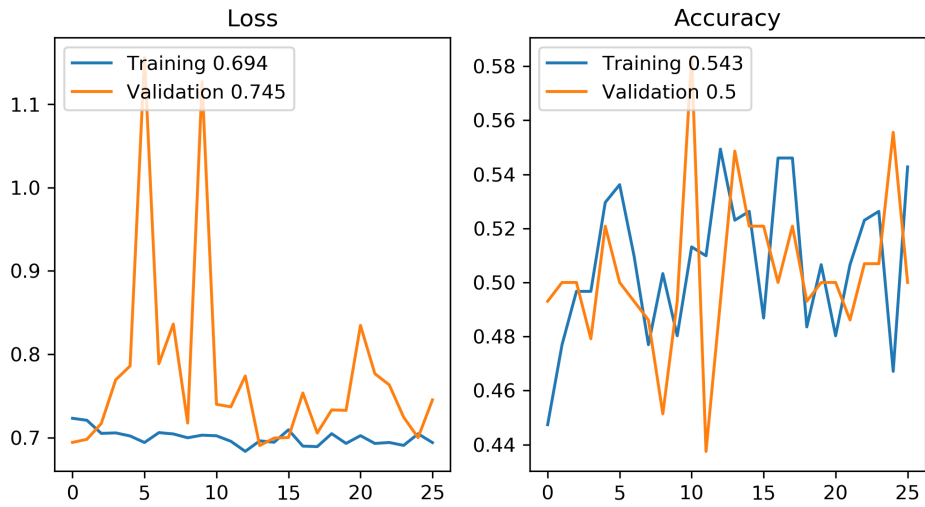
Figure 105. Chart of CNN training for index 31 using CNNSRIM1.
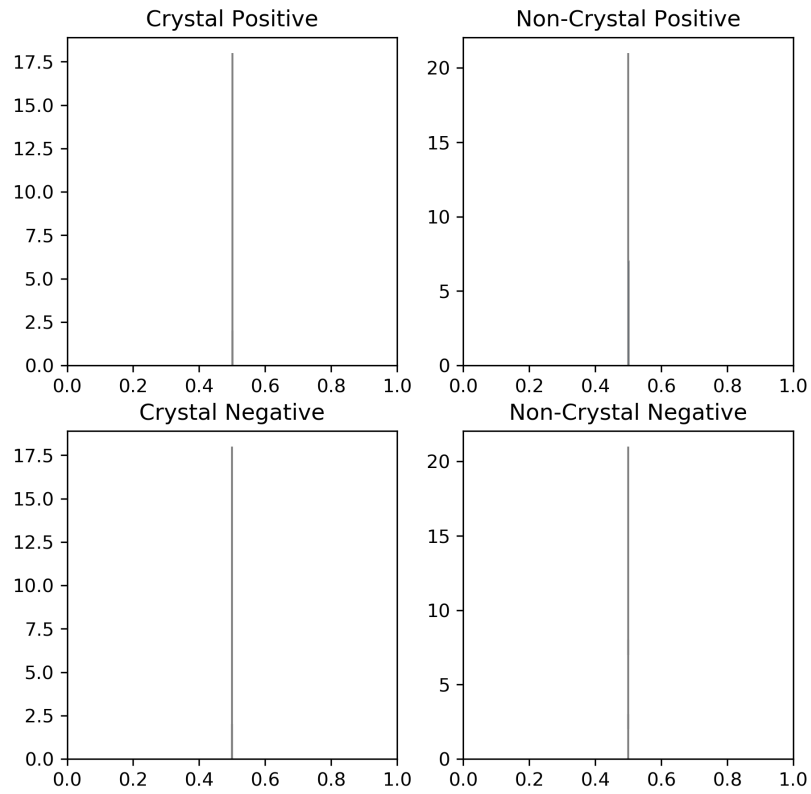
Figure 106. Histograms of validation set results for index 32 using CNNSRIM1.
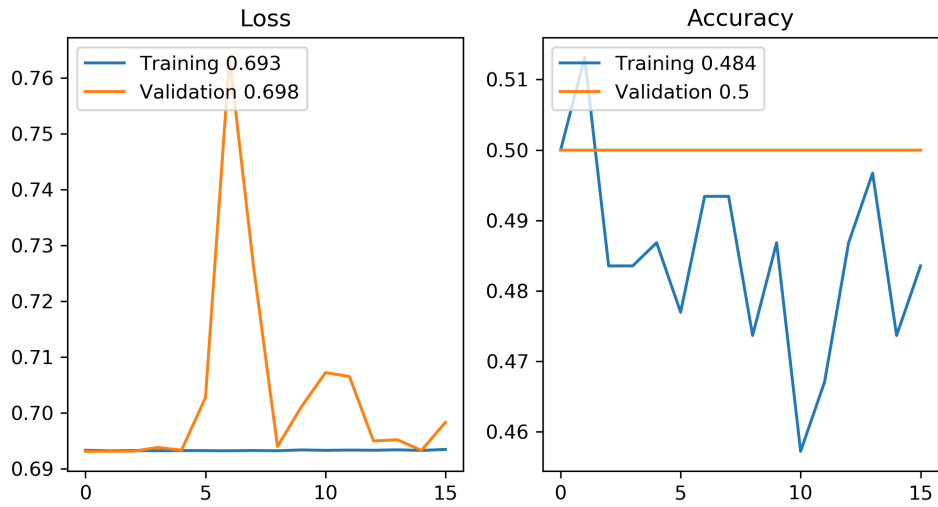
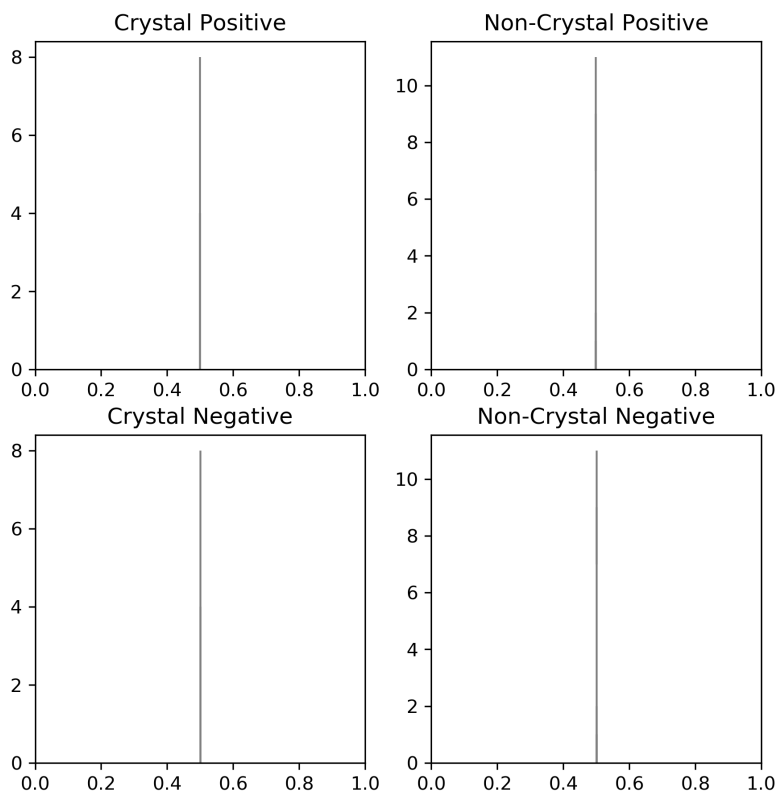Figure 107. Chart of CNN training for index 32 using CNNSRIM1.

APPENDIX D

CNNSRIM2 RESULTS
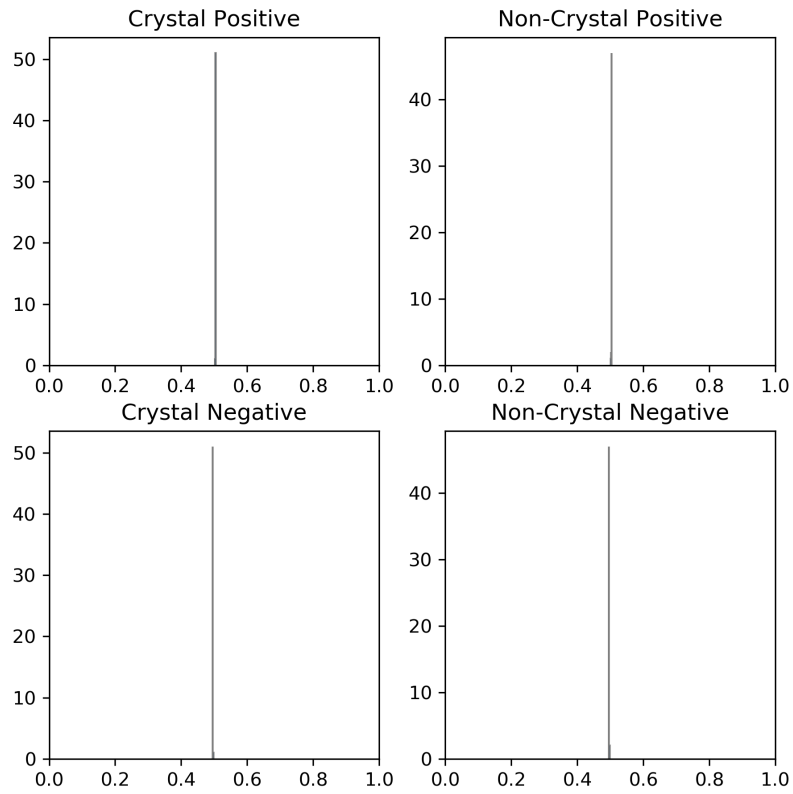
Figure 108. Histograms of validation set results for index 1 using CNNSRIM2.
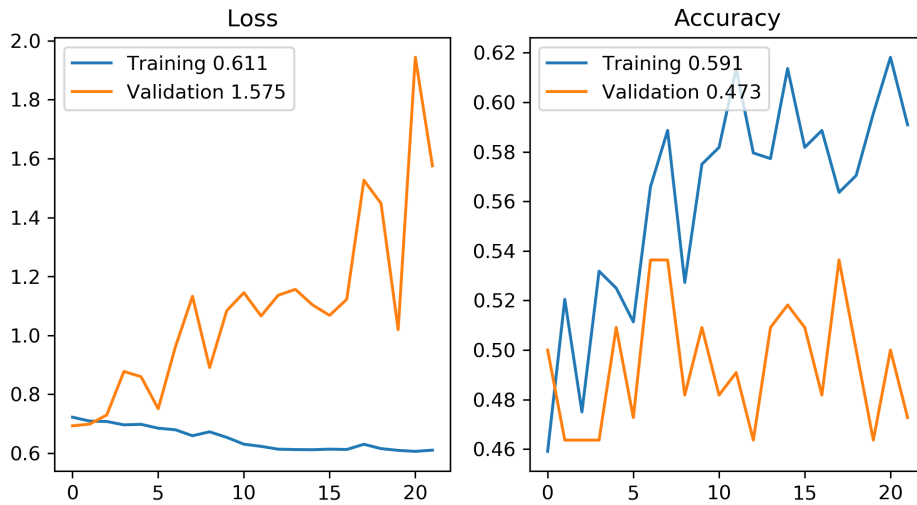
Figure 109. Chart of CNN training for index 1 using CNNSRIM2.
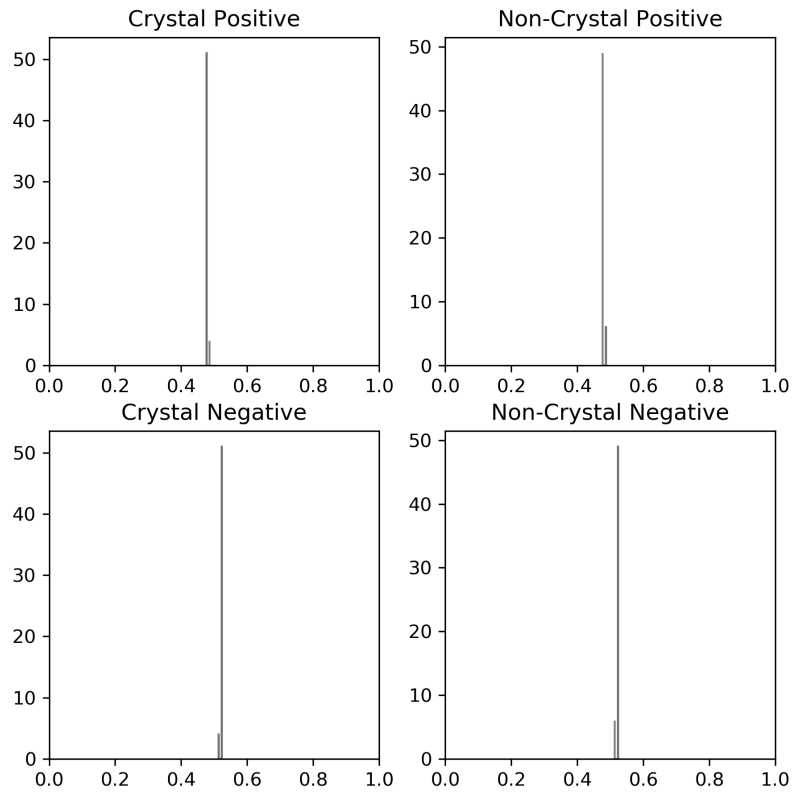
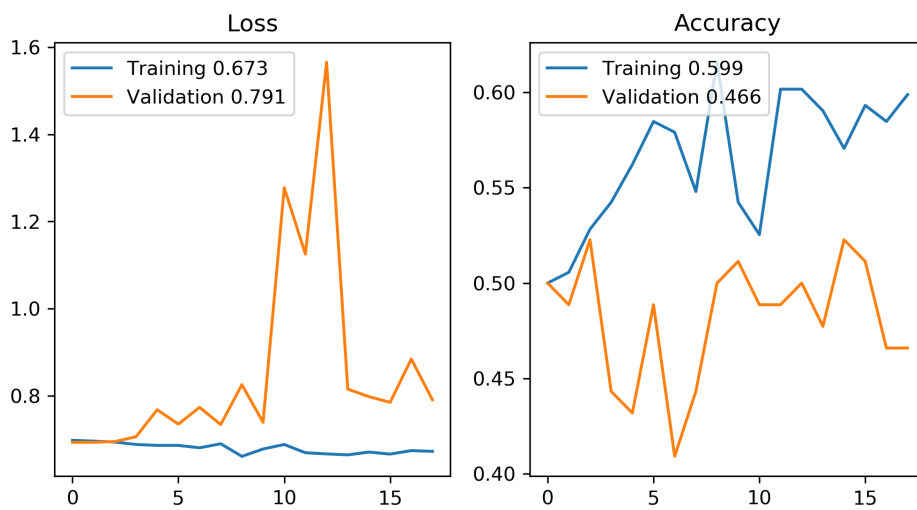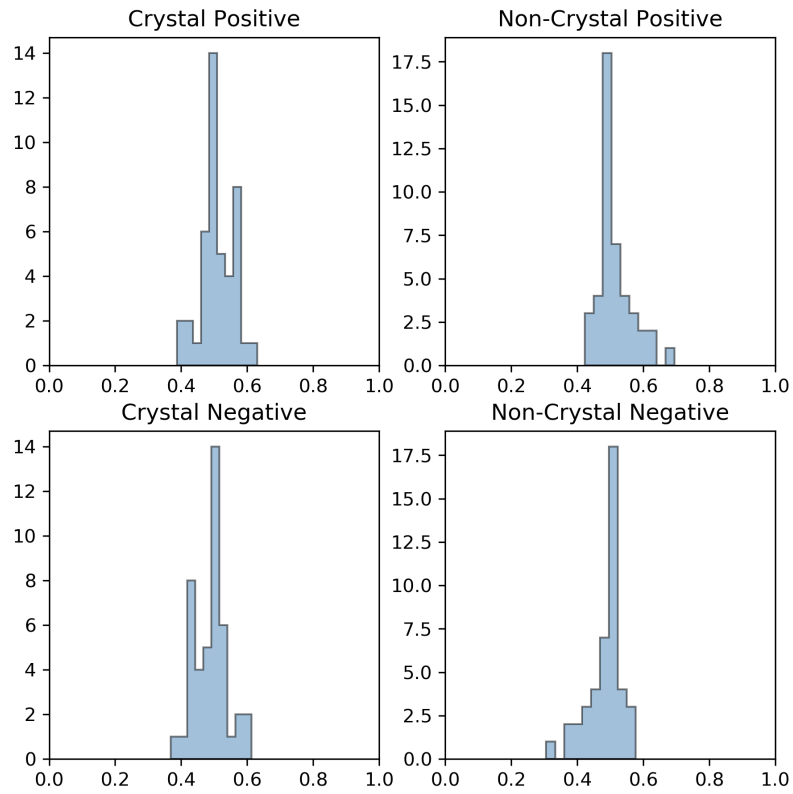Figure 110. Histograms of validation set results for index 2 using CNNSRIM2.
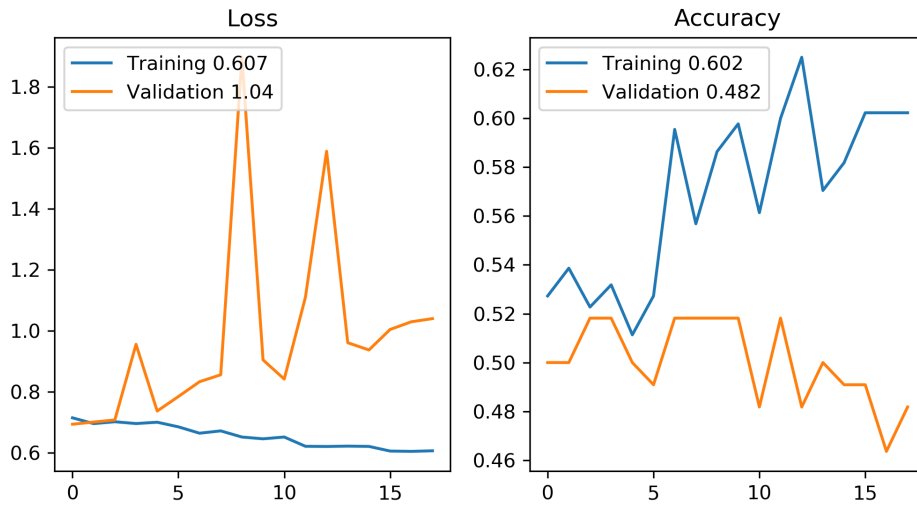
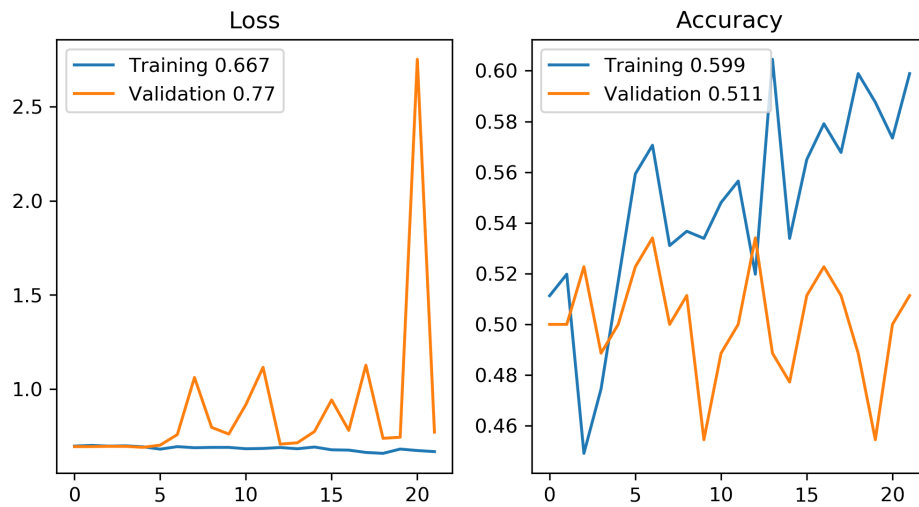Figure 111. Chart of CNN training for index 2 using CNNSRIM2.
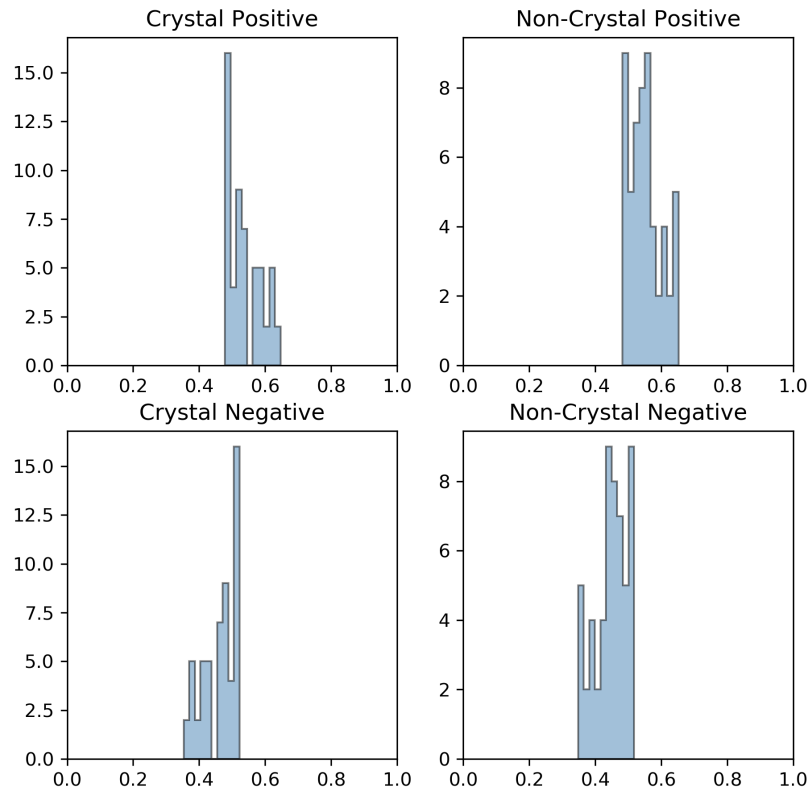
Figure 112. Histograms of validation set results for index 3 using CNNSRIM2.

Figure 113. Chart of CNN training for index 3 using CNNSRIM2.
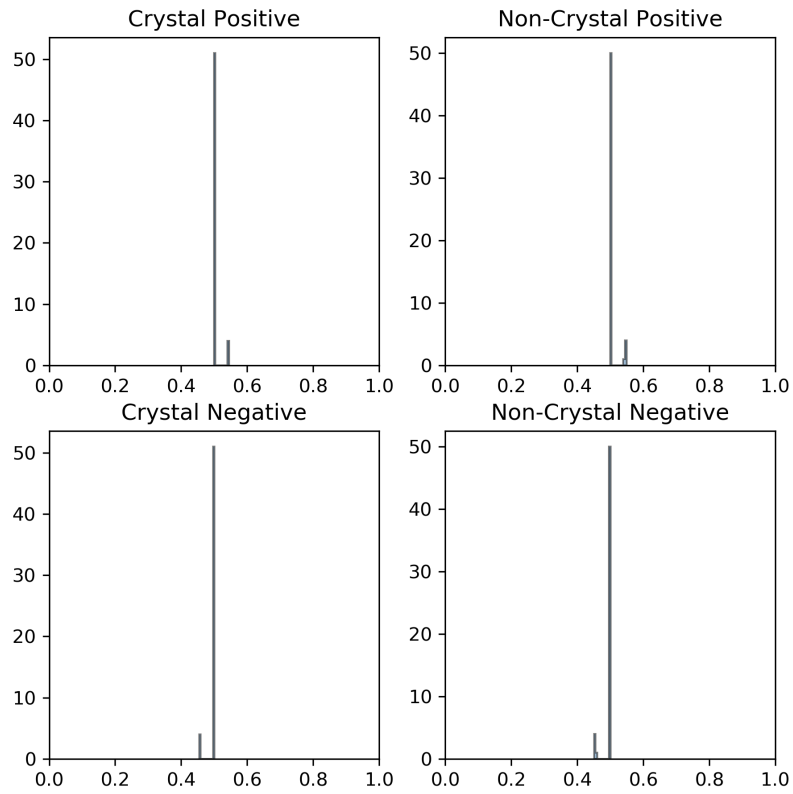
Figure 114. Histograms of validation set results for index 4 using CNNSRIM2.
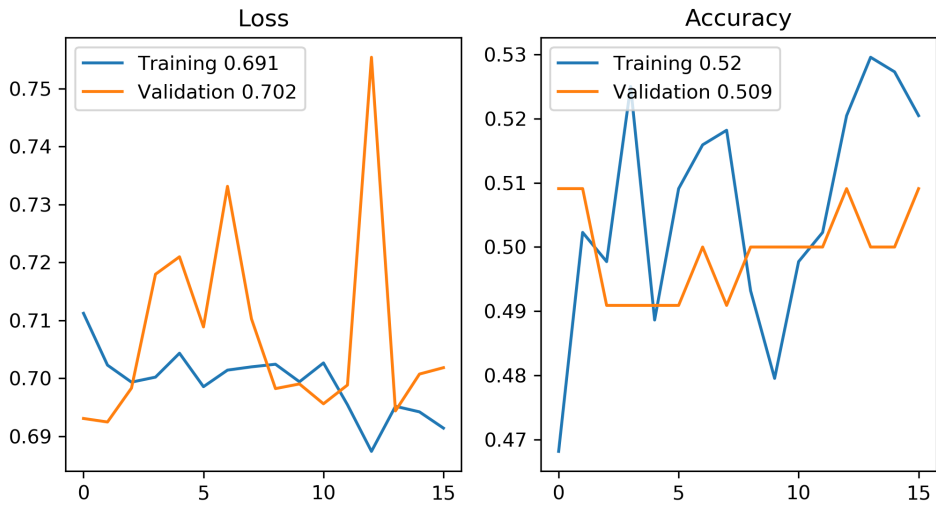
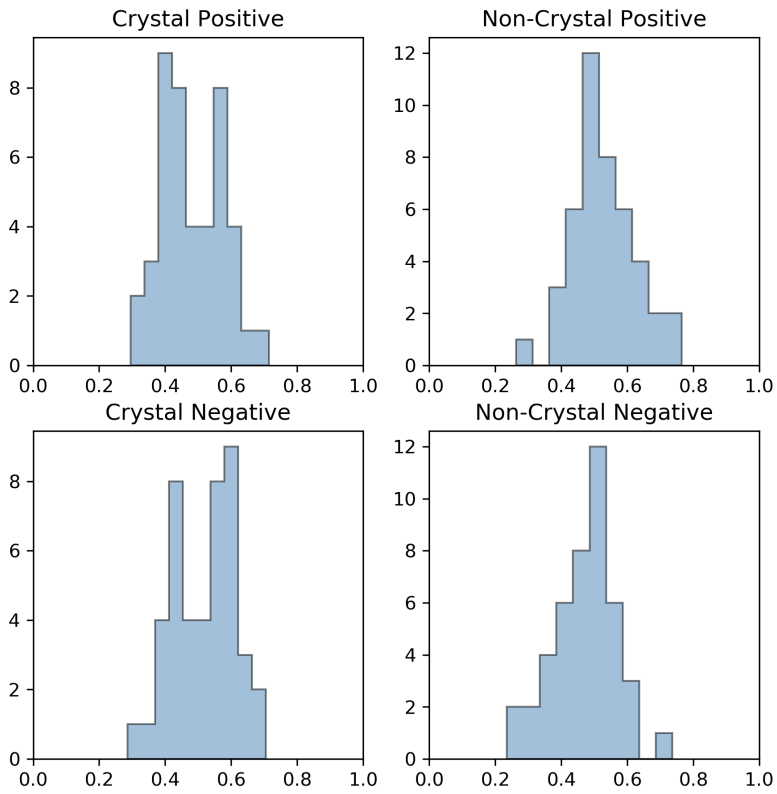Figure 115. Chart of CNN training for index 4 using CNNSRIM2.
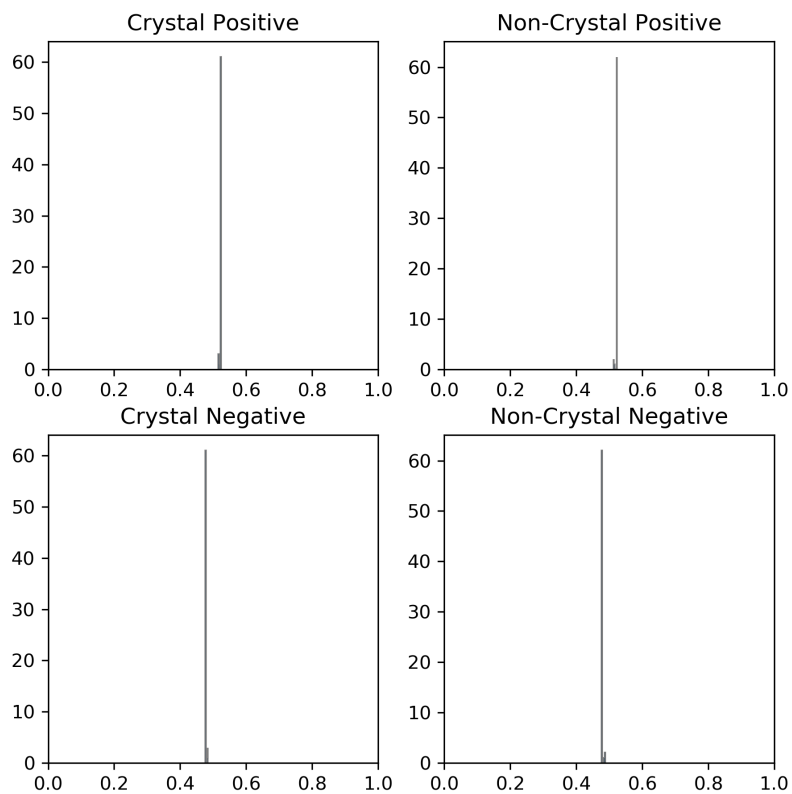
Figure 116. Histograms of validation set results for index 5 using CNNSRIM2.
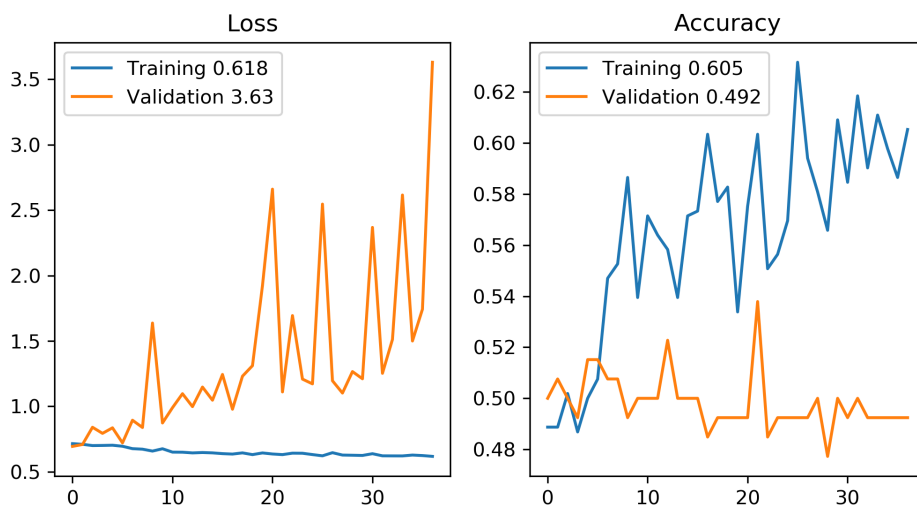
Figure 117. Chart of CNN training for index 5 using CNNSRIM2.
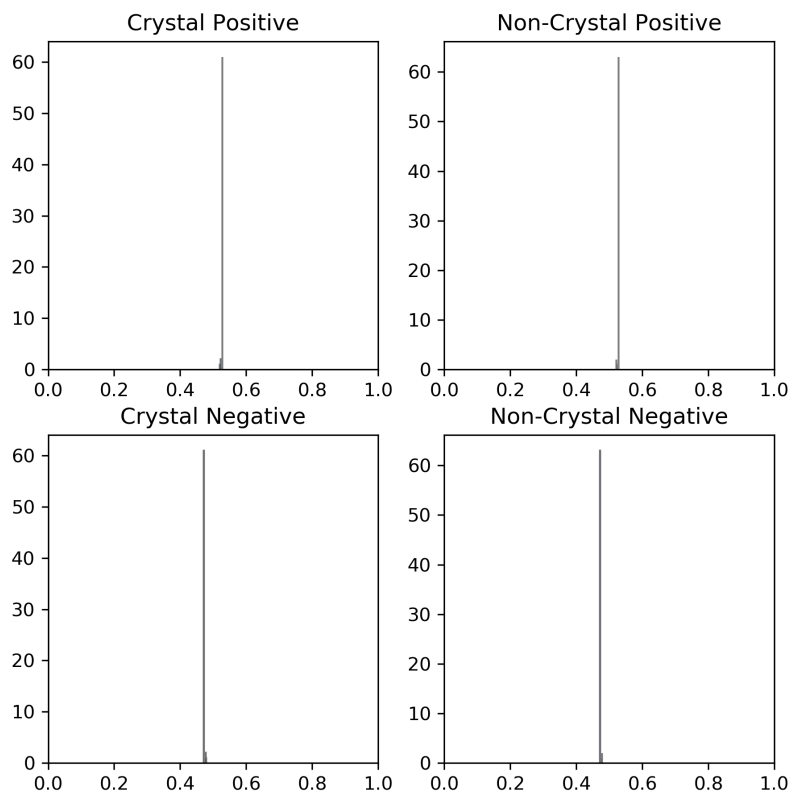
Figure 118. Histograms of validation set results for index 6 using CNNSRIM2.

Figure 119. Chart of CNN training for index 6 using CNNSRIM2.
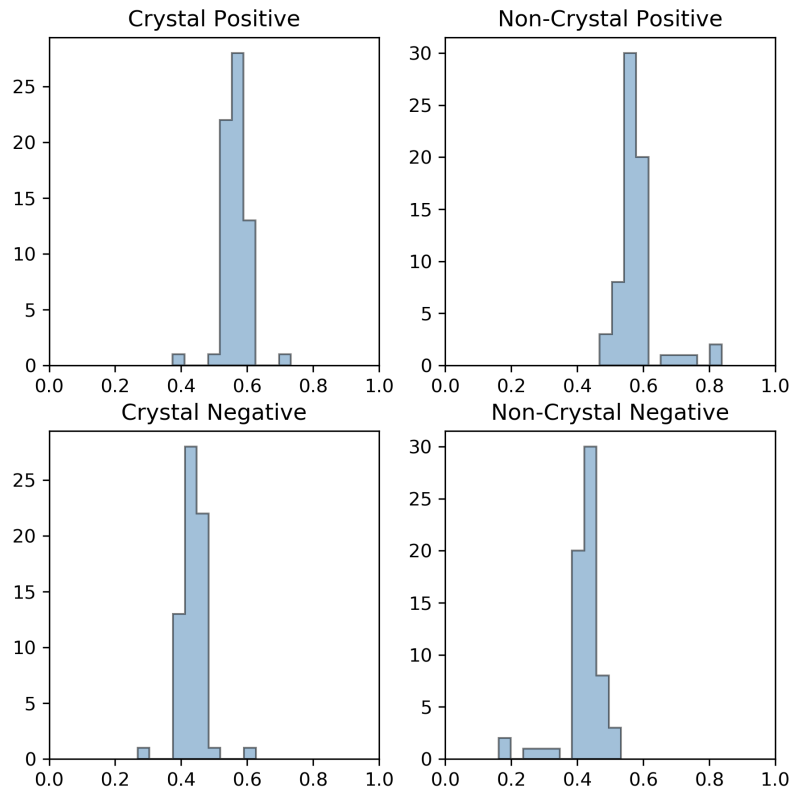
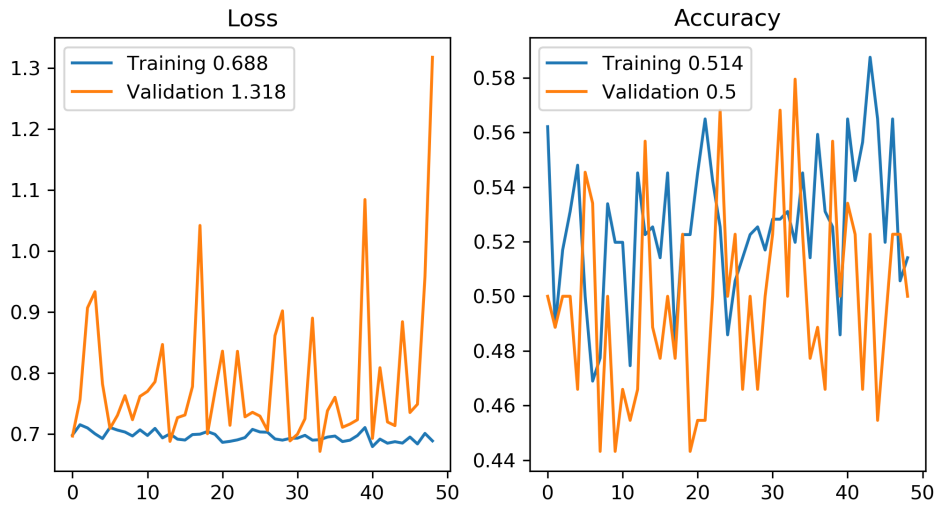Figure 120. Histograms of validation set results for index 7 using CNNSRIM2.
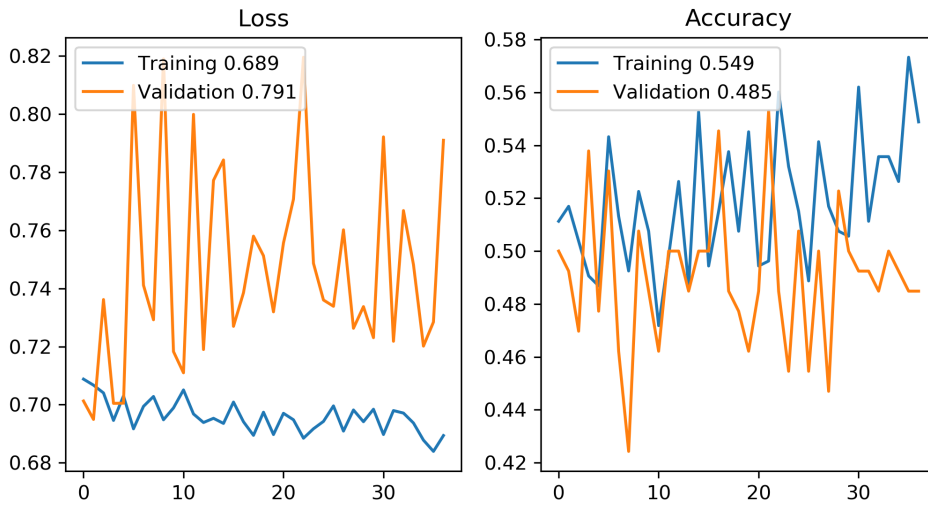
Figure 121. Chart of CNN training for index 7 using CNNSRIM2.
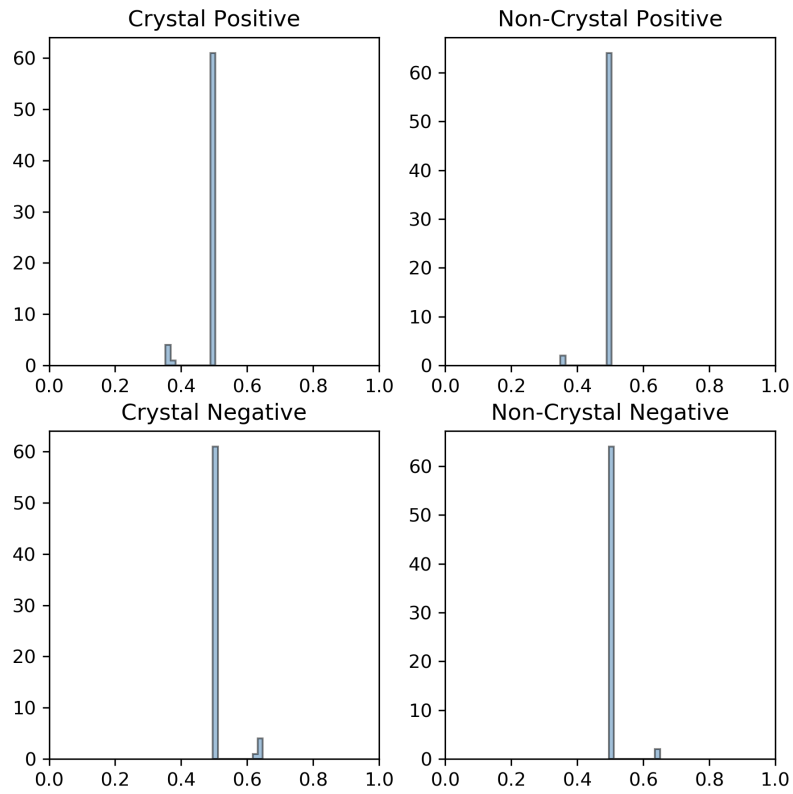
Figure 122. Histograms of validation set results for index 8 using CNNSRIM2.
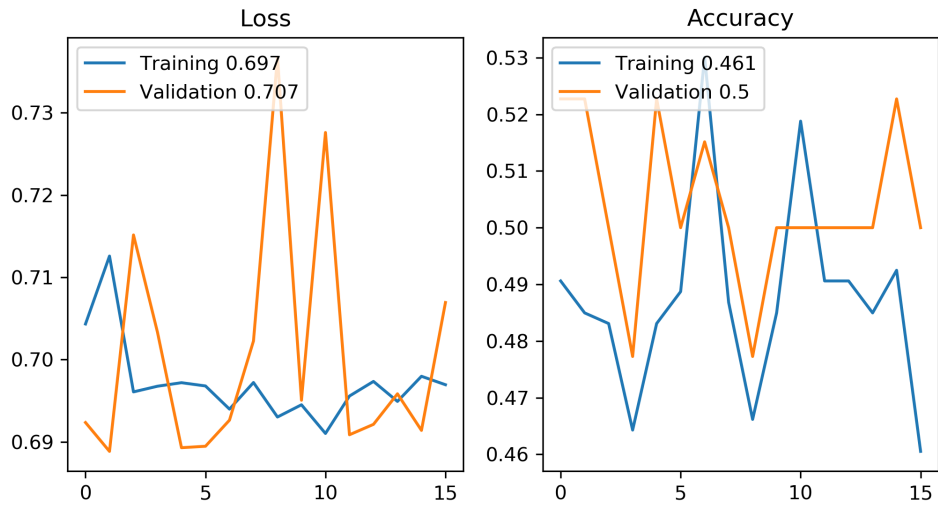
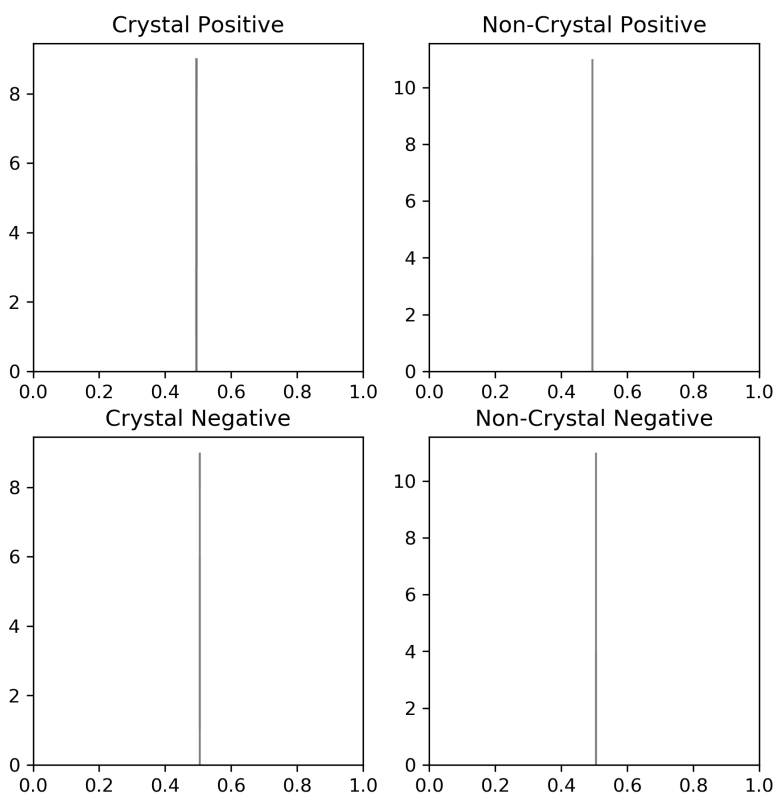Figure 123. Chart of CNN training for index 8 using CNNSRIM2.
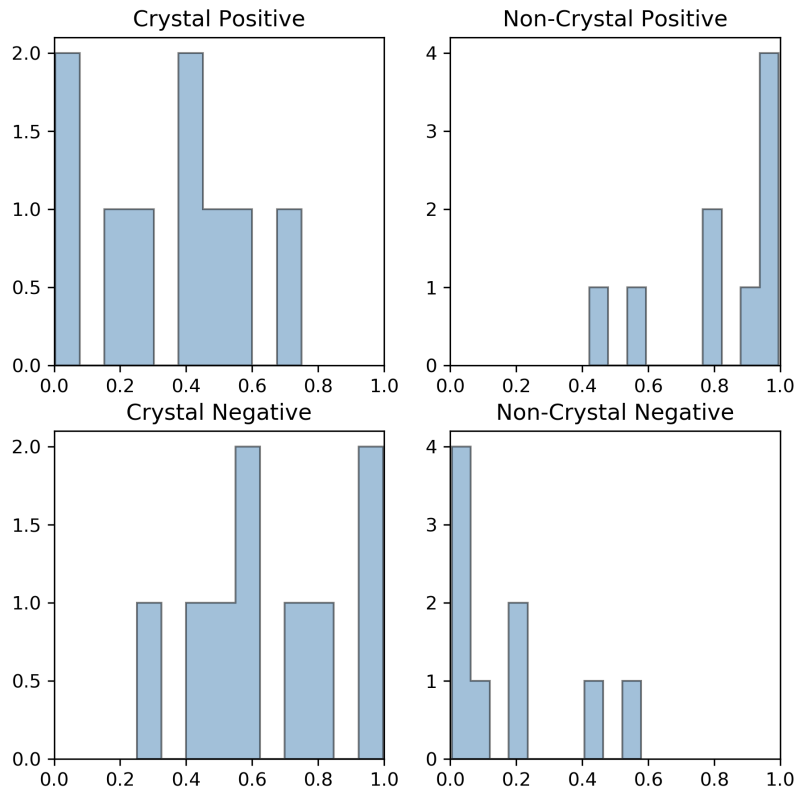
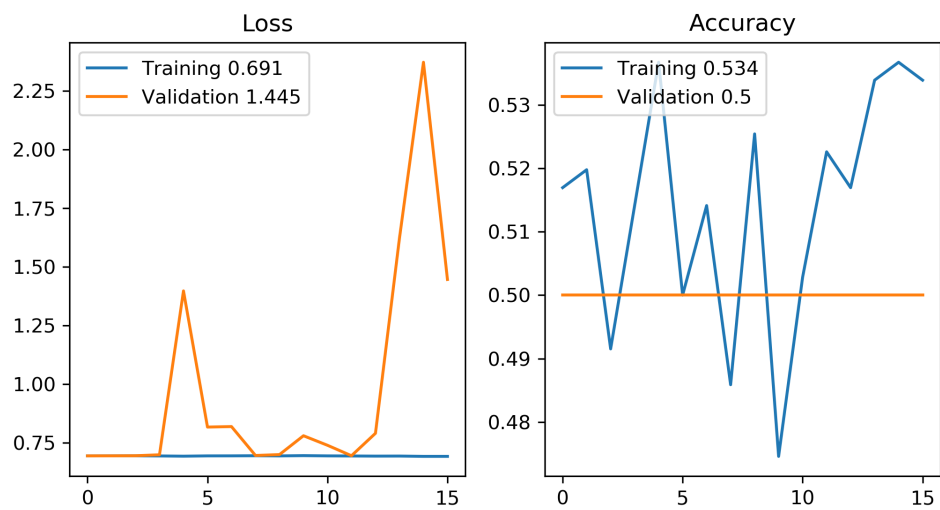Figure 124. Histograms of validation set results for index 9 using CNNSRIM2.
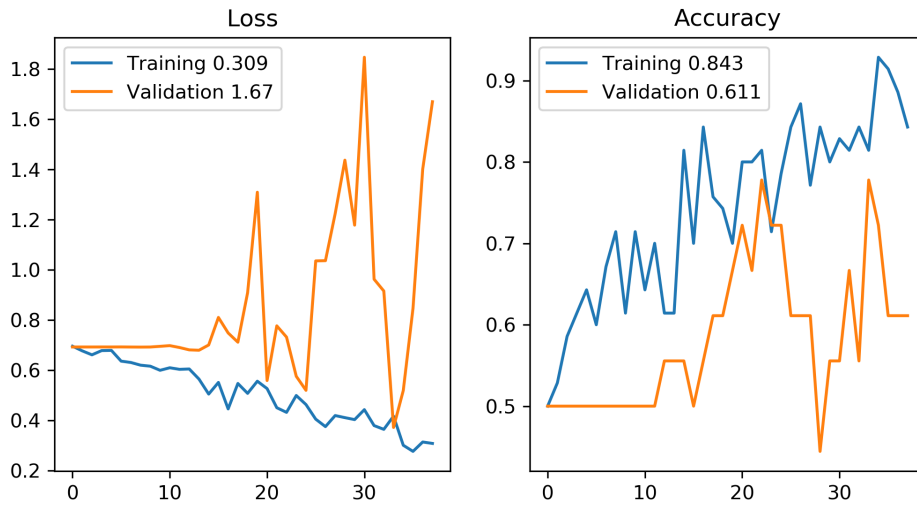
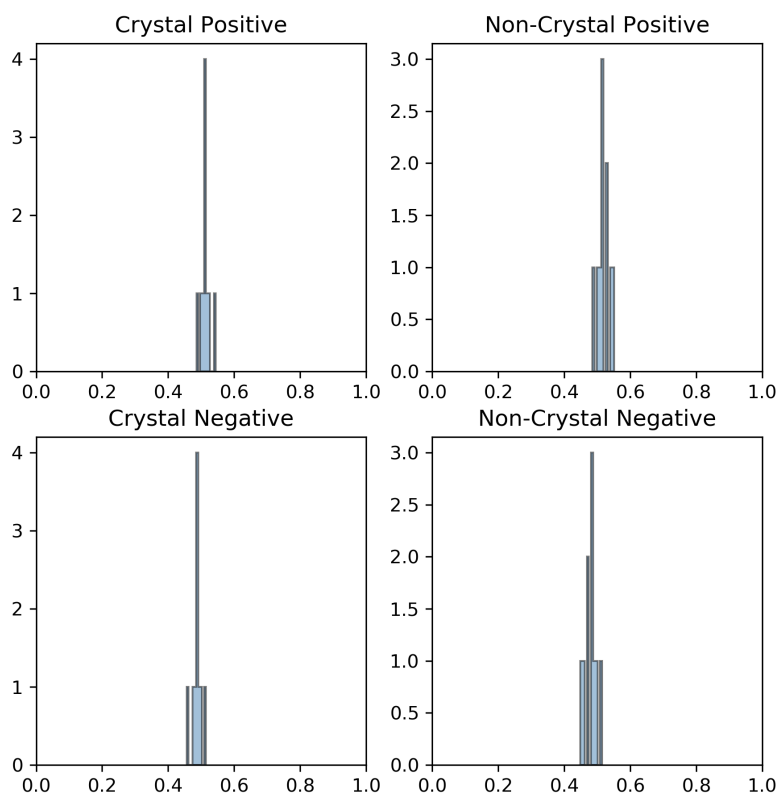Figure 125. Chart of CNN training for index 9 using CNNSRIM2.

Figure 126. Histograms of validation set results for index 10 using CNNSRIM2.

Figure 127. Chart of CNN training for index 10 using CNNSRIM2.

Figure 128. Histograms of validation set results for index 11 using CNNSRIM2.

Figure 129. Chart of CNN training for index 11 using CNNSRIM2.

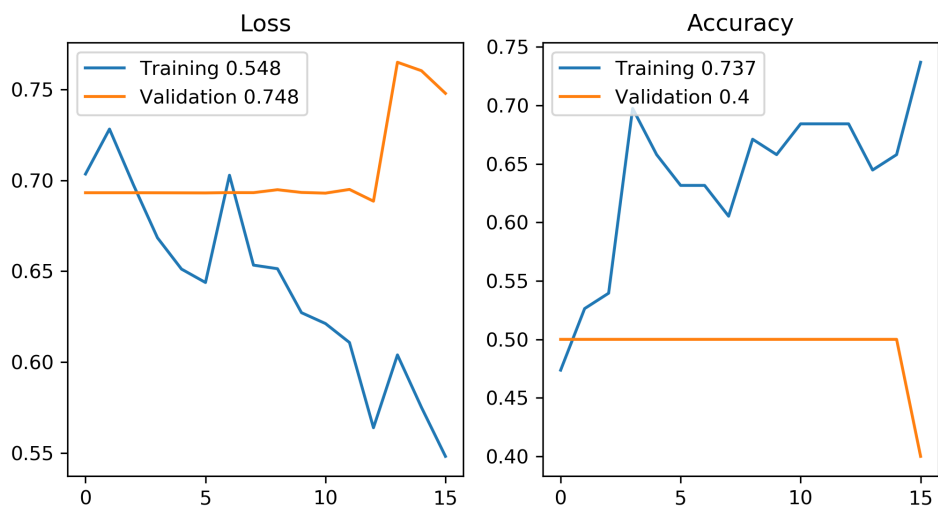Figure 130. Histograms of validation set results for index 12 using CNNSRIM2.

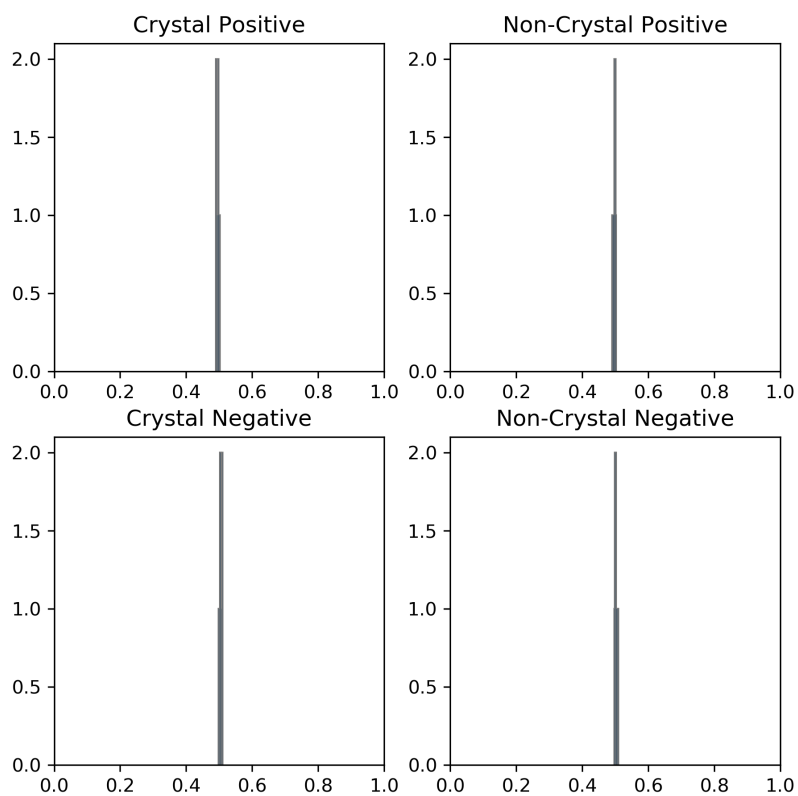Figure 131. Chart of CNN training for index 12 using CNNSRIM2.

Figure 132. Histograms of validation set results for index 13 using CNNSRIM2.

Figure 133. Chart of CNN training for index 13 using CNNSRIM2.

Figure 134. Histograms of validation set results for index 14 using CNNSRIM2.

Figure 135. Chart of CNN training for index 14 using CNNSRIM2.

Figure 136. Histograms of validation set results for index 15 using CNNSRIM2.

Figure 137. Chart of CNN training for index 15 using CNNSRIM2.

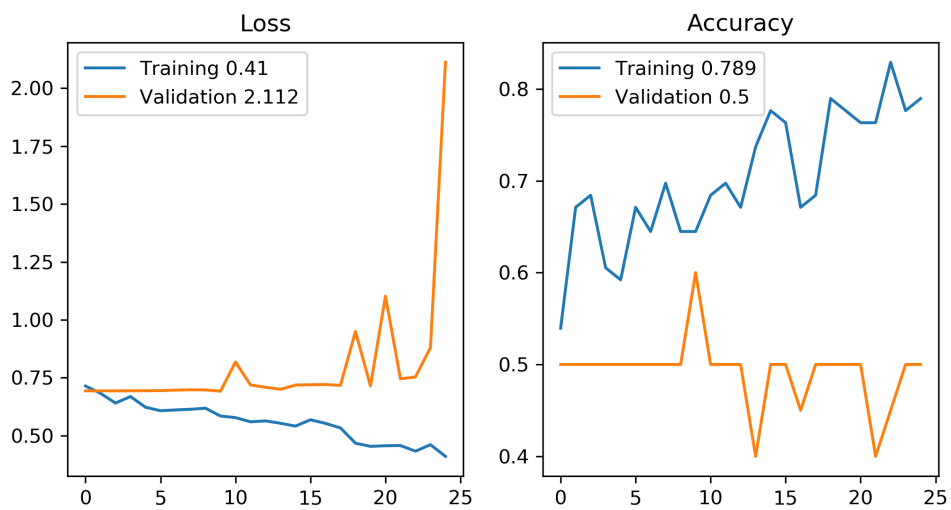Figure 138. Histograms of validation set results for index 16 using CNNSRIM2.

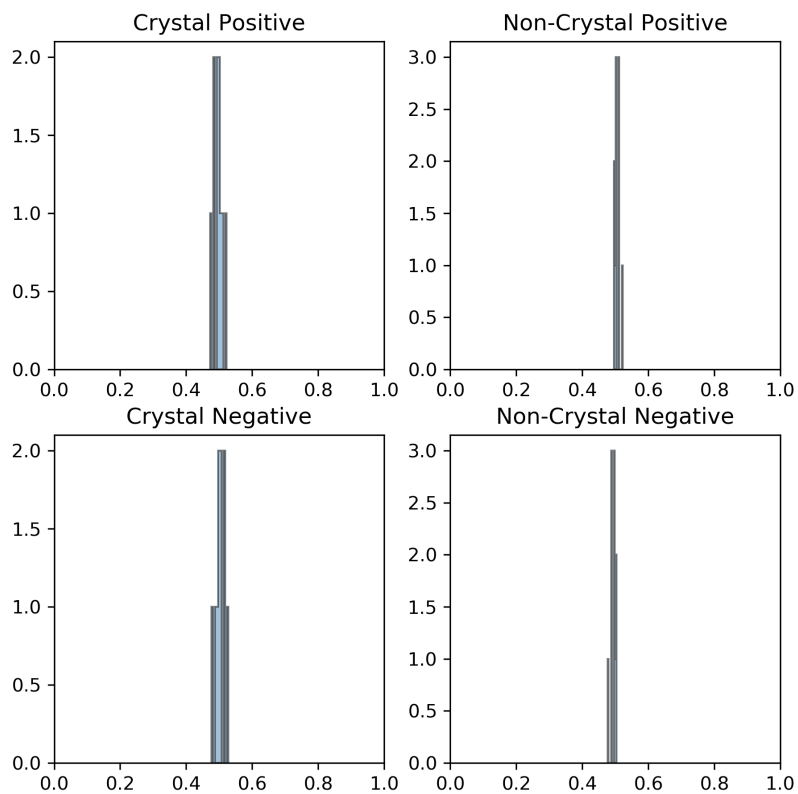Figure 139. Chart of CNN training for index 16 using CNNSRIM2.

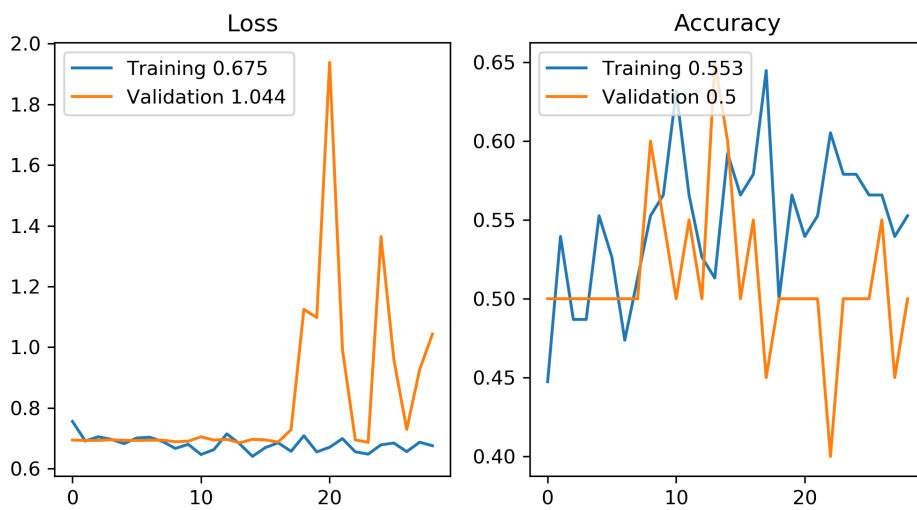Figure 140. Histograms of validation set results for index 17 using CNNSRIM2.

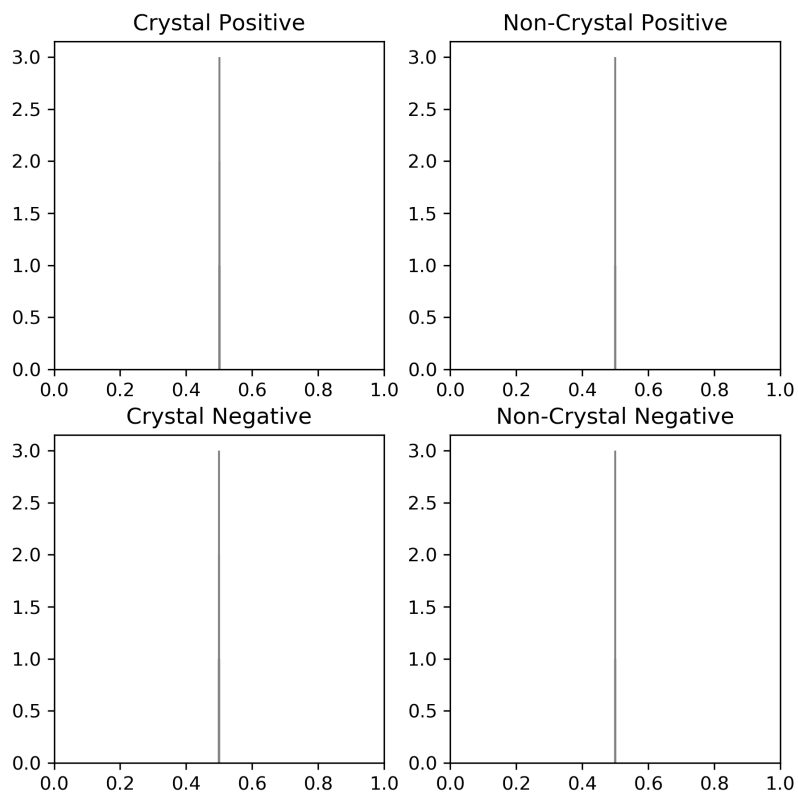Figure 141. Chart of CNN training for index 17 using CNNSRIM2.

Figure 142. Histograms of validation set results for index 18 using CNNSRIM2.

Figure 143. Chart of CNN training for index 18 using CNNSRIM2.

Figure 144. Histograms of validation set results for index 19 using CNNSRIM2.

Figure 145. Chart of CNN training for index 19 using CNNSRIM2.

Figure 146. Histograms of validation set results for index 20 using CNNSRIM2.

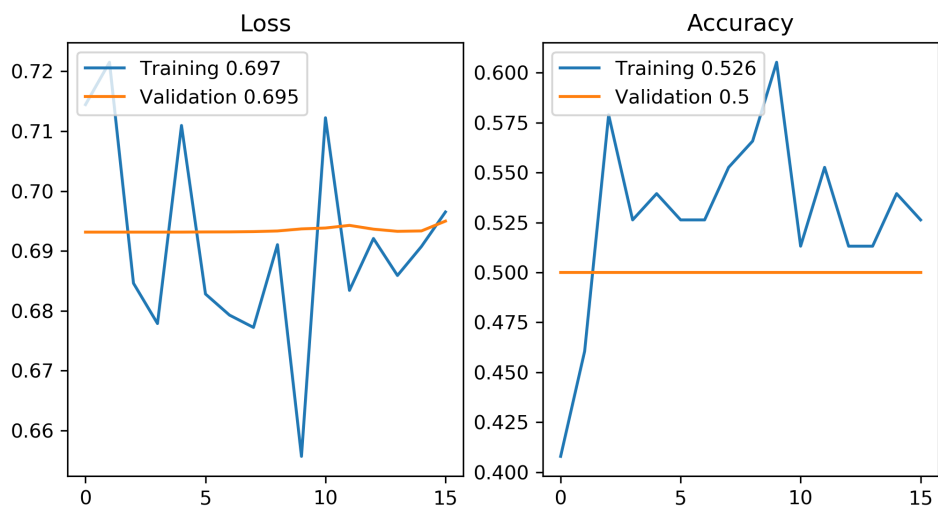Figure 147. Chart of CNN training for index 20 using CNNSRIM2.

Figure 148. Histograms of validation set results for index 21 using CNNSRIM2.

Figure 149. Chart of CNN training for index 21 using CNNSRIM2.

Figure 150. Histograms of validation set results for index 22 using CNNSRIM2.

Figure 151. Chart of CNN training for index 22 using CNNSRIM2.

Figure 152. Histograms of validation set results for index 23 using CNNSRIM2.

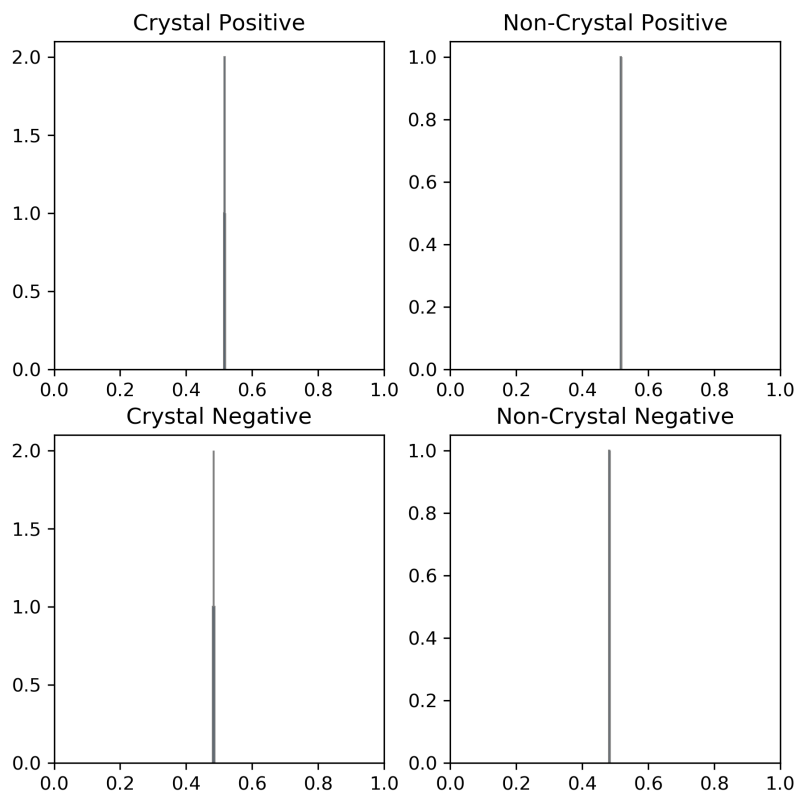Figure 153. Chart of CNN training for index 23 using CNNSRIM2.

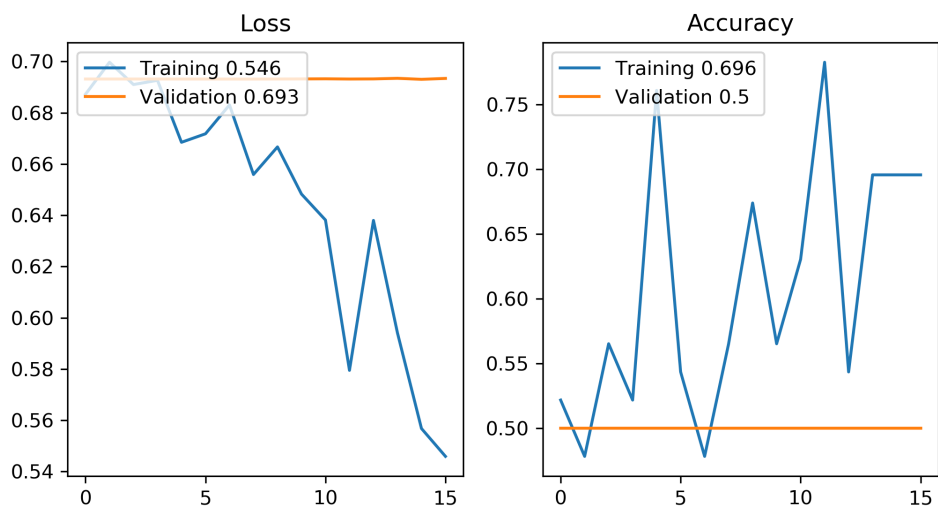Figure 154. Histograms of validation set results for index 24 using CNNSRIM2.

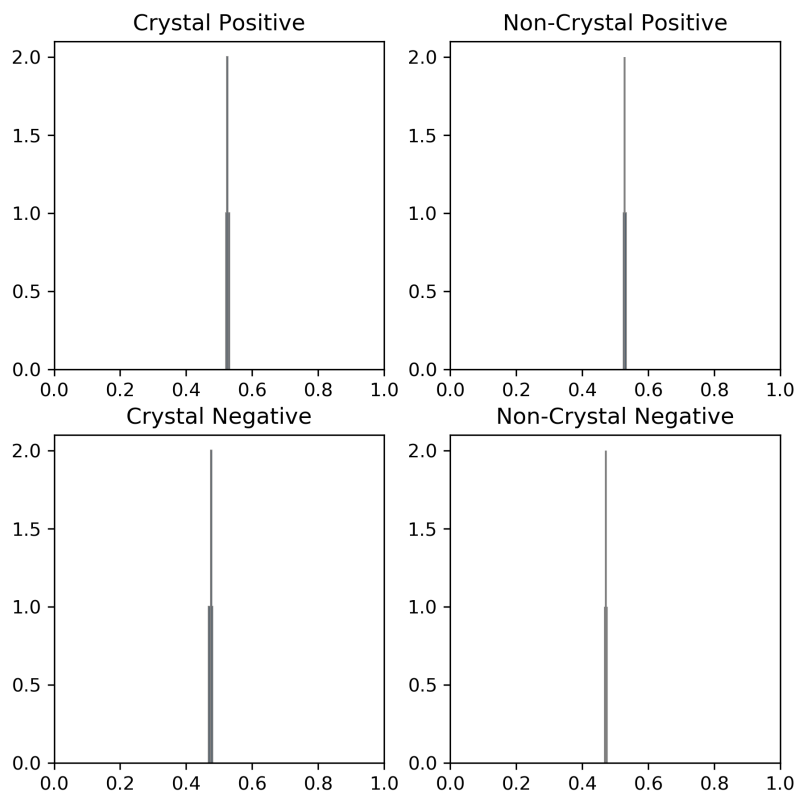Figure 155. Chart of CNN training for index 24 using CNNSRIM2.

Figure 156. Histograms of validation set results for index 25 using CNNSRIM2.

Figure 157. Chart of CNN training for index 25 using CNNSRIM2.

Figure 158. Histograms of validation set results for index 26 using CNNSRIM2.

Figure 159. Chart of CNN training for index 26 using CNNSRIM2.

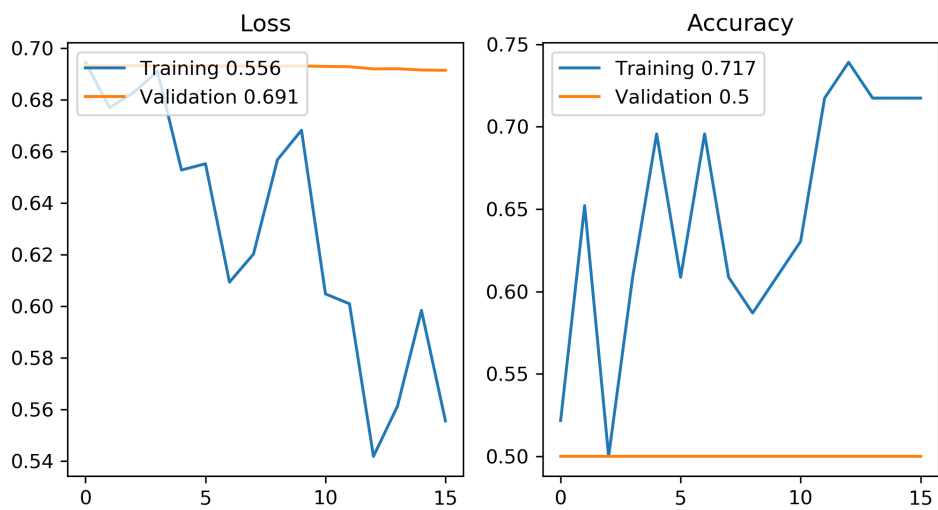Figure 160. Histograms of validation set results for index 27 using CNNSRIM2.

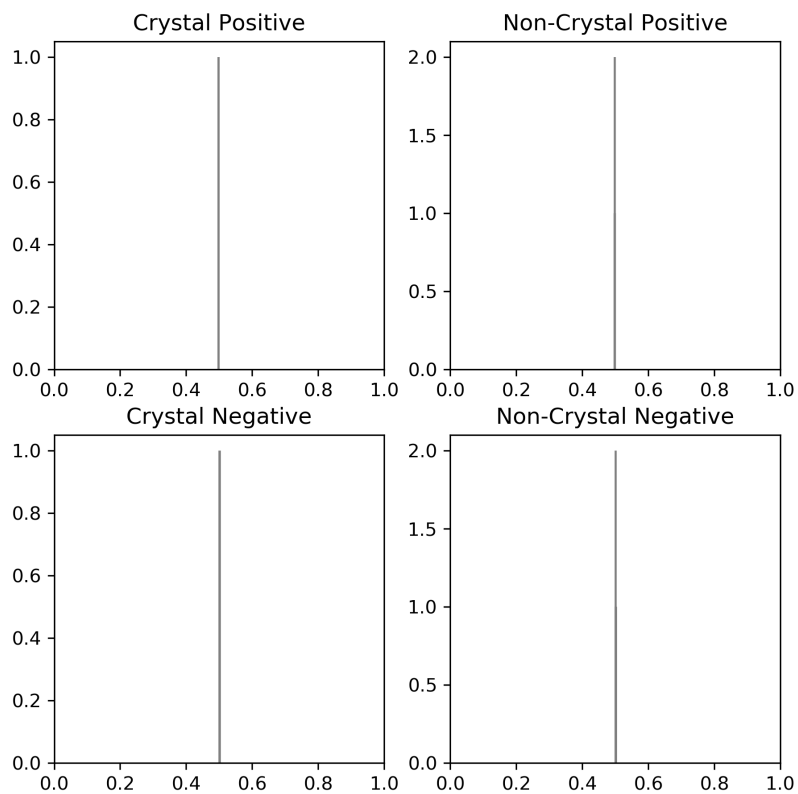Figure 161. Chart of CNN training for index 27 using CNNSRIM2.

Figure 162. Histograms of validation set results for index 28 using CNNSRIM2.

Figure 163. Chart of CNN training for index 28 using CNNSRIM2.

187

Figure 164. Histograms of validation set results for index 29 using CNNSRIM2.

Figure 165. Chart of CNN training for index 29 using CNNSRIM2.

Figure 166. Histograms of validation set results for index 30 using CNNSRIM2.

Figure 167. Chart of CNN training for index 30 using CNNSRIM2.

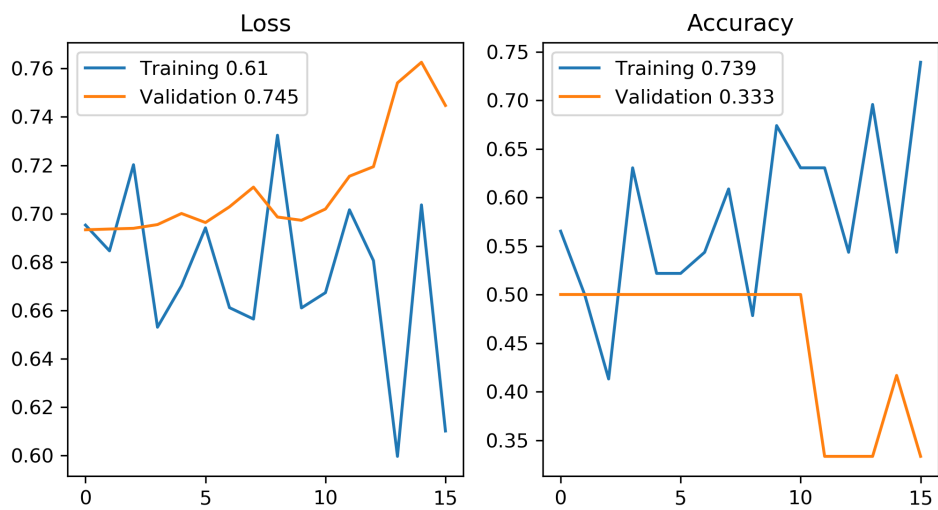Figure 168. Histograms of validation set results for index 31 using CNNSRIM2.

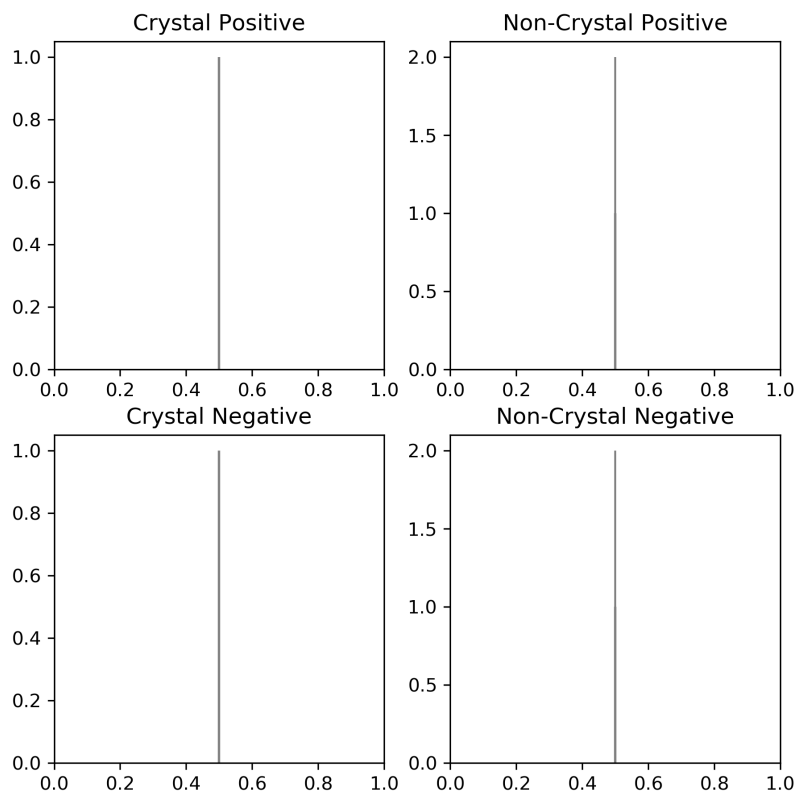Figure 169. Chart of CNN training for index 31 using CNNSRIM2.

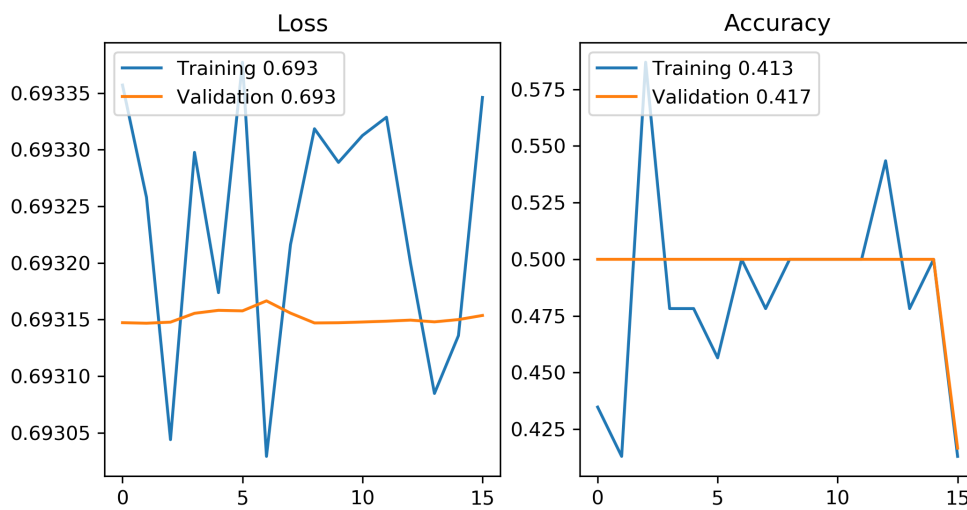Figure 170. Histograms of validation set results for index 32 using CNNSRIM2.

Figure 171. Chart of CNN training for index 32 using CNNSRIM2.